



# **Magnetic Resonant Reflectometry on Exchange Bias Systems**

Sebastian Brück



# Magnetic Resonant Reflectometry on Exchange Bias Systems

Von der Fakultät Mathematik und Physik der Universität Stuttgart  
zur Erlangung der Würde eines Doktors der  
Naturwissenschaften (Dr. rer. nat.) genehmigte Abhandlung

Vorgelegt von  
Sebastian Brück  
aus Tübingen

Hauptberichter: Prof. Dr. G. Schütz  
Mitberichter: Prof. Dr. J. Wrachtrup

Tag der mündlichen Prüfung: 26. Juni 2009

Max-Planck-Institut für Metallforschung, Stuttgart

2009



# Contents

|          |  |           |
|----------|--|-----------|
| <b>1</b> | <b>Zusammenfassung der Arbeit</b>                                | <b>7</b>  |
| <b>2</b> | <b>Introduction</b>  | <b>15</b> |
| <b>3</b> | <b>Scientific Background</b>                                     | <b>19</b> |
| 3.1      | Magnetism . . . . .  | 21        |
| 3.1.1    | Exchange Interaction – Collective Magnetism . . . . .            | 22        |
| 3.1.2    | Magnetocrystalline Anisotropy . . . . .                          | 28        |
| 3.1.3    | Bloch- & Néel- Domain Walls . . . . .                            | 29        |
| 3.1.4    | Stoner-Wohlfahrt Model . . . . .                                 | 33        |
| 3.2      | Exchange Anisotropy . . . . .                                    | 36        |
| 3.2.1    | Phenomenology of Exchange Bias . . . . .                         | 37        |
| 3.2.2    | Theoretical Considerations . . . . .                             | 45        |
| 3.2.3    | The Interface – a Spin Glass . . . . .                           | 51        |
| 3.2.4    | Stability of the Antiferromagnet – Training & Blocking . . . . . | 55        |
| 3.3      | Resonant Scattering & Magnetic Circular Dichroism . . . . .      | 59        |
| 3.3.1    | A Scattering Formalism for X-rays . . . . .                      | 60        |
| 3.3.2    | Non-Resonant Magnetic Scattering . . . . .                       | 63        |
| 3.3.3    | Resonant Magnetic Scattering . . . . .                           | 64        |
| 3.3.4    | X-ray Magnetic Circular Dichroism . . . . .                      | 68        |
| 3.4      | Magnetic Reflectivity . . . . .                                  | 73        |
| 3.4.1    | Reflectivity & Scattering Geometry . . . . .                     | 74        |
| 3.4.2    | Magneto Optical Description . . . . .                            | 77        |
| <b>4</b> | <b>Aspects of Data Processing</b>                                | <b>89</b> |
| 4.1      | Processing of Reflectivity Data . . . . .                        | 90        |
| 4.2      | The Optical Constants . . . . .                                  | 92        |

|          |  |            |
|----------|--|------------|
| 4.3      | Correction of the Sample Illumination . . . . .                    | 98         |
| <b>5</b> | <b>XRMR on Exchange Bias Systems</b>                               | <b>103</b> |
| 5.1      | Pinned and Rotatable Moments in MnPd/Fe . . . . .                  | 105        |
| 5.1.1    | Preparation of the Samples . . . . .                               | 107        |
| 5.1.2    | Crystallographic & Magnetometric Characterization . . . . .        | 107        |
| 5.1.3    | X-ray Absorption Spectroscopy and Optical Constants . . . . .      | 109        |
| 5.1.4    | Structural Characterization . . . . .                              | 116        |
| 5.1.5    | Magnetic Reflectivity . . . . .                                    | 118        |
| 5.1.6    | The Problem of Measuring Pinned Moments . . . . .                  | 121        |
| 5.1.7    | Rotatable Magnetic Moments in a-Axis MnPd . . . . .                | 122        |
| 5.1.8    | Pinned Uncompensated Mn Moments in a-Axis MnPd . . . . .           | 126        |
| 5.1.9    | Significance & Validity of XRMR of Localized Moments . . . . .     | 130        |
| 5.1.10   | Fe NEXAFS for Samples FD041, 042 and 043 . . . . .                 | 133        |
| 5.1.11   | Chemical Profile of FD042 and FD043 Compared to FD041 . . . . .    | 136        |
| 5.1.12   | Effect of the Interfacial Roughness on the Reflectance . . . . .   | 139        |
| 5.1.13   | FD042 & FD043 – Magnetic Reflectivity of Manganese . . . . .       | 141        |
| 5.1.14   | Conclusions for MnPd . . . . .                                     | 142        |
| 5.2      | Orbital Moments in FeMn and Their Role for Exchange Bias . . . . . | 144        |
| 5.2.1    | Preparation . . . . .  | 147        |
| 5.2.2    | TEM Investigation . . . . .  | 149        |
| 5.2.3    | Magnetometry . . . . .   | 151        |
| 5.2.4    | Co XAS and & XMCD of Sample SP032 . . . . .                        | 154        |
| 5.2.5    | Absorption Spectroscopy & XMCD for FeMn . . . . .                  | 156        |
| 5.2.6    | Optical Constants for FeMn and Co . . . . .                        | 159        |
| 5.2.7    | Temperature Dependence of Pinned Fe Moments in FeMn . . . . .      | 160        |
| 5.2.8    | Azimuthal Dependence of Pinned Fe Moments in FeMn . . . . .        | 165        |
| 5.2.9    | The Role of Orbital Moments for Exchange Bias . . . . .            | 167        |
| 5.2.10   | Conclusion . . . . .   | 170        |
| 5.3      | Temperature Dependence of the Co Moment In Co/NiCoO . . . . .      | 172        |
| 5.3.1    | Sample Preparation & Characterization . . . . .                    | 174        |
| 5.3.2    | X-ray Absorption Spectroscopy & XMCD of Co . . . . .               | 176        |
| 5.3.3    | XAS & XMCD of Nickel . . . . .                                     | 181        |

---

|          |  |            |
|----------|--|------------|
| 5.3.4    | Magnetometry & Interpretation of the Results . . . . . | 184        |
| <b>6</b> | <b>Experimental Aspects</b>                            | <b>189</b> |
| 6.1      | ERNSt – An Advanced Magnetic Reflectometer . . . . .   | 190        |
| 6.1.1    | General Setup . . . . .                                | 190        |
| 6.1.2    | Cryo-Sample-VTI . . . . .                              | 194        |
| 6.1.3    | Detector Systems . . . . .                             | 195        |
| 6.1.4    | Magnet-System . . . . .                                | 198        |
| 6.1.5    | Control & Instrumentation . . . . .                    | 199        |
| 6.1.6    | The New Continuous Measurement Mode . . . . .          | 201        |
| 6.2      | First Results (With ERNSt) . . . . .                   | 204        |
| 6.3      | L-MOKE Add-On . . . . .                                | 208        |
| 6.3.1    | The Magneto Optical Kerr Effect . . . . .              | 209        |
| 6.3.2    | Experimental Setup – the Optical Path . . . . .        | 210        |
| 6.3.3    | Tests & Results . . . . .                              | 212        |
| 6.4      | ReMagX - A Tool To Fit Magnetic Reflectivity . . . . . | 214        |
| 6.4.1    | The Matrix Formalism in ReMagX . . . . .               | 214        |
| 6.4.2    | Fit Algorithms . . . . .                               | 215        |
| <b>7</b> | <b>Summary</b>   | <b>219</b> |
|          | <b>Bibliography</b>                                    | <b>225</b> |





# 1 Zusammenfassung der Arbeit

## Einleitung

Magnetische Kopplungsphänomene und Austauschwechselwirkungen an inneren Grenzflächen bilden die Grundlage für viele moderne magnetische Anwendungen. Vor allem dünne Filme bestehend aus Schichten mit verschiedenen magnetischen Eigenschaften haben in den letzten 20 Jahren zu wichtigen Fortschritten und Entwicklungen auf diesem Gebiet beigetragen.

Einer der prominentesten und technologisch erfolgreichsten Vertreter dieser Klasse von Systemen ist die unidirektionale Austauschwechselwirkung, oder auch *Exchange Bias*. Werden ein Ferro- und ein Antiferromagnet, zum Beispiel in einem Dünnschichtsystem, zusammengebracht tritt eine Austauschwechselwirkung an der Grenzfläche der beiden Schichten auf, die zu einer effektiven Verankerung des Ferromagneten durch den Antiferromagneten führen kann. Das Resultat dieser Kopplung ist eine Verschiebung der Hysterese des Ferromagneten sowie typischerweise eine Erhöhung seiner Koerzitivfeldstärke. Obwohl Exchange Bias bereits in den 1950er Jahren von W. H. Meiklejohn und C. P. Bean entdeckt wurde dauerte es doch bis zur Entdeckung des Riesenmagnetowiderstands (GMR) durch die Gruppen von P. Grünberg und A. Fert 1988 bis Exchange Bias technologisch interessant wurde. Im Zuge der Entwicklung von leistungsfähigen GMR Elementen zeigt es sich, dass Exchange Bias ideal geeignet ist um eine der beiden ferromagnetischen Schichten im GMR Element zu verankern und so den Riesenmagnetowiderstand zu verursachen. Obwohl Exchange Bias heute in den meisten Festplatten-Leseköpfen Verwendung findet, sind die mikroskopischen Vorgänge an der Grenzfläche zwischen Ferro- und Antiferromagnet immer noch nicht vollständig verstanden. Ziel dieser Arbeit ist es einige der wichtigsten und dringendsten Fragen in diesem Zusammenhang zu beantworten.

Die genaue magnetische Konfiguration an der Grenzfläche zwischen Ferro- und

Antiferromagnet soll mit möglichst hoher Auflösung bestimmt werden. Besonders die Frage der Existenz und Position von verankerten, unkompensierten magnetischen Momenten im Antiferromagneten, die für das Auftreten der unidirektionalen Austauschwechselwirkung verantwortlich sind, steht dabei im Vordergrund. In einem zweiten Schritt soll auf die physikalischen Eigenschaften dieser verankerten Momente eingegangen werden. Dabei kommt eine neue Röntgenanalysemethode, die resonante magnetische Röntgenreflektometrie, englisch abgekürzt XRMR, zum Einsatz.

Resonante magnetische Röntgenreflektometrie stellt die Erweiterung der herkömmlichen Röntgenreflektometrie durch den zusätzlichen Kontrast des Röntgenzirkulardichroismus dar. Neben polarisierter Neutronenstreuung ist XRMR eine der Methoden die sich am Besten zur Untersuchung von inneren, magnetischen Grenzflächeneffekten in Dünnschichten eignet. Zwar liefert die Röntgenbasierte Reflektometrie nur Projektionen des magnetischen Moments und nicht wie Neutronen eine vektorielle Information allerdings wird dieser Nachteil durch eine Vielzahl an Vorteilen mehr als aufgewogen: XRMR ist, genau wie XMCD, Element selektiv. Außerdem ist es deutlich sensitiver aufgrund der resonanten Überhöhung und dem daraus resultierenden großen Streuquerschnitt. Aus diesem Grund ist XRMR, im Gegensatz zu Neutronen, auch in der Lage dünne Filme oder kleine Proben zu untersuchen. Als letzter sehr wichtiger Punkt bleibt noch der  $q_z$  Raum zu nennen, also der instrumentell erreichbare Impulsübertrag beim Streuprozess, dieser ist bei XRMR um einen Faktor 4 bis 5 grösser.

Durch Messung der Reflektionsspektren auf der Resonanzenergie eines magnetisch sensitiven Übergangs wie zum Beispiel die L-Kanten der Übergangsmetalle bzw. die M-Kanten der Seltenerd-Metalle wird eine Asymmetrie erzeugt die Informationen über das Tiefenprofil des Magnetismus des entsprechenden Elements beinhaltet. XRMR erlaubt es also sowohl strukturelle wie auch magnetische Tiefenprofile eines Mehrlagensystems gleichzeitig und elementselektiv zu messen. Für die vorliegende Arbeit wurden drei verschiedene Ferromagnet/Antiferromagnet Doppelschichten mit unidirektionaler Austauschwechselwirkung untersucht.

## Ergebnisse

Bei dem ersten untersuchten Probensystem handelt es sich um epitaktisch gewachsenes Fe/MnPd, ein System mit metallischem Antiferromagneten. Diese Untersuchung ist eine Zusammenarbeit mit der Gruppe von Prof. K. M. Krishnan an der University of Washington in Seattle, USA, die die Proben zur Verfügung gestellt hat. Ich möchte mich an dieser Stelle nochmals bei Prof. Krishnan und seinen Mitarbeitern für die hervorragenden Proben und die gute Zusammenarbeit bedanken.

Ein hoch präzises, magnetisches Tiefenprofil des Mangan im Antiferromagneten ist mittels XRMR bestimmt worden. Es liefert die exakte magnetische Konfiguration an der Grenzfläche zwischen Ferro- und Antiferromagneten.

- Direkt an der Grenzfläche zum ferromagnetischen Fe existiert ein 1–2 Monolagen ( $(4 \pm 1) \text{ \AA}$ ) dicker Bereich mit rotierbaren, sprich sich ferromagnetisch verhaltenden Mn Momenten im Antiferromagneten.

Der Grund für das Verhalten der Manganatome ist die direkte Nachbarschaft zum ferromagnetischen Eisen und der zugehörigen starken ferromagnetischen Kopplung. Diese ist so dominant, dass die Kopplung an das darunterliegende antiferromagnetische Spingitter aufbricht und das Manganatom mit dem Fe rotiert. Die Interpretation wird gestützt von der Tatsache dass der Bereich mit rotierbaren Mn Momenten exakt mit der Grenzflächenrauhigkeit in der Probe korreliert. Außerdem zeigt das rotierbare Mangan genau das gleiche Verhalten bei Magnetisierungsumkehr wie das darüber liegende Fe.

Greift man an dieser Stelle auf die weiter unten aufgeführten Ergebnisse in Co/FeMn und Co/NiCoO vor so zeigt sich, dass dieser Befund allgemein auftritt. In allen hier untersuchten Exchange Bias Systemen finden sich rotierbare Momente im Antiferromagneten direkt an der Grenzfläche zum Ferromagneten. Untersuchungen von anderen Gruppen bestätigen diese Beobachtung auch für andere Systeme. Daraus kann man schließen, dass die Existenz von unkompenzierten rotierbaren Momenten an der Grenzfläche zum Ferromagneten ein allgemeines Merkmal von Antiferromagneten in Exchange Bias Systemen ist.

Neben den rotierbaren Mn Momenten wurde auch nach verankerten Momenten

im Antiferromagneten des Fe/MnPd Systems gesucht dabei liefert das mittels XRMR gemessene Tiefenprofil für diese Momente den folgenden Befund:

- Verankerte, unkompensierte Mn Momente existieren im Antiferromagneten. Sie treten nur in einem  $(13 \pm 1)$  Å breiten Bereich direkt unterhalb der Grenzfläche zum Ferromagneten auf.

Dies ist der erste direkte Nachweis von verankerten unkompensierten Momenten in einem metallischen Antiferromagneten. Um den direkten Zusammenhang zwischen den gefundenen verankerten Mn Momenten und der Verschiebung der Hysterese durch den Exchange Bias nachzuweisen wurde die azimutale Abhängigkeit des Signals überprüft. Aufgrund des unidirektionalen Charakters der Austauschwechselwirkung verschwindet der Exchange Bias bei Messung in senkrechter Richtung. Dieses Verhalten findet sich eins zu eins im Signal der verankerten, unkompensierten Mn Momente wieder womit der Zusammenhang einwandfrei gezeigt ist.

Das zweite Exchange Bias System welches im Rahmen dieser Arbeit untersucht wurde besteht aus ferromagnetischem Kobalt auf  $\gamma$ -FeMn als Antiferromagnet. Das Hauptaugenmerk dieser Untersuchung ist es den spektralen Charakter der verankerten unkompensierten Fe Momente im Antiferromagneten aufzuklären. Dazu wurde die energieabhängige Streuung an der Fe  $L_{2,3}$ -Kante mittels zirkular dichroischem Licht an zwei Proben untersucht. Die Proben zeichnen sich durch eine unterschiedliche Magnitude und Temperaturabhängigkeit der unidirektionalen Austauschwechselwirkung, beziehungsweise der Verschiebung der Hysterese aus. Die erste Probe zeigt bei Raumtemperatur keine Verschiebung der Hysterese. Erst nach kühlen in einem externen Feld auf eine Temperatur von 50 K zeigt sich ein deutlicher Exchange Bias von  $\approx 30$  mT. Im Gegensatz dazu weist die zweite untersuchte Probe bereits eine deutliche Verschiebung bei Raumtemperatur auf. Bei dieser zweiten Probe wurde die azimutale Abhängigkeit des Signals analog zu der bereits besprochenen Untersuchung am Fe/MnPd System untersucht.

- Das, den verankerten, unkompensierten Fe Momenten zuzuordnende Differenzsignal weist in beiden Proben dieselbe Abhängigkeit auf wie die Verschiebung der Hysterese aufgrund des Exchange Bias.
- Die Form des Differenzsignals das von den verankerten, unkompensierten Fe

---

Momenten in Co/FeMn herrührt besitzt eindeutig einen orbitalen Charakter.

- Das bedeutet, dass Bahnmomente im Antiferromagneten für die Verschiebung der Hysterese im Co/FeMn Exchange Bias System verantwortlich sind.

Dieses Ergebnis liefert zum ersten Mal einen eindeutigen Hinweis auf die physikalischen Eigenschaften von verankerten, unkompensierten Momenten in einem Antiferromagneten. Der vergleichende Charakter der Untersuchung an zwei unterschiedlichen Proben mit unterschiedlichen Abhängigkeiten, nämlich Temperatur bei der Ersten und Azimut bei der Zweiten, lässt keinen Zweifel an diesem Ergebnis zu.

Die Tatsache, dass die gemessenen Spektren fast ausschließlich einen Bahnmomentcharakter aufweisen impliziert noch eine weitere wichtige Schlussfolgerung: Die Eisenatome die diese Momente tragen besitzen natürlich auch ein großes Spinmoment welches aber offensichtlich keine Rolle für die hier gemessenen Spektren spielt. Das lässt sich nur damit erklären, dass dieses Spinmoment rotierbar ist und somit keine Differenz erzeugt. Mit anderen Worten, im Antiferromagneten existieren Fe Atome die ein rotierbares Spinmoment und gleichzeitig ein signifikantes verankertes Bahnmoment besitzen. Eine antiparallele Stellung dieser beiden Momente wird durch Überkommen der Spin-Bahn Kopplung erreicht. Dieses Ergebnis stellt eine logische Schlussfolgerung aus der hier beobachteten Form der zugehörigen Spektren dar und muss in der Zukunft noch eingehender untersucht werden.

Als drittes und letztes Exchange Bias System wurde Co/NiCoO, ein System mit oxidischem Antiferromagneten, mittels XMCD untersucht. Bei dieser Untersuchung handelt es sich um eine Zusammenarbeit mit Prof. A. E. Berkowitz und seiner Gruppe an der University of California in San Diego, USA. Mein besonderer Dank gilt Prof. Berkowitz für die gute Zusammenarbeit und Hilfe bei der Interpretation der Ergebnisse. Die Untersuchung der Temperaturabhängigkeit des XMCD an der Kobalt  $L_{2,3}$ -Kante ergibt Folgendes:

- Ungefähr  $\sim 10\%$  des Kobaltmoments verschwinden wenn die Probe von Raumtemperatur auf 80 K herunter gekühlt wird.

Eine detaillierte magnetometrische Untersuchung der Temperaturabhängigkeit der zugehörigen Hysteresekurven zeigt, dass es sich dabei vermutlich um Kobaltmo-

mente im Antiferromagneten aber in direkter Nachbarschaft zum Ferromagneten handelt, die erst beim herunter kühlen mit dem Antiferromagneten koppeln. Der Großteil der verschwindenden rotierbaren Co Momente koppelt antiferromagnetisch bei tiefen Temperaturen. Ein kleiner Anteil wird jedoch unkompensiert verankert und ist damit vermutlich für die beobachtete Temperaturabhängigkeit des Exchange Bias in der Probe verantwortlich.

### **Methodische Fortschritte**

Im Rahmen dieser Arbeit wurde ein neues verbessertes, magnetisches UHV-Reflektometer für den Einsatz an Synchrotronstrahlungsquellen entwickelt und gebaut. Basierend auf den Erfahrungen die in den letzten 20 Jahren auf dem Gebiet gesammelt werden konnten stellt es ein extrem vielseitiges und leistungsfähiges Instrument zur Messung von Streuung und Reflektion von Röntgenstrahlung im weichen Röntgenbereich dar. Die wichtigsten Merkmale lassen sich wie folgt zusammenfassen:

- UHV (typisch besser  $5 \cdot 10^{-10}$  mbar) im gesamten Experiment und während der Messung.
- Simultane Erfassung von TEY, TFY, reflektiertem Strahl, diffusem Anteil und  $I_0$ .
- Variables Magnetfeld in der Strahlebene von bis zu 260 mT (bzw. 630 mT optional).
- Motor getriebene, azimutale Probenrotation ( $360^\circ$ ).
- Temperaturbereich von 38 bis 480 K für alle Messungen.
- Probentransfersystem und Schleuse mit Magazin zur Lagerung von 6 Proben unter UHV Bedingungen.
- Strahllagemonitor zur Kontrolle der horizontalen Lage des Synchrotronstrahls.

Neben diesen rein instrumentellen Fortschritten wurden während der letzten Jahre auch einige grundlegende methodische Erfolge bei der Auswertung erreicht. Die Wichtigste ist sicherlich die Implementierung der so genannten magneto-optischen Methode für die Berechnung der Reflektivität eines Schichtstapels. Dabei wird

der bisher verwendete Parratt Algorithmus durch eine Beschreibung mittels  $4 \times 4$ -Matrizen ersetzt, die es erlaubt den magneto-optischen Effekt exakter zu berechnen. Ein weiterer wichtiger Punkt ist die Entwicklung eines neuen Fit Algorithmus basierend auf dem Konzept der Evolutionsstrategie. Mit diesem *genetischen Algorithmus* wird das globale Minimum trotz größerer Anzahl freier Parameter zuverlässiger gefunden als mit Hilfe der bisher verwendeten Verfahren. Die letzte wichtige Verbesserung wurde bei der numerischen Abarbeitung der Kramers-Kronig Transformation erreicht. Hier steht nun ein schnelles und hoch präzises Werkzeug zur Verfügung.





## 2 Introduction

Modern magnetic thin film devices owe their success in large part to effects related to interlayer coupling and exchange interaction at interfaces.

Particularly research on layered thin film systems with different magnetic properties or phases has flourished during the last two decades. The 2007 Nobel Prize for the discovery of the Giantmagnetoresistance (GMR) by Peter Grünberg and co-workers and by Albert Fert and co-workers is just one example for this boom. Crucial for the realization of any GMR element but also tunneling magnetoresistance (TMR) elements is the antiparallel alignment of two ferromagnetic layers separated by a spacer layer. There is one effect which is extremely well suited to effectively pin a ferromagnet and thus create an antiparallel alignment: exchange bias.

Exchange bias is an interfacial exchange coupling which can occur if a ferromagnet is in direct contact to an antiferromagnet. The presence of the antiferromagnet induces an additional unidirectional anisotropy to the ferromagnet which results in a horizontal shift of the hysteresis loop. This “bias” is ideally suited to pin one of the two ferromagnetic layers in a GMR element and accordingly all modern GMR and TMR elements use exchange bias. However, the physical understanding of the latter is still very limited and mostly phenomenological. No model exists to date which explains all facets of the effect in a comprehensive way.

The aim of this thesis was to investigate several open questions and problems related to the basic physics of the exchange bias effect: First of all to find direct evidence for the existence and location of pinned uncompensated moments in the antiferromagnet. These moments are discussed as the origin of the exchange bias loop shift already since the time of its discovery. But direct evidence for their existence, amount and correlation with the effect were mostly missing. Another very important point is the magnetic configuration at the interface between ferro- and

antiferromagnet. This is especially important because several prior investigations by other groups had found hints for the existence of rotatable moments in the antiferromagnet. Finally experimental results indicating the microscopic mechanism responsible for the unidirectional character of the loop shift were completely missing.

The reason why the just framed questions and problems are so difficult to address is that the signal from the pinned moments is diminutive and the presence of the ferromagnet makes it even more difficult to separate it. Accordingly there are very few techniques which are sensitive enough to resolve such a signal.

In this thesis, X-ray magnetic reflectivity (XRMR) and X-ray magnetic circular dichroism (XMCD) were used to carry out a detailed investigation on three prominent exchange bias systems in order to answer the questions just framed. XRMR uses standard X-ray reflectivity and extends it by the additional contrast from the XMCD. As a result, XRMR provides structural, i.e., thickness and roughness information of a sample and also yields information on the magnetic profile along the z-direction. Magnetic reflectivity is a young technique whose theoretical basis was led just 20 years ago by J.P. Hannon and others [1]. Nevertheless it already proved to be a very powerful and versatile tool for investigating miscellaneous layered magnetic systems [2–4]. It provides an outstanding element specific sensitivity due to the large jump in optical properties when measuring at an absorption edge. The same reason also leads to an extremely high sensitivity of the reflectivity to small variations of the magnetism in the layers. XRMR is capable of probing smallest variations of the local magnetic profile. It can detect fractions of monolayers of magnetic material in an element specific and non-destructive way.

Main goal of the work presented here is to find evidence for pinned uncompensated moments in an exchange bias system and identify their spectroscopic character. For this purpose, three different systems were investigated:

- Fe/MnPd – an epitaxially grown system with metallic antiferromagnet. In this exchange bias system, the nominal spin configuration and roughness at the interface can be controlled by the growth conditions. Accordingly, the investigation focuses on the precise magnetic configuration of the Fe/MnPd interface depending on these properties. The Fe/MnPd samples were provided

---

by the group of Prof. K. M. Krishnan from the University of Washington, Seattle, USA.

- Co/FeMn – which is again an exchange bias system based on a metallic antiferromagnet but this time the samples are polycrystalline. The investigation is aiming at the spectroscopic character of the magnetic moments responsible for the exchange bias loop shift. By varying the thickness of the antiferromagnetic FeMn layer the temperature properties of the exchange bias effect in the system can be altered in a controlled way. All Co/FeMn samples were prepared at the Max-Planck-Institut für Metallforschung.
- Co/NiCoO – the only oxidic antiferromagnet which was investigated during this work. Purpose of this project was to reconfirm the findings from the two other exchange bias systems. Such a test proves the significance of the results and, even more important, demonstrates their general character for the exchange bias effect. The Co/NiCoO sample investigated here was prepared by the group of Prof. A. E. Berkowitz from the University of California in San Diego, USA.

At this point I want to take the opportunity and thank my two collaborators in the United States, Prof. Krishnan and his group from the University of Washington in Seattle and Prof. Berkowitz with his group at the University of San Diego in La Jolla for the excellent and productive collaborations.

The XRMR investigation of the Fe/MnPd samples reveals a rich and complex magnetic interface configuration in the antiferromagnet close to the interface. Rotatable and pinned uncompensated manganese moments are found in the vicinity of the interface. Their relative position and couplings are derived from the data. Eventually the direct correlation of pinned moments with the exchange bias loop shift is proven from analyzing the azimuthal dependence of the effect.

Energy dependent scattering at the Fe L-edges in the FeMn/Co exchange bias system reveals the physical character of the pinned uncompensated Fe in the antiferromagnet. An unexpected spectral shape is found which corresponds to a purely orbital moment. This finding implies several new and fundamental per-

spectives for the microscopic understanding of the exchange bias in the samples investigated here.

The thesis is organized in four parts: First the scientific frame and background is presented in Section 3 followed by some considerations about the data processing in Section 4. Then the results for all three investigated exchange bias systems along with the interpretation of these findings are discussed in detail in Section 5. Section 6 outlines the most important experimental advances and achievements which have been accomplished with this thesis. Eventually the work closes with a summary of the results obtained and their significance for the general understanding of the exchange bias effect.

### 3 Scientific Background

In the following Section, the scientific background and the theoretical models will be introduced which form the basis for this work. Most of the topics are discussed in a qualitative way describing the phenomenon and its relation to the present work. However, selected topics are discussed in more detail especially when their quantitative aspect is of relevance.

This thesis involves two very distinct parts of modern magnetism research, the magnetic coupling phenomenon of exchange bias and on the other hand, the analytical method of X-ray magnetic reflectometry. The former is a magnetic coupling effect which occurs when a ferromagnet is in direct contact to an antiferromagnet causing an exchange interaction between the two. The latter is a novel measurement technique based on X-ray resonant scattering which allows determining the chemical and magnetic depth profile of layered thin film samples.

Accordingly, the scientific framework for the thesis breaks up into two large parts which have to be discussed: In the first half of the Section, exchange bias and related topics will be introduced. Concepts from general magnetism like for example exchange interactions and anisotropies are briefly introduced in a qualitative way since they form the basis for the quantitative description of exchange bias.

The exchange interaction between a ferromagnet and an antiferromagnet will be introduced on a phenomenological basis which involves the early very simple model proposed by its discoverers W. H. Meiklejohn and C. P. Bean. Subsequently the most important theoretical models developed over the last decades will be discussed followed by a section about the concept of a spin glass state at the interface and a recent approach to a quantitative description. Eventually the section closes with a brief introduction of stability criteria for exchange bias, namely the phenomena of training and blocking in the antiferromagnet.

The second half of the scientific background is devoted to the concepts of resonant scattering and the quantitative description of specular reflection of X-rays in solids. Therefore the scattering mechanisms of X-rays in solids are introduced and the inclusion of a magnetic contribution is outlined. The section closes with the magneto-optical description of the scattering problem of X-rays in magnetic matter.

## 3.1 Magnetism

In the following section, selected, basic concepts of magnetism will be introduced briefly. They have been chosen according to their importance for the description of the exchange bias phenomenon which will be discussed in Section 3.2. The first part of the chapter treats general topics of magnetism. Namely exchange interactions and the band model are discussed followed by a brief introduction of the concept of magnetocrystalline anisotropy (MCA). The former being integral for a microscopic description of exchange coupling as it occurs in exchange bias systems while the latter is believed to be the origin of the loop shift in exchange bias systems. The general concept of magnetic domain formation is discussed in the third section since it is needed for the description of the spin state of the antiferromagnet. In the last part, the Stoner-Wohlfarth model is introduced. This model is extremely useful to qualitatively describe the magnetisation reversal behaviour of exchange bias systems.

For further information and especially a more thorough description of these phenomena, refer to a textbook on magnetism like for example [5, 6] or [7].

The presence of a magnetic moment in an atom is the result of a partially filled valence shell. Orbits which are only partially filled show a remaining net spin and orbital momentum which can interact with external fields. Accordingly, atomic magnetism is governed by the filling condition described by Hund's rules. These rules arise from Coulomb repulsion of the electrons and spin-orbit-coupling. The situation becomes more complex when more than one atom is involved. Magnetism of a single atom is exclusively governed by the interaction of its own electrons in the valence shell. In contrast, the magnetic moment of an atom in solids and compounds is affected by interaction and coupling with the magnetic moments of its neighbors; magnetism becomes a collective effect.

During the last decades, a number of concepts have been developed in order to account for exchange interaction. In the following section, the most fundamental one will be briefly introduced and discussed.

### 3.1.1 Exchange Interaction – Collective Magnetism

Collective magnetism is a phenomenon observed when many atoms with their electrons are neighboring each other like e.g. in solids. Then the electrons “feel” the presence of their neighbors, either their dipole field or by direct exchange interaction and behave like a collective. While the former of the two effects is very weak and only comes into play for very low temperatures, the exchange interaction is the origin of magnetic ordering at higher temperatures.

The term exchange interaction refers to a quantum mechanical interaction which is the direct consequence of the fermion nature of the electron. The Pauli exclusion principle states that no two electrons with same quantum numbers may occupy the same state. Their total wavefunction has to be antisymmetric. Accordingly, two electrons with the same spin direction will maintain a larger distance between each other than with antiparallel spin. This has two competing results: the potential energy stored in the Coulomb interaction of the two electrons is reduced for parallel arrangement due to the increased distance. In contrast the kinetic energy of the system increases for parallel alignment since the electrons will maintain a larger distance or in case of a band structure occupy two distinct states in the density of states. Which of the two contributions dominates strongly depends on the system.

The idea is to express this concept by an additional term in the Hamiltonian. The result is the Heisenberg-Hamiltonian, a spin-spin interaction of two localized electrons on different atomic sites of the form

$$H_{\text{Heis}} = -2 \sum_{i < j} J_{ij} \mathbf{S}_i \mathbf{S}_j. \quad (3.1)$$

Here,  $\mathbf{S}_i$  and  $\mathbf{S}_j$  denote the spin direction of the two electrons and  $J_{ij}$  the coupling sign and strength. The sum runs over all atom sites in the system. An obvious conclusion from this Hamiltonian is that for  $J_{ij} > 0$  the spins will align parallel thus couple ferromagnetic while for  $J_{ij} < 0$ , antiferromagnetic coupling is energetically favorable. If the wavefunctions of the electrons in the system have a mostly localized character, which means they are either really localized or itinerant but with confined wavefunction, their Hamiltonian (3.1) can be simplified by



assuming only next-nearest-neighbor interactions. A second simplification can be made if one assumes that all these exchange interactions  $J_{ij}$  are the same for all electrons (no inhomogeneity). With these two assumptions, the Hamiltonian can be simplified to

$$E_J = -\frac{1}{2} \sum_i (-2J \mathbf{S}_i \sum_j \mathbf{S}_j) \quad (3.2)$$

where the inner term refers to the interaction of atom  $i$  with its nearest neighbors  $j$  and the outer sum then sums up all these contributions to give the total exchange energy  $E_J$  of the system.

Still equation (3.2) requires a summation over all atomic sites making it difficult to solve it. Therefore a second simplification step is necessary. By assuming that the pairwise interactions can be replaced by a magnetic moment ( $g\mu_B \mathbf{S}_i$ ) which interacts with an effective field  $H_{\text{eff}}$  the problem can be reduced to a mean-field problem. The formula then takes the form

$$E_{\text{exch}}^i = \mu_0 g \mu_B \mathbf{S}_i H_{\text{eff}}. \quad (3.3)$$

In terms of energy,  $J$  is on the order of  $10^{-2}$  eV/atom (from [5]) which means it is by orders of magnitude larger than the spin-orbit coupling which is  $\approx 10^{-4}$  eV/atom for non-metals (see e.g. [8]). But it's much smaller than the coulomb interaction of the electrons in an atom which are on the order of 1 – 10 eV (refer to any textbook on atomic physics).

The Heisenberg or mean field model is the basic model to describe collective behaviour of spins in solids like it is for example observed in ferromagnets. Its only restriction is that the wavefunctions of the involved electrons are localized since otherwise the simplification in equation (3.2) fails. This is fulfilled for systems with localized electrons and also most itinerant ones (like in metals). This general character makes the Heisenberg model very important for the description of ferromagnetism.

Before analyzing the effect of exchange coupling in solids further, an exception from the Heisenberg model shall be discussed: Metal oxides exhibit an interatomic bonding of metal and oxygen which is mostly of ionic nature. The electrons

in this system are strongly localized hence magnetism in the system should be described properly by the Heisenberg Hamiltonian. Investigations of the spin structure in antiferromagnetic CoO and NiO showed that the transition metal (TM) ion has nearest-neighbors with both parallel spin alignment and antiparallel aligned spins in the same distance and angle (diagonal). On the other hand the next nearest neighbor atoms are all antiparallel. Across the intermediate oxygen ion, the TM ions always couple antiferromagnetic (equiv.  $J < 0$ ). Since there is no direct overlap of the wavefunctions of next nearest neighbors, Heisenberg interaction cannot be responsible for this coupling. Instead, magnetism in such systems is described by a second-nearest neighbor interaction called *superexchange* (see e.g. [5,6]).

The mechanism leading to superexchange is illustrated in Fig. 3.1. Two TM ions are coupling to an oxygen ion in the middle. Therefore, both TMs give one electron from their  $3d_{x^2-y^2}$  to the oxygen  $2p_x$  orbital. Since we are interested in magnetic TM atoms, let's assume that the remaining TM still has a net moment which leads to the ground state configuration shown in row (a) and (d) in Fig. 3.1.

Although the character of the bond is mostly ionic a certain degree of covalent character is also present. Therefore the electrons can hop from one atom to the other forming a bonding or anti-bonding molecular orbit ( $\sigma$  and  $\sigma^*$ ). If now the  $p_x$  electron with spin down forms a bonding orbital with the TM on the left, the remaining electron has spin up (see Fig. 3.1 (b)). This remaining electron can only form a bonding orbital with the other TM on the right if the ground state moment of the second TM is antiparallel with respect to the first one. In this case, as shown in Fig. 3.1 (c), the electron can form a bonding orbital and thus minimize the energy of the overall molecular orbital. If, in contrast, the TM spins left and right are parallel to each other, the second hopping process is forbidden due to spin conservation and as a result the lowest energy state is not allowed as indicated by the crossed out second jump in Fig. 3.1 (e) to (f). The mechanisms responsible for superexchange are the spin conservation and the symmetry of the involved orbitals. The symmetry of the orbits is marked in Fig. 3.1 by a (+) for symmetric wavefunction and a (-) for the antisymmetric one. While the  $p_x$  orbital

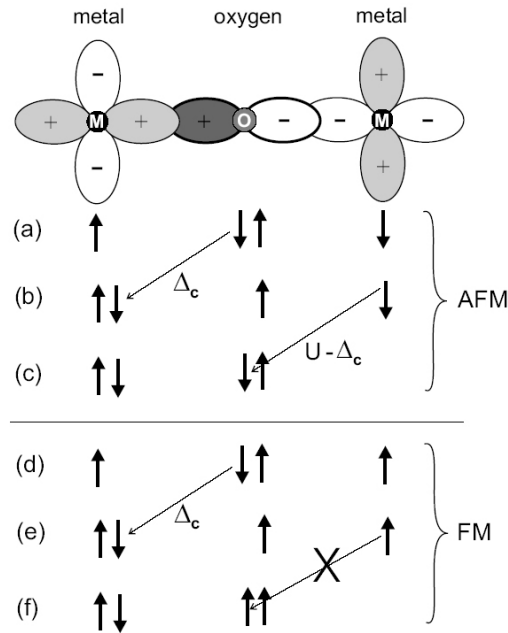


Figure 3.1: Simple illustration of the superexchange between two TM atoms over an intermediate oxygen atom. The TMs couple via  $d_{x^2-y^2}$  orbitals while the oxygen couples via  $p_x$ . For a description of the individual steps refer to the details given in the text.  $\Delta_C$  is the energy gained by forming a bonding orbital while  $U$  is the potential energy due to ionization (image reproduced from [6]).

used here as an example has a  $360^\circ$  rotational symmetry, the  $3d_{x^2-y^2}$  orbitals have  $180^\circ$ . This difference leads to the shown spin configuration with opposite sign for the two bonds.

In the final part of this section, a basic model for the description of metallic ferromagnetism will be presented. While oxides and isolators can be described by simple pairwise interactions due to the localized character of the electron wavefunctions in such systems, metallic systems exhibiting a band structure are more complex due to delocalization.

A first hint that the ferromagnetism in metals can not be explained by the filling of the valence shell is the uneven magnetic moment found for the transition metals. Co for example has 7 electrons in its  $3d$  shell thus 3 sites are unoccupied (also for  $\text{Co}^{2+}$  ions). This should result in a magnetic moment of  $m_s = 3\mu_B$ . Instead, a magnetic moment of  $1.715\mu_B$  (value for bulk, hcp Co taken from [6])

for bulk Co is found experimentally which is nearly half the expected value and even more important, it is not integer. Similar discrepancies are observed in Fe ( $2.216 \mu_B$ ) and Ni ( $0.616 \mu_B$ ) [6].

The puzzle of these broken Bohr magneton numbers can be solved if one assumes a band model for the ferromagnetism in metals. In the following the most simple band magnetism model, the Stoner- or Rigid-Band-Model will be introduced.

A free atom has orbitals which are discrete and can carry two electrons each. However, upon forming a solid, the proximity of neighboring orbitals leads to the formation of so called bands. The individual orbitals degenerate and form a valence and a conduction band. This band structure of the electrons in solids not only affects the electric properties but also the magnetism in this materials. One can no longer speak of individual magnetic moments interacting with each other as for the Heisenberg model or the superexchange.

Instead, magnetism in the light of band structure is given by the density of states of the two spin directions and the position of the Fermi energy relative to them. Fig. 3.2 shows the formation of a band structure upon nearing of the atoms in a solid and the resulting density of states and their splitting according to the spin orientation. This splitting is the key to band magnetism since differences in the filling of the two different bands leads to a remaining net moment and thus magnetism. The bands are named majority band for the more populated one and minority band for the one with less atoms. By definition, the spin of the electrons in the minority band, or of the holes in the majority band, always point into the direction of the magnetisation  $\mathbf{M}$  (see e.g. [6,9]). In the framework of this model, the difference between majority and minority electrons determines the magnetic moment of the metal.

The Rigid-Band model as the most simple band model assumes that the shape of the respective bands ( $s, d$  etc.) is rigid thus stays the same for all elements and only the Fermi energy level is moved up or down when going from one element to the next one in the periodic table of elements. This assumptions makes it very simple to derive the majority and minority spin densities, i.e., the magnetic moment of alloys. However, this assumption is certainly too simple and in reality the band structures vary strongly even for direct neighbors in the periodic table.

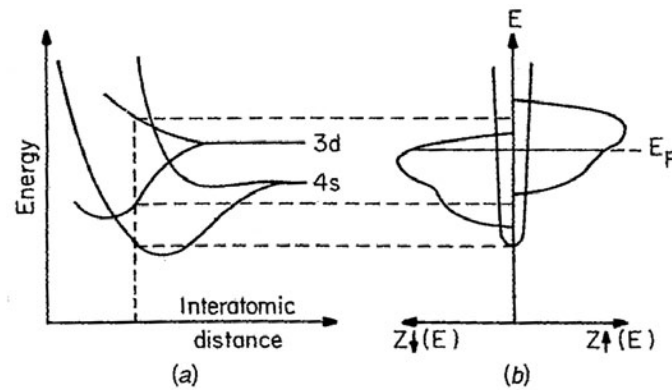


Figure 3.2: The left sketch illustrates the formation of a band structure for decreasing interatomic distance between two atoms. The sketch on the right shows an exchange split density of states for the two spin directions in a ferromagnet. The DOS difference between up and down for a filling up to the Fermi energy  $E_F$  is the origin of ferromagnetism (image reproduced from [5]).

Examples for the valence bands and the corresponding Fermi energy  $E_F$  of iron and Ni are shown in Fig. 3.3. The states in the valence band close to the Fermi

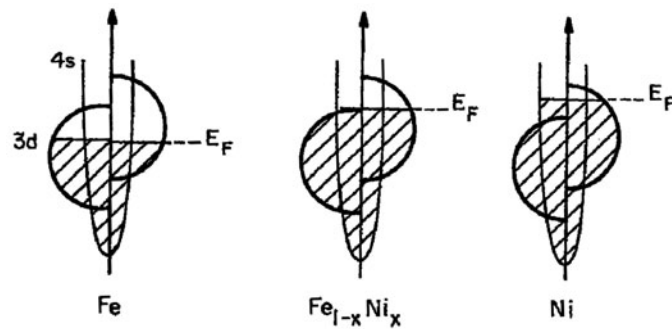


Figure 3.3: Simple illustration of the rigid-band model for Fe and Ni and the effect of alloying between the two. The composition dependent filling of the bands leads to the shift of  $E_F$  and thus the variation of the resulting net magnetic moment. In reality however, alloying also affects the shape of the band (image reproduced from [5]).

energy are formed by the  $3d$  electrons in these metals (same holds for Mn, Co, Cu etc.) and the magnetic moment is therefore given by the difference between the

$d$ -electrons in in the majority and minority band according to:

$$\mu_m \approx (n_d^\uparrow - n_d^\downarrow)\mu_B \quad (3.4)$$

where  $n_d^\uparrow$  and  $n_d^\downarrow$  refer to the subband populations.

### 3.1.2 Magnetocrystalline Anisotropy

Very often for single-crystals, the magnetisation behaviour along the crystallographic axes is different. Two effects are responsible for such anisotropic variation of the magnetisation behaviour, the shape anisotropy and the magnetocrystalline anisotropy (MCA). The former is related to a minimization of the dipole-dipole interactions for a non symmetric shape of the ferromagnet. It is a result of the macroscopic shape of the film and the necessity to minimize the energy stored in its external stray field. Detailed descriptions of form anisotropy can be found in [5, 7] or any other textbook on basic magnetism.

The MCA on the other hand is an anisotropy which is, as its name implies related to the crystallography thus the electronic environment of the magnetic atom. For example in Fe, the hysteresis measured along the [100] direction has a smaller coercivity, thus requires less energy for the reversal process, than along the [110] or [111] direction [10]. Since the magnetic moment in metals is mostly carried by the spin who by itself is isotropic, a coupling has to exist which couples the spin to the surrounding crystal field.

Spin-orbit coupling is the only coupling available which can mediate an anisotropy of the electronic configuration onto the spin of an electron. In an intuitive picture MCA is the result of an asymmetric electronic environment, or crystal field which is transferred to the magnetic spin moment via the spin-orbit coupling. Such a qualitative description is found in most magnetism textbooks [5, 11].

P. Bruno first derived a more precise microscopic picture of the MCA and its relation to spin-orbit coupling and especially orbital moments. He could show theoretically, that the anisotropy of the spin-orbit energy, the origin of MCA, is directly related to the orbital moment for the case of a more than half filled  $3d$

band. The crystal field couples with the orbital moment which by itself couples to the spin moment through the spin-orbit coupling. According to Bruno [12], the anisotropy of the spin-orbit coupling and thus the MCA is given by:

$$\Delta E_{MCA} = \frac{\xi}{4\mu_B} (m_l^{easy} - m_l^{hard}), \quad (3.5)$$

where  $\xi$  is the strength of the spin-orbit coupling and  $m_l^{easy}$  and  $m_l^{hard}$  are the expectation values of the orbital moments along the easy and hard axes, respectively. It is noteworthy that the Bruno model only states that the orbital momentum along the easy axis is larger than along the hard axis.

As already mentioned above, the Bruno model requires that the  $3d$  band is more than half filled which excludes all the lighter  $3d$  elements from this model. To overcome this restriction, Gerrit van der Laan extended the description by accounting for higher order perturbations [13]. In the framework of the van der Laan model, the MCA takes the form:

$$\begin{aligned} \Delta E_{MCA} \approx -\frac{\xi}{4} \hat{\mathbf{S}} \cdot [\langle \mathbf{L}^\downarrow \rangle - \langle \mathbf{L}^\uparrow \rangle] + \frac{\xi^2}{\Delta E_{ex}} \left[ \frac{21}{2} \hat{\mathbf{S}} \cdot \langle \mathbf{T} \rangle + 2 \langle (L_\xi S_\xi)^2 \rangle \right] \\ \equiv E_L^\downarrow + E_L^\uparrow + E_T + E_{LS}. \end{aligned} \quad (3.6)$$

Here, the anisotropy of the orbital moments is expressed by the difference of the projected minority and majority orbital moments ( $\langle \mathbf{L}^\downarrow \rangle - \langle \mathbf{L}^\uparrow \rangle$ ).

Besides the anisotropy from the orbital moments two other contributions are found. The magnetic dipole term  $T_Z$  (compare 3.3.4) and the squared diagonal spin-orbit interaction  $\langle (L_\xi S_\xi)^2 \rangle$  which conserves the spin in the excitation [13].

### 3.1.3 Bloch- & Néel- Domain Walls

A ferromagnet which is magnetised in one direction produces a large dipole field in its surrounding in order to close the magnetic loops. Since this requires a large amount of energy it is often easier for the ferromagnet to break into small parts, i.e., domains which have different orientation of their magnetisations. The driving force of domain formation is the energy gained from avoiding the external stray

field. However, domains also cost energy: in the areas in between two domains of different magnetisation orientation, the spins have to rotate which requires energy. This wall energy is the counterbalance to the stray field energy. If, for example the ferromagnet is very small, i.e., it has a small volume, a stray field might be energetically favorable. In contrast, a large slab of iron will for sure do better by breaking into domains than building up a large dipole field. The most simple domain state in a rectangular sample is shown in Fig. 3.4a). The sample is split in two domains with opposite magnetisation direction. Anyway, some stray field remains and the ferromagnet can solve this problem by forming so called closure domains at the end as shown in Fig. 3.4b). For a small and thin soft-ferromagnetic rectangle, this configuration is the energetically most favorable. In the four domain state of Fig. 3.4b) two different kinds of magnetic walls are

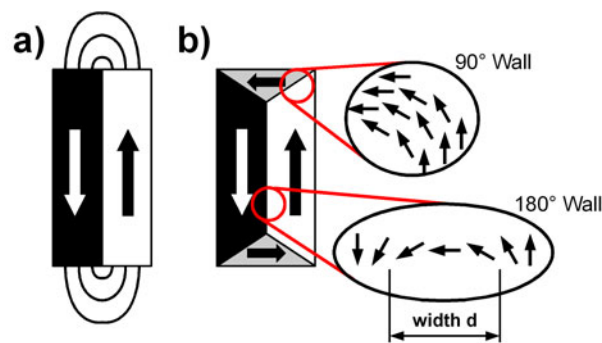


Figure 3.4: a) shows the most simple case of a two domain state in a rectangle. To avoid the remaining stray field shown in a), the ferromagnet subdivides further and forms closure domains at the end as is shown in b). In such a 4 domain state, two different types of domain walls are found,  $90^\circ$  and  $180^\circ$ . Both cases illustrated here represent Néel type domain walls.

found,  $90^\circ$  and  $180^\circ$ .

Domain walls can not only differ in angle but also in the way the moments reorient in the wall itself and one distinguishes two cases: In a Bloch type domain wall, the moments rotate out of the sample plane on a screw like trajectory. A



Néel type domain wall on the other hand has its moment rotating in the plane as it is shown for example on the right side of Fig. 3.4.

The question now is: When does a ferromagnet form domains, what is the size of this domains and what's their wall width  $d$ . For the spins in a ferromagnet, two energy contributions determine the local orientation, the exchange interaction with the neighboring spins and the magnetocrystalline anisotropy which is the interaction with the electronic surrounding (compare 3.1.2) of an electron via its spin-orbit coupling. Accordingly the wall properties depend on these two contributions and a quantitative approach starts from this point.

The wall energy per unit area of the wall surface required to form a  $180^\circ$  Bloch wall for a ferromagnet with only one anisotropy direction  $K_F$  (e.g. bcc Co) is given by:

$$E_{\text{DW}}^{\text{B}} = 4\sqrt{J K_F} \quad (3.7)$$

where  $J$  is the exchange constant (also see 3.1.1) and  $K_F$  the anisotropy constant which is the strength of the MCA. The corresponding wall width is then given by

$$d_{\text{DW}}^{\text{B}} = \pi\sqrt{\frac{J}{K_F}}. \quad (3.8)$$

From this equation the parameters of a  $180^\circ$  Bloch wall in bcc Co at room temperature are a wall width of  $d_{\text{DW}} = 18 \text{ nm}$  and a wall energy per unit area of  $E_{\text{DW}} = 9 \text{ mJ/m}^2$  [14].

A Néel wall in contrast has, in general, a higher domain wall energy per unit area since it is not free of stray fields. The wall energy per unit area of the surface is given by

$$E_{\text{DW}}^{\text{N}} = 4\sqrt{J(K_F + 2\pi J_S^2)} \quad (3.9)$$

and the corresponding domain wall thickness  $d_{\text{DW}}^{\text{N}}$  is

$$d_{\text{DW}}^{\text{N}} = \pi\sqrt{\frac{J}{K_F + 2\pi J_S^2}}. \quad (3.10)$$

As a consequence the formation of Bloch type domain walls is favored in bulk

materials since they require less energy during the formation. The situation is different in very thin films. If the film thickness is on the order of the domain wall size, the spin reorientation process in a Bloch wall causes a surface moment which leads to an external stray field. In this case a Néel wall becomes favorable. Fig. 3.5 shows the wall energy and wall width for both wall types depending on the film thickness. As can be seen, for thin samples it is energetically favorable to form

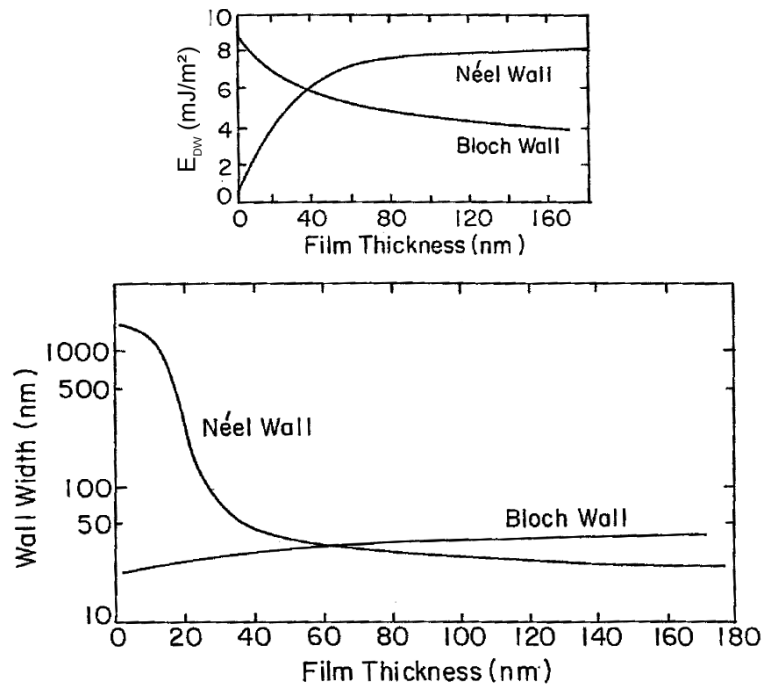


Figure 3.5: Domain wall energy per unit area ( $E_{DW}$ ) and the wall width,  $d_{DW}$ , for Néel and Bloch type domain walls depending on the film thickness of the ferromagnet (image reproduced from [5]).

Néel walls since they have a smaller stray field. For thicker samples, Bloch walls become favorable because they can now form closure domains to avoid surface charges and thus minimize their stray field.

For further reading on domain walls refer to the textbook by A. Hubert and R. Schäfer [15].

### 3.1.4 Stoner-Wohlfarth Model

In 1948 E. C. Stoner and E. P. Wohlfarth presented a model to quantitatively describe the magnetisation reversal of small magnetic particles [16,17]. This model, nowadays called Stoner-Wohlfarth (SW) model, describes the interplay of applied field, Zeeman energy and anisotropy contributions in a ferromagnet. For simplicity, it only accounts for coherent rotation of the moments and completely ignores the existence of domain walls. On the first glance, this seems to limit the usability of the model to small particles exhibiting a single-domain state. But it turns out that it is also applicable for thin-film samples and for bulk materials as long as the domains are pinned.

The free energy density per unit volume of a ferromagnet can be written as

$$E = -\mu_0 H_{appl} M_F \cos(\Theta - \beta) - K_F \sin^2(\beta) \quad (3.11)$$

with  $M_F$  being the saturation magnetisation of the ferromagnet,  $H_{appl}$  the externally applied field and  $(\Theta - \beta)$  the angle between magnetisation and external field. The second term describes the anisotropy in the system by a constant  $K_F$  and the angle to the magnetisation  $\beta$ . The anisotropy is uniaxial and can either be related to the shape or to magnetocrystalline anisotropy or a mixture of the two. The corresponding geometry for this model is shown in Fig. 3.6. To find the

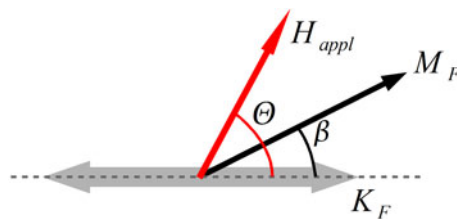


Figure 3.6: Definition of the parameters  $M_F$ ,  $K_F$  and  $H_{appl}$  and their relative orientations needed for the Stoner-Wohlfarth model.

equilibrium state, the total energy is minimized with respect to  $\beta$  yielding the

following formula,

$$\mu_0 H_{appl} M_F \sin(\Theta - \beta) + K_F \sin(2\beta) = 0. \quad (3.12)$$

The stability condition for this equation reads

$$\frac{\partial^2 E(\beta)}{\partial \beta^2} = \mu_0 H_{appl} M_F \cos(\Theta - \beta) + 2K_F \cos(2\beta) > 0. \quad (3.13)$$

Replacing the anisotropy constant by the corresponding anisotropy field  $H_A = 2K_F/\mu_0 M_F$  and additionally substituting  $H/H_A = h$ , equation (3.13) can be solved for  $\beta$ . This provides the magnetisation component parallel, i.e., longitudinal  $m_{\parallel} = \cos(\beta - \Theta)$  and perpendicular or transverse  $m_{\perp} = \sin(\beta - \Theta)$  with respect to the applied field.

From equation (3.12) the coercive field, i.e., the critical field value where the magnetisation component  $m_{\parallel}$  is zero can easily be derived. It is found that the angular dependence of  $H_C$  on  $\Theta$  is of the form [18]:

$$H_C(\Theta) = \frac{2K_F}{\mu_0 M_F} |\cos \Theta|. \quad (3.14)$$

Depending on the angle  $\Theta$  between the applied field and the easy-axis, very different shapes of the hysteresis curve are found. Example curves for  $\Theta = 0^\circ, 30^\circ, 45^\circ, 60^\circ$  and  $90^\circ$  are shown in Fig. 3.7 for the parallel magnetisation component  $m_{\parallel}$ . For  $\Theta = 0^\circ$ , the hysteresis is perfectly square shaped because the moments are aligned with the easy axis. The corresponding transverse component (not shown) is zero. The coercive field for this case is given by the anisotropy field  $H_A = 2K_F/\mu_0 M_F$ . At this field value, the external field overcomes the anisotropy which keeps the magnetisation aligned and the moments are rotated. In contrast when applying a field along the hard magnetisation axis thus for  $\Theta = 90^\circ$ , the hysteresis has a linear slope and no coercivity. For intermediate values of  $\Theta$ , the hysteresis is rounded before the effective direction change takes place. For small enough fields, the magnetisation starts to rotate towards the easy axis depending on the strength of  $K_F$ . This leads to a reduction of the magnetisation along the field direction depending on the angle  $\Theta$ . Only the projection of  $\mathbf{M}$  along  $m_{\parallel}$  and

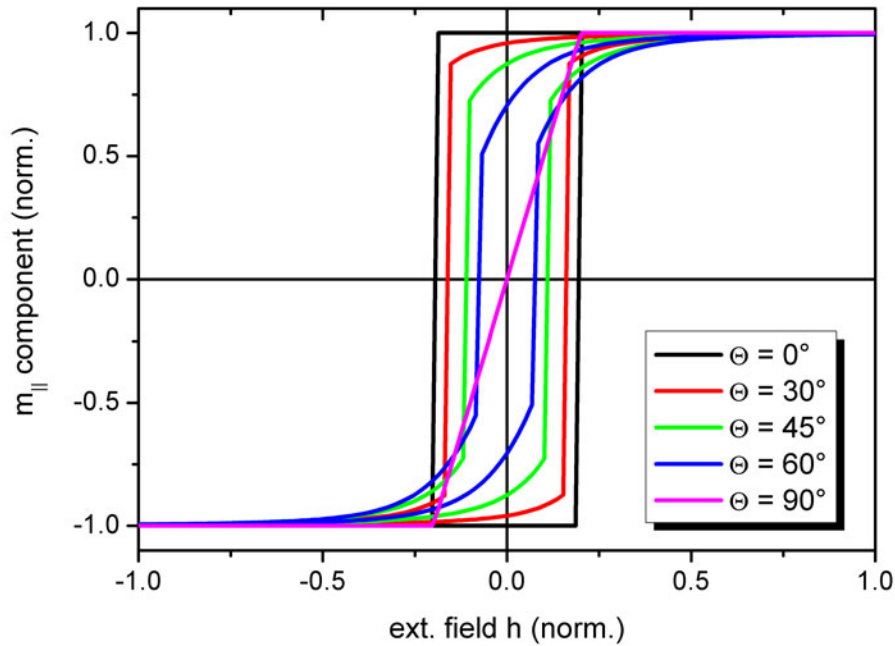


Figure 3.7: Longitudinal component of the magnetisation for different angles  $\Theta$  between field and easy direction of the anisotropy. The data have been obtained using a script provided by the University of Regensburg which does the necessary minimization of equation (3.13)

$h$  contributes to the curve.

Another important critical field accessible from the SW model is the so called irreversible switching field  $H_{irr}$ . This is the critical field value where the magnetisation change can not be reversed and the hysteresis opens. Starting from equations (3.12) and (3.13), then eliminating  $\beta$  and solving the resulting asteroid equation for the field component, the following formula is obtained [18],

$$\frac{H_{irr}}{H_A} = \frac{1}{[(\sin^2 \Theta)^{2/3} + (\cos^2 \Theta)^{2/3}]^{3/2}}. \quad (3.15)$$

Along the easy axis,  $\Theta = 0^\circ$ , the irreversible field equals the anisotropy field  $H_A$  while for  $\Theta = 45^\circ$  it is exactly half the anisotropy field ( $H_{irr}(\pi/4) = H_A/2$ ).

Experimentally, the coercive field can be obtained from measuring the longitudinal magnetisation component  $m_{\parallel}$  as is shown in Fig. 3.7 and the irreversible field  $H_{irr}$  from the transverse component  $m_{\perp}$ .

## 3.2 Exchange Anisotropy

More than fifty years ago, W. H. Meiklejohn and C. P. Bean published a work where they reported on a "New Magnetic Anisotropy". They had observed a shift of the hysteresis loop of Co/CoO nanoparticles (10 – 100 nm size) after cooling them in an external field through the antiferromagnetic ordering temperature of CoO [19]. Without the antiferromagnetic CoO shell or with the shell being in the paramagnetic state, the effect did not occur so they concluded that the presence of an antiferromagnet in direct contact to the ferromagnet is responsible for the loop shift.

Fig. 3.8 shows the original measurement by Meiklejohn and Bean on Co/CoO particles. Clearly the loop shift and also the increase of the coercivity are visible when comparing the field-cooled (solid) to the zero-field-cooled (dashed) curve. Both hystereses have been measured at 77 K after field cooling or zero-field cooling from room temperature. The Néel temperature of CoO is 291 K.

Meiklejohn and Bean named this new effect *exchange bias* since it can be interpreted as a bias field which is induced by the antiferromagnet via interfacial exchange. Another name commonly used is *unidirectional anisotropy*.

Exchange bias has since then become a major topic of magnetism research and still is. Mostly because it is a paragon for a magnetic coupling phenomenon between different magnetic phases. Although the target of intense research, even today the microscopic mechanisms at the ferromagnet/antiferromagnet interface are not fully understood. Another important point is its technological relevance. Exchange bias is used to effectively pin soft-magnetic layers in a very controlled way and thereby forms the basis for GMR (giant magneto-resistance) systems based on the spin-valve principle. Along with the rise of GMR read-heads and sensors, exchange bias saw increased research activity since the early 90s.

The following section reviews some basic concepts and models to describe exchange bias quantitatively. It closes with a discussion of the recently introduced spin glass model.

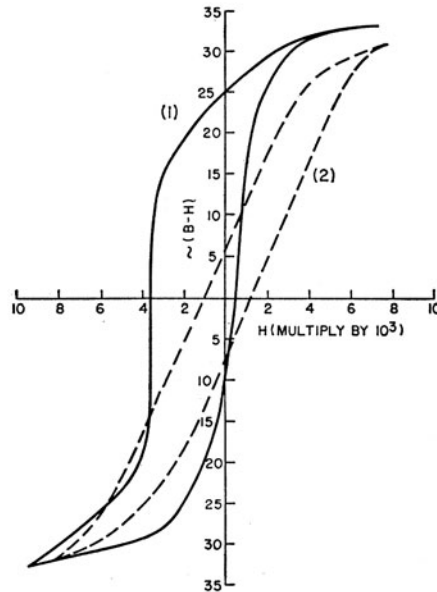


Figure 3.8: First measurement of exchange bias in Co/CoO particles (10–100 nm) by Meiklejohn and Bean 1957. The curves have both been recorded at 77 K. The solid one shows the hysteresis after cooling in field, the dashed one has been zero-field-cooled (graph reproduced from the original paper by Meiklejohn and Bean [19]).

### 3.2.1 Phenomenology of Exchange Bias

In systems where a ferromagnet is in direct contact to an antiferromagnet, a coupling across the interface of the two occurs. If the system has been field cooled, the antiferromagnet induces a unidirectional anisotropy to the ferromagnet leading to a shift of the hysteresis loop by the so called exchange bias field  $H_{eb}$ . Besides the shift  $H_{eb}$ , an increase of the coercive field  $H_C$  is usually observed as well. The origin of  $H_{eb}$  is the exchange coupling between the ferromagnet and the antiferromagnet across the interface and the existence of a pinned net moment in the antiferromagnet. This is quite strange since antiferromagnets in the first place are fully compensated hence have no moments or spins which could couple to external moments.

In a first attempt to explain the effect, Meiklejohn and Bean formulated a very simple and intuitive picture of the ferro-/antiferromagnet interface [19, 20]. They assumed an antiferromagnet where the individual monolayers are not compen-

sated. Moreover the interface between ferro- and antiferromagnet is assumed to be perfect, i.e., atomic flat. In this case the last row of spins in the antiferromagnet would be uncompensated since the neighboring spins in the antiferromagnet only compensate half of their net moment. Another restriction has to be made for the coupling across the interface, it has to be either ferromagnetic as it is the case in Fig. 3.9, or antiferromagnetic but no mixtures.

If the sample is now field cooled from a temperature  $T$  below the Curie temperature of the ferromagnet but above the Néel temperature of the antiferromagnet  $T_N < T < T_C$ , the antiferromagnet will align in a way that minimizes the coupling energy with the ferromagnet. The ferromagnetic moment direction is *imprinted* into the antiferromagnet [21] as shown in the inset of Fig. 3.9. At first, the

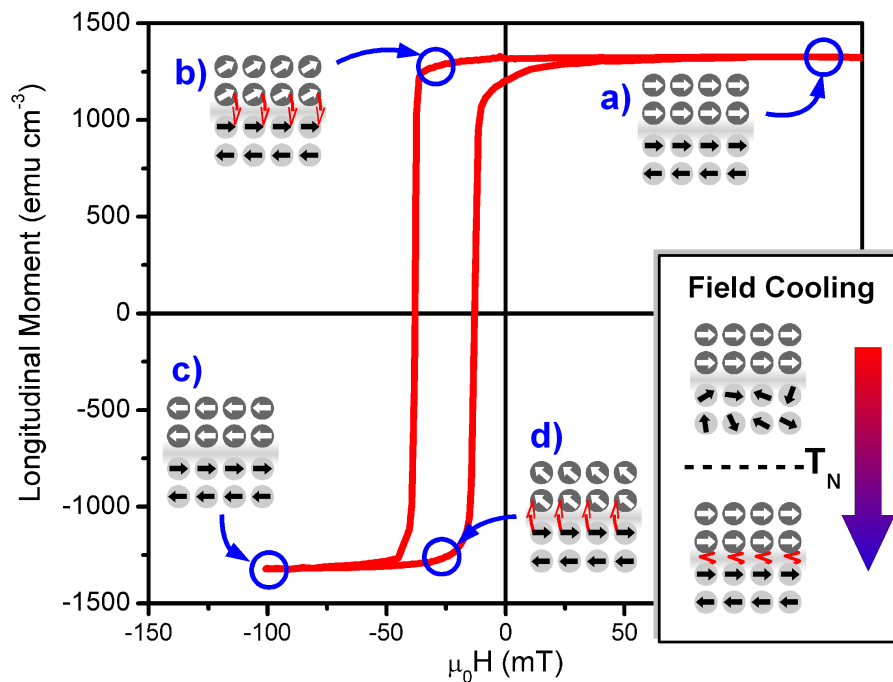


Figure 3.9: Simple phenomenological picture describing the effect of an interfacial exchange coupling on the hysteresis of a ferromagnet. More details are given in the text. The inset illustrates the creation of a unidirectional anisotropy by aligning the uncompensated moments of the antiferromagnet by the adjacent ferromagnet during field cooling through the ordering temperature of the antiferromagnet.



magnetisation in the sample is saturated in positive field direction as shown in Fig. 3.9a). If the external field is now reduced to zero, the ferromagnet is fixed in positive direction by the additional unidirectional anisotropy imposed by the antiferromagnet. However, for a negative external field, a torque starts to act on the moments and they try to rotate. This description will only consider coherent rotation to simplify things. Situation b) in Fig. 3.9 shows the ferromagnetic moments already rotated by some degree but still the coupling to the antiferromagnet keeps them in the positive direction. Virtually a competition of the Zeeman energy from the external field and the unidirectional anisotropy takes place. At some negative field value, the Zeeman energy overcomes the anisotropy energy and the ferromagnet rotates to the negative direction, state c) in Fig. 3.9. When the field now returns to the positive direction, the anisotropy and field work in the same direction. This means that the ferromagnet might even rotate back to positive values while the field is still in the negative direction as is indicated in Fig. 3.9d). The interplay of the two competing forces on the moments determines the rotation and thus the coercive fields.

Before continuing with the discussion, it is useful to introduce some basic definitions and nomenclature for the description of exchange bias and the properties of a shifted loop. By generally accepted convention [22–24], the loop shift  $H_{eb}$  and the coercivity  $H_C$  are defined by

$$H_{eb} = \frac{(H_{C1} + H_{C2})}{2} \quad H_C = \frac{(-H_{C1} + H_{C2})}{2}, \quad (3.16)$$

where  $H_{C1}$  is the smaller of the two coercive fields while  $H_{C2}$  is the larger one. Fig. 3.10 shows the four relevant properties of an exchange biased hysteresis loop.

The magnetic hysteresis loop of an exchange bias system as it is shown in Fig. 3.9 can be described in the framework of the Stoner-Wohlfarth model which has been introduced in Section 3.1.4. To do so, certain assumptions have to be made about the ferromagnet and the antiferromagnet:

- The antiferromagnetic spin lattice can be rotated as a whole, its rigidness is defined by the anisotropy constant  $K_{AF}$ ;

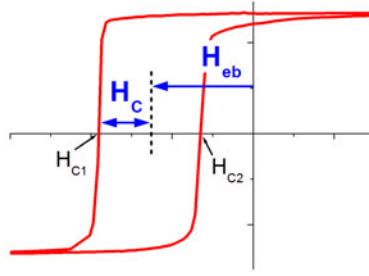


Figure 3.10: Definition of the relevant exchange bias parameters of a shifted hysteresis loop.

- No domains are formed in the ferromagnet nor in the antiferromagnet;
- Ferro- and antiferromagnet couple across the interface by a coupling parameter  $J_{eb}$ ;
- The interface is atomically flat.

Based on these assumptions, the total free energy per unit area from section 3.1.4 can be extended to:

$$E = -\mu_0 H_{appl} M_F t_F \cos(\Theta - \beta) - K_F t_F \sin^2(\beta) - J_{eb} \cos(\beta - \alpha) + K_{AF} t_{AF} \sin^2(\alpha). \quad (3.17)$$

Two new terms have been introduced in equation (3.17) to consider the existence of a unidirectional anisotropy or exchange bias. The first term  $J_{eb} \cos(\beta - \alpha)$  is the interfacial coupling of the antiferromagnet with the ferromagnet.  $J_{eb} [\text{J/m}^2]$  is the corresponding interface exchange constant and  $(\beta - \alpha)$  the angle between the magnetisation of the ferromagnet and the direction of the antiferromagnets' sub-lattice moments. Here, the antiferromagnet is allowed to rotate as a whole and this rotation is described by the magnetisation  $M_{AF}$  which is the direction of the moments in one of the two antiferromagnetic sub-lattices. The idea is that the spin structure of the antiferromagnet can be divided into two sub-lattices with antiparallel moment orientation. Each sub-lattice can then be treated like a ferromagnet e.g. by assigning a magnetisation direction. The second term is the anisotropy energy related to the antiferromagnet.  $K_{AF}$  is the anisotropy constant and for simplicity it is assumed to be parallel or collinear with the ferromagnets anisotropy. Furthermore the thickness of ferro- and antiferromagnet,  $t_F$  and

$t_{AF}$  is included in equation (3.17). The geometry for equation (3.17) including the anisotropy easy-axis of the antiferromagnet and its magnetisation direction is sketched in Fig. 3.11. Now equation (3.17) can be minimized with respect to  $\alpha$

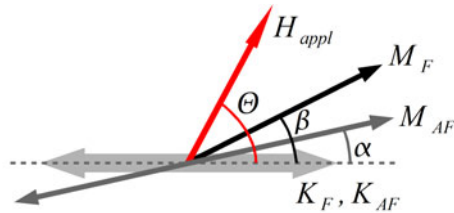


Figure 3.11: Definition of the parameters  $M_F$ ,  $K_F$  and  $H_{appl}$  together with their respective orientations expressed by the angles  $\alpha$ ,  $\beta$  and  $\Theta$ .

and  $\beta$  in a way as described in Section 3.1.4. Before discussing the general set of equations, two special cases will be addressed since they provide fundamental insights.

First, the situation when the antiferromagnet is perfectly rigid with an infinitely large anisotropy will be investigated. Then the antiferromagnetic moments can not rotate and the last term in equation (3.17) becomes zero. In this case, the loop shift is found to be:

$$H_{eb}^{\infty} = \frac{J_{eb}}{M_F t_F}. \quad (3.18)$$

This formula directly relates the loop shift with the interface coupling  $J_{eb}$  and is therefore of great importance. Note that  $J_{eb}$  obtained from measuring  $M_F$ ,  $t_F$  and  $H_{eb}$  by e.g. magnetometric means is the only proper measure characterizing the strength of exchange bias in a system.

The second special situation is when the antiferromagnet has zero anisotropy. In this case, the moments in the antiferromagnet as a whole can rotate freely. The ferromagnet couples via  $J_{eb}$  to the antiferromagnets sub-lattice moments and takes the whole antiferromagnet with him upon reversal. Since the antiferromagnet has to be rotated out of its easy direction defined by  $K_{AF}$ , the coercive field increases but the loop remains symmetric with respect to the y-axis. Hence, for

the occurrence of a loop shift in an exchange bias system the following condition has to be fulfilled:

$$K_{AF} t_{AF} \leq J_{eb} \quad (3.19)$$

Next, the general outcome of the minimization of equation (3.17) will be analysed. For consistency reasons, the discussion will use the nomenclature of reference [18]. It is found that the magnetisation reversal process obeys the following set of equations:

$$\begin{aligned} \frac{H}{H_{eb}^{\infty}} \sin(\Theta - \beta) + \sin(\beta - \alpha) &= 0 \\ R \sin(2\alpha) - \sin(\beta - \alpha) &= 0. \end{aligned} \quad (3.20)$$

Here,  $H_{eb}^{\infty}$  is the exchange bias in the case of a rigid antiferromagnet as defined by equation (3.18) and  $R$  is a ratio of the form

$$R = \frac{K_{AF} t_{AF}}{J_{eb}}, \quad (3.21)$$

which arises from the inequality (3.19). Finally note that the anisotropy of the ferromagnet is set to zero in equation (3.20), thus  $K_F = 0$ , to simplify the following considerations.

In reference [18], the dependent equations (3.20) have been evaluated numerically to obtain the relevant angles  $\alpha$  and  $\beta$  as a function of the applied field. The former angle,  $\alpha$ , describes the orientation of the antiferromagnetic spins with respect to the anisotropy direction while the latter describes the ferromagnets' one. From this numerical evaluation it turns out that the loop shift and the coercive field only depend on the angle  $\beta$  while  $\alpha$  only influences the shape of the hysteresis loop for small values of the ratio  $R$ . The rotation  $\beta$  of the ferromagnetic spins is determined by  $R$  which makes the ratio (3.21) the key parameter of an exchange bias system. Remember that the ferromagnets anisotropy is set to zero so the coercive field only originates from the antiferromagnets anisotropy!

Three regions for  $R$  can be distinguished by their characteristic magnetisation reversal:

- $R \geq 1$ : the antiferromagnetic spins are more or less rigid. They do not rotate.
- $0.5 \leq R \leq 1$ , in this region the spins rotate irreversible with the ferromagnet. However, the rotation is not coherent but in jumps depending on the interplay of anisotropy and coupling.
- For  $R \leq 0.5$ , the spins rotate coherently with the ferromagnetic spins. No jumps occur as can be seen also from the angular dependency shown in Fig. 3.12 f).

Example hysteresis loops for all three regions of  $R$  are shown in Fig. 3.12. The right column shows the corresponding rotation angle  $\alpha$  of the antiferromagnetic moments depending on the rotation angle  $\beta$  of the ferromagnetic moments. For  $R = 20$ , the loop is shifted but shows no coercivity since the antiferromagnet is very rigid (and the ferromagnet itself has no anisotropy here!). Accordingly the antiferromagnetic spins do not rotate out of the anisotropy direction as can be seen from Fig. 3.12b). For smaller  $R$  (but still  $\geq 1$ ), the antiferromagnetic spins start to rotate out of the anisotropy axis but still do not change direction, the rotation is reversible. This affects the loop shape upon magnetisation reversal. The second region for  $R$  in the range from 1 to 0.5 exhibits no loop shift (Fig. 3.12c)) since now the inequality (3.19) is not fulfilled. The antiferromagnetic spins rotate irreversible with the ferromagnet and change direction upon magnetisation reversal. However, compared to hystereses from the third region which are shown in 3.12e), the hystereses in region two have a more rounded shape. For  $0.5 \leq R \leq 1$ , the antiferromagnetic spins show a sudden direction change when  $J_{eb}$  overcomes the anisotropy  $K_{AF} t_{AF}$ , as can be seen from the jumps of the antiferromagnetic spin angle  $\alpha$  in Fig. 3.12d). If the anisotropy is further reduced, thus for  $R \leq 0.5$ , the antiferromagnetic spins rotate coherently with the ferromagnet leading to a square shaped hysteresis with no loop shift and a coercive field which is determined by  $R$ .

Before the section closes, some important further results of the numerical evaluation of equations (3.20) shall be briefly discussed.

The loop shift  $H_{eb}$  for  $R \geq 1$  depends on  $R$  and thus is altered compared to the

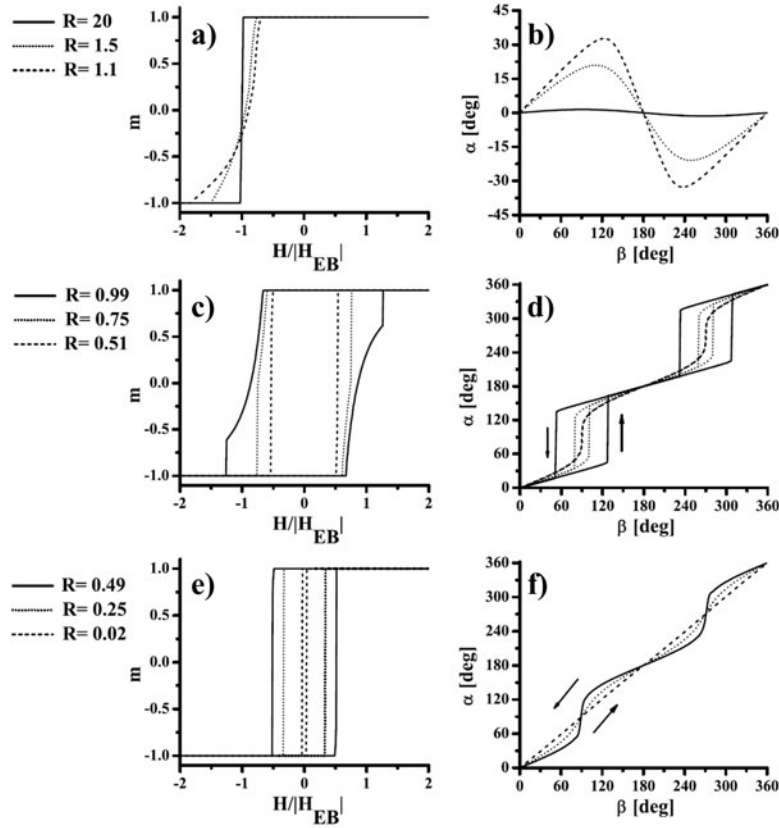


Figure 3.12: Simulated hysteresis loops for different values of the R-ratio which accounts for the anisotropy of the antiferromagnet. The left column, subfigures a), c), and e) show the longitudinal magnetisation component while the right column ( b),d) and f) ) are the corresponding rotation angle of the antiferromagnet,  $\alpha$  depending on the ferromagnet,  $\beta$ , during the reversal (image reproduced from [18]).

ideal case from equation (3.18). The strength of the exchange bias for  $\Theta = 0^\circ$  and  $K_F = 0$  and  $R \geq 1$  is given by

$$H_{eb} = H_{eb}^\infty \sqrt{1 - \frac{1}{4R^2}} \quad , \text{ for } R \geq 1. \quad (3.22)$$

Another general aspect which directly follows from equation (3.19) is that there is a critical thickness for the antiferromagnet. If the antiferromagnet is too thin, the anisotropy of its spin lattice is too weak to withstand the force imposed by the

exchange interaction  $J_{eb}$  upon reversal of the ferromagnet:

$$t_{AF}^{critical} = \frac{J_{eb}}{K_{AF}}. \quad (3.23)$$

Below this threshold value, the whole interfacial energy is transformed into coercivity.

Finally, we will investigate the dependence of the exchange bias  $H_{eb}$  on the direction of the applied field with respect to the anisotropy direction. This azimuthal dependence of  $H_{eb}$  on the angle  $\Theta$  (compare Fig. 3.11) can be derived from calculating the coercive fields  $H_{C1}$  and  $H_{C2}$  by numerically solving equation (3.20). A dependence of the exchange bias on the angle  $\Theta$  and the ratio  $R$  of the form

$$H_{eb}(\Theta) = \frac{-J_{eb}}{\mu_0 M_F t_F} \cos(\alpha(R, \Theta + \pi/2) - \Theta) \quad (3.24)$$

is found. Here,  $\alpha(R, \Theta + \pi/2)$  is the angle of the antiferromagnetic spins at the coercive field.

### 3.2.2 Theoretical Considerations

In the previous section, the Meiklejohn & Bean model has been discussed. Although the model properly describes the qualitative behaviour of an exchange bias system, it fails when it comes to a quantitative description. The experimentally found interfacial coupling  $J_{eb}$  is by two-to-three orders of magnitudes smaller than predicted from the M&B model (the M&B model predicts a  $J_{eb} \approx 10 \text{ mJ/m}^2$  [18, 23] for experimental values refer to [22]). The reason for this discrepancy is related to the basic assumptions made for the M&B model: It is assumed that the interface between the two layers is perfectly or atomically flat. Another point is that the M&B model requires an antiferromagnet with uncompensated planes. However, exchange bias can also be observed in systems where the individual monolayers of the antiferromagnet are fully compensated [22], in fact the effect can be even larger than [25, 26].

To overcome these limitations of the M&B model and properly explain the magnitude of exchange bias, a multitude of models have been proposed during

the last decades. This section will briefly introduce the most prominent of these models and their underlying concepts.

**Néels Approach** Louis Néel was the first to propose an alternative model for exchange bias [27]. Using a continuum approach to split the ferromagnet/antiferromagnet system in small slices parallel to the interface he could show that parallel partial domains can be formed in both the ferromagnet and the antiferromagnet. This partial domain formation significantly lowers the shift of the hysteresis loop since it stores a large amount of the exchange energy. Fig. 3.13(b) illustrates this concept showing a partial domain wall formed in the antiferromagnet according to the later described Mauri model. The drawback however is that to justify the continuum approach, the model is limited to very thick layers (thickness  $> 1000 \text{ \AA}$ ) and that it requires a low anisotropy antiferromagnet to form the partial domain wall in a reasonable distance to the interface.

**The Malozemoff model** In 1987, Malozemoff suggested another model to explain the experimentally observed loop shifts [28]. The Malozemoff model assumes a non-perfect interface between ferro- and antiferromagnet making this model especially appealing since a real interface is never atomically flat. The randomly distributed defects at the interface result in a random field which leads to a domain formation in the antiferromagnet perpendicular to the interface.

The effect of random impurities or disorder on ordering phenomena, such as ferro- and antiferromagnetism has already been discussed by Y. Imry and S. Ma in a more general context. They showed that for large ordered systems, small random fields as would be caused by impurities or lattice distortion lead to a breakup of the whole sample into domains [29].

To illustrate the origin of the random field in the framework of the Malozemoff model consider a single mono atomic defect in the form of a bump at the interface. In Fig. 3.13(a) the three possible moment configurations under the presence of a bump defect are sketched. Due to the bump, several frustrated magnetic couplings occur in the system. A coupling between two of the atoms is considered



frustrated when two neighboring atoms are forced to an orientation of their magnetic moments which does not fit to their exchange interaction (e.g.  $J > 0$  but forced to align antiparallel).

It is obvious that this frustrated exchange interaction is not favorable in terms of energy and the system will try to minimize them. This gives rise to a local energy difference with each interface irregularity which can be described by an intrinsic local field. Due to the random distribution of defects, this field is of random character similar to those introduced by Imry & Ma [29].

As already mentioned, the presence of such a random field will lead to domain formation either in the ferromagnet or in the antiferromagnet. Restricting the description to a region with a single domain ferromagnet, the antiferromagnet has to break into domains in order to minimize the free energy from the random field. It is energetically favorable to form domains with walls lying perpendicular to the interface as is shown in Fig. 3.13(a). Within the Malozemoff model, the relevant parameters for such an antiferromagnetic domain are its diameter  $L$  and height  $h$  (compare Section 3.1.3). It is noteworthy that the presence of a uniform in-plane anisotropy  $K_{AF}$  of the antiferromagnet, as has to be the case when a shift of the hysteresis loop is observed, forces the domains to shrink until their size reaches the domain wall width  $\delta_{dw}$ . The reason for this shrinking is the additional energy required in the domains' walls. So the upper limit for the size of a domain formed in an antiferromagnet due to the presence of a random field is given by:

$$L \approx \pi \sqrt{A_{AF}/K_{AF}}$$

and

$$h = L/2,$$
(3.25)

with  $A_{AF}$  being the exchange stiffness of the antiferromagnetic moments and  $h$  the characteristic height of the domain. The exchange stiffness plays a major role here because it determines how many moments are required to rotate the magnetisation by for example  $180^\circ$ . According to Malozemoff, the strength of the

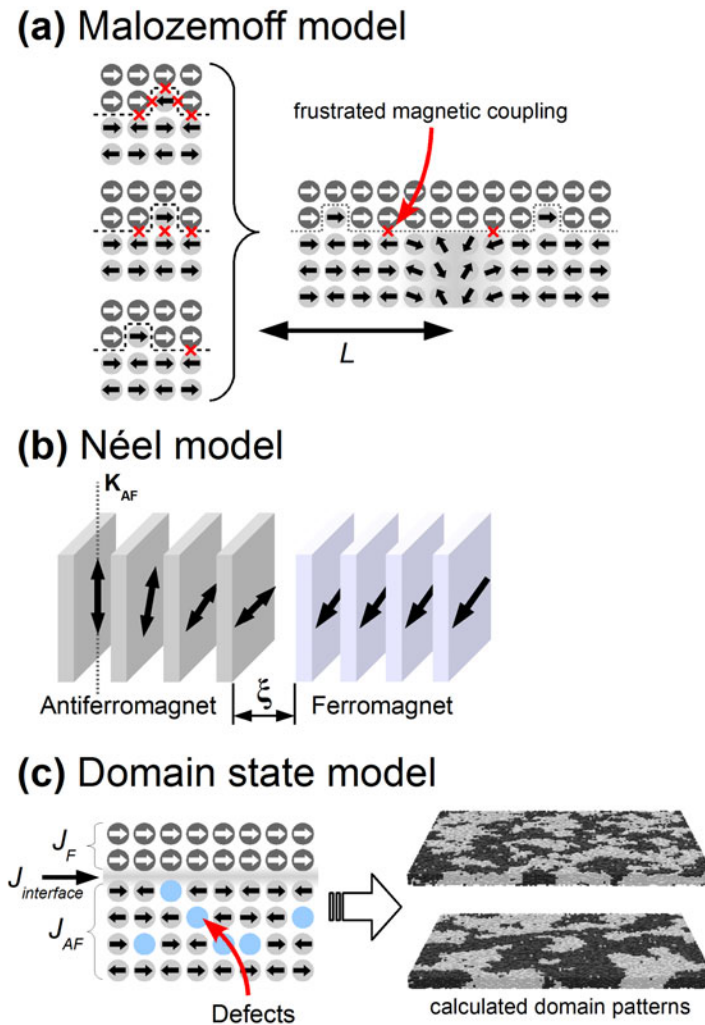


Figure 3.13: In (a), the principle mechanisms of the Malozemoff model are shown. An atomic bump at the interface creates several frustrated magnetic couplings (marked by  $\times$ ). This causes a random field which results in a break up of the antiferromagnet into domains as is shown on the right. The second sketch (b) is a schematic representation of the Néel model (or Mauri model) and shows the formation of a parallel domain wall in the antiferromagnet. The last image (c) illustrates the domain state model. The antiferromagnet contains several defects (marked as blue dots) in the form of stoichiometric changes, impurities or imperfections which cause a volume random field. As a consequence, domains with walls both parallel and perpendicular to the interface are formed. On the right, calculated domain distributions in an antiferromagnet are shown (these are reproduced from [30]).

exchange bias in such a system is found to be

$$H_{eb} = \frac{2z\sqrt{A_{AF}K_{AF}}}{\pi^2 M_F t_F}. \quad (3.26)$$

Here,  $z$  is a parameter characterizing the frustrated states at the interface and which due to the domain formation is of the order of unity.

The Malozemoff model was the first model taking into account the roughness of the interface making it the first model for a realistic description of the effect. Accordingly the quantitative predictions from the Malozemoff model are reasonable. For example in reference [18], the exchange bias for a CoO(25 Å)/Co(119 Å) bilayer has been calculated using an interface parameter of  $z = 1$  (compare reference [28]). From that, a theoretical value of  $H_{eb} = 48.7$  mT is found which corresponds well with experimental data for CoO/Co [22].

However, the defect density required to obtain reasonable values for  $H_{eb}$  from the Malozemoff model is too large compared to experimental observations [24]. Furthermore results from Neutron and X-ray techniques show that the treatment of the interface as it is assumed by the Malozemoff model is still too idealistic [31–36].

**The Mauri et al. approach** In the same year as Malozemoff, D. Mauri and co-workers published a simple extension of the M&B model [37] to overcome the quantitative problems mentioned in Section 3.2.1. This model, also referred to as "Mauri model", is based on the assumption that a parallel domain wall can form in the antiferromagnet directly below the interface as it is illustrated in Fig. 3.13(b). Further assumptions are: the ferromagnet is thinner than its domain size thus it is single domain (note the difference to Néels continuum approach); the interface is atomically flat and finally that the antiferromagnet is uncompensated. The last two assumptions are problematic because an atomically flat interface without any alloying or defects doesn't exist. Moreover exchange bias is also found in antiferromagnets with compensated interfaces.

The situation in the vicinity of the interface as proposed by Mauri et al. is sketched schematically in Fig. 3.13(a). The easy axis of the antiferromagnet as

well as the field cooling direction point along the z-direction. In the antiferromagnet the two sub-lattices (compare earlier in this section) are sketched as a double arrow indicating the easy axis. A parallel domain wall is formed in the antiferromagnet directly below the interface. The width of this domain wall depends on the exchange stiffness of the antiferromagnetic spin lattice and the anisotropy constant  $K_{AF}$ . Exchange interaction  $J_{eb}$  is assumed to depend on the exchange stiffness of the last row of antiferromagnetic moments and their distance  $\xi$  to the neighboring ferromagnet thus being  $J_{eb} = A_{12}/\xi$ . The exchange bias can then be calculated by

$$H_{eb} = \begin{cases} -J_{eb}/(\mu_0 M_F t_F) & \text{for } \lambda \ll 1, \\ -2(\sqrt{A_{AF}K_{AF}})/(\mu_0 M_F t_F) & \text{for } \lambda \gg 1. \end{cases} \quad (3.27)$$

with  $\lambda = A_{12}/\xi 2\sqrt{A_{AF}K_{AF}}$  being the interface exchange whose strength determines whether  $H_{eb}$  depends on the interfacial exchange coupling ( $\lambda \ll 1$ ) or is limited by the domain wall width ( $\lambda \gg 1$ ).

**Domain State Model** The Domain State (DS) model introduced by U. Nowak and co-workers [30] is, like the Malozemoff model, a defect driven concept. While Malozemoff considered only interfacial defects, the DS model focuses on the effect of impurities and defects on the bulk antiferromagnet. They consider the antiferromagnet as a diluted Ising antiferromagnet in an external field (DAFF). By replacing atoms from the antiferromagnet with non-magnetic atoms or defect sites, the number of antiferromagnetically coupled spins in the region is reduced. If the density of such impurities is not balanced between the two sub-lattices of the antiferromagnet, a local net magnetisation remains. Since such a net magnetisation would couple to an external field, it is favorable to form a 3-dimensional domain in the antiferromagnet to lower the free energy of the system. The energy costs thereby incurred can be minimized if the domain wall mainly sits on impurity sites. A schematic representation of the situation found in a DS antiferromagnet is shown in 3.13(c).

Certainly not all theoretical models which have been developed for exchange bias

can be discussed here. The selected models introduced in the preceding section, however, provide a good overview over principle concepts and the related problems. Namely the role of the interface and the magnetic state of the antiferromagnet have been subject to intense work. More detailed and comprehensive descriptions of the theoretical background of exchange bias can be found in the review by M. Kiwi [24] as well as in the works by R. Stamps [38] and F. Radu and H. Zabel [18].

### 3.2.3 The Interface – a Spin Glass

A major issue for all models discussed in the last section is the question of the magnetic configuration of the interface. Since Meiklejohn and Bean came up with their first very intuitive explanation for exchange bias, the role of the local magnetic coupling at the interface has attracted more and more attention. During the last decade X-ray based techniques which provide the necessary element selectivity could show that neither the structural nor the magnetic interface can be seen as a sharp borderline. Especially the existence of induced ferromagnetism in the antiferromagnet [31–36] raises the question whether the interface can really be described by such models as the one presented in the last Section.

It was only 2 years after the discovery of exchange anisotropy, that J. S. Kouvel reported on exchange bias in a spin glass system [39]. Meanwhile a broad variety of spin glass systems which show a significant exchange bias have been found [40–42]. Although their spin lattice is not ordered and one can not speak of a clear magnetic phase separation to the ferromagnet these systems exhibit the typical loop shift as well as an increase of the coercivity [43, 44].

Having the spin glasses in mind and thinking of the problems with the ferromagnet/antiferromagnet interface it seems natural to combine the two issues and develop a model based on a spin glass like state for the interfacial part of the antiferromagnet.

The idea of spin glass like magnetic disorder at the interface of an antiferromagnet/ferromagnet system has first been proposed by Schlenker and co-workers [45]. However, it took the results from X-ray spectroscopy to bring the idea back to life and recently a more thorough analysis of the impact of spin glass like

behaviour at the interface has been undertaken [18].

In the following section we will briefly recapitulate the major aspects of this model for exchange bias based on the review of F. Radu and H. Zabel [18].

It is assumed that the interface region of the antiferromagnet, thus atoms from the antiferromagnet at the interface or close to it are frustrated due to the reduced order in the region. The presence of the ferromagnet along with structural disorder as it is always present at a realistic interface weakens the ordering of the antiferromagnetic spin lattice and as a result, two distinct magnetic configurations can be expected in the region:

1. Uncompensated antiferromagnetic spins whose coupling to the rest of the antiferromagnetic spin lattice is weak and in consequence they are rotatable.
2. Uncompensated spins which are coupled tight to the antiferromagnetic spin lattice. These spins cause the loop shift.

Certainly the decision whether a magnetic moment at the interface is ferromagnetic, i.e., it is rotatable or whether it is pinned, depends on the local coupling environment.

To illustrate the complexity of the problem we can think of a single atom of the antiferromagnet located in the interface region. Due to chemical roughness it has several atoms of the ferromagnetic layer above sitting on direct neighbor positions. But also atoms from the antiferromagnet occupy a part of the neighboring sites. Especially the whole layer below is purely antiferromagnetic and for simplicity reasons we confine the discussion to a single-crystalline cubic system with epitaxy so that all atomic distances are the same. Then the atom feels the coupling  $J$  from the ferromagnetic and the antiferromagnetic partners and it is a matter of strength of each of the couplings and number of neighbors and maybe additionally orientation which determines the behaviour of the magnetic moment of this specific atom.

The model proposed by F. Radu and H. Zabel assumes that the interface splits into two sections, one, which is closer to the ferromagnet, where the antiferromagnetic spins are mostly rotatable. And a second region below the the rotatable moments, where the spins are also uncompensated but pinned to one direction by

the neighboring antiferromagnetic spin lattice. The latter would then cause the loop shift while the former causes the increase of coercivity.

To quantitatively account for the random character of the frustrated spins in the glassy region, a new effective uniaxial anisotropy  $K_{SG}^{eff}$  is introduced to the equation (3.17) (see 3.2.1). However, the spin glass state not only adds a new anisotropy to the system but it reduces at the same time the exchange coupling across the interface. The ideal  $J_{eb}$  of a perfectly flat interface without any glass state is weakened by the interfacial disorder or frustration and a new exchange coupling  $J_{eb}^{eff}$  takes place at the interface.

For a quantitative investigation it is convenient to describe both contributions, the newly introduced effective anisotropy of the frustrated interface spins  $K_{SG}^{eff}$ , and the resulting effective interface coupling  $J_{eb}^{eff}$  by one parameter. Therefore the ordering parameter  $f$  is defined which relates the two quantities to the unperturbed exchange coupling  $J_{eb}$ :

$$\begin{aligned} K_{SG}^{eff} &= (1 - f)J_{eb} \\ \text{and} \\ J_{eb}^{eff} &= f J_{eb}. \end{aligned} \tag{3.28}$$

So for a perfectly flat interface with no spin glass state, the ordering parameter is  $f = 1$  and the situation of the Meiklejohn & Bean model described in Section 3.2.1 is found. On the contrary, for a small  $f$ , the interface is strongly perturbed and for  $f = 0$  the interface is fully disordered respectively the spin glass state is so large that no coupling takes place at all.

With these substitutions, the equation (3.17) from Section 3.2.1 takes the form

$$\begin{aligned} E &= -\mu_0 H_{appl} M_F t_F \cos(\Theta - \beta) - K_F t_F \sin^2(\beta) \\ &\quad - f J_{eb} \cos(\beta - \alpha) + K_{AF} t_{AF} \sin^2(\alpha) \\ &\quad + K_{SG}^{eff} \sin^2(\beta - \gamma). \end{aligned} \tag{3.29}$$

The angle  $\gamma$  describes the anisotropy direction of the whole frustrated spin system at the interface. Note how the exchange coupling is modified by the ordering parameter and that a new term accounts for the different anisotropy energy of the

spin glass state. Minimizing this equation yields a new more complex stability condition and equation compared to the one described in 3.2.1:

$$\begin{aligned} \frac{H}{h} \sin(\Theta - \beta) + \frac{(1-f)}{f} \sin(2(\beta - \gamma)) + \sin(\beta - \alpha) &= 0 \\ r \sin(2\alpha) - \sin(\beta - \alpha) &= 0, \end{aligned} \quad (3.30)$$

with the reduced loop shift for a perfectly rigid antiferromagnet (compare equation (3.18))

$$h = -\frac{f J_{eb}}{\mu_0 M_F t_F}$$

and the new reduced  $r$

$$r = \frac{1}{f} R.$$

The equation set (3.30) can now be solved numerically similar to the Meiklejohn & Bean model. The resulting longitudinal and transverse magnetic components of an exchange bias system exhibiting a spin glass state at the interface are shown in Fig. 3.14 for three different amounts of interfacial disorder. As can be seen, the

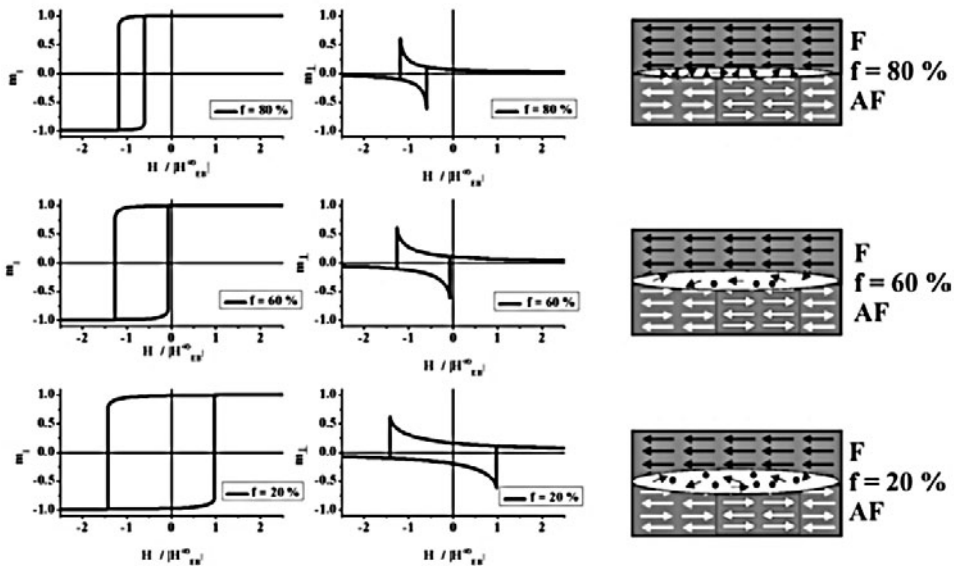


Figure 3.14: Example hysteresis for a system with a spin glass like layer at the interface between ferro- and antiferromagnet as derived numerically from equation (3.30) (image reproduced from reference [18]).



hysteresis loops show a variation of the coercivity and the loop shift depending on the disorder at the interface. The ferromagnet again has no MCA (thus  $K_F = 0$ ) to simplify the discussion and the anisotropy of the antiferromagnet which is described by the  $R$  factor is set to  $R = 62.5$  in this example. This value was chosen because it represents a standard CoO antiferromagnet with 100 Å thickness [18].

The spin glass model introduced by F. Radu and H. Zabel is interesting because it uses a very simple approach to account for the interfacial frustrated spins in the antiferromagnet. However, a direct proof of the existence of the ordering parameter  $f$ , thus a direct relation between the hysteresis loop shape and the structural and magnetic properties of the interface is still missing. In fact the model suffers from the fact that without experimental determination of  $f$ , introducing it as a free parameter into the Stoner-Wohlfarth model automatically leads to better agreement with experimental results.

Eventually remember that a spin glass system is characterized by its unique dynamic behaviour: A spin glass which is field cooled from above its glass transition temperature shows a remanent magnetisation which is decaying on a very long time scale [46]. This behaviour is in contrast to other magnetic phases which show very fast dynamics when going to an equilibrium but then remain constant in this state. If the antiferromagnet in exchange bias systems really has a kind of spin glass like interface with the ferromagnet, the spins affected should show a similar long timescale decay of their remanence. It would be very interesting to investigate the dynamics of the uncompensated rotatable moments which are discussed in the results section (compare 5.1) of this thesis to check whether there are long time variations.

### 3.2.4 Stability of the Antiferromagnet – Training & Blocking

In the last section on exchange bias, we will discuss effects related to the intrinsic stability of the antiferromagnet, namely the concepts of blocking temperature and training in such systems.

The term training of an exchange bias system refers to the irreversible change of the shape of the hysteresis loop in consecutive magnetisation reversals directly

after an initial field cooling. Paccard and co-workers were the first to report on training in exchange bias systems [47] in 1966 and since then this facet of exchange bias has been observed in nearly all material combinations. Different kinds of training can be observed in exchange bias. In most cases training manifests itself in a decrease of  $H_{C1}$ , i.e., the coercive field opposite to the field cooling direction, upon the first consecutive magnetisation reversals after initializing the antiferromagnet. In some cases also a decrease of  $H_{C2}$  is observed [48]. Here only the general case of  $H_{C1}$  reduction shall be discussed.

It is widely accepted that the origin of standard  $H_{C1}$  training is an irreversible change of the spin configuration at the interface between ferromagnet and antiferromagnet. Here, two cases have to be distinguished. The first possibility is a reorientation of the antiferromagnetic domain or the spin lattice of the antiferromagnet with respect to the field cooling direction. The second scenario is based on the spin glass model introduced in the previous section and assumes a change of the anisotropy axis of the frustrated, rotatable spins at the interface during the first hysteresis loops.

So in conclusion, either the antiferromagnetic unidirectional anisotropy changes its angle  $\Theta_{AF}$  which is the angle between the anisotropy  $K_{AF}$  and the field cooling direction, or the rotatable spin glass state at the interface changes its anisotropy axis which is defined by the angle  $\gamma$  (compare equation (3.29)).

Interestingly, the resulting training and magnetisation reversal is distinct for both cases so that it is possible to identify the training mechanism in a sample from its magnetisation reversal. Fig. 3.15 shows the longitudinal and transverse magnetisation component simulated using the Meiklejohn & Bean model introduced in 3.2.1 and the spin glass model (3.2.3). The image is reproduced from [18]. The authors assumed a conversion factor of 60% for the interface irreversibility and a value of  $R = 62.5/f$  for the R-ratio to simulate the curves. While the longitudinal curves look quite similar, a different reversal mechanism is found from the transverse signal. An irreversible change of the antiferromagnetic domain direction, thus a change of the antiferromagnetic anisotropy away from the field cooling direction ( $\Theta_{AF} \neq 0$ ) leads to a magnetisation reversal where the ferromagnetic spins always rotate on the same side. Actually, one could say that

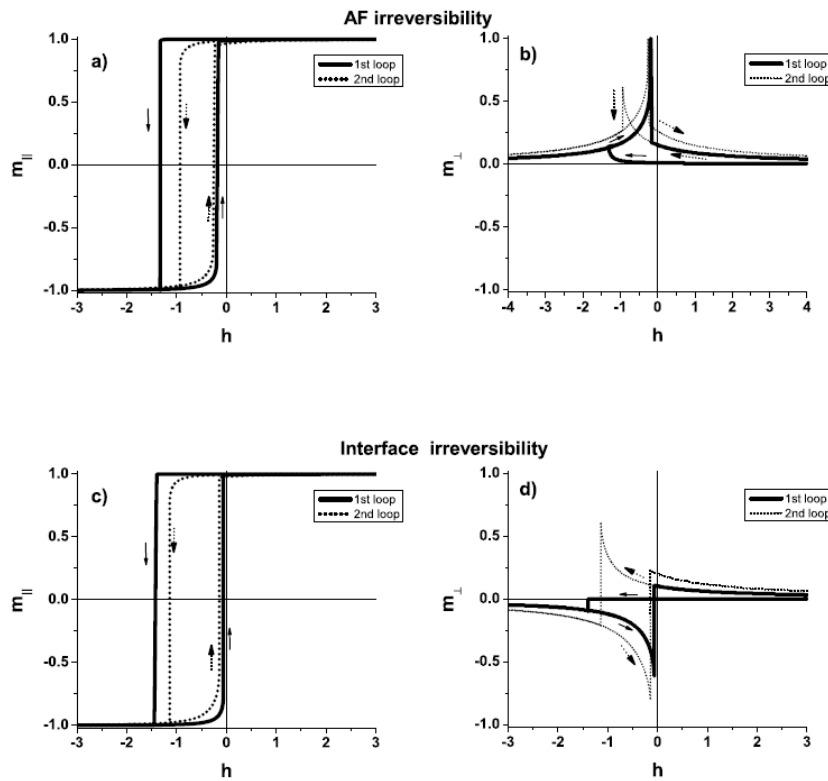


Figure 3.15: Simulated longitudinal and transverse magnetisation for an exchange bias system exhibiting training. The upper two graphs a) and b) show the case for an irreversible change of the antiferromagnetic domain orientation during the first loops. The lower plots show the training effect caused by a change of the anisotropy of the frustrated interfacial spins c) and d) (image reproduced from [18]).

the antiferromagnet *defines* a new direction of exchange bias which differs from the field cooling direction and is given by its anisotropy direction. In contrast the interface irreversibility leads to a transverse magnetisation component which rotates using both sides.

The second important concept for the stability of the antiferromagnetic spin lattice is the so called blocking temperature  $T_B$ . A crucial parameter for any exchange bias sample is the thermal stability of the antiferromagnetic spin lattice since it determines the temperature range where the effect can be observed. While the antiferromagnetic ordering temperature of a bulk antiferromagnet, which is named Néel temperature  $T_N$  in honor of Louis Néel, is a well defined point in the magnetic phase diagram, it is often observed, especially for polycrystalline

samples, that the exchange bias vanishes already at much lower temperatures. The temperature at which the exchange bias in a sample vanishes is referred to as the blocking temperature  $T_B$ .

In fact, it is often observed that the increase of the coercive field already starts for a temperature  $T_B < T < T_N$ , close to  $T_N$  while the loop shift just sets in below  $T_B$ . Another observation is, that  $T_B$  scales with the film thickness and the grain size in the sample. Hence it is obvious that the stability of the antiferromagnetic spin lattice, especially its anisotropy  $K_{AF}$  which is the source of the loop shift is affected by the volume of the antiferromagnet. As a consequence, polycrystalline samples exhibit a distribution of blocking temperatures which corresponds to the distribution of crystallite sizes.

### 3.3 Resonant Scattering & Magnetic Circular Dichroism

The energy dependent interaction of X-rays with matter is what is generally called X-ray spectroscopy. For X-rays with an energy ranging from  $\sim 100$  eV up to hundred keV this interaction is dominated by photoabsorption and coherent scattering at the electron shell of the atoms in a material (see e.g. [6, 49]). The attenuation of X-rays traveling through a material of thickness  $d$  is given by the Lambert-Beer law which states that the intensity is decreasing exponentially with the thickness according to

$$I(d, \lambda) = I_0 e^{-\mu(\lambda)d}. \quad (3.31)$$

$\mu(\lambda)$  is the attenuation length which is directly related to the absorption in the material.

Depending on whether the incident photon energy  $\hbar\omega$  corresponds to the excitation energy  $\Delta E$  of an electron state in the material the absorption process or excitation is either resonant or not. Resonant absorption takes place for  $\hbar\omega = \Delta E$  while in all other cases a non-resonant transition occurs. Another prerequisite is of course that the process of absorption/excitation fulfills all conservation rules (e.g. energy, momentum etc.) which gives rise to the so called dipole selection rules. A dramatic increase of the absorption is observed at the resonance frequency. Besides the energy differences of the bound states in the material, the polarization of the photon does play a major role for both processes, absorption and scattering. This polarization dependence can lead to several different effects which can be classified as follows

- **Birefringence** – when two distinct indices of refraction exist for horizontally and vertically polarized light.
- **Dichroism** describes polarization dependent absorption in a material.
- **Rotation** of the direction of linear polarized light (e.g. Kerr, Faraday).

To describe all these different effects taking into account resonant effects and the presence of magnetism is the aim of this section. First the general concept of non-resonant and resonant scattering will be discussed. The X-ray Magnetic Circular Dichroism (XMCD) is introduced and its relation to the scattering formalism is

explained.

### 3.3.1 A Scattering Formalism for X-rays

The scattering of an incident photon at the electron shell of an atom depends on several mechanisms which can be summarized as shown in Fig. 3.16.

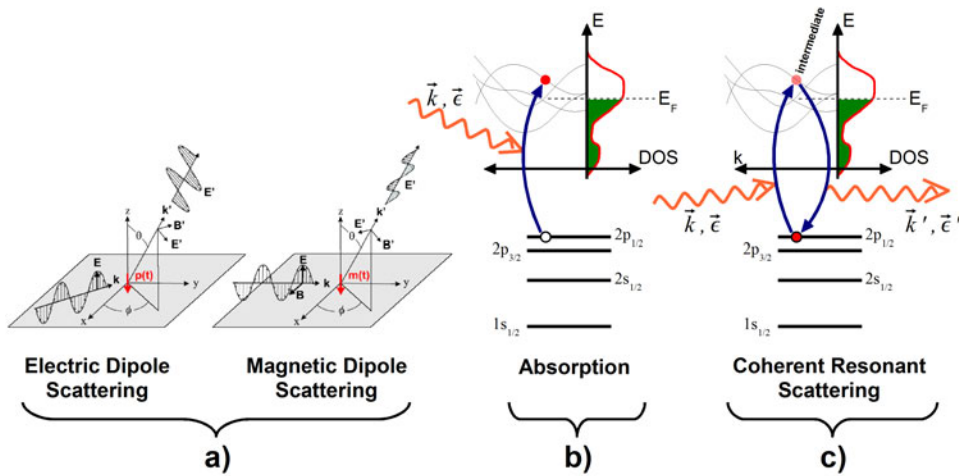


Figure 3.16: Different mechanisms for scattering of a polarized X-ray photon on an atom (the left part of the figure is reproduced from reference [6]).

On the left, Fig. 3.16(a) illustrates the scattering of an incident electromagnetic wave on the charge associated electric dipole moment  $\mathbf{p}(t)$  and its magnetic dipole moment  $\mathbf{m}(t)$ . Fig. 3.16(b) and (c) show the two resonant processes involving the excitation of a bound electron.

An atomistic description of all four interaction processes can be achieved using a general scattering approach (see for example [50]). From experiment, the scattered intensity  $I$  in the solid angle  $d\Omega$  is obtained. In this very general approach, a proportion of the incident light  $I_0$  is scattered into the angle segment  $[\Omega, \Omega + d\Omega]$  defined by the proportionality factor, i.e., the differential scattering cross-section which is given by

$$\left(\frac{d\sigma}{d\Omega}\right)^{scat} = |f(\mathbf{Q}, E)|^2. \quad (3.32)$$

The intensity scattered into the solid angle  $d\Omega$  is given by the square of the scattering amplitude  $f(\mathbf{Q}, E)$  which is also known as scattering length or scattering factor. This scattering amplitude is usually dependent on the direction of the incident light  $\mathbf{k}$  or the momentum transfer  $\mathbf{Q} = \mathbf{k} - \mathbf{k}'$  of the process and on the energy of the incident X-ray photon. To obtain the scattering amplitude of an atom, time dependent perturbation theory has to be used. While the processes shown in Fig. 3.16(a) can be described by a semi-classical treatment involving the respective dipole moments, the resonant effects 3.16(b) and (c) require a full quantum mechanical treatment. Following the approach by M. Blume [51] to describe charge and magnetic dipole scattering without anomalous dispersion, equation (3.32) can be rewritten as

$$\left(\frac{d\sigma}{d\Omega}\right)^{scat} = |f(\mathbf{Q}, E)|^2 = \left(\frac{1}{I_0}\right) P_{i \rightarrow f} \cdot \rho(E_f) \quad (3.33)$$

now relating the scattered intensity to the transition probability  $P_{i \rightarrow f}$  multiplied by the density of the intermediate states  $\rho(E_f)$  and normalized to the intensity of the incident light  $I_0$ . The transition probability  $P_{i \rightarrow f}$  per time unit for second order perturbation theory is given by

$$P_{i \rightarrow f} = \frac{2\pi}{\hbar} \left| \langle f | H | i \rangle + \sum_n \frac{\langle f | H | n \rangle \langle n | H | i \rangle}{E_i - E_n} \right|^2 \times \delta(E_i - E_f). \quad (3.34)$$

The eigenstates  $|i\rangle$  and  $|f\rangle$  describe the initial and final state of the overall system while  $|n\rangle$  is the intermediate state of the excitation as defined in Fig. 3.16(c). Thus in the initial state  $|i\rangle$ , the material is characterized by an electronic ground state  $|a\rangle$  and the incident photon with wavevector  $\mathbf{k}$  and polarization vector  $\boldsymbol{\epsilon}$  thus giving  $|i\rangle = |a; \mathbf{k}, \boldsymbol{\epsilon}\rangle$ . Then the Hamiltonian  $H$  for example might induce a transition of the system to a new eigenstate  $|f\rangle = |b; \mathbf{k}', \boldsymbol{\epsilon}'\rangle$  where the photon now has the new wavevector  $\mathbf{k}'$  and polarization vector  $\boldsymbol{\epsilon}'$ . The interaction Hamiltonian in equation (3.34) for the case of a quantized electromagnetic field as it is induced

by the X-rays is then,

$$H = -\frac{e^2}{2mc^2} \sum_n \mathbf{A}^2(\mathbf{r}_j) \quad (3.35)$$

$$- \frac{e}{mc} \sum_n \mathbf{A}(\mathbf{r}_j) \cdot \mathbf{p}_j \quad (3.36)$$

$$- \frac{e\hbar}{mc} \sum_n \mathbf{s}_j \cdot [\nabla \times \mathbf{A}(\mathbf{r}_j)] \quad (3.37)$$

$$- \frac{e^3\hbar}{2mc^4} \sum_n \mathbf{s}_j \cdot [\dot{\mathbf{A}}(\mathbf{r}_j) \times \mathbf{A}(\mathbf{r}_j)]. \quad (3.38)$$

$\mathbf{A}(\mathbf{r}_j)$  is the vector potential of the electromagnetic wave and is linked to the electric,  $\mathbf{E}(\mathbf{r})$  and magnetic field  $\mathbf{M}(\mathbf{r})$  vectors of the wave via the Maxwell equations [52]. The  $j$  electron states are described by  $\mathbf{r}_j$ ,  $\mathbf{p}_j$ , and  $\mathbf{s}_j$  their position, impulse and, spin, respectively.

The term (3.35) describes the radiation field itself while the interaction of the electron with this field is introduced by (3.36) corresponding to a charge dipole term. Term (3.37) represents the interaction of the electromagnetic wave with the spin and the final term (3.38) accounts for spin-orbit coupling. Splitting the Hamiltonian in equation (3.34) to the respective contributions leaves the linear term only depending on contributions quadratic in  $\mathbf{A}$  which are (3.35) and (3.38). While the second order term only depends on (3.36) and (3.37). From this ansatz, the full elastic scattering amplitude can be calculated and the result has the form:

$$\begin{aligned} f_{full} = & \frac{e^2}{mc^2} \left[ \langle b | \sum_j e^{i\mathbf{Q}\cdot\mathbf{r}_j} | a \rangle (\boldsymbol{\epsilon}' \cdot \boldsymbol{\epsilon}) \right. \\ & - i \frac{\hbar\omega}{mc^2} \langle b | \sum_j e^{i\mathbf{Q}\cdot\mathbf{r}_j} \mathbf{s}_j | a \rangle (\boldsymbol{\epsilon}' \times \boldsymbol{\epsilon}) \\ & + \frac{\hbar^2}{m} \sum_c \frac{\langle b | \mathbf{M}_i(\mathbf{k}', \boldsymbol{\epsilon}') | c \rangle \langle c | \mathbf{M}_j(\mathbf{k}, \boldsymbol{\epsilon}) | a \rangle}{(E_a - E_c) + \hbar\omega - i\Gamma_c/2} \\ & \left. + \frac{\hbar^2}{m} \sum_c \frac{\langle b | \mathbf{M}_j(\mathbf{k}, \boldsymbol{\epsilon}) | c \rangle \langle c | \mathbf{M}_j(\mathbf{k}', \boldsymbol{\epsilon}') | a \rangle}{(E_a - E_c) - \hbar\omega'} \right] \\ & \times (E_a - E_b + \hbar\omega - \hbar\omega'). \end{aligned} \quad (3.39)$$

The first two terms account for the charge and spin distribution related scattering



while the third and fourth term incorporate the resonant excitation. The finite width of the energy distribution of the intermediate state  $|c\rangle$  introduces a modification of the denominator in the form of an inverse lifetime  $\Gamma_c$ . Note that the intermediate state is now expressed by the electronic eigenstate  $|c\rangle$ . The transition matrices  $\mathbf{M}_{i,j}(\mathbf{k}, \boldsymbol{\epsilon})$  are given by

$$\mathbf{M}_{i,j}(\mathbf{k}, \boldsymbol{\epsilon}) = \sum_h \left( \frac{\boldsymbol{\epsilon} \cdot \mathbf{P}_{i,j}}{\hbar} + i(\mathbf{k} \times \boldsymbol{\epsilon}) \cdot \mathbf{s}_{i,j} \right) e^{-i\mathbf{k} \cdot \mathbf{r}_{i,j}}. \quad (3.40)$$

They contain interaction of the polarization  $\boldsymbol{\epsilon}$  with the orbital momentum  $\mathbf{P}_i$  which is a real number and an imaginary part caused by the interaction of the spin moment  $\mathbf{s}_i$  with the vector product of wave vector and polarization ( $\mathbf{k} \times \boldsymbol{\epsilon}$ ).

Equation (3.39) describes most of the phenomena related to X-ray scattering like birefringence, dichroism and polarization rotation to order  $(\hbar\omega/mc^2)^2$ .

### 3.3.2 Non-Resonant Magnetic Scattering

First the special case of magnetic scattering far away from resonance as derived by M. Blume [51] will be investigated. For elastic scattering with  $\omega(\mathbf{k}') \sim \omega(\mathbf{k}) \gg (E_a - E_c)/\hbar$  the transition of the second order terms is possible and has to be considered but it is not resonant thus the denominators can be neglected. Simplifying the two second order terms in (3.39) and solving the equation, the scattering amplitude for non-resonant charge and magnetic scattering is

$$\begin{aligned} f^{non-res} = & \frac{e^2}{mc^2} \langle b | \sum_j e^{i\mathbf{Q} \cdot \mathbf{r}_j} | a \rangle (\boldsymbol{\epsilon}' \cdot \boldsymbol{\epsilon}) \\ & - i \frac{\hbar\omega e^2}{m^2 c^4} \langle b | \sum_j e^{i\mathbf{Q} \cdot \mathbf{r}_j} \left( i \frac{\mathbf{Q} \times \mathbf{P}_j}{\hbar k^2} \cdot \mathbf{A} + \mathbf{s}_j \cdot \mathbf{B} \right) | a \rangle (\boldsymbol{\epsilon}' \times \boldsymbol{\epsilon}) \end{aligned} \quad (3.41)$$

with the substitution vectors for the polarization

$$\mathbf{A} = 2(1 - \mathbf{k} \cdot \mathbf{k}')(\boldsymbol{\epsilon}' \times \boldsymbol{\epsilon}) - (\mathbf{k} \times \boldsymbol{\epsilon}')(\mathbf{k} \times \boldsymbol{\epsilon}) + (\mathbf{k}' \times \boldsymbol{\epsilon}')(\mathbf{k}' \times \boldsymbol{\epsilon})$$

and

$$\mathbf{B} = (\boldsymbol{\epsilon} \times \boldsymbol{\epsilon}') + (\mathbf{k}' \times \boldsymbol{\epsilon}')(\mathbf{k}' \times \boldsymbol{\epsilon}) - (\mathbf{k} \times \boldsymbol{\epsilon}')(\mathbf{k} \times \boldsymbol{\epsilon}) - (\mathbf{k}' \times \boldsymbol{\epsilon}')(\mathbf{k} \times \boldsymbol{\epsilon}).$$

It is worth realizing that  $\mathbf{A}$  and  $\mathbf{B}$  are formally different which means that spin and orbital momentum contribute differently and thus can be distinguished experimentally.

Using the Fourier transformed of the charge density  $\mathbf{n}(\mathbf{Q})$ , the orbital momentum  $\mathbf{L}(\mathbf{Q})$  and spin density  $\mathbf{S}(\mathbf{Q})$ , equation (3.41) can be further simplified to the final form

$$f^{non-res} = \mathbf{n}(\mathbf{Q})(\boldsymbol{\epsilon}' \cdot \boldsymbol{\epsilon}) - i \frac{\hbar\omega}{mc^2} f_D \left[ \frac{1}{2} \mathbf{L}(\mathbf{Q}) \cdot \mathbf{A} + \mathbf{S}(\mathbf{Q}) \cdot \mathbf{B} \right]. \quad (3.42)$$

This equation now describes the scattering from charge distributions with the first term and from magnetisation densities with the second term.  $f_D$  is the Debye-Waller factor. Note how the magnetic contribution is smaller by  $\hbar\omega/mc^2$  than the charge term. Finally equation (3.42) can be used to compare the magnetic signal to the charge contribution. The ratio between the two is given by

$$\frac{\sigma_{mag}}{\sigma_{charge}} \approx \left( \frac{\hbar\omega}{mc^2} \right)^2 \frac{N_{mag}^2}{N} \langle \mathbf{s} \rangle^2 \frac{f_{mag}^2}{f^2}. \quad (3.43)$$

$N_{mag}$  is the number of magnetic electrons while  $N$  is the overall number. M. Blume calculated the ratio of equation (3.43) for the example Fe and 10 keV photons. He finds a ratio of  $\sim 4 \times 10^{-6} \langle \mathbf{s} \rangle^2$ . Since  $\langle \mathbf{s} \rangle$  is unity at very low temperatures and goes to zero at the Curie temperature, the ratio is generally even smaller.

In conclusion the non-resonant magnetic contribution to the scattering factor is neglectable compared to the resonant ones discussed in the next section.

### 3.3.3 Resonant Magnetic Scattering

We will now consider the case when the incident photon has an energy  $\hbar\omega$  which corresponds to the transition energy of a bound electron state in the atom ( $E_a - E_c$ ). The scattering amplitude is then dominated by the third term in the scattering amplitude (3.39) and the transition matrix element  $\mathbf{M}_i(\mathbf{k}, \boldsymbol{\epsilon})$  has to be determined for the respective electric  $2^\ell$ -pole transition ( $E\ell$ ). It is obvious from equation (3.39) that the lifetime  $\Gamma_c$  of the intermediate excited state directly influences the

scattering amplitude. In other words the transition is directly proportional to the density of unoccupied states in the conduction band above the Fermi-energy  $E_F$ .

The following discussion will focus on the electric dipole (E1,  $\ell = 1$ ) transition, the corresponding quadrupole resonant (E2) transition can be found in the literature [1,53]. Within the dipole approximation the transition matrix element (3.40) reduces to

$$\mathbf{M}(\mathbf{k}, \boldsymbol{\epsilon}) = \sum_N \sum_n \mathbf{p}_n \cdot \boldsymbol{\epsilon} e^{i\mathbf{k} \cdot \mathbf{r}_N} \quad (3.44)$$

where  $\mathbf{p}$  is the position vector of the electron,  $\mathbf{p}$  the electron momentum vector,  $\boldsymbol{\epsilon}$  the polarization vector of the incident light, and finally  $\mathbf{k}$  the wavevector of the photon. The sum goes over all atoms  $N$  in the unit cell and over all core electrons  $n$  of the atom.

The calculation of the transition matrix elements for the resonant E1 transition is lengthy and will not be done explicitly. However, the course of action necessary to derive the elements can be summarized as follows [54]: First the wavefunctions of  $|a\rangle$ ,  $|b\rangle$  and  $|c\rangle$  have to be expressed in terms of atomic orbitals. These orbitals can be described by a radial component  $R_{n,\ell}(r)$  and an angular part containing both, angular and spin contribution. The  $2p$  core levels exhibit a strong spin-orbit splitting so that the angular momentum is given by  $\vec{j} = \vec{l} + \vec{s}$ . The Clebsch-Gordon coefficients allow expressing the spin-orbit coupled term by a linear combination of uncoupled terms and thus simplify the problem significantly. The wavefunction can be written as a linear combination of three individual components: The radial component  $R_{n,\ell}(r)$  with the quantum numbers  $n$  for the shell and  $l$  for the angular momentum. The spherical harmonic  $Y_{\ell,m}$  which describes the angular part and finally  $\chi_{s,m_s}$  which accounts for the spin part [50]. The important dipole selection rules which apply to transitions between such states are given by [8]:

$$\begin{aligned} \Delta\ell &= \pm 1 \\ \Delta m_\ell &= 0, \pm 1 \\ \Delta s &= 0 \end{aligned} \quad (3.45)$$

and

$$\Delta m_s = 0$$

Using the wavefunction and taking into account the dipole selection rules, equation (3.39) can be solved for the case of a resonant  $2^\ell$ -pole transition and the resulting contribution to the scattering amplitude as derived by J.P. Hannon and co-workers [1] is given by:

$$f_{\text{El}}^{\text{res}} = (\mathbf{k}, \boldsymbol{\epsilon}; \mathbf{k}', \boldsymbol{\epsilon}') = \frac{4}{k} f_D \sum_{m=-\ell}^{\ell} [\boldsymbol{\epsilon}' \cdot Y_{\ell,m}(\mathbf{k}') Y_{\ell,m}^*(\mathbf{k}) \cdot \boldsymbol{\epsilon}] F_{\ell,m}(\omega), \quad (3.46)$$

with the factor  $F_{\ell,m}(\omega)$  determining the strength of the resonance according to

$$F_{\ell,m}(\omega) = \sum_{\alpha,\eta} \frac{P_\alpha P_\alpha(\eta) \Gamma_x(\alpha M \eta; \text{E}\ell) / \Gamma_\eta}{\chi(\alpha, \eta) - i}. \quad (3.47)$$

Here the subscripts  $\ell$  and  $m$  refer to the orbital and magnetic transitions, respectively. Equation (3.46) is only valid if the involved material is isotropic which means either a centrosymmetric single-crystal or a polycrystalline sample. Then an asymmetry only originates from the magnetism in the sample.

From experiment it is well known that the magnetism of the  $3d$  transition metal ions strongly affects the  $2p \rightarrow 3d$  excitation (also see Section 3.3.4) and that the electric dipole transition E1 is the dominant transition in these systems. Then  $\ell = 1$  and  $m = 0, \pm 1$  and the vector spherical harmonics in equation (3.46) can be calculated. The scattering amplitude then takes the following form:

$$\begin{aligned} f_{\text{E1}}^{\text{res}} = & \frac{3}{4k} [F_{11} + F_{1-1}] (\boldsymbol{\epsilon}' \cdot \boldsymbol{\epsilon}) - i \frac{3}{4k} [F_{11} - F_{1-1}] (\boldsymbol{\epsilon}' \times \boldsymbol{\epsilon}) \cdot \mathbf{M} \\ & + \frac{3}{4k} [2F_{10} - F_{11} - F_{1-1}] (\boldsymbol{\epsilon}' \cdot \mathbf{M}) (\boldsymbol{\epsilon} \cdot \mathbf{M}). \end{aligned} \quad (3.48)$$

This equation fully describes anomalous scattering from charge and magnetism within the dipole approximation. Note how the first term does not depend on the magnetic moment  $\mathbf{M}$  and thus is a pure charge contribution related to the resonant enhancement at the absorption edge. The second term which depends on the difference  $[F_{11} - F_{1-1}]$  of the transition matrix elements for left and right circular polarized light and scalar product of the incident X-ray polarization and the magnetisation  $\mathbf{M}$ . This, namely the imaginary part of  $F_{11}$  and  $F_{1-1}$ , is the origin of the magnetism dependent resonant scattering amplitudes and moreover

the X-ray magnetic circular dichroism (XMCD) which will be introduced in the following section. XMCD is a special case of resonant magnetic scattering as will be shown later. Finally the last term which is quadratic in  $\mathbf{M}$  is the origin of the so called X-ray magnetic linear dichroism [54].

Concluding all processes derived on the last pages one can now define a general representation of the scattering amplitude (3.33) which contains the contributions according to their relation to magnetism in the sample

$$f = f_0 + f_{mag}^{non-res} + f'_{charge} + if''_{charge} + f'_{mag} + if''_{mag}, \quad (3.49)$$

$f_0$  is the normal Thomson charge scattering and  $f_{mag}^{non-res}$  accounts for contributions from the magnetism in the material far off from resonant excitations and is given by the second term in equation (3.42).  $f'_{charge}$  and  $f''_{charge}$  are the anomalous charge scattering at the resonance given by the first term in equation (3.48) ( $[F_{11} + F_{1-1}]$ ). These describe the resonant enhancement, the so called *white lines* at the resonant edges of an atom. Finally  $f'_{mag}$  and  $f''_{mag}$  describe the magnetic resonant contribution at the resonant edges and are given by  $[F_{11} - F_{1-1}]$ . The third term in equation (3.48) which is quadratic in  $\mathbf{M}$  is omitted here since it is usually by orders of magnitude smaller than the circular dichroism from the second term. There are however systems like antiferromagnets which do not show a magnetic circular dichroism but a magnetic linear dichroism thus only a contribution from the third term. Note that in the following Sections,  $f_{mag}^{non-res}$  is also omitted since it is by several orders of magnitude smaller than the  $2p \rightarrow 3d$  circular dichroism [3].

To illustrate the effect of the various contributions to the overall scattering amplitude, Fig. 3.17 shows the Fe  $L_{2,3}$  edge, i.e.,  $2p_{\frac{3}{2}} \rightarrow 3d$  and  $2p_{\frac{1}{2}} \rightarrow 3d$  scattering amplitude for circular polarized light. The grey solid line is obtained from the Henke-Gullikson atomic scattering parameter tables [49] and contains the Thomson or charge scattering (3.41) and the non-resonant dispersive part  $f'$  and the absorptive part  $f''$ . The latter two are calculated from equation (3.39) in a similar way as the non-resonant magnetic contribution from equation (3.41). Adding resonant enhancement which is described by the first term in equation

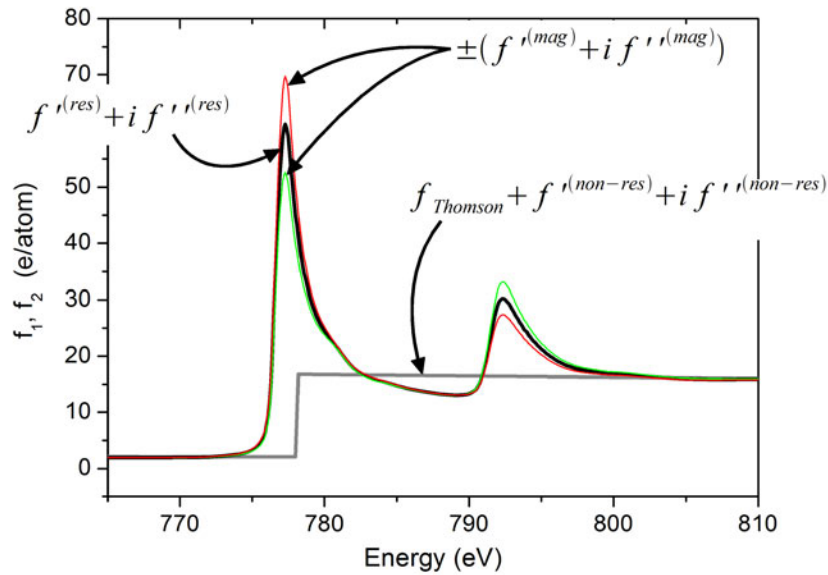


Figure 3.17: Co  $L_{2,3}$  absorption edges at eV ( $2p_{3/2}^3 \rightarrow 3d$ ) and eV ( $2p_{1/2}^1 \rightarrow 3d$ ) showing the various contributions to the scattering amplitude  $f$ . More details are given in the text.

(3.48) one obtains the black curve which now shows the characteristic enhanced absorption white lines. Finally introducing magnetism by using circular polarized X-rays, the second term of equation (3.48), i.e.,  $[F_{11} - F_{1-1}]$  comes into play modifying the absorption. This last step leads to two different curves (red & green in the figure) whose intensity depends on the alignment of the photon polarization  $\epsilon$  and the magnetisation  $\mathbf{M}$ .

Before we will use the findings of this Section, namely equation (3.48) and (3.49) to describe X-ray resonant magnetic reflectivity, the special case of magnetic circular dichroism in absorption shall be briefly reviewed.

### 3.3.4 X-ray Magnetic Circular Dichroism

Since its experimental confirmation by Gisela Schütz and co-workers in the mid 80s [55], XMCD has become one of the major techniques to investigate the local magnetic moment of an atom in a quantitative and element selective way. As it has been mentioned in the previous section, XMCD in absorption can be seen as a special case of the more general resonant magnetic scattering formalism containing

both dispersive ( $f'$ ) and absorptive ( $f''$ ) parts.

The link between the two considerations is the *Optical Theorem*. It states that in the long wavelength limit for  $\mathbf{Q} = \mathbf{k} - \mathbf{k}' = 0$ , the imaginary part of the scattering amplitude is directly linked to the total atomic absorption cross section [6, 50]. Another formulation of this theorem is that the momentum transfer in the direction of the scattering structure, which is here the z-direction, has to be very small. This is fulfilled for hard X-rays only for very small angles while for soft X-rays it is generally applicable.

From the optical theorem the relation between scattering cross section and scattering amplitude is:

$$\sigma^{abs} = \frac{r_0 \lambda^2}{2\pi} n_i f'' \quad (3.50)$$

where  $r_0$  is the classical electron radius ( $r_0 = 2.8179 \cdot 10^{-15}$  m),  $\lambda$  the wavelength of the incident photon and  $n_i$  the atomic density according to  $n_i = N_a \rho / A$  ( $N_a$  is the Avogadro constant and  $A$  the atomic mass).

Phenomenologically speaking, XMCD is the intensity difference of the white line intensity of a magnetic ion between parallel and antiparallel alignment of the samples magnetisation and the photon polarization vector. The XMCD effect is directly proportional to the atomic magnetic moment or the net magnetisation  $M$ . This situation can be cast into the following relation

$$\Delta I_{XMCD} = I_{\uparrow\downarrow} - I_{\uparrow\uparrow} \propto \mu^+ - \mu^- \propto \mathbf{P} \cdot \mathbf{M} \quad (3.51)$$

where now  $\mathbf{P}$  is used for the photon polarization vector. The arrows refer to the possible directions of  $\mathbf{M}$  and  $\mathbf{P}$  with respect to each other. This notation here follows the general consensus that the XMCD is calculated in a way that the  $L_3$  XMCD is negative for positive circular X-rays. Fig. 3.18 shows the X-ray absorption spectra at the Co  $L$  edges for parallel and antiparallel alignment and the calculated XMCD effect according to equation (3.51).

XMCD can be explained by a simple two-step model. First the incident circular polarized X-ray photon which carries a spin angular momentum of  $\pm\hbar$  is absorbed exciting a photoelectron. Angular momentum conservation requires that this spin

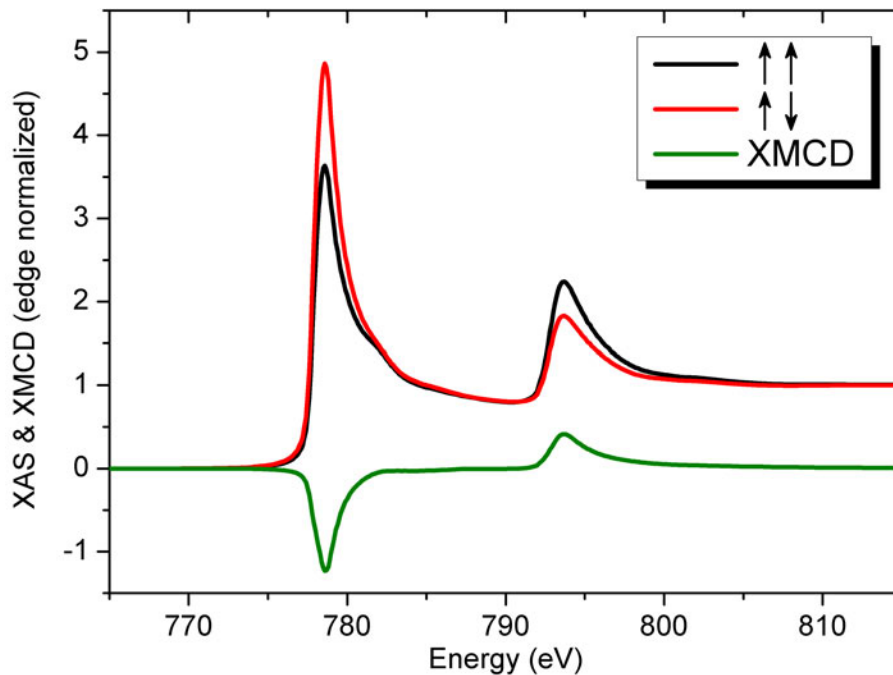


Figure 3.18: Co absorption fine structure (red & black solid lines) around the  $L_{2,3}$  edges measured using circular polarized X-rays. The green solid line is the difference intensity of the two spectra.

angular momentum of the photon is transferred to the electron. For a spin-orbit split level as are for example the  $2p$  core levels ( $2p_{\frac{3}{2}}$  and  $2p_{\frac{1}{2}}$ ) the spin orbit coupling allows to transfer part of the photon spin to the electron spin leading to a spin polarized photoelectron (note that some momentum remains with the electrons orbital). Furthermore the difference in spin-orbit coupling between  $2p_{\frac{3}{2}}$  and  $2p_{\frac{1}{2}}$  ( $l + s$  and  $l - s$ , respectively) leads to opposite spin polarization for the two levels. A photon with  $+\hbar$  (positive helicity) thus creates photoelectrons with positive spin polarization for the  $L_3$ -transition and negative ones for the  $L_2$ . We assume here that the spin quantization axis and the X-ray propagation direction which is also the direction of  $\mathbf{P}$  are either parallel or antiparallel. Note also that the  $2p_{\frac{3}{2}}$  and  $2p_{\frac{1}{2}}$  states are degenerate by a ratio 4 : 2 due to the spin orbit coupling.

The second step is the excitation of the spin polarized electron to an empty state above the Fermi-Energy  $E_F$  in, for example, the  $3d$  shell (for a transition metal ion). The unoccupied density of states now acts as a detector for the spin polarized electrons. Since the dipole excitation affects the spin only slightly (spin



conservation) an unequal amount of unoccupied states for spin-up and spin-down in the  $3d$  shell leads to a difference in the transition probability. However, since the sample is magnetised and the density of states is Zeeman split (see also: Stoner criterion in [5]), there are more empty spin-up states than spin-down which leads to different transition probabilities for the two final states.

**Sum Rules** The direct relation of the XMCD magnitude and the magnetic moment implies a general quantitative character of the method. Indeed it is possible to obtain quantitative information by using the important XMCD sum rules which have been derived by B.T. Thole and P. Carra in the early 90s. Using a single ion approximation they could derive a sum rule for the projection of the orbital moment  $\langle L_z \rangle$  [56] and also for the projected spin moment  $\langle S_z \rangle$  [57]. For the  $2p \rightarrow 3d$  excitation of the transition metals, the X-ray sum rules are given by

$$m_{sp} = -\frac{6 \int_{L_3} (\mu^+ - \mu^-) dE - 4 \int_{L_3+L_2} (\mu^+ - \mu^-) dE}{\int_{L_3+L_2} (\mu^+ + \mu^-) dE} \left( 1 + \frac{7 \langle T_z \rangle}{2 \langle S_z \rangle} \right) n_h \mu_{Bohr} \quad (3.52)$$

and

$$m_{orb} = -\frac{4 \int_{L_3+L_2} (\mu^+ - \mu^-) dE}{3 \int_{L_3+L_2} (\mu^+ + \mu^-) dE} n_h \mu_{Bohr}. \quad (3.53)$$

Equation (3.52) describes the spin moment part while equation (3.53) provides the orbital magnetic momentum.  $\mu^+$  corresponds to the parallel configuration and  $\mu^-$  to the negative one and  $n_h$  is the number of valence holes in the  $3d$ -shell. The spin magnetic moment  $m_{sp}$  exhibits an additional dependency on the magnetic dipole term  $\langle T_z \rangle$  which corresponds to a quadrupolar spin density distribution. Theoretical calculations by Wu et al. [58] however showed that this contribution is neglectable for bulk samples with cubic symmetry. Fig. 3.19 illustrates the three relevant contributions to the sum rules and how they are weighted against each other to calculate the spin and orbital momentum  $m_{sp}$  and  $m_{orb}$ , respectively.

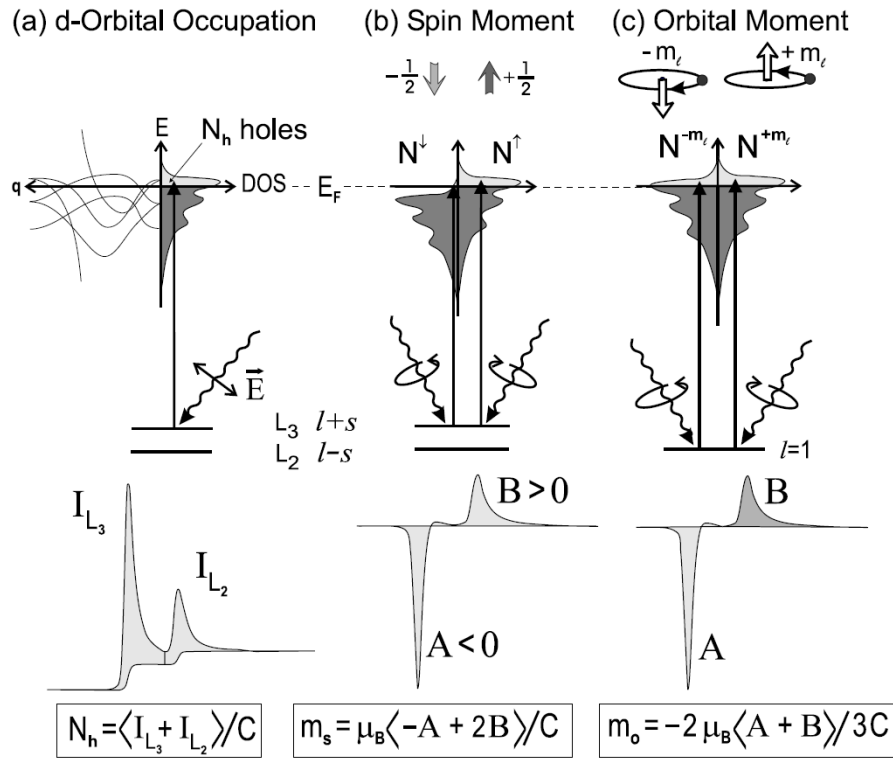


Figure 3.19: Schematic illustration of the absorption process of circular polarized X-rays in a 3d transition metal ion. Figure (a) shows how the spin-orbit coupling and the density of unoccupied states at the Fermi level leads to the near edge X-ray fine structure of the spectrum. In (b) the origin of the X-ray magnetic circular dichroism for magnetic spin moments is illustrated. The different densities of unoccupied states at the Fermi level for up and down spins lead to a difference intensity depending on the helicity of the incident X-rays. On the right, (c) shows the contribution of an orbital moment to the absorption curve (image reproduced from [6]).

### 3.4 Magnetic Reflectivity

In the preceding Section, the basic concept of resonant scattering of X-rays on a magnetic ion has been introduced. With this method at hand, the reflection of X-rays on single interfaces and multilayers shall now be discussed in more detail. Especially the effect of magnetic layers on the reflection of a X-ray beam will be derived.

Conventional non-magnetic X-ray reflectivity (XRR) is a standard technique to determine the structure, i.e., the chemical profile of materials. Usually carried out far away from any resonant edge using characteristic Cu or Mg  $K_\alpha$  X-rays ( $\lambda = 1.54056 \text{ \AA}$  and  $\lambda = 0.70930 \text{ \AA}$ ) the interaction, i.e., reflection is dominated by the dispersion in the material. Hence a reflected X-ray beam contains information on the samples' optical properties and thus chemistry in the form of constructive and destructive interference.

In general, most detectors measure the intensity of a beam which means they detect the square of the electric field vector according to

$$I = |\mathbf{E}|^2. \quad (3.54)$$

This however introduces a severe loss of information since upon squaring, phase information from the electric field vector is lost, a phenomenon usually named the *optical phase problem*. In effect, the measured intensity curve of a reflectivity experiment is not invertible which means that no direct analytic relation exists between the reflectivity curve and the underlying optical profile. Instead, the optical density profile is obtained by an iterative simulation and comparison approach. The reflectivity curve is simulated based on an artificial optical profile and the result is compared to the measurement. The parameter set for the simulation is then refined and the process repeated until a certain degree of convergence is reached. This method has proven to be extremely successful for XRR (see e.g. [59, 60]) and nowadays also for the magnetic reflectivity [2, 3, 61].

Of course it requires a physically correct formalism to simulate the reflectivity of an arbitrary sample taking into account roughness and also magnetism. In this

section some general concepts for XRR like Fresnel reflectivity and the Parratt formalism for multilayer reflection will be introduced. Further a model to consider roughness in the Parratt formalism will be discussed briefly. In the second half, the magneto-optical approach based on a matrix representation which has been introduced by J. Zak and co-workers [62–64] will be discussed in detail.

### 3.4.1 Reflectivity & Scattering Geometry

The very first step is defining the scattering geometry of the experiment as it is done in Fig. 3.20. Here the scattering plane and the reflecting interface plane

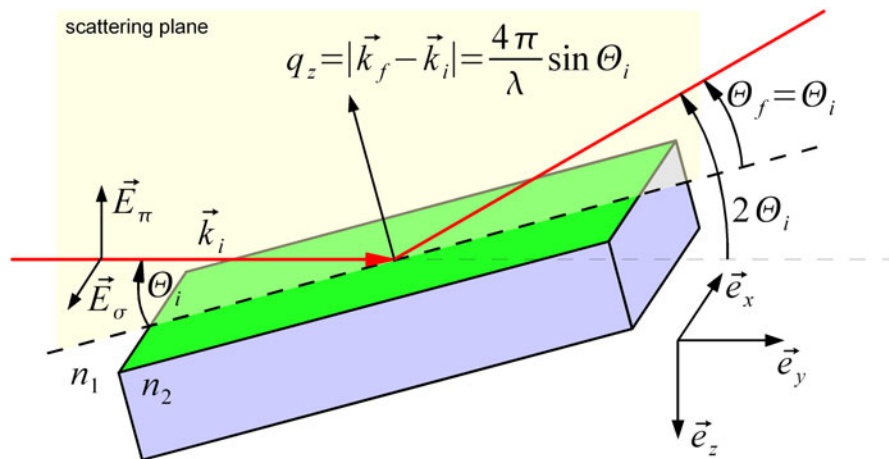


Figure 3.20: Definition of the scattering geometry for magnetic reflectivity.

define a coordinate system in which the scattering process is described. It is common within this geometry to describe the propagating X-ray beam by two components,  $E^\sigma$  and  $E^\pi$  which are the perpendicular ( $\sigma$ , or,  $s$ ) and parallel ( $\pi$ , or,  $p$ ) component with respect to the scattering plane. Another possible description is based on the  $z$ -components  $k_z$  of the corresponding wave vector  $\mathbf{k}$ .

The next necessary step is to investigate the process of reflection and transmission of light at an interface, i.e., at a change of the index of refraction. The well known Fresnel equations describe the reflected and transmitted fractions of an

incident beam at an interface. Expressing the problem by the above mentioned propagation vector  $\mathbf{k}$  or its z-component  $k_z$ , the Fresnel equations for light with a linear polarization pointing perpendicular to the scattering plane ( $\sigma$  polarization) are given by [65]:

$$\begin{aligned} r^\sigma &= \frac{k_{z,i} - k_{z,i+1}}{k_{z,i} + k_{z,i+1}} \\ t^\sigma &= \frac{2k_{z,i+1}}{k_{z,i} + k_{z,i+1}} = 1 - r^\sigma. \end{aligned} \quad (3.55)$$

Here,  $k_{z,i+1}$  and  $k_{z,i}$  are the z-components of the wavevectors in the two media and  $r^\sigma$  and  $t^\sigma$  are the Fresnel coefficients for the reflected and transmitted fraction, respectively. Note that equations (3.55) are only valid for  $\sigma$  or perpendicular to the scattering plane linear polarized light while for parallel or  $\pi$  polarization they read:

$$\begin{aligned} r^\pi &= \frac{N_{i+1}^2 k_{z,i} - N_i^2 k_{z,i+1}}{N_{i+1}^2 k_{z,i} + N_i^2 k_{z,i+1}} \\ t^\pi &= \frac{2k_{z,i+1}}{k_i + k_{z,i+1}} = 1 - r^\pi. \end{aligned} \quad (3.56)$$

It is worth remembering that the z-component of  $\mathbf{k}$  is given by the index of refraction in the respective medium along with the direction sine according to

$$\begin{aligned} k_{z,i} &= \frac{2\pi}{\lambda(E)} \sin \Theta_i \\ &\text{with} \\ \Theta_i &= 2\pi \sqrt{N_i^2 - 1 + \sin \Theta}. \end{aligned} \quad (3.57)$$

The index of refraction  $n$  used here is a dimensionless complex number which describes the dispersive and absorptive behaviour of light in matter. It is generally defined as [11]

$$N = n = 1 - \delta(E) + i\beta(E) \quad (3.58)$$

where  $\delta(E)$  describes the dispersive behaviour and  $\beta(E)$  the corresponding absorption depending on the energy of the incident light. The two quantities can be

associated with the corresponding total scattering cross section and are linked to the scattering amplitude  $f$  via the *Optical Theorem* (see equation (3.50) in Section 3.3.4 and equation (4.10) and (4.11) in Section 4.2).

With equations (3.55) and (3.56) and the index of refraction we have all necessary tools at hand to develop a description of the reflectivity from a multilayered sample. In 1950 L.G. Parratt [59, 60] developed a recursive formalism to analytically solve the reflectivity for up to three layers. His approach can also be used to numerically solve the reflection from more than three layers and this method has become the standard method for XRR [66] analysis.

Using boundary conditions either expressed by the tangential electric field components  $E_n$  [59] or the Poynting vector  $\mathbf{S}$  and the corresponding wave vectors [67] one ends up with a set of two equations describing the refraction. This approach is analogous to the quantum mechanical description of a plane wave incident on a potential barrier as it can be found in textbooks (see e.g. [50]). However, instead of solving the set of equations for a special case, one can cast it into a recursion formalism which takes the form [3, 59, 67]:

$$R_i^\pi = \frac{r_{i,i+1}^\pi + R_{i+1}e^{-2ik_{i+1}\cdot\Delta z}}{1 + r_{i,i+1}^\pi R_{i+1}e^{-2ik_{i+1}\cdot\Delta z}} \quad (3.59)$$

and

$$R_i^\sigma = \frac{r_{i,i+1}^\sigma + R_{i+1}e^{-2ik_{i+1}\cdot\Delta z}}{1 + r_{i,i+1}^\sigma R_{i+1}e^{-2ik_{i+1}\cdot\Delta z}} \quad (3.60)$$

for  $\pi$  and  $\sigma$  polarization, respectively.  $R_i$  and  $R_{i+1}$  are the reflected fractions and  $r_{i,i+1}$  etc. are the corresponding Fresnel coefficients. By assuming that the substrate is infinitely thick it follows that  $R_{N+1} = 0$  (where  $N$  is the index of the last layer) and one can solve the equation either for  $\pi$  or  $\sigma$  recursively and obtain the overall reflected intensity.

Up to here, the simulated reflectivity describes only perfectly flat interfaces which is of course never the case in a real sample. To cope with this problem, L. Nevot and P. Croce developed a simple analytical extension for the Fresnel

equations [68]. Assuming a Gaussian distributed roughness or diffusion zone at the interface, the change in the optical constants can be described by an error function like profile. The transmission and reflection coefficients are therefore modified by an exponential function, i.e., the Gaussian of the error function. The modified coefficients then take the form of

$$\begin{aligned} r'_{i,i+1} &= r_{i,i+1} e^{-2k_i k_{i+1} \sigma^2} \\ &\text{and} \\ t'_{i,i+1} &= t_{i,i+1} e^{0.5(k_i - k_{i+1})^2 \sigma^2}, \end{aligned} \tag{3.61}$$

where  $\sigma$  is the RMS roughness of the interface between layers  $i$  and  $i + 1$ .

### 3.4.2 Magneto Optical Description

As mentioned in the previous section, the Parratt formalism has certain limitations describing magnetic scattering, namely the polarization dependence. While the polarization dependence is neglectable for the hard-X-ray range due to the forward scattering character and the associated small scattering cross section, it becomes important when measuring in the soft X-ray regime [2, 69]. In this case, a formalism has to be used which allows intensity to be transferred from  $\sigma$  to the  $\pi$  component and vice versa during the scattering process.

In 1990 J. Zak and co-workers formulated a simple formalism with a vector representation of the electric field vectors and scattering matrices for the interface [62–64] which will be used throughout this work. In the following it will be referred to as the *Magneto Optical Approach*. Note that there are several other formulations of the same principles which also lead to a complete description [69, 70].

The Parratt formalism described in the preceding section does not account for relative intensity changes between the two polarization states  $\pi$  and  $\sigma$  when calculating the reflection coefficient of the individual layers. Although it does sum them properly in the end, a change somewhere in the layer stack is not considered since the entering intensity does not account for variations between the  $\pi$  and  $\sigma$  fractions. Here the magneto-optical approach does a much better job. The matrix multiplication which replaces the iterative Parratt algorithm

calculates both relative intensities, the  $\pi$  and the  $\sigma$  polarization for each layer before continuing to the next layer. It fully accounts for intrinsic changes between the relative intensities of the two polarization states.

On the following pages, a detailed discussion of the magneto-optical approach as it was formulated by J. Zak and co-workers [62–64] will be presented. The approach follows particularly reference [64] and the related erratum [71]. Since the full calculus is very thorough and therefore a bit tedious the following pages are only recommended to the gentle reader.

The very first step in describing an electromagnetic wave at an interface is to consider the boundary conditions for both components, the electric and magnetic field  $\mathbf{E}$  and  $\mathbf{M}$ , respectively. The boundary conditions are, as already mentioned in Section 3.4.1, given by the Maxwell equations [52] and it is found that the tangential components  $(E_x, E_y)$  and  $(H_x, H_y)$  are conserved at the interface. Expressing this conservation by a vector representation then takes the form:

$$\mathbf{F} = \begin{pmatrix} E_x \\ E_y \\ H_x \\ H_y \end{pmatrix}, \quad (3.62)$$

where at an interface  $F_i = F_{i+1}$  has to be fulfilled. For the propagating wave fields in the medium it is more convenient to express the whole field by their respective electric field vectors since the Maxwell equations link both fields,  $\mathbf{E}$  and  $\mathbf{M}$ . Instead of using cartesian coordinates it is, from an experimentalist point of view, more practical to switch to a basis which describes the ray with respect to the scattering plane and its propagation direction given by  $\mathbf{k}$ . In this basis, the electric field vector is described by the components  $E_\sigma$  and  $E_\pi$  which are the perpendicular ( $s$  or  $\sigma$ ) and parallel ( $p$  or  $\pi$ ) component with respect to the scattering plane.

Now, for an interface the incoming and outgoing wavefields can be cast into a



vector representation of the form

$$\mathbf{P} = \begin{pmatrix} E_{\sigma}^i \\ E_{\pi}^i \\ E_{\sigma}^r \\ E_{\pi}^r \end{pmatrix}, \quad (3.63)$$

where the index  $i$  and  $r$  refer to the incident and reflected beam, respectively and the index  $\sigma$  and  $\pi$  to the polarization state of the light. In a more general picture the two wave fields are not incident or reflected, but represent the two propagation directions in the layer, forth and back. Note that each component of (3.63) itself represents a wave field which is described by  $(E_x, E_y, E_z)$ .

Then a matrix, the so called medium boundary matrix  $\mathbf{A}$ , connects the propagating field vector  $\mathbf{P}$  with the boundary-field vector  $\mathbf{F}$  according to

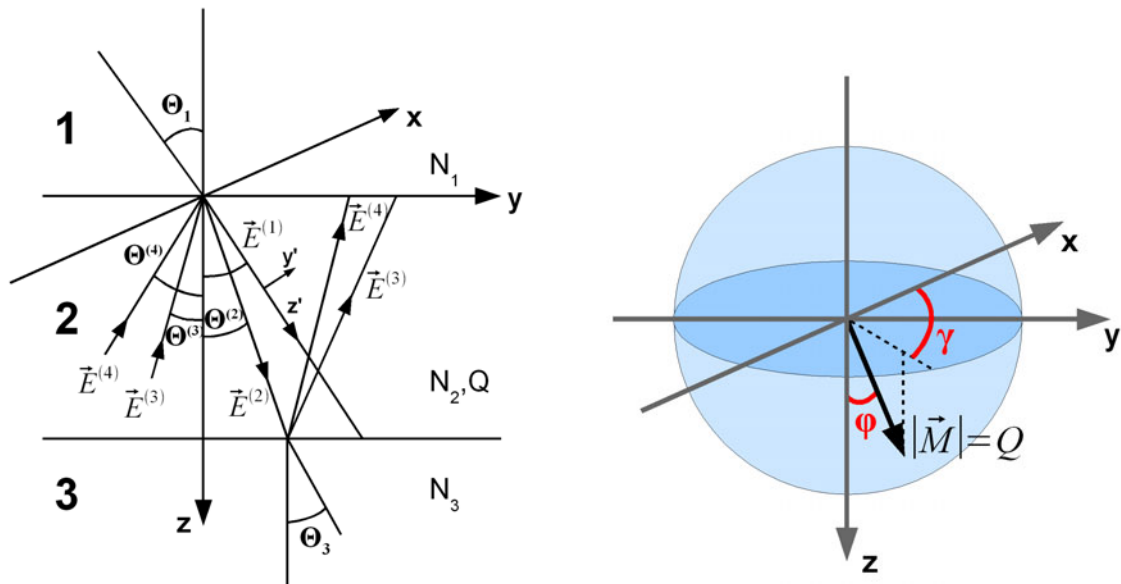
$$\mathbf{F} = \mathbf{A} \mathbf{P}. \quad (3.64)$$

This matrix fully transforms a wave field propagating in medium 1 (see Fig. 3.21(a)) into a boundary field which can then be linked to another medium's equation by

$$\mathbf{A}_i \mathbf{P}_i = \mathbf{A}_{i+1} \mathbf{P}_{i+1}. \quad (3.65)$$

Now one only has to find the proper medium boundary matrices  $\mathbf{A}$  and solve the vector equation to obtain all electric field amplitudes in the two media.

Before we will derive the medium boundary matrix, some geometrical considerations have to be discussed. For simplicity we will confine the following discussion to only two media and one interface. Later this can be extended unambiguously to more interfaces. The geometry of the reflection is shown in Fig. 3.21(a). The  $y$ - and  $z$ -axes lie in the drawing plane while the  $x$ -axis is normal to it and the lower layer (labeled 2) of the two layers is ferromagnetic (also indicated by the  $Q$ ). The naming of the components of the respective  $\mathbf{P}$  is thus that corresponding components have the same propagation direction, i.e.,  $E^i$  always is in positive  $z$ -direction and  $E^r$  in the opposite for both layers. This reflects the general character of the approach as has already been mentioned above.



(a) Reflection at a simple 3 layer system with one magnetic layer in the middle.

(b) Magnetization vector  $\mathbf{M}$  expressed by the magnitude  $Q = \delta_{mag} + i\beta_{mag}$  which corresponds to the isotropic magneto-optical constants and the two angles  $\gamma$  and  $\phi$ .

Figure 3.21: General naming and geometry definitions for the description of magnetic reflectivity using the magneto-optical approach.

Now the two medium boundary matrices shall be derived. This will be done for a general approach, i.e., a magnetic interface because the non-magnetic case can simply be obtained by setting all magnetic contributions to zero. For clarity we redefine the naming of the eigenmodes according to  $E_\sigma^i = E^{(1)}$ ,  $E_\pi^i = E^{(2)}$  and so on for the reflected ones. Eventually this leads to  $E^{(j)}$  where  $j = 1 \dots 4$ , the eigenmodes according to definition (3.63) which are present in the medium (forth and backwards) at the interface.

As already mentioned, each ray (i.e., each component of (3.63)) can be described by the three cartesian components  $(E_x, E_y, E_z)$ . These components have to satisfy the Fresnel equations which means they are inter-connected and for example  $E_y^i$  and  $E_z^i$  can be expressed by  $E_x^i$ . To properly account for this relationship, the vector describing the correspondent electric displacement field  $\mathbf{D}$  is used which is defined as

$$\mathbf{D}_j = \sum_{j'} \epsilon_{jj'} \mathbf{E}_{j'}, \quad (3.66)$$

where the indices  $j$  and  $j'$  refer to the different components  $(x, y, z)$  of the wave field and  $\epsilon_{jj'}$  is the dielectric tensor. Note that each of the vectors  $E^{(j)}$  has three components  $x$ ,  $y$  and  $z$  making 12 cartesian components to describe the electric field in each layer. In order to express the components  $E_y^{(j)}$  and  $E_z^{(j)}$  by the  $x$ -component  $E_x^{(j)}$ , the only one which is independent of the propagation direction in Fig. 3.21(a), one has to switch to the coordinate system  $x, y', z'$  of the traveling ray (see Fig. 3.21(a)). In this coordinate system, the corresponding  $D$  vectors for  $D_{y'}$  and  $D_x$  are connected via

$$(D_{y'}/D_x)_{1,2} = \mp i, \quad (3.67)$$

with  $\mp i$  for positive and negative circular polarized light, respectively.

Next the dielectric tensor is formulated for the case of a magnetic contribution. The magnetisation  $\mathbf{M}$  is in general a vector whose components can be described using polar coordinates:

$$M_x = Q \cos \gamma \sin \phi \quad (3.68a)$$

$$M_y = Q \sin \gamma \sin \phi \quad (3.68b)$$

$$M_z = Q \cos \phi \quad (3.68c)$$

according to the geometry shown in Fig. 3.21(b). Note that the magnitude  $M$  of the magnetisation vector has already been replaced by the corresponding isotropic magneto-optical contribution

$$Q = \delta_{mag}(E) + i\beta_{mag}(E) \quad (3.69)$$

according to the analogue expressions in equation (3.58) in Section 3.4.1. This leads to a dielectric tensor of the form

$$\epsilon_{jj'} = N^2 \begin{pmatrix} 1 & i \cos \phi Q & -i \sin \gamma \sin \phi Q \\ -i \cos \phi Q & 1 & i \cos \gamma \sin \phi Q \\ i \sin \gamma \sin \phi Q & -i \cos \gamma \sin \phi Q & 1 \end{pmatrix}, \quad (3.70)$$

where  $N$  refers to the index of refraction according to definition (3.58) and  $\gamma, \phi$

and  $Q$  to the magnetic contribution. Note that for  $Q = 0$ , equation (3.70) takes the form of the isotropic dielectric tensor [65], which means it is just a factor  $N^2$ .

The relation of the direction angles  $\Theta^{(j)}$  of the four rays  $j = 1, 2, 3, 4$  in the media as they are defined in Fig. 3.21(a) are given by Snell's law of refraction which reads here

$$N_1 \sin \Theta_1 = N_2 \sin \Theta_2 = n^{(1,2)} \sin \Theta^{(1,2)} = n^{(3,4)} \sin \Theta^{(3,4)}, \quad (3.71)$$

where  $\Theta_1$  is the angle of incidence in layer 1 and  $\Theta_2$  is an auxiliary angle used to relate the respective  $\Theta^{j,j'}$  to.  $n$  is the full index of refraction which also contains the magneto-optical contribution according to

$$n = N(1 \pm \frac{1}{2}Q \cos(\mathbf{kM})). \quad (3.72)$$

With equation (3.71), the direction sines and cosines of the four waves take the following forms:

$$\sin \Theta^{(1,2)} \equiv \alpha_y^{(1,2)} = \sin \Theta(1 \mp \frac{1}{2}g_i Q) \quad (3.73a)$$

$$\cos \Theta^{(1,2)} \equiv \alpha_z^{(1,2)} = \cos \Theta(1 \pm \frac{1}{2}g_i Q) \quad (3.73b)$$

$$\sin \Theta^{(3,4)} \equiv \alpha_y^{(3,4)} = \sin \Theta(1 \mp \frac{1}{2}g_r Q) \quad (3.73c)$$

$$\cos \Theta^{(3,4)} \equiv \alpha_z^{(3,4)} = -\cos \Theta(1 \pm \frac{1}{2}\frac{\sin^2 \Theta}{\cos^2 \Theta}g_r Q) \quad (3.73d)$$

with

$$g_i = \cos \phi \cos \Theta + \sin \Theta \sin \gamma \sin \phi \quad (3.74a)$$

$$g_r = -\cos \phi \cos \Theta + \sin \Theta \sin \gamma \sin \phi. \quad (3.74b)$$

With the relations from (3.73), equation (3.67) can be back transformed to the

cartesian coordinates  $x, y$  and  $z$  and one finds

$$(D_y/D_x)_{1,2} = \mp i\alpha_z^{(1,2)} \quad (3.75a)$$

$$(D_z/D_x)_{1,2} = \pm i\alpha_y^{(1,2)} \quad (3.75b)$$

and

$$(D_y/D_x)_{3,4} = \mp i\alpha_z^{(3,4)} \quad (3.75c)$$

$$(D_z/D_x)_{3,4} = \pm i\alpha_y^{(3,4)}. \quad (3.75d)$$

All necessary relations to find the connection between  $\mathbf{P}$  and  $\mathbf{F}$  have been derived. It is now straightforward to show that  $E_y^{(1,2)}$ ,  $E_y^{(3,4)}$  etc. can be expressed by  $E_x^{(1,2)}$  and  $E_x^{(3,4)}$  using relation (3.75), (3.73), and (3.70):

$$E_y^{(1,2)} = E_x^{(1,2)} \left( \mp i\alpha_z^{(1,2)} + i(\alpha_y^{(1,2)})^2 Q \cos \phi - i\alpha_y^{(1,2)} \alpha_z^{(1,2)} Q \sin \gamma \sin \phi \pm \alpha_y^{(1,2)} Q \cos \gamma \sin \phi \right) \quad (3.76a)$$

$$E_z^{(1,2)} = E_x^{(1,2)} \left( \pm i\alpha_y^{(1,2)} - i(\alpha_z^{(1,2)})^2 Q \sin \gamma \sin \phi \pm \alpha_z^{(1,2)} Q \cos \gamma \sin \phi + i\alpha_y^{(1,2)} \alpha_z^{(1,2)} Q \cos \phi \right) \quad (3.76b)$$

and

$$E_y^{(3,4)} = E_x^{(3,4)} \left( \mp i\alpha_z^{(3,4)} + i(\alpha_y^{(3,4)})^2 Q \cos \phi - i\alpha_y^{(3,4)} \alpha_z^{(3,4)} Q \sin \gamma \sin \phi \pm \alpha_y^{(3,4)} Q \cos \gamma \sin \phi \right) \quad (3.76c)$$

$$E_z^{(3,4)} = E_x^{(3,4)} \left( \pm i\alpha_y^{(3,4)} - i(\alpha_z^{(3,4)})^2 Q \sin \gamma \sin \phi \pm \alpha_z^{(3,4)} Q \cos \gamma \sin \phi + i\alpha_y^{(3,4)} \alpha_z^{(3,4)} Q \cos \phi \right) \quad (3.76d)$$

and further

$$E_x^{(1,2)} = \frac{1}{2}(E_\sigma^i \pm iE_\pi^i), \quad (3.77a)$$

$$E_x^{(3,4)} = \frac{1}{2}(E_\sigma^r \pm iE_\pi^r). \quad (3.77b)$$

Finally, the tangential components  $H_x$  and  $H_y$  in (3.62) can be obtained from

the boundary condition  $\mathbf{H} = \mathbf{n} \times \mathbf{E}$ . Where  $\mathbf{E}$  is the electric field and  $\mathbf{n}$  a vector which points in the propagation direction ( $\mathbf{k}$ ) and has the magnitude of the index of refraction.

The medium boundary matrix for an arbitrary magnetisation direction in the material then has the form (see [64] and [71]):

$$\mathbf{A} = \begin{pmatrix} 1 & 0 \\ \frac{i}{2} Q \tan \Theta (\sin \Theta g_i - 2 \sin \phi \sin \gamma) & \cos \Theta + i \sin \Theta \sin \phi \cos \gamma Q \\ \frac{i}{2} N g_i Q & -N \\ N \cos \Theta & \frac{iN}{2 \cos \Theta} g_i Q \\ 1 & 0 \\ -\frac{i}{2} Q \tan \Theta (\sin \Theta g_r - 2 \sin \phi \sin \gamma) & -\cos \Theta + i \sin \Theta \sin \phi \cos \gamma Q \\ \frac{i}{2} N g_r Q & -N \\ -N \cos \Theta & -\frac{iN}{2 \cos \Theta} g_r Q \end{pmatrix} \quad (3.78)$$

This is the main matrix describing the reflection and transmission for arbitrary polarized light at an interface between to arbitrary magnetised materials. Since  $\mathbf{A}$  in it's general form (3.78) is quite bulky, we will in the following, write down some special cases.

First for the non-magnetic (thus  $Q = 0$ ) case, the matrix (3.78) has the simple form:

$$\mathbf{A}^{non-mag} = \begin{pmatrix} 1 & 0 & 1 & 0 \\ 0 & \cos \Theta & 0 & -\cos \Theta \\ 0 & -N & 0 & -N \\ N \cos \Theta & 0 & -N \cos \Theta & 0 \end{pmatrix} \quad (3.79)$$

for in-plane magnetisation parallel to the propagation vector  $\mathbf{k}$  of the incident light, i.e., the so called longitudinal geometry, the magnetisation vector is

$$\mathbf{M} = \begin{pmatrix} 0 \\ 1 \\ 0 \end{pmatrix},$$

as can be seen from Fig. 3.21(b) and the corresponding longitudinal boundary

matrix takes the form:

$$\mathbf{A}^{long} = \begin{pmatrix} 1 & 0 & 1 & 0 \\ \frac{i}{2} Q \tan \Theta (\sin^2 \Theta - 2) & \cos \Theta & -\frac{i}{2} Q \tan \Theta (\sin^2 \Theta - 2) & -\cos \Theta \\ \frac{i}{2} Q N \sin \Theta & -N & \frac{i}{2} Q N \sin \Theta & -N \\ N \cos \Theta & \frac{i}{2} Q N \tan \Theta & -N \cos \Theta & -\frac{i}{2} Q N \tan \Theta \end{pmatrix}. \quad (3.80)$$

The second important magnetisation direction is the case of pure polar magnetisation with

$$\mathbf{M} = \begin{pmatrix} 0 \\ 0 \\ 1 \end{pmatrix}.$$

In this case, the boundary matrix takes the form:

$$\mathbf{A}^{pol} = \begin{pmatrix} 1 & 0 & 1 & 0 \\ \frac{i}{2} Q \sin^2 \Theta & \cos \Theta & \frac{i}{2} Q \sin^2 \Theta & -\cos \Theta \\ \frac{i}{2} Q N \cos \Theta & -N & -\frac{i}{2} Q N \cos \Theta & -N \\ N \cos \Theta & \frac{i}{2} Q N & -N \cos \Theta & \frac{i}{2} Q N \end{pmatrix} \quad (3.81)$$

With equation (3.65) and the corresponding boundary matrix (3.78) the refraction of polarized light at a magnetic interface is fully described. In the case of circularly polarized light and for known medium boundary matrices  $A_1$  and  $A_2$ , the reflected and transmitted intensities of a single interface are given by the corresponding  $P$ -vectors

$$A_1 \begin{pmatrix} 1 \\ \pm i \\ E_{1\sigma}^r \\ E_{1\pi}^r \end{pmatrix} = A_2 \begin{pmatrix} E_{2\sigma}^t \\ E_{2\pi}^t \\ 0 \\ 0 \end{pmatrix} \quad (3.82)$$

where it has been assumed that no reflected ray from medium 2 is present, thus  $E_{2\sigma}^r = E_{2\pi}^r = 0$ .

For more than one interface, propagation through the medium in between has to be considered. A propagation matrix  $\widetilde{\mathbf{D}}$  is introduced which accounts for damping

of the wave fields by absorption and also properly describes any associated phase shift. Based on the absorption of X-rays (or light in general) in a material due to the corresponding absorption cross section one can derive the absorption for one of the components of (3.63) using the Lambert-Beer law (3.31). The amplitude of the relevant x-component of the respective ray at a depth  $z$  is then given by:

$$E_x^{(j)}(0) = E_x^{(j)}(z) e^{\left(-i\frac{2\pi}{\lambda} n^{(j)} \alpha_z^{(j)} z\right)}, \quad (3.83)$$

where  $\lambda$  is the wavelength,  $n^{(j)}$  the corresponding index of refraction given by equation (3.71),  $\alpha_z^{(j)}$  the direction sine according to (3.73) and  $z$  the position in the material with respect to the interface at  $z = 0$ . Equation (3.83) needs now to be rewritten for the general wave vector  $\mathbf{P}$ . This can easily be done using relation (3.77). For a layer with thickness  $d$ , the propagation matrix  $\tilde{\mathbf{D}}$  is then given by [64]:

$$\tilde{\mathbf{D}} = \begin{pmatrix} U & U\delta_i & 0 & 0 \\ -U\delta_i & U & 0 & 0 \\ 0 & 0 & U^{-1} & -U^{-1}\delta_r \\ 0 & 0 & U^{-1}\delta_r & U^{-1} \end{pmatrix} \quad (3.84)$$

with

$$\begin{aligned} U &= e^{\left(-i\frac{2\pi}{\lambda} Nd \cos \Theta\right)} \\ \delta_i &= \frac{\pi}{\lambda} Nd \frac{Q}{\cos \Theta} g_i \\ \delta_r &= \frac{\pi}{\lambda} Nd \frac{Q}{\cos \Theta} g_r \end{aligned} \quad (3.85)$$

where  $g_i$  and  $g_r$  are given by relation (3.74). The intensity of  $\mathbf{P}$  at a level  $z$  in , for example, medium 2 (according to Fig. 3.21(a)) is then given by

$$\mathbf{P}_2(0) = \tilde{\mathbf{D}}_2 \mathbf{P}_2(z). \quad (3.86)$$

So far only the reflection and transmission at a single interface (see equation (3.82)) and the modification of the wave field, i.e.,  $\mathbf{P}$  while propagating through a medium of thickness  $d$  has been discussed. This approach can easily be extended



to describe multilayers. With the relation (3.86) for the propagation and relation (3.65) for the interface it is straightforward to define the matrix equation for the three layer example system from Fig. 3.21(a)

$$\mathbf{A}_1 \mathbf{P}_1(0) = \mathbf{A}_2 \widetilde{\mathbf{D}}_2 \mathbf{A}_2^{-1} \mathbf{A}_3 \mathbf{P}_3(d) \quad (3.87)$$

where  $d$  is the thickness of layer 2. This description can be generalized for an arbitrary number of layers to

$$\mathbf{A}_i \mathbf{P}_i = \prod_{m=1}^l (\mathbf{A}_m \widetilde{\mathbf{D}}_m \mathbf{A}_m^{-1}) \mathbf{A}_f \mathbf{P}_f. \quad (3.88)$$

For solving the matrix equation, the same assumption as for the Parratt formalism (compare Section 3.4.1) can be used: The last layer, which is the substrate, is approximated as being of infinite thickness. This assumption is justified since the extinction length of X-rays is usually much shorter than the thickness of a substrate. Then, the reflected components of the vector  $\mathbf{P}_f$  become  $E_{f\sigma}^r = E_{f\pi}^r = 0$  simplifying the equation significantly. This leads to a situation as it is indicated by Fig. 3.22 where a stack of three layers on a substrate along with its relevant rays is shown:

The incident intensity is given by the first two components of the vector  $\mathbf{P}_i$  and are for right/left circular polarized light given by  $E_{i\sigma}^i = 1$  and  $E_{i\pi}^i = \pm i$  (according to Jones calculus [72]). The measured incident intensity is given by

$$I_0 = |1 \pm i|^2, \quad (3.89)$$

The whole matrix equation for the layer stack of Fig. 3.22 reads:

$$\mathbf{A}_1 \begin{pmatrix} 1 \\ \pm i \\ E_{1\sigma}^r \\ E_{1\pi}^r \end{pmatrix} = \mathbf{A}_2 \widetilde{\mathbf{D}}_2 \mathbf{A}_2^{-1} \mathbf{A}_3 \widetilde{\mathbf{D}}_3 \mathbf{A}_3^{-1} \mathbf{A}_f \begin{pmatrix} E_{f\sigma}^t \\ E_{f\pi}^t \\ 0 \\ 0 \end{pmatrix} \quad (3.90)$$

and the reflected intensity, as it is measured in a reflectivity experiment, is then

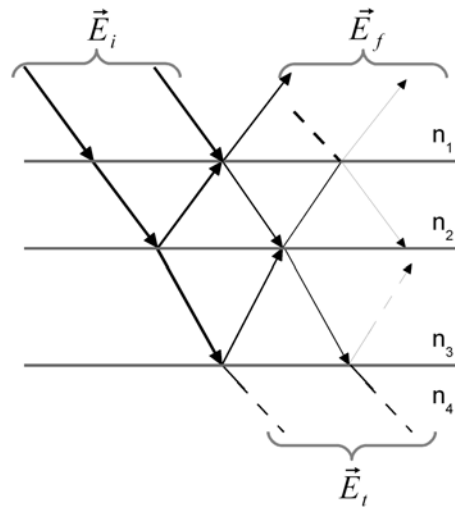


Figure 3.22: Example for reflected and transmitted beams in the case of a three layer stack on a substrate material. The incident (reflected) intensities of the substrate layer are zero due to its thickness compared to the X-ray extinction length.

given by

$$I = \frac{|E_{1\sigma}^r + E_{1\pi}^r|^2}{|1 \pm i|^2}. \quad (3.91)$$

This magneto-optical description, i.e., the calculus derived on the last pages, has been included in the simulation tool ReMagX (see also Section 6.4) allowing even more precise calculations of the reflectivity from an arbitrary stack of magnetic and non-magnetic layers.

## 4 Aspects of Data Processing

A reflectivity curve contains information on the optical profile, i.e., the structural properties of a sample and in the case of circular polarized X-rays also the magnetic depth profile. However, this information can not be retrieved directly since due to the loss of phase information when detecting with a photodiode, no analytic relation exists between the reflected intensity and the structural properties or optical profile. Therefore a comparative approach is used to obtain this information and the whole processing can be outlined as follows:

- Processing of the measured data, namely normalization and correction of systematic errors.
- Determination of the optical constants for each material or layer in the sample.
- Simulation of the reflectivity curve based on the magneto-optical approach or Parratt algorithm.
- Comparison of simulated and measured curve.
- Iterative fit of simulation to measurement by refinement of simulation parameters.

The sample properties used to calculate the best fit result then correspond to the samples parameters. The individual steps will be described in detail in the following section.

## 4.1 Processing of Reflectivity Data

As measured, raw reflectivity curves have to be post-processed before they are ready for the above mentioned fitting procedure. The measurement software saves  $\Theta$  for the x-value, and  $I_{Det}$  as well as  $I_{FYZ}$  and  $I_0$  as data.  $I_{FYZ}$  is the fluorescence background measured 28 mm above the scattering plane (see also Section 6.1.3). When using  $I_{FYZ}$  to correct the background of a measurement, the detector aperture and geometric issues (shading by the magnet) have to be considered.

By convention, reflectivity curves and also accompanying asymmetries are always represented and processed as a function of the z-component  $q_z$  of the scattering vector.  $q_z$  is calculated from  $\Theta$  and the energy  $E$  by:

$$q_z(\text{\AA}^{-1}) = \frac{4\pi e}{ch} 10^{-10} \cdot E(\text{eV}) \cdot \sin \Theta \equiv 0.001013546247 \cdot E(\text{eV}) \cdot \sin \Theta. \quad (4.1)$$

Next, the measured intensity of the specularly reflected beam  $I_{Det}$  is background corrected and normalized to the incident intensity  $I_0$  according to the following scheme:

$$I_{refl} = (I_{Det} - I_{background})/I_0. \quad (4.2)$$

The background  $I_{background}$  can be derived from  $I_{FYZ}$  considering the above mentioned systematic errors. An example for a dichroic reflectivity curve obtained from this process is shown in Fig. 4.1(a) as black and red curves. For dichroic curves which have been obtained by measuring both directions of the external magnetic field at each angle, the so called *North-South effect* occurs. The strong magnetic field leads to slight offsets in the detector diode (for absorption spectra namely TEY, capacities lead to the same problem) which are not related to the optical properties of the sample and therefore cause an unwanted offset in the magnetic asymmetry and in the XMCD curve. Although these offsets vanish after a few seconds, waiting would increase the measurement time drastically. A special measurement scheme is used to minimize the amount of field and energy changes. The scheme is outlined in the following [10]:

$$\Theta_N(\mathbf{N}) \rightarrow \Theta_N(\mathbf{S}) \rightarrow \Theta_{N+1}(\mathbf{S}) \rightarrow \Theta_{N+1}(\mathbf{N}) \rightarrow \Theta_{N+2}(\mathbf{N}) \rightarrow \Theta_{N+2}(\mathbf{S}) \rightarrow \dots$$

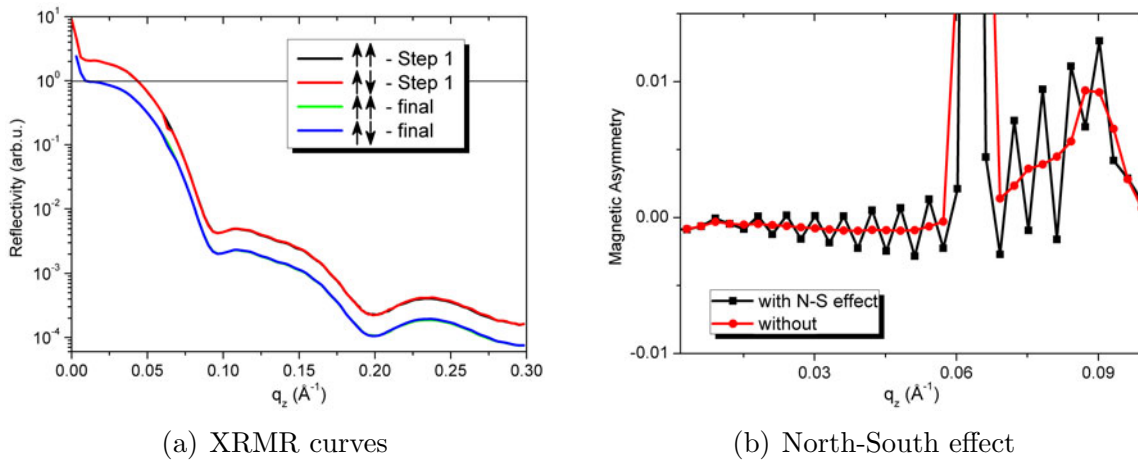


Figure 4.1: The left image shows an example reflectivity curve before and after normalization to a reflected intensity of 1 for  $\Theta = 0^\circ$ . On the right a zoom of the magnetic asymmetry of the left reflectivity curves is shown before (black) and after (red) removing the North-South effect according to the calculus described in the text.

where the subscript  $N$  refers to the  $\Theta$  angle index and  $\mathbf{N}$ , and  $\mathbf{S}$  refer to *North* and *South* which is the direction of the external magnetic field with respect to the incident beam direction.

The second step to reduce the N-S effect in dichroic reflectivity curves (absorption spectra) is to average each curve using a weighted running average. Each value is calculated new from adding itself and the two neighbor values with the weight 1:2:1. The corresponding scheme is given by

$$\tilde{I}_{refl}(\Theta_N) = \frac{1}{4} I_{refl}(\Theta_{N-1}) + \frac{1}{2} I_{refl}(\Theta_N) + \frac{1}{4} I_{refl}(\Theta_{N+1}), \quad (4.3)$$

where  $\tilde{I}_{refl}$  is the new averaged value. Fig. 4.1(b) shows the magnetic asymmetry calculated from the curves in Fig. 4.1(a) before and after the N-S correction.

Finally the reflectivity curves are normalized to 1 for  $\Theta = 0^\circ$ . This is justified because the beam does not enter the sample and thus the reflectance of any surface is by definition 1 for zero degrees. The resulting normalized reflectivity curves which are plotted in Fig. 4.1(a) as green and blue lines are now ready for further processing.

## 4.2 The Optical Constants

Whether the simulation of the reflectivity is carried out using the magneto-optical approach introduced in Section 3.4.2 or the Parratt algorithm described in Section 3.4.1 (and in references [3, 67]), knowing the optical properties of all involved materials for all layers is a necessary prerequisite. As described in Section 3.4.1, the index of refraction is a complex number where the real part  $\delta$  is the dispersion in the sample while the imaginary part  $\beta$  describes the absorption.

$$N(\omega) = 1 - \delta(\omega) + i\beta(\omega) \quad (4.4)$$

For energies far above a resonant edge ( $> 100$  eV), the scattering factors can be calculated from first principles starting from equation (3.39) (see e.g. [49]). These non-resonant scattering factors are in good agreement with experimentally obtained values and therefore commonly used for non-resonant X-ray reflectivity. Popular compilations of scattering factors are the Henke-Gullikson table [73] and the Chantler table [74]. The former being the older one based on the first compilation of optical constants by B.L. Henke, E.M. Gullikson and J.C. Davis [49] while the latter was published by C.T. Chantler in the mid 90s [75, 76]. The Chantler table is distinct since it considers the spin-orbit coupling of the initial  $2p$  states.

It is worth noting that the scattering amplitude  $f$  used throughout Section 3.3 is not provided directly from the tables. Instead atomic scattering factors  $f_1$  and  $f_2$  are given following the notation of Henke & Gullikson who defined those factors in the limit of small  $|\mathbf{Q}|$  (so for soft X-rays or grazing incidence) by:

$$\begin{aligned} f_1 &= Z + F'(E) \\ f_2 &= F''(E). \end{aligned} \quad (4.5)$$

Where  $Z$  is the atomic number, i.e., the total number of electrons in the atom, and  $F'$  and  $F''$  are the normal atomic scattering factors which are linked to the scattering amplitude by the geometry and polarization of the incident light according to

$$f(\mathbf{Q}, E) = r_0 \boldsymbol{\epsilon} \cdot \boldsymbol{\epsilon}' F(\mathbf{Q}, E) \quad (4.6)$$

XRMR and XMCD depend on resonant transitions from core states to the unoccupied states at the Fermi energy. The optical properties close to a resonant edge depend on the near edge fine structure of the spectrum and this in turn depends on the chemistry in the material. Therefore it is in general not possible to use tabulated values such as the one mentioned above or calculate them from first principles. Instead the scattering factors and from those the index of refraction has to be determined experimentally.

An absorption experiment directly provides the X-ray absorption coefficient  $\mu_z$  which is related to the absorption cross section of an individual atom in the sample by

$$\mu_z = \rho_a \sigma^{abs} = \frac{N_A}{A} \rho \sigma^{abs}. \quad (4.7)$$

Here  $\rho_a$  is the atomic number density (atoms/volume),  $\rho$  the normal mass density (mass/volume),  $N_A$  is Avogadro's constant and  $A$  is the atomic mass number (mass/mol). From the absorption cross section  $\sigma^{abs}$ , the imaginary part of the scattering factor  $F'' = f_2$  can be obtained directly via the optical theorem (3.50) which was introduced in Section 3.3.4. However, this direct link is limited to small  $|\mathbf{Q}|$  which is fulfilled for soft X-rays in general and hard X-rays in grazing incidence geometry.

$$F''(E) = f_2(E) = \frac{1}{2r_0\lambda(E)} \sigma^{abs}(E) = \frac{1}{\rho_a 2r_0\lambda(E)} \mu_z(E) \quad (4.8)$$

The real part  $F'$  (or  $f_1$ ) can then be calculated from  $F''$  or  $f_2$  using a Kramers-Kronig transform which will be described later. The same procedure is applied to the XMCD spectra, i.e., the magnetic  $f_2$  to obtain the magneto-optical contribution:

$$Q = \delta_{mag}(E) + i\beta_{mag}(E) \quad (4.9)$$

which has been introduced in Section 3.4.2.

The relation between the scattering factors  $f_1$ , and  $f_2$  and its corresponding

optical constants  $\delta$  and  $\beta$  is then given by

$$\delta(E) = \frac{N_A \rho r_0 \lambda^2}{A} f_1(E) = \frac{N_A \rho r_0 \lambda^2}{A} (Z + F') \quad (4.10)$$

$$\beta(E) = \frac{N_A \rho r_0 \lambda^2}{A} f_2(E) = \frac{N_A \rho r_0 \lambda^2}{A} (F'') \quad (4.11)$$

where  $r_0$  is the classical electron radius of  $r_0 = 2.8179 \times 10^{-15}$  m,  $N_A$  is the Avogadro constant,  $A$  is the atomic mass number in (mass/mol),  $\rho$  is the mass density in (mass/volume) and  $\lambda$  is the wavelength of the incident X-rays (see also equation (3.50) in Section 3.3.4).

Absorption and dispersion, i.e., real and imaginary part of the scattering factors are not independent quantities. The absorption of light is an energy dissipative process who depends on the phase shift between driving force (the electric field vector) and the medium (electrons). Causality then demands that both quantities, phase shift and energy dissipation are directly linked to each other. The mathematical calculus which connects real and imaginary part is the Kramers-Kronig relation (KK) which can be applied for any complex function which is analytical in the upper half-plane. The KK for X-rays in its general form reads [77, 78]:

$$F'(E) = \frac{2}{\pi} \mathcal{P} \int_0^\infty \frac{\epsilon \sigma^{abs}(\epsilon)}{(E^2 - \epsilon^2)} d\epsilon. \quad (4.12)$$

where  $\mathcal{P}$  denotes the Cauchy principal value of the integral. Replacing  $\sigma^{abs}$  by the corresponding Henke-Gullikson scattering factor  $f_2$  which is used for the tabulated data mentioned above by taking equation (4.8) into account the KK modifies to

$$f_1(E) = Z - \frac{2}{\pi} \mathcal{P} \int_0^\infty \frac{\epsilon^2 f_2(\epsilon)}{(E^2 - \epsilon^2)} d\epsilon. \quad (4.13)$$

For real, experimental values the KK relation has to be modified to account for the discrete character of measured data and also for the limited range available. While equation (4.12) integrates from 0 to  $\infty$  this is in reality not possible. A measured absorption spectra usually spans  $\sim 100$  eV and can only be extended using tabulated values which are available for energies from 10 to 400,000 eV. The



numerical integration of equation (4.12) is further complicated by the singularity at  $(E_i^2 - \epsilon^2)$  which is the reason for the Cauchy principal value  $\mathcal{P}$  in equations (4.12) and (4.13).

The discrete form of equation (4.13) which is used in this thesis is:

$$f_1(i) = Z - \frac{2}{\pi} \sum_{E_1}^{E_n} \frac{\epsilon^2 f_2(\epsilon)}{(E_i^2 - \epsilon^2)} d\epsilon. \quad (4.14)$$

The Cauchy principal value has been omitted since the numerical integration approximates it. The corresponding algorithm in pseudo-code is:

```

for ( i=0; i < (n-1); i++){
  newE = 0.5*(E[i] + E[i+1])
  for ( j=0; j < (n-1); j++){
    if ( abs(E[i] - E[j]) < 200 ){
      m = (f2[j+1] - f2[j]) / (E[j+1] - E[j])
      b = f2[j+1] - m * E[j+1]

      f1[i] += 0.5*b*log(abs(-E[j+1]^2 + newE^2)/abs(-E[j]^2 + newE^2))
              + -m*(E[j+1] - E[j])
              + 0.5*newE*m*log((newE + E[j+1])/(newE + E[j]))
              - 0.5*newE*m*log(abs(newE - E[j+1])/abs(newE - E[j]))
    }
    else{
      dEnergy = 0.5*(E[j] + E[j+1])
      f2_before = (f2[j] * E[j])/(newE^2 - E[j]^2)
      f2_after = (f2[j+1] * E[j+1])/(newE^2 - E[j+1]^2)
      f1[i] += dEnergy*(f2_before + f2_after)
    }
  }
}
f1[i] = (Z + frel) - f1[i]
}

```

Before applying this calculus to an absorption curve it has to be normalized and

fitted to the tabulated scattering factors. The whole processing scheme of fitting the measured near edge fine structure onto the Henke or Chantler table and then applying the Kramers-Kronig relation to obtain the dispersive part  $f_1$  is outlined in Fig. 4.2.

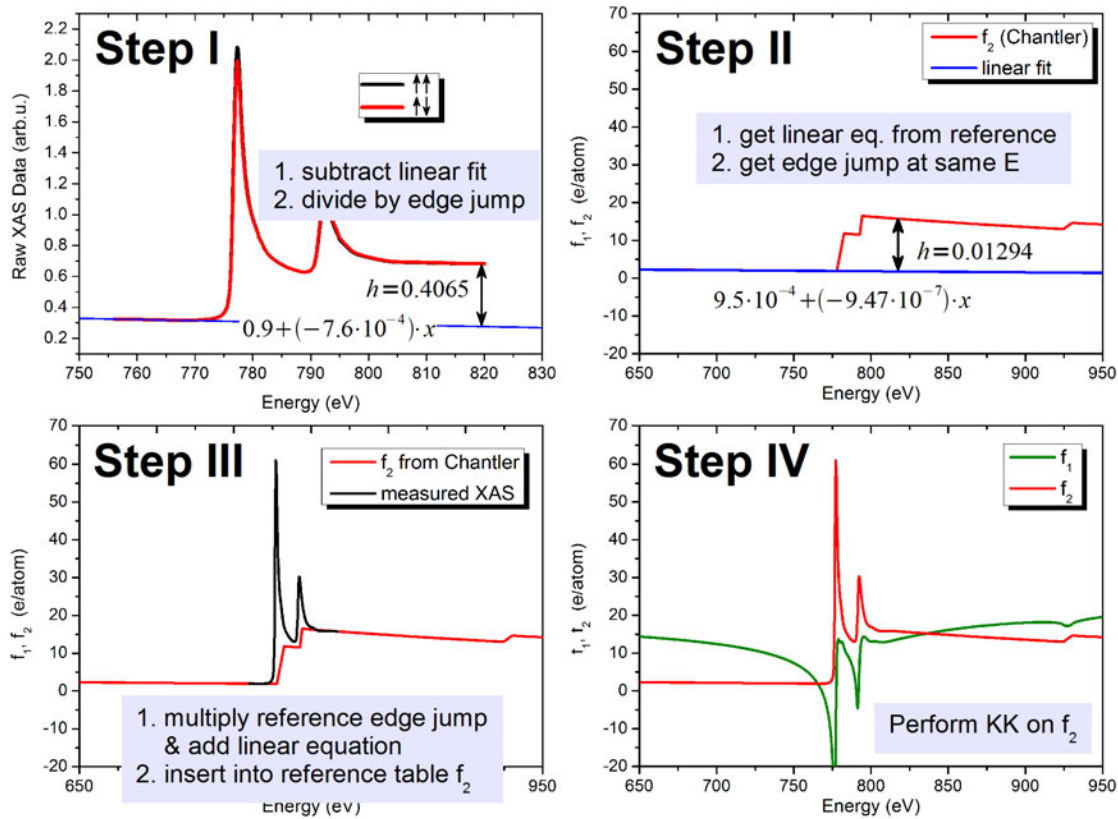


Figure 4.2: Processing scheme. First the measured absorption spectra has to be edge normalized by subtracting the slope and dividing by the edge jump. Next slope, y-offset and edge jump have to be derived for the absorptive scattering factor  $f_2$  from the reference Henke/Chantler table (step II). Then the normalized XAS data is multiplied by the reference  $f_2$  edge jump and the linear equation is added to move and tilt the curve. This curve can now be inserted into the reference dataset of the imaginary part  $f_2$ . Finally the Kramers-Kronig calculus defined in equation (4.14) is applied to obtain the real part  $f_1$  of the scattering factor (step IV).

The very first step is to correct the measured absorption spectrum for unwanted systematic errors and offsets. That means that for dichroic spectra the already mentioned North-South effect (compare 4.1) has to be removed by applying the calculus described by equation (4.3). Secondly a possible offset between the two curves (parallel and antiparallel) has to be removed. The curves are therefore divided by each other and the resulting curve which resembles the XMCD signal should then be exactly 1 in the pre-edge region. If that's not the case, a factor is multiplied to the antiparallel curve to bring the pre-edge region to one.

Next step is, to edge normalize the measured absorption spectra. A linear fit on the pre-edge region of the curve provides slope and y-offset and the corresponding line is then subtracted from the data. Next, the data is divided by the edge jump  $h$  which is taken from an energy far above the resonance.

A  $f_2$  table for the corresponding element or alloy has to be generated from the Henke or Chantler datasets for a large energy range (ideally 10 to 400,000 eV). Next, slope, y-offset and edge jump of the absorptive part  $f_2$  of the table have to be determined at exactly the same energy values and ranges such as has been chosen for the data normalization. This means  $f_2$  has to be linearly fitted in the energy range where the measured data is zero. The edge jump has to be determined from the value of this linear fit compared to the tabulated value at the very same energy as it has been derived in the measured XAS spectrum. The resulting factor (edge jump) is then multiplied to the XAS data and subsequently the line (slope and offset) added. The resulting curve should now perfectly fit into the reference Henke/Chantler curve such as the black curve in Fig. 4.2(III). This curve is now inserted into the absorptive scattering factor  $f_2$  from the Henke or Chantler reference data compilation.

Then the  $f_2$  curve which contains the measured XAS data is processed using the discrete Kramers-Kronig relation defined by equation (4.14) or its corresponding numerical algorithm to obtain the dispersive, i.e., real part  $f_1$  of the scattering factors.

Finally the optical constants  $\delta$  and  $\beta$  are calculated from  $f_1$  and  $f_2$  using equations (4.10) and (4.11), respectively.

The XMCD data, thus the difference signal from the two curves (red and black) in Fig. 4.2(I), is processed by multiplying the edge jump  $h$  from the reference  $f_2$  curve (shown in 4.2(II)) to the XMCD curve. It is sufficient to use the measured data range as long as the XMCD signal is back to zero at the limits. The Kramers-Kronig relation from equation (4.14) can then be used to derive the real part  $f_1^{mag}$ .

### 4.3 Correction of the Sample Illumination

The finite size of the sample, the detector and the X-ray beam lead to several systematic errors for the very first degrees of a reflectivity curve. The following finite sizes apply for nearly all reflectivity measurements performed throughout this work: the beam has a diameter of roughly  $700\ \mu\text{m}$  at the detector position (roughly 500 mm behind the focus), the sample size is roughly 5 – 10 mm length along the beam direction and finally the detector size which is determined by the detector slit opening is usually 2 mm [79].

Two main effects alter the shape of the reflectivity curve and thus affect the intensity measured on the detector: The direct beam which hits the detector for very small angles and the incomplete illumination of the sample by the beam. The former dominates the shape of the curve for very small angles and can be used for alignment while the latter imposes a systematic error on the reflectivity curve over a relatively large angular range.

Fig. 4.3(a) shows the reflected intensity (red) for the very first degrees as measured with the reflectometer setup described in 6.1 The uppermost sketch represents the situation at  $\Theta = 0^\circ$  and for the very first degrees. Due to the sample position in the middle of the beam, half the direct beam is shut off. Nevertheless the other half directly hits the detector leading to a constant signal for the very first degrees. The intensity plateau caused by this situation is clearly visible in the reflectivity curve.

The beams horizontal width and the detector aperture determine the angle at which the detector starts to move out of the direct beam. Note that the intensity might already be reduced slightly at this point due to a shut off from the sample.

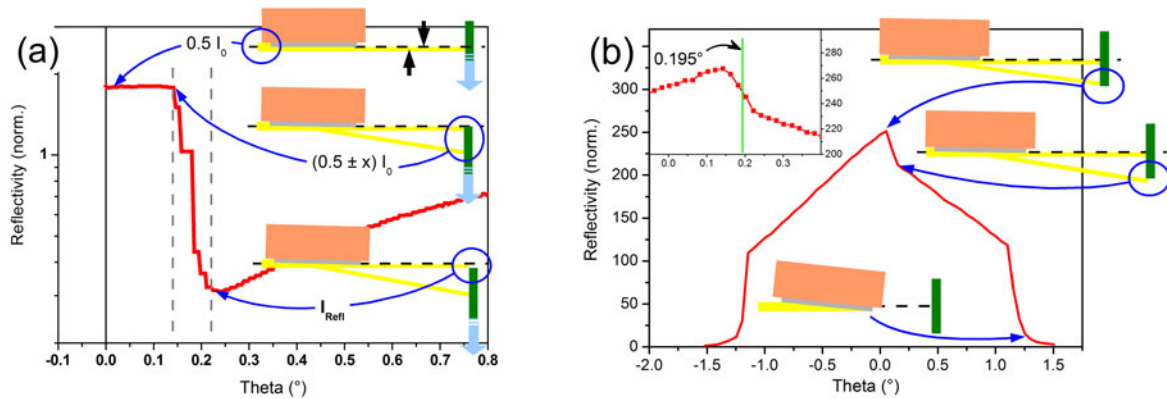


Figure 4.3: The left Fig. 4.3(a) shows the systematic influence of the experimental geometry on a normal  $\Theta$ - $2\Theta$  scan. The sketches illustrate the movement of the detector out of the direct beam. On the right, Fig. 4.3(b) shows how the reflected beam moves out of the detector which is located at  $0^\circ$  and how a corresponding  $\Theta$ -scan curve can be used to calibrate the sample axis.

Anyway a drastic decrease of the measured intensity takes place while the direct, i.e., the transmitted beam leaves the detector as can be seen in the reflectivity curve in Fig. 4.3(a).

As mentioned above, this geometric issue can also be used to align the sample by calibrating the  $0^\circ$  angle of the sample axis. The shape of the  $\Theta$ - $2\Theta$  scan shown in Fig. 4.3(a) around zero is governed by the detector moving out of the direct beam. If one instead measures the reflected beam moving out of the detector, the measurement depends on the  $0^\circ$  calibration of the sample. Fig. 4.3(b) shows a  $\Theta$  scan from  $-1.5^\circ$  to  $+1.5^\circ$  with fixed detector. An inset shows a close-up of the region around  $0^\circ$ . The sketch in the figure illustrates the relevant processes and also shows the difference to the one described in Fig. 4.3(a).

It is now straightforward to calculate the nominal position of the drop visible in the inset of Fig. 4.3(b) from the geometry of the experiment. The angle of the centre of the decrease is determined by the radius of the detector axis and the detector aperture according to the following formula:

$$\Theta_{center} = \frac{1}{2} \tan^{-1} \left( \frac{\text{Half Aperture} = 1\text{mm}}{(\text{Distance Sample} - \text{Detector}) = 146\text{mm}} \right) = 0.196^\circ \quad (4.15)$$

Here, the factor  $\frac{1}{2}$  accounts for the fact that the detector defines the double angle  $2\Theta$ . With the given values, the centre of the decrease should take place at  $\Theta = 0.196^\circ$ . This method provides a precise absolute calibration for  $\Theta = 0^\circ$  and allows aligning the setup or correcting the data accordingly.

The systematic error related to incomplete illumination of the sample originates from the finite size of the sample compared to the beam diameter. If the beam is broader than the projected area of the sample across the beam diameter, a part of the beam is not reflected but passes unaffected. This effect is also illustrated in some of the sketches in Fig. 4.3. While it is in principle possible to correct this effect by considering the geometry of the experiment, this method turns out to be error-prone due to the many unknown parameters. Especially the beam shape and diameter as well as the precise shape of the sample in the beam are difficult to determine in-situ. Instead, we will make use of an additional information which is usually available from the measured data, the TEY signal.

The TEY signal of a reflectivity spectrum contains experimental information on the illumination of the sample. Two effects affect the TEY intensity for a given energy which are both related to the angle of incidence  $\Theta$ . For small angles, the sample is not fully illuminated and thus the TEY is reduced. Illumination causes the TEY to be dramatically reduced for grazing incidence and the signal recovers back to full intensity for larger angles when full illumination is reached. The second effect is the absorption in the sample which also depends on the angle of incidence. For small values, most of the X-rays are absorbed in a region close to the surface and thus produce electrons which fully contribute to the TEY. On the other hand, for large angles of incidence most absorption takes place deep in the samples where the produced electrons are not able to leave the sample, the TEY decreases.

Eventually it is found that the former of the two effects leads to an increase while the latter corresponds to an exponential decrease. Assuming that the film thickness  $d$  is much larger than  $\frac{1}{\xi} + \frac{\mu}{\sin\Theta}$  which is certainly fulfilled here since the substrate has to be considered as well, the exponential decrease can be approxi-

mated by [80]

$$I \propto \frac{\frac{\mu}{\sin \Theta}}{\frac{\mu}{\sin \Theta} + \frac{1}{\xi}}, \quad (4.16)$$

with  $\mu$  being the energy dependent absorption length and  $\xi$  being the electron escape length which is usually on the order of 1 – 3 nm [81].

The idea is now to divide the initial TEY signal which contains both contributions by a decay of the form of equation (4.16). By choosing the parameters  $\mu$  and  $\xi$  in a way, that the result is constant for larger angles, the self-absorption contribution is fully removed and the remaining curve corresponds to the unnormalized illumination. Finally, the reflectivity curve is corrected using the normalized illumination curve (constant part equals 1).

The whole process of illumination correction using the TEY signal is shown for real, measured data in Fig. 4.4. As expected, the raw TEY curve, 4.4(a), shows the above described behaviour by first increasing due to the illumination which is then overlaid by the exponential decrease. It has to be mentioned that the origin of the bump at roughly  $7^\circ$  is unknown. Fig. 4.4(b) shows the decrease which produces the illumination curve shown in the same graph. The parameters were  $\mu = 1/100$  nm and  $\xi = 1$  nm which are reasonable for the sample shown here. The last figure (Fig. 4.4(c)) shows the original, uncorrected reflectivity curve and the result after dividing it by the normalized illumination curve from Fig. 4.4(b).

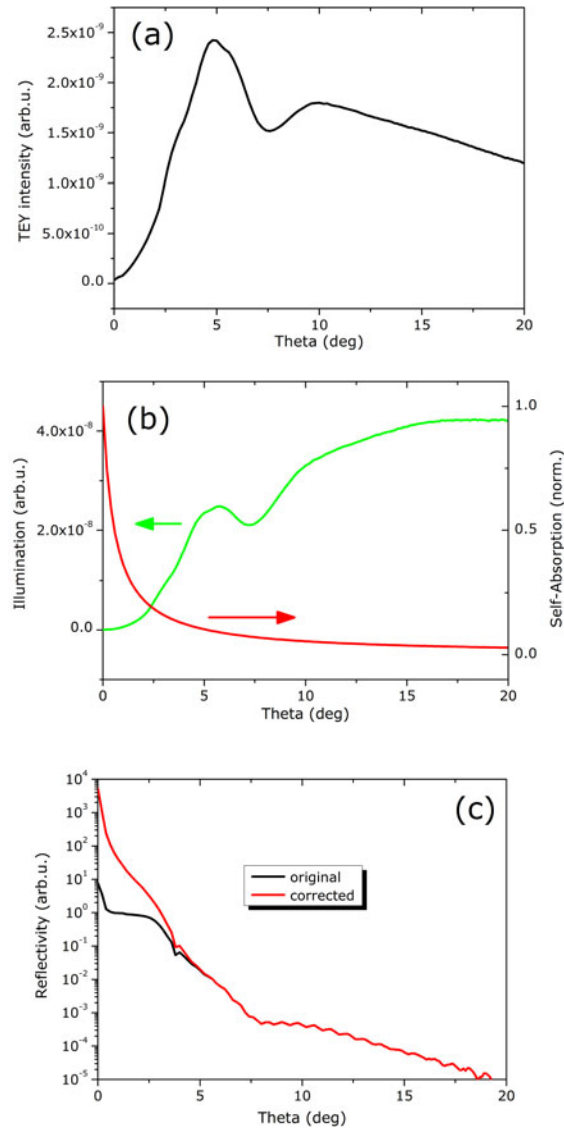


Figure 4.4: Correction of the systematic error of incomplete sample illumination for smaller angles in a reflectivity experiment. Figure a) shows the initial TEY curve such as measured during the reflectivity scan. The graph in b) shows the fitted decay in red and the resulting illumination after dividing the TEY (Fig. a)) by the decay. The final plot c) shows the initial, raw reflectivity curve (black) and the corrected one (red) which has been obtained by applying the normalized illumination curve.



## 5 XRMR on Exchange Bias Systems

In the very intuitive picture introduced in Section 3.2.1, uncompensated antiferromagnetic spins at the interface couple to the ferromagnet inducing an additional resistance to the reversal of the ferromagnet. If the uncompensated AF spins involved are free, this results in an enhancement of coercivity; on the other hand, if the antiferromagnetic spins involved are pinned it results in an additional unidirectional anisotropy, i.e., an exchange bias. The reason for this different behaviour is the anisotropy, i.e., the rigidity of the antiferromagnet as it is described in detail in Section 3.2.1.

However, the experimentally observed effect differs by orders of magnitude from the predictions of this simple model. To overcome the discrepancy, several alternative models of exchange bias, mostly based on a weakening of the antiferromagnet by domain formation, have been developed [24, 28, 30, 82, 83]. In contrast, recent experimental results [33, 84] point more and more towards the interface and its magnetic configuration as the main parameter for exchange bias.

Element selective X-ray techniques [6, 85] for example revealed the existence of induced ferromagnetism in the antiferromagnetic layer in various exchange bias systems [31, 33, 34, 86]. Such induced ferromagnetism complicates simple theoretical descriptions since most models till now assume a clear structural borderline between the ferromagnet and the antiferromagnetic layer. The presence of ferromagnetism in the antiferromagnet immediately raises the question of where the pinned moments which are responsible for the loop shift, are located. It is obvious that a better understanding can only be achieved by obtaining a precise atomic scale mapping of the interfacial magnetic configuration for each element involved. The fact, that the interface is deeply buried in the sample limits the available techniques to neutron and X-ray scattering/spectroscopy. Especially, the soft X-ray resonant magnetic reflectometry (XRMR) which has been introduced in Section

3.4 has been demonstrated to be a powerful method for investigating magnetism at buried interfaces [34, 87].

Using the new XRMR experiment which has been set up during this thesis (compare 6.1 and ref. [79]), a series of very different exchange bias systems was investigated in order to identify the microscopic mechanisms at the interface and especially the local magnetic configuration.

Chapters 5.1.4, 5.1.7 and 5.1.8 reprinted with permission from: Sebastian Brück, Gisela Schütz, Eberhard Goering, Xiasong Ji and Kannan M. Krishnan, *Physical Review Letters*, **101**, 126402, 2008. "Copyright 2008 by the American Physical Society."

## 5.1 Pinned and Rotatable Moments in MnPd/Fe

$\text{Mn}_{52}\text{Pd}_{48}$  is an antiferromagnet with a Néel temperature of  $T_N \approx 500$  K for this composition and a CuAu-I-type crystal structure [88]. From polarized neutron studies of MnPd, the spin structure of the antiferromagnetic phase can be derived [88]. The found configuration is illustrated in Fig. 5.1. Depending on the

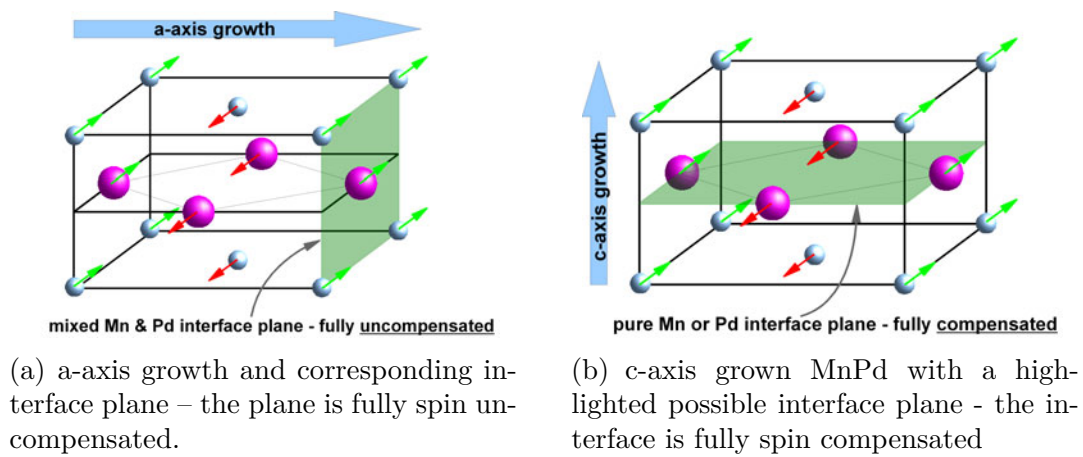


Figure 5.1: Antiferromagnetic spin configuration of CuAu-I-type  $\text{Mn}_{50}\text{Pd}_{50}$  as derived from powder neutron diffraction [88]. Possible interface planes for a- and c-axis growth are highlighted

interface plane, MnPd has either a fully compensated (see 5.1(b)) or a fully uncompensated spin configuration at the interface (see 5.1(a)). Since, at least in a strongly simplified model, exchange bias depends on the antiferromagnetic spin configuration at the interface, this difference between a-axis and c-axis growth should yield differences in the exchange bias of corresponding samples. This is the reason why epitaxial MnPd is an appealing system to investigate exchange bias since it allows changing the spin configuration at the interface drastically while having the same material and thus X-ray properties. P. Blomqvist and co-workers (i.e., the group of Prof. Krishnan) showed that by controlling the substrate temperature during growth, it is possible to influence the structural properties of the MnPd including its crystallographic orientation relationship, i.e., a- or c-axis

orientation with respect to the substrate [89, 90]. For temperatures  $T < 100^\circ\text{C}$ , MnPd grows in a-axis orientation while for temperatures  $T > 450^\circ\text{C}$  a pure c-axis growth takes place. In between, a mixture of both phases is found [90, 91]

Aim of this work is to investigate a- and c-axis oriented MnPd samples by XRMR and XMCD and search for differences in the interfacial configuration of the uncompensated moments in the antiferromagnet. A correlation with the exchange bias is expected. For this investigation, a set of four samples has been prepared by the group of Prof. Krishnan, namely by X. Ji at the University of Washington in Seattle, USA. In the following, the samples will be introduced and their preparation discussed:

- The first sample, labeled FD040 is a c-axis grown MnPd film without ferromagnet. This sample is very important since the Mn is not buried beneath a ferromagnet, in contrast to the other samples, and so the X-ray absorption of the Mn L edge can be measured by TEY. To prevent degradation of the MnPd, a 15 Å Pt cap was deposited on top.
- Sample FD041 was grown at a substrate temperature of  $85^\circ\text{C}$  and accordingly has an a-axis orientation of the MnPd. However, since the MnPd is chemically unordered after growth at low temperatures, a heat treatment is necessary to form the ordered MnPd phase. Therefore, the sample was annealed for 1h at  $250^\circ\text{C}$  in vacuum. Besides, a magnetic field is applied during the annealing process to induce a well-defined uniaxial anisotropy along the Fe[100] direction. The epitaxial relation for the layers then reads: Fe[110]//MnPd[100]//MgO[100]. Note that the a-axis orientation has a bicrystal orientation and might exhibit a twinned crystal structure [90, 91].
- The two samples FD042 and FD043 were both grown at elevated temperatures favoring c-axis growth. However temperatures were varied to create different interface properties. FD042 was grown at  $325^\circ\text{C}$  while FD043 was grown at a slightly reduced temperature of  $290^\circ\text{C}$ . Since both temperatures are too low for pure c-axis growth (compare above) a mixture of both orientations can be expected. The crystallographic relationship for c-axis MnPd reads: Fe[001]//MnPd[001]//MgO[001]. It is noteworthy that the samples have been grown in-field in order to induce exchange bias.

The following section will describe the preparation and general crystallographic and magnetometric characterization of all samples. Then the results of an extensive XRMR investigation of sample FD041 (a-axis MnPd) will be presented and discussed. Finally the section closes with a comparison of the spectroscopic, structural and magnetic properties of all three samples, FD041, FD042 and FD043.

### 5.1.1 Preparation of the Samples

Bilayer samples with nominal thicknesses of  $\text{Mn}_{52}\text{Pd}_{48}$  (750 Å)/Fe(70 Å)/Pt(15 Å) were grown epitaxially on MgO(001) substrates in an ultrahigh vacuum ion-beam sputter deposition system with a base pressure of  $10^{-9}$  mbar. Before mounting the substrates in the preparation chamber, all of them were cleaned by Acetone and Ethanol and subsequently degased at 500 °C for 1h to remove any adsorbat from the surface. The film growth was then carried out at the specified temperatures.

For the c-axis samples, FD042 and FD043, the elevated temperature during the sputtering process leads to a ordered chemical state directly after growth. By applying a magnetic field during the deposition, exchange bias has been induced in a controlled way in these samples. In contrast the a-axis sample FD041 is grown at a substrate temperature of only 85 °C, which, at first, leads to chemically disordered MnPd. By a subsequent annealing at 250 °C for 1h in vacuum, a chemically ordered phase is formed which exhibits a very good crystallographic orientation relationship such that its a-axis is normal to the sample surface. Furthermore a magnetic field is applied during this annealing process to induce a well defined uniaxial anisotropy.

Note that the exchange bias has been induced along the Fe (100) direction, i.e., the easy axis of the ferromagnet, for all samples, FD041, FD042, and FD043.

### 5.1.2 Crystallographic & Magnetometric Characterization

X-ray diffraction (XRD) spectra have been measured to check the orientation of the deposited films. Both crystallographic orientations, a- and c-axis grown MnPd are easily distinguished from each other by their characteristic MnPd reflections.

While the c-axis orientation shows MnPd(001) and MnPd(002) peaks, the a-axis orientation only shows a MnPd(200) peak. The XRD spectra have been measured by Xiaosong Ji at the University of Washington in Seattle, USA. The measured spectra of all four samples are shown in Fig. 5.2, they have been shifted vertically for better readability. The absence of the MnPd(001) and MnPd(002) reflections

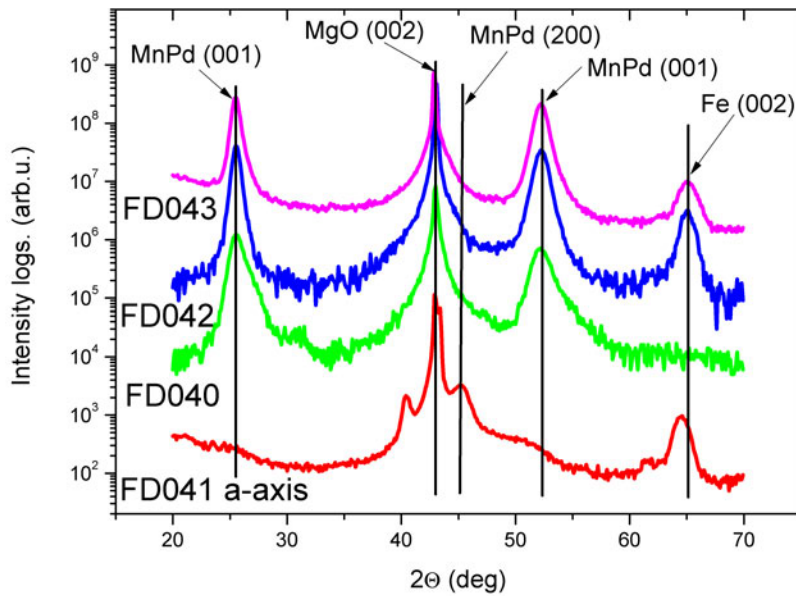


Figure 5.2: X-ray diffraction (XRD) data of all four investigated samples, FD040 (MnPd only sample), FD041 (a-axis), FD042 (c-axis/325 °C) and FD043 (c-axis/290 °C).

clearly identifies FD041 as the a-axis oriented MnPd, while all other samples are c-axis. However, the small bump at  $52.2^\circ$  in the XRD spectra of FD041 might indicate some c-axis contribution in this sample. The same applies for sample FD042 which shows a small hillock at the MnPd(200) angle indicating some a-axis contribution.

Vibrating sample magnetometry (VSM) has been used to characterize the room temperature magnetic properties of samples FD041, FD042, and FD043. The external magnetic field was applied along the direction of  $H_{eb}$ . These measurements

have also been done by X. Ji at the University of Washington. The resulting hysteresis loops are shown in Fig. 5.3 for all three samples. The room temperature hysteresis measured along the Fe (100) direction of sample FD041 (a-axis growth, i.e., spin uncompensated interface) is shifted by  $H_{eb} = -4.8$  mT and the coercive field is  $H_C = 13$  mT. Sample FD042 (c-axis grown at 325 °C) shows a slightly larger exchange bias of  $H_{eb} = -6.4$  mT as well as an increase in coercivity to  $H_C = 16$  mT. Compared to typical values for c-axis MnPd [90, 91], these values are too small. This might be related to the already mentioned presence of a-axis grown MnPd in the sample. Sample FD043 (c-axis grown at 290 °C) which is grown at lower temperatures compared to FD042, exhibits the largest coercive field of all three samples with  $H_C$  being 30 mT. On the other hand, the loop shift is  $H_{eb} = -5$  mT which is far too small. But while the XRD of FD042 shown in Fig. 5.2 implies an a-axis contribution for this sample, FD043 seems to be only c-axis MnPd. Another explanation might be that the anisotropy of the antiferromagnet is lower in this sample. A small anisotropy  $K_{AF}$  leads to a large coercivity and a reduced or vanishing loop shift (see also Section 3.2.1).

### 5.1.3 X-ray Absorption Spectroscopy and Optical Constants

From here on, the discussion will focus on the investigation of sample FD041 (a-axis MnPd) and the pinned and rotatable uncompensated moments which were found there. Later, the results of the two other samples will be discussed and compared to FD041.

Optical constants for both relevant elements, Fe and Mn were obtained by measuring the near edge X-ray absorption fine structure using the TEY and TFY mode (compare 6.1.3 and 6.2). Due to the problem of self-absorption, the TFY measurements can not be used for a quantitative analysis and the determination of the optical constants. On the other hand, TEY is also no option since the layer is too deeply buried beneath the ferromagnet in sample FD041. Therefore the Mn fine structure of the L edges was measured on sample FD040. This sample does not have a ferromagnetic layer and thus the TEY of the Mn is measurable.

The sample was rotated to an angle of incidence of  $\Theta = 45^\circ$  and the TEY and

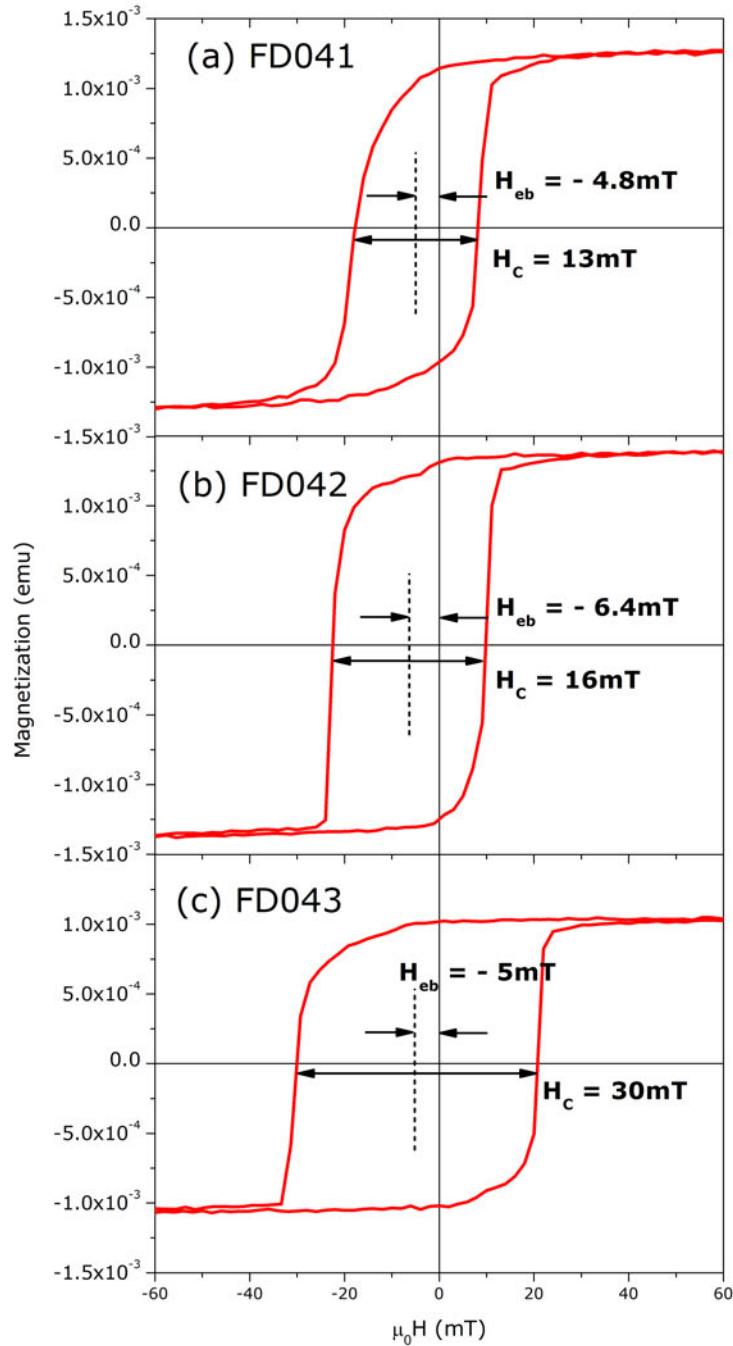


Figure 5.3: Magnetization loops of all three investigated samples, FD041 (a-axis), FD042 (c-axis/325 °C) and FD043 (c-axis/290 °C) measured by VSM (measurements performed by X. Ji at the Univ. of Washington, USA).



TFY have been measured for each energy point using linear polarized X-rays. The resulting curves are then edge normalized according to the scheme described by Fig. 4.2 in Section 4.2. The Mn L edge NEXAFS of sample FD040 obtained from the TEY signal is shown in Fig. 5.4. The spectrum shows a very narrow

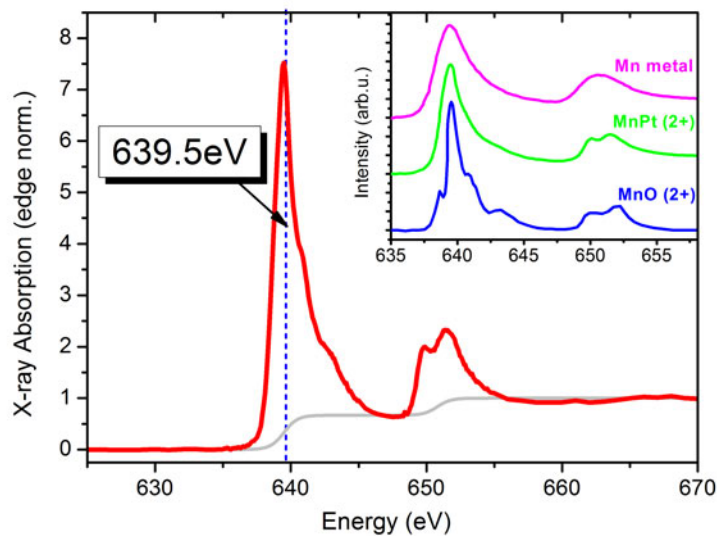


Figure 5.4: High resolution X-ray absorption spectrum of the Mn L edges of sample FD040 (MnPd w/o ferromagnet). The highlighted energy of 639.5 eV is the one where most of the XRMR spectra discussed in the following were measured. The inset shows reference curves for metallic Mn [92], MnPt [93], and MnO [94], respectively.

peak with two shoulders at the  $L_3$  edge and a double peak structure for the  $L_2$  edge. The inset shows reference spectra for metallic Mn [92], MnPt [93], and MnO [94], respectively. Comparison with the reference spectrum for metallic Mn [92,95] clearly shows differences between the spectrum of manganese in MnPd and metallic ones. Bulk, metallic Mn exhibits a broad  $L_3$  peak without shoulders and a single  $L_2$  peak which is narrower compared to the double peak structure found here.

The XAS spectrum of MnO on the other hand exhibits a multi peak structure

similar to the one found here [94, 96] although the structures are less pronounced in MnPd. In MnO, the manganese is in the 2+ electronic configuration ( $3d^5$ ) with fully localized electrons.

If the spectrum would be due to surface oxidation of the MnPd, the more bulk sensitive spectrum obtained from measuring the fluorescence yield (compare below) should differ significantly. As can be seen from the data shown in Fig. 5.5(a), this is not the case. Another point is the 15 Å thick platinum layer on top of the MnPd which is sufficient to prevent any oxidation of the MnPd layer. Finally a similar feature rich Mn spectrum is found in MnPt [93], a system which should be very similar from its chemical behaviour.

So it can be concluded that the Mn in MnPd is in a  $Mn^{2+}$  configuration but due to the Pd and not oxidation. This finding is supported by the fact that Pd (and also Pt) has a considerably higher electronegativity of 2.20 (2.28 for Pt) compared to Mn which has only 1.51 [97]. Anyway the electrons are less localized than in MnO and accordingly the spectrum contains less structure.

Before continuing with the results of the Fe XAS, it is worth considering the question whether the found absorption spectrum is the same in the bulk of the sample. And even more important whether it is the same in the buried MnPd layers of samples FD041, FD042, and FD043. Fig. 5.4 is obtained by measuring the total electron yield (TEY), a technique which is mostly surface sensitive. To verify that the observed Mn spin configuration is of general character in MnPd and not confined to the surface region or maybe even related to oxidation of the latter, the total fluorescence yield (TFY) has been measured simultaneously. TFY probes very deep into the sample and therefore the bulk properties dominate the spectrum. The resulting TFY spectrum of sample FD040 (MnPd w/o ferromagnet) is shown in Fig. 5.5(a) along with the corresponding TEY spectrum. Both spectra are not normalized. As can be seen, both spectra resemble each other nearly perfectly proving that the surface Mn and the bulk Mn in MnPd are really the same here.

Eventually, the TFY at the Mn  $L_{2,3}$  edges has also been measured in the sample FD041 (a-axis MnPd) to ensure that the MnPd layer of the samples with ferromagnet (thus FD041, FD042 and FD043) really have the same spectral shape for the Mn. The result is shown in Fig. 5.5(b). Although the shape of the curve

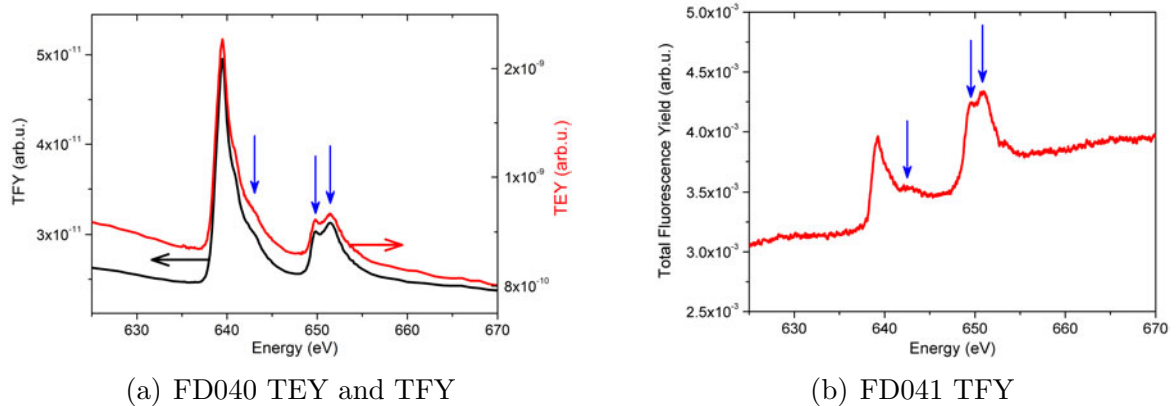


Figure 5.5: The left figure shows the Mn NEXAFS of sample FD040 (MnPd w/o Fe) measured by TEY and TFY at the same time. Both spectra resemble each other quite good proving that bulk and surface are the same in this sample. The right figure shows a TFY spectrum of sample FD041 (a-axis MnPd). Although the spectrum is strongly affected by self-absorption, the relevant features are clearly visible verifying that the MnPd exhibits the same Mn configuration.

seems to be heavily affected by self-absorption in the sample (see for example [98] and references therein) which leads to a strongly suppressed  $L_3$ -peak, the relevant features, especially the double peak structure at the  $L_2$  edge are clearly visible. It can be expected that the two other samples also have their Mn in this configuration and the conclusion can be drawn that all four samples have a typical metallic  $Mn^{2+}$  configuration with a localized character of the electrons due to the electronegativity of the Pd in the  $Mn_{52}Pd_{48}$  layer.

Next the XAS and XMCD of the Fe layer is investigated and discussed. Circular polarized X-rays with positive helicity were used for these measurements. A magnetic field of 85 mT was applied parallel and antiparallel with respect to the incident beam direction to flip the magnetisation of the sample at each energy value thus providing a XMCD difference signal. However, to reduce the signal to noise ratio for the TEY signal the magnetic field has only been applied shortly to reorient the magnetisation and was then turned off during the measurement. The remanence of the sample is sufficient to allow such a procedure as can be seen from the VSM hystereses in Fig. 5.3. Besides these changes, the same procedures and settings (namely  $\Theta = +45^\circ$ ) as for the Mn XAS were used. The resulting XAS

for both field directions (indicated by  $\uparrow\uparrow$  and  $\uparrow\downarrow$ ) as well as the XMCD difference signal at the Fe L edge of sample FD041 is shown in Fig. 5.6. The spectrum of

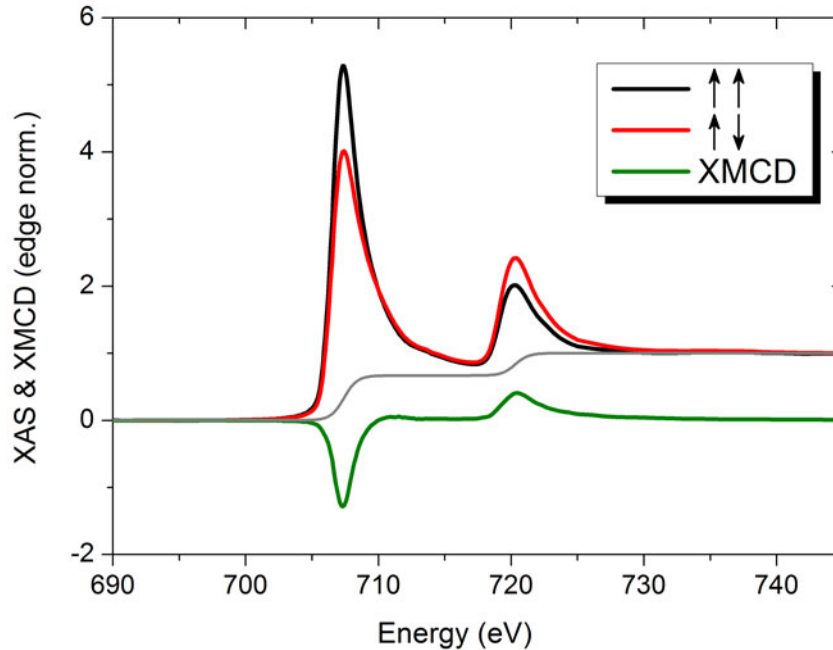


Figure 5.6: XAS and XMCD at the Fe  $L_{2,3}$  edge of sample FD041 (a-axis MnPd) measured by TEY at an angle of incidence of  $\Theta = +45^\circ$  and with positive circular polarized X-rays.

sample FD041 corresponds in shape and magnitude well with reference data for metallic Fe [89, 99].

To quantify the magnetic spin and orbital moments, XMCD sum rules (equation (3.53) and (3.52) from Section 3.3.4) have been applied. A standard two step background as it is indicated in the graph was subtracted and the resulting curve was then integrated. The result was multiplied by the number of  $3d$  holes  $n_h$  which is  $n_h = (10 - n_{3d})$ . From theoretical calculations, the number of electrons is  $n_{3d} = 6.61$  for Fe which yields a hole number of  $n_h = 3.39$  [89]. Furthermore the result has been corrected for the degree of circular polarization of the X-rays of 90 % and for the angle of incidence of  $\Theta = 45^\circ$  which means that the measured moment is by a factor of  $\sqrt{2}$  too small. Eventually, the remanent magnetisation

has to be considered because, as can be seen from the corresponding hysteresis shown in Fig. 5.3(a), the sample is not fully saturated in remanence. As a consequence, the measured moment has to be multiplied by a factor of 1.176.

The corrected spin and orbital moments of the sample are given in table 5.1 along with reference data for thin-film (bcc) Fe obtained from XMCD [89]. The

| Sample  | $m_{\text{orb}}/m_{\text{sp}}$ | $m_{\text{orb}}$ | $m_{\text{sp}}$ |
|---------|--------------------------------|------------------|-----------------|
| FD041   | 0.021                          | 0.041            | 1.98            |
| Fe(bcc) | 0.043                          | 0.085            | 1.98            |

Table 5.1: Corrected spin and orbital moments of FD041 derived from Fig. 5.6 using XMCD sum rules. For comparison, literature values for bcc Fe are provided for comparison. [89].

found value for the spin moment of the Fe in sample FD041 agrees very good with the reference data from C.T. Chen et al. [89] and references therein. For the orbital momentum, the value found here is by a factor of 2 too small. A possible reason for this might be the error of the determination of such a small moment.

Based on the XAS and XMCD data of Figs. 5.4 and 5.6, the optical constants  $\delta$  and  $\beta$  and the magneto-optical constants  $\delta_{\text{mag}}$  and  $\beta_{\text{mag}}$  were evaluated using the scheme described in Section 4.2. Fig. 5.7(b) shows exemplarily the resulting Fe optical constants of sample FD041. Note that Fe was derived from the XAS/XMCD data for each sample individually while the MnPd optical constants use the XAS measured on sample FD040 (MnPd w/o ferromagnet). Based on the optical and magneto-optical constants derived in this paragraph, non-magnetic and magnetic reflectivity curves can be simulated and fitted to measured curves to determine the chemical and magnetic profile in an element selective way.

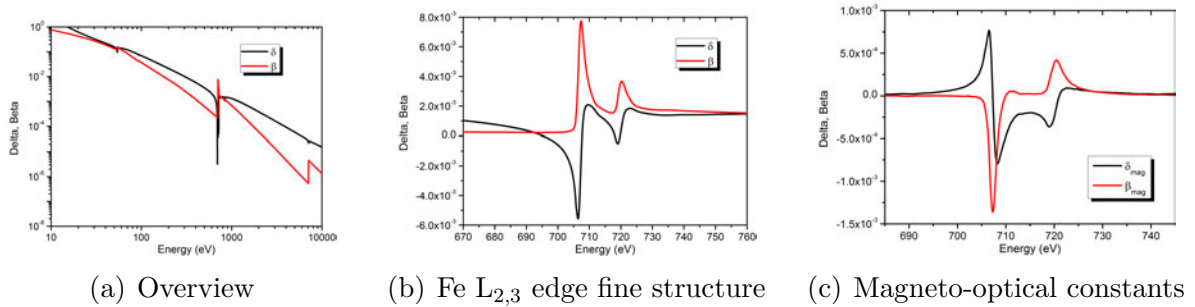


Figure 5.7: Optical Constants for the Fe layer of sample FD041 as derived using the scheme described in Section 4.2. The left graph shows an overview of the optical constants of Fe in a double log representation. The middle graph is a zoom of the fine structure of  $\delta$  and  $\beta$  at the Fe L<sub>2,3</sub> edge. Subfigure 5.7(c) shows the corresponding magneto-optical constants derived from the XMCD signal of Fe.

#### 5.1.4 Structural Characterization

The chemical profile which is the thickness of the individual layers and their interfacial roughness was determined by non-magnetic X-ray reflectivity measurements. Magnetic contributions only take place when measuring at the resonant edges using circular polarized light. Therefore the following measurements were carried out either far away from any resonant edge or on resonant but using linear polarized light. Linear polarized light is a superposition of half intensity with left and the other half with right circular polarized light. Accordingly the magnetic contributions in the sample are averaged out when using linear polarized X-rays. Here in particular, linear polarized light with a horizontal polarization plane, i.e., parallel light with respect to the scattering plane was used. The X-ray reflectivity curve discussed in the following paragraph was measured during the May 2007 beamtime at the UE56/2-PGM1 beamline at BESSY II [79]. The as-measured raw curves were normalized to the  $I_0$  intensity reference signal (compare Section 6.1.3) and the simultaneously measured fluorescence background was subtracted from the curve. Finally the curves were normalized to have an initial intensity of  $I_{ref}(\Theta = 0^\circ) = 1$ . A more detailed description of the scheme is given in Section 4.1.

With the simulation tool ReMagX (see 6.4) and the optical constants derived

in the last section, the reflectivity curves are then simulated and the result is compared to the measurement. In an iterative process, the parameters for the simulation are refined to fit it to the measurement. After sufficient convergence of the fit its parameters provide the thickness and roughness for each layer.

In Fig. 5.8(a) the normalized reflectivity curve measured at the Mn L<sub>3</sub> edge (639.5 eV) with linear polarized X-rays is shown as black solid line. The associated best fit solution for the measurement is included in the same graph as red solid line. The corresponding optical, i.e., chemical profile of this best fit solution is shown in Fig. 5.8(b). A strong nearly undamped oscillation is found which corresponds to

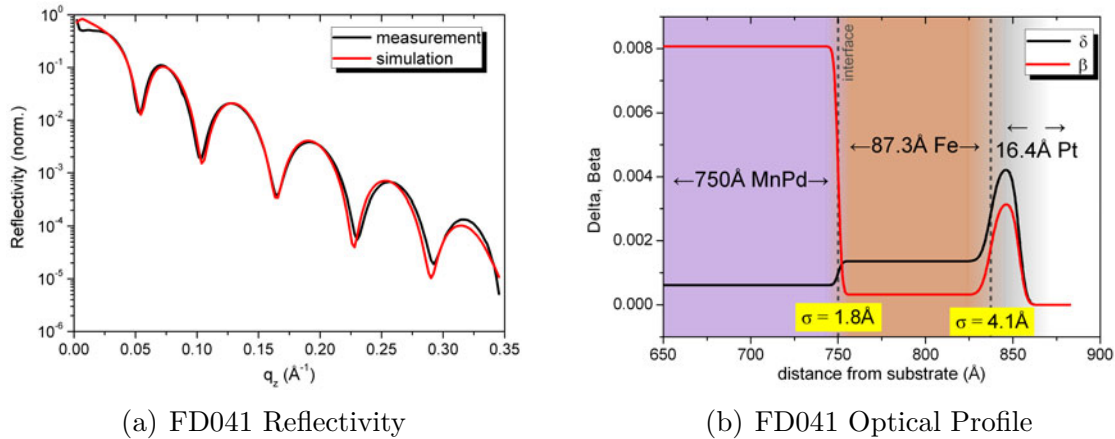


Figure 5.8: Resonant reflectivity curve measured at the Mn L<sub>3</sub> edge at an energy of 639.5 eV and the corresponding fit result (red curve). Fig. 5.8(b) shows the optical, i.e., chemical profile of sample FD041.

interference between reflections from the sample surface and from the Fe/MnPd interface. The reason is that the interfaces vacuum/sample and Fe/MnPd exhibit the largest changes of the optical constants. The latter because at the Mn L edge  $\beta$  is very large. Accordingly the wavelength of the oscillations correlates with the summed thickness of the Fe and Pt layers. The damping of the oscillations is related to the quality of the involved interfaces and will be discussed in more detail later (see Section 5.1.11). To properly determine roughness and absorption in the sample, a simulated curve based on the above-mentioned magneto-optical

approach is fitted to the measurement. The fit result (red solid lines) is in very good agreement with the measured data. Only for very small and very large angles, a larger discrepancy is visible which is related to systematic errors. For angles close to  $0^\circ$ , incomplete illumination of the sample leads to a reduction of reflected intensity. For large angles, the signal to noise ratio decreases and the diffuse background increases leading to a poor quality of the data. Therefore for the fitting procedure only values in the range from  $q_z = 0.03 \text{ \AA}^{-1}$  to  $q_z = 0.3 \text{ \AA}^{-1}$  have been used.

Eventually, the resulting structural parameters of sample FD041, as they are obtained from analyzing the resonant XRR at the Mn  $L_3$  edge are given in Table 5.2. It should be mentioned that the thickness of the MnPd layer itself can not be

| Layer     | thickness ( $\text{\AA}$ ) | $\sigma_{\text{RMS}}$ ( $\text{\AA}$ ) |
|-----------|----------------------------|--|
| vacuum    |                            | 3.1                                    |
| Pt        | 16.4                       | 4.1                                    |
| Fe        | 87.3                       | 1.8                                    |
| MnPd      | 750                        | ?                                      |
| substrate |                            |  |

Table 5.2: Final structural parameters of sample FD041 as obtained from fitting the reflectivity curve shown in Fig. 5.8(a).

determined from this measurement since due to its thickness (nominally  $750 \text{ \AA}$ ) and the strong absorption at the Mn edge, no X-rays get through the layer.

### 5.1.5 Magnetic Reflectivity

Magnetic reflectivity curves have been measured at the energy of the maximal Fe XMCD ( $707.2 \text{ eV}$ ), the maximum of the Mn  $L_3$  peak in Fig. 5.4 at  $639.5 \text{ eV}$



and the Mn  $L_2$  peak at 651.5 eV. An external magnetic field of  $\mu_0 H_{ext} = 67$  mT was applied. As can be seen from the VSM hysteresis in Fig. 5.3(a), this field is sufficient to fully saturate the sample. The reflectivity was measured for both directions of the applied field, parallel and antiparallel at each angle value thus providing dichroic reflectivity data. Also each measurement was carried out for positive and negative circular polarized light which gives a total of four reflectivity curves according to the scheme  $\uparrow\uparrow$ ,  $\uparrow\downarrow$ ,  $\downarrow\uparrow$  and  $\downarrow\downarrow$ .

The resulting four dichroic reflectivity curves are shown in Fig. 5.9(a). The

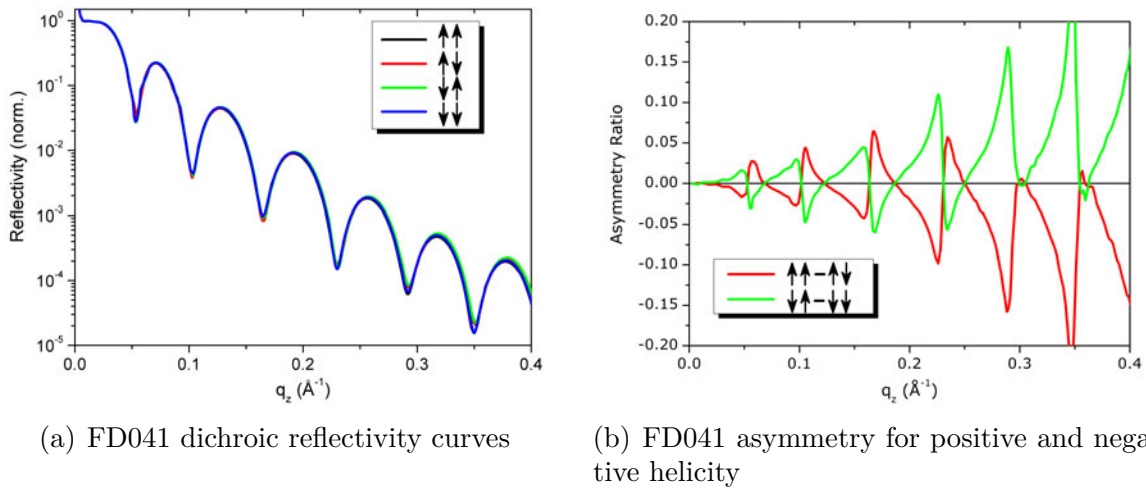


Figure 5.9: Mn  $L_3$  edge XRMR of sample FD041 (a-axis MnPd). The left graph shows the four original dichroic reflectivity curves while the right graph shows the processed asymmetry for both helicities of the X-rays.

curves show nearly no difference meaning that the magnetic contribution is very small. To separate the magnetic contribution from the chemical reflectivity curve, a difference signal similar to the XMCD is used. The reflectivity analogon to the XMCD difference signal is the asymmetry ratio  $A$  which is defined as the weighted difference signal of parallel and antiparallel alignment according to

$$A = \frac{(I_{\uparrow\uparrow} - I_{\uparrow\downarrow})}{(I_{\uparrow\uparrow} + I_{\uparrow\downarrow})}. \quad (5.1)$$

The direction of the first arrow represents the helicity and the second arrow the relative orientation of the external magnetic field or the magnetisation in the sample. Note that in the case of purely rotatable, i.e., ferromagnetic moments, flipping the field or switching the helicity leads to the same results as long as the sample is fully saturated when measuring the respective direction.

The magnetic contribution was obtained from the reflectivity curves by applying equation (5.1) and the resulting curves for the two measured X-ray helicities are shown in Fig. 5.9(b). The sample clearly shows a magnetic asymmetry signal proving the existence of rotatable Mn moments in the nominally antiferromagnetic MnPd. The magnitude of this asymmetry signal reaches up to 20%.

It is instructive at this point to compare the result for the Mn  $L_3$  edge to the asymmetry signal from the ferromagnetic Fe layer on top. The dichroic reflectivity measured at the Fe  $L_3$  edge at an energy of 707.2 eV using positive circular polarized light is shown in Fig. 5.10 along with the corresponding asymmetry. A

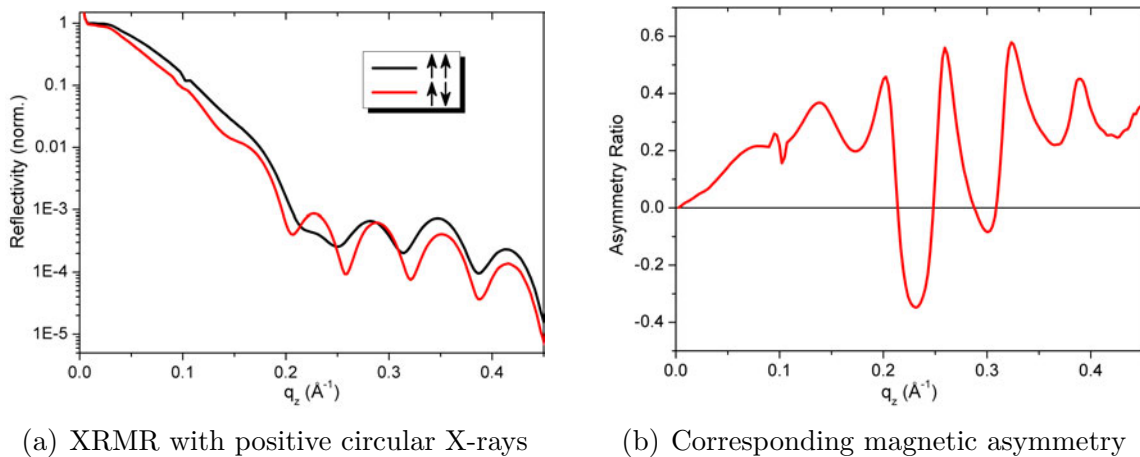


Figure 5.10: XRMR measurement at the  $L_3$  edge at 707.2 eV using positive circular polarized X-rays. The corresponding asymmetry ratio as calculated using equation (5.1) is shown on the right. A magnetic asymmetry of nearly 60% is found in the sample (source: M235 - May08, BESSY).

magnetic signal of nearly 60% is found for the Fe. That is not surprising because

the whole Fe layer is ferromagnetic and already the XMCD signal was significant compared to the overall absorption. However, this comparison shows that the rotatable magnetic moments in the Mn either carry a much smaller moment or that only a small fraction of the Mn is rotatable.

### 5.1.6 The Problem of Measuring Pinned Moments

Rotatable magnetic moments can be measured by either switching the magnetisation direction in the sample or alternatively by flipping the helicity of the X-rays while holding the moments aligned in one direction. Anyway both methods usually provide the same XMCD difference signal since the absorption is proportional to the scalar product of  $\mathbf{M}$  and  $\mathbf{P}$  (see also equation (3.51) in Section 3.3.4).

For pinned moments the situation is more complicated. Because the moments are not rotatable, it is not possible to change the relative orientation to obtain a difference signal similar to XMCD just by flipping an external magnetic field. Only by flipping the helicity of the used X-rays, the necessary change in alignment can be achieved. However if the material contains both, rotatable and pinned moments, they are not separable for a measurement where only the helicity is changed. The solution to this problem is a new asymmetry, labeled here as *pinned asymmetry* which is obtained by flipping both, the external field and the helicity. By doing so, the rotatable magnetic moments are kept parallel or antiparallel for both measurements and any resulting difference in the curve, either in the XAS or the reflectivity curve is then solely related to pinned magnetic moments in the material. The calculus for the pinned asymmetry is defined as

$$\begin{aligned}\tilde{A} &= \frac{(I_{\uparrow\uparrow} - I_{\downarrow\downarrow})}{(I_{\uparrow\uparrow} + I_{\downarrow\downarrow})}, \\ \text{or} & \\ \tilde{A} &= \frac{(I_{\uparrow\downarrow} - I_{\downarrow\uparrow})}{(I_{\uparrow\downarrow} + I_{\downarrow\uparrow})}.\end{aligned}\tag{5.2}$$

The following sketch 5.11 illustrates the situation in a material exhibiting rotatable and pinned moments at the same time, and how the two different con-

tributions are separated. In the upper sketch, the difference leading to normal

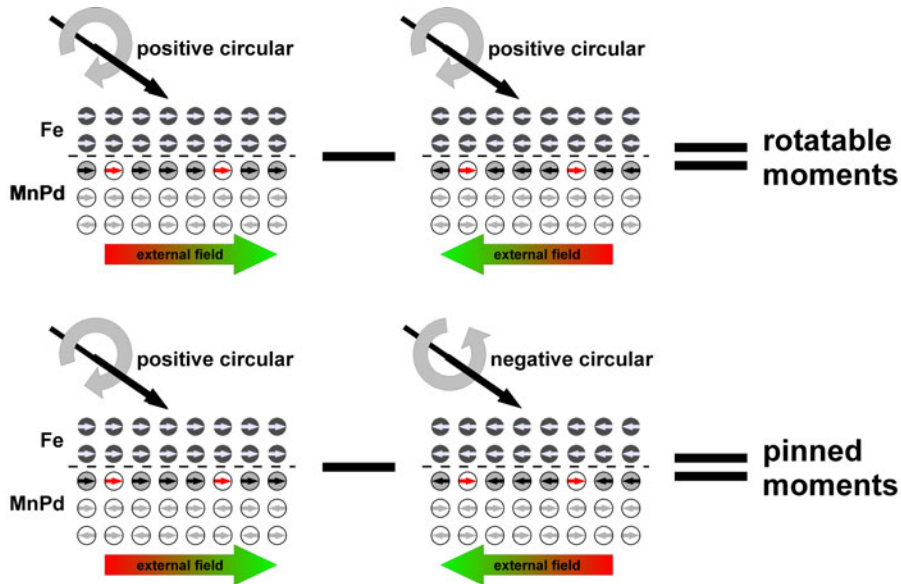


Figure 5.11: Sketches illustrating the difference between normal asymmetry  $A$  related to rotatable magnetic moments and the pinned asymmetry  $\tilde{A}$ .

asymmetry and XMCD is shown. Note how the pinned moments (marked in red) remain fixed while the rotatable ones (gray with black arrow) reverse direction upon flipping the external field. Accordingly, the difference from these two situations provides a measure for the rotatable magnetic moments in the sample.

In the lower sketch the rotatable moments are also reversed from positive to negative direction but at the same time, the helicity also changes from plus to minus keeping the scalar product  $(\mathbf{M} \cdot \mathbf{P})$  parallel meaning that no difference in the absorption from the rotatable moments will take place. On the other hand the change of the photon helicity leads to a difference signal from the pinned moments.

### 5.1.7 Rotatable Magnetic Moments in a-Axis MnPd

Fig. 5.12(a) once again shows the asymmetry ratio at the Mn  $L_3$  edge as it is obtained by applying equation (5.1) to the respective XRMR data from Fig. 5.9.

Note that this asymmetry only originates from Mn in the sample and is measured at an energy of 639.5 eV and by using positive circular polarized light.

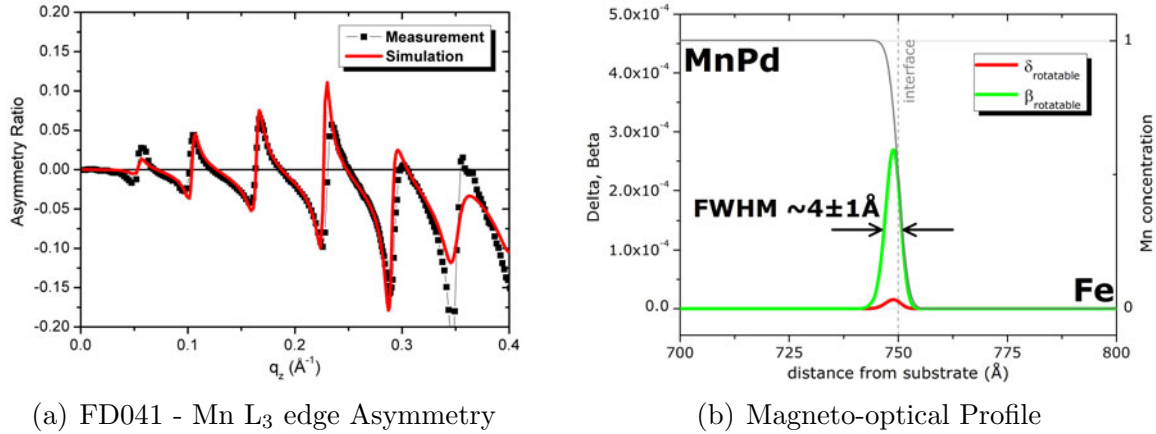


Figure 5.12: Asymmetry ratio of sample FD041 measured at the Mn  $L_3$  edge (639.5 eV) measured with positive circular polarized light as it is calculated from Fig. 5.9 using equation (5.1). The final result of fitting a simulation to the data is shown as red curve.

As already mentioned above, a pronounced asymmetry of up to 20% is found for the Mn in FD041 clearly proving the existence of rotatable Mn moments in the sample. To answer the question whether these rotatable Mn moments are located at the interface or in the bulk, the asymmetry curve has been fitted using the magneto-optical simulation technique (see Sections 3.4.2 and 6.4). Making use of the already known structural information from Fig. 5.8, the circular dichroic contribution was simulated using a Gaussian shaped distribution of localized magnetic moments located directly at the interface. The moment was set to  $\sim 1.2 \mu_B$  per Mn atom corresponding to values found in ultra-thin Mn layers on top of a ferromagnetic substrate [92,99]. The final fit is plotted as red solid line along with the measured asymmetry of sample FD041 in Fig. 5.12(a) As can be seen, the measured asymmetry is reproduced perfectly by the simulation. Note that the poor fit for  $q_z > 0.35$  is related to the signal to noise ratio of the measurement.

The magneto-optical profile of the rotatable Mn moments is shown in Fig.

5.12(b) as solid lines ( $\delta_{\text{rotatable}}$ ,  $\beta_{\text{rotatable}}$  as red and green, respectively) along with the Mn concentration (gray line) in the sample.

Rotatable Mn moments are only found in a narrow region of  $(4 \pm 1)$  Å width directly at the interface with the Fe. This corresponds to roughly two monolayers of MnPd and correlates with the roughness of the MnPd/Fe interface which is 3.6 Å (FWHM). The general Mn depletion (chemical profile) at the interface leads to a cut-off or a slightly steeper decrease at the right side of the distribution. The maximum of the rotatable moments lies  $\sim 1$  Å below the nominal interface position.

To determine the coupling direction of the rotatable Mn moments with the Fe atoms above, the following reasoning can be used: From the direction of the magneto-optical profile at the  $L_3$  and the  $L_2$  edge, the direction of the underlying XMCD difference signal (i.e., the absorptive part) can be estimated. The coupling direction is then found by comparing the sign of this XMCD curve to the corresponding XMCD of Fe (see Fig. 5.20) for the same X-ray helicity.

In Fig. 5.13 the Mn  $L_2$  edge asymmetry is shown along with the fit solution. The data has been measured at an energy of 651.5 eV using positive circular polarized X-rays. The found asymmetry is much smaller compared to the  $L_3$  edge asymmetry as is expected from the  $L_3/L_2$  XMCD ratio. A maximum asymmetry ratio of  $\sim 2\%$  is found for the rotatable Mn at the  $L_2$  edge.

Although the small amplitude results in a poor quality of the fit especially for smaller values of  $q_z$ , the general shape and magnitude is reproduced well by the fit and the corresponding magneto-optical profile is shown in Fig. 5.13(b). Here,  $\delta_{\text{rotatable}}$  and  $\beta_{\text{rotatable}}$  are of different sign but more or less of the same magnitude. Note that all other parameters (also position and width of the Gaussian) were kept fixed for the fitting process.

In conclusion, the corresponding absorption curve, i.e., the XMCD difference signal is positive at the  $L_3$  and negative at the  $L_2$ . By comparing this result to the corresponding positive helicity XMCD of Fe shown in Fig. 5.10, antiferromagnetic coupling is found between Fe and Mn.

To further explore the nature of the rotatable Mn moments, their magnetisation

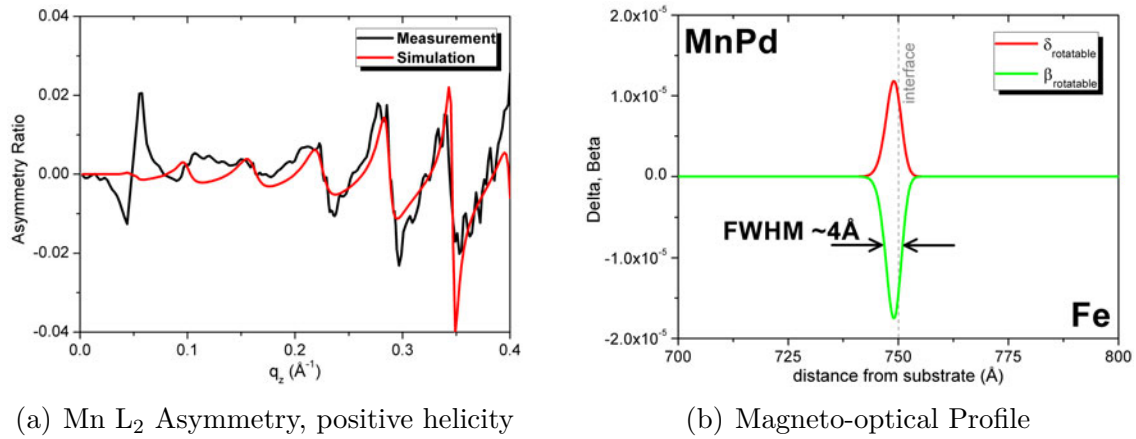


Figure 5.13: Asymmetry from the rotatable Mn moments measured at the Mn  $L_2$  edge (651.5 eV). The best fit result is given by the red solid line in the same graph. Note that the poor quality of the fit is related to the signal magnitude which is roughly  $10\times$  smaller than at the  $L_3$  edge. The corresponding magneto-optical profile is given on the right.

reversal was investigated using element selective magnetic reflectivity. Therefore the specular reflection at the Mn  $L_3$  edge at an angle of incidence of  $\Theta = 9.5^\circ$  (corresponding to  $q_z = 0.107 \text{ \AA}^{-1}$ ) has been measured while varying the external field from positive to negative saturation. The result, shown in Fig. 5.14, is a typical ferromagnetic hysteresis loop. For comparison, the corresponding Fe hysteresis is shown in the same graph as black line with circles. The Fe hysteresis is measured at an energy of 707.2 eV and at an angle of incidence of  $\Theta = 11^\circ$  (corresponding to  $q_z = 0.137 \text{ \AA}^{-1}$ ). Fe and Mn hysteresees resemble each other perfectly in shape as well as magnetic key figures such as coercivity and loop shift.

The fact that the induced ferromagnetism is strongly located at the interface along with the similar shape of the Mn and Fe hysteresis loops indicates that the short range interaction from the Fe dominates the Mn behaviour. Due to the Fe and the accompanying presence of a strong magnetic coupling, neighboring Mn atoms are forced to rotate with the ferromagnet instead of coupling to the AF spin lattice. However, the relative orientation of the Fe and Mn rotatable moments is antiparallel. This interpretation is supported by neutron reflectivity investigations of MnPd which showed that the antiferromagnetic spin lattice is very sensitive to

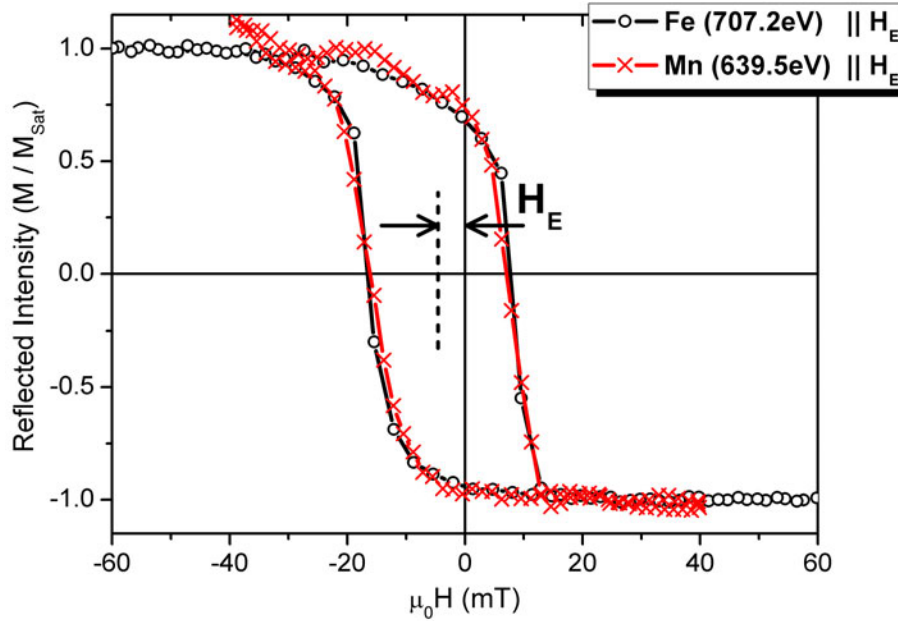


Figure 5.14: Hysteresis loops for Fe and Mn measured in reflection parallel to the Fe[100] exchange bias direction. The Fe hysteresis ( $\circ$ ) is measured at an energy of 707.2 eV and at an angle of incidence of  $\Theta = 11^\circ$ . The Mn hysteresis ( $\times$ ) is measured at 639.5 eV and  $\Theta = 9.5^\circ$ . Mn and Fe exhibit a strong coupling as can be seen from the similar shape of the hystereses.

changes in stoichiometry and or ferromagnetic add atoms [88].

### 5.1.8 Pinned Uncompensated Mn Moments in a-Axis MnPd

The unidirectional anisotropy, i.e., the exchange bias in the sample has to be related to pinned uncompensated moments in the antiferromagnet. As explained in Section 5.1.6, these pinned moments are only accessible by measuring both helicities and both field directions and then applying the calculus defined by equation (5.2). The pinned asymmetry for the Mn  $L_3$  edge is shown in Fig. 5.15(a) as solid squares. A small signal of 2.5% is found which is on average 5 times smaller than the rotatable contribution (see Fig. 5.12). To identify the location of the pinned Mn moments in the antiferromagnet, the same simulation and refinement process described for the normal asymmetry has been used. The final result of the fitting process is shown in Fig. 5.15(a) as red solid line. Although the signal is nearly 5



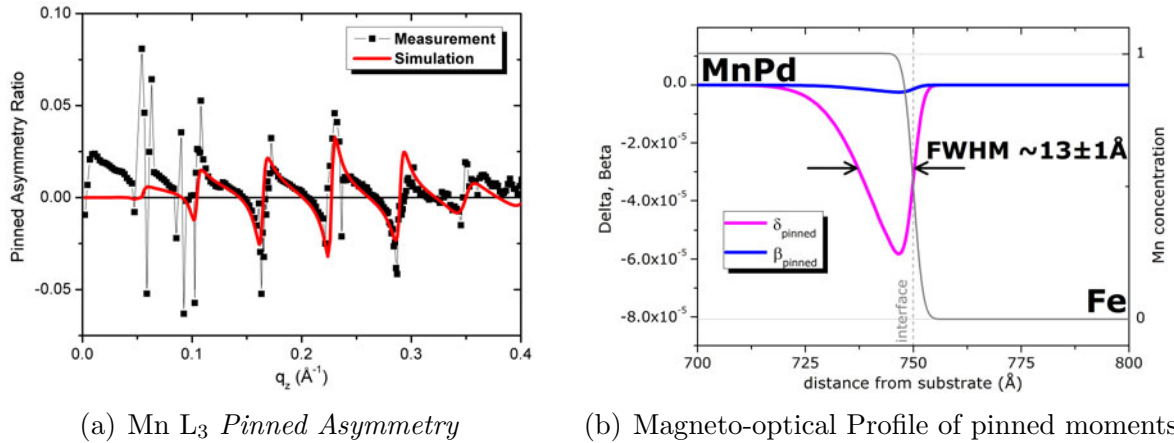


Figure 5.15: Pinned asymmetry ratio as calculated from Fig. 5.9 using equation (5.2). Although the signal is relatively small, a clear structure is visible and the red solid line represents the best fit solution for that curve. The graph on the right is the corresponding magneto-optical profile from the pinned uncompensated Mn moments in the MnPd derived from the fitting process.

times smaller than the one from the rotatable Mn, good agreement of simulation and measurement is reached by the fitting process.

The contribution of the pinned uncompensated Mn moments to the magneto-optical constants is plotted in Fig. 5.15(b) as magenta ( $\delta_{\text{pinned}}$ ) and blue ( $\beta_{\text{pinned}}$ ) line, respectively. As expected from the different magnitudes, the contribution is several times smaller than the one from the rotatable part. It is found, that pinned Mn moments occur in a much wider region of  $(13 \pm 1) \text{\AA}$  (FWHM) in width with the maximum of the pinned moment distribution  $\sim 2 \text{\AA}$  below the maximum for the rotatable moments. Here, the cut-off effect caused by the interface (chemical profile) is even more pronounced. Moreover the magneto-optical constants of the pinned moments show an unexpected behaviour: While one would expect a large absorptive part  $\beta_{\text{pinned}}$ , since the measurement is carried out at the maximum of the  $L_3$  edge, the simulation yields, on the contrary, a very large dispersive part  $\delta_{\text{pinned}}$  and only a small absorption. This effect might result from a modified shape and/or position of the magnetic spectra of the pinned Mn atoms as it is imposed for example by a change of the local chemical environment.

The coupling of the pinned moments is estimated by comparing the sign of the

magneto-optical constants to ferromagnetic metallic Mn reference data [92].

Fig. 5.16 shows in its centre the magneto-optical constants  $\delta$  and  $\beta$  for metallic ferromagnetic Mn obtained from the work of W. L. O'Brien and B. P. Tonner [92]. From the general shape of the XMCD curve, three different regions around the  $L_3$  edge can be identified:

- Before the  $L_3$  edge,  $\delta$  and  $\beta$  have different sign and either  $\beta$  is larger than  $\delta$  (very close to the  $L_3$ ) or they are of same magnitude. This region is marked green.
- Directly on the  $L_3$  (the maximum of the absorption),  $\beta$  is very large while  $\delta$  is zero or close to it. The region is marked red in the figure.
- Behind the  $L_3$  edge,  $\delta$  and  $\beta$  have the same sign and their relative strength varies from being equal (closer to the  $L_3$ ) to a large  $\delta$  and small  $\beta$  (right side of the marked region).

In the same figure, simulations are shown for all the four mentioned cases, before the  $L_3$  edge, on the  $L_3$ , and the two cases behind the  $L_3$  (closer and further afar). As can be seen, the sign and relative magnitude of the two parameters strongly affects the shape of the simulated curve and also its slope. The simulation and values of the graph marked *Case 4* are the final fit solution used in the discussion above (compare Fig. 5.15). Although the XMCD data is obtained for ferromagnetic Mn, the shape of the curve is of general character so it is justified to assume that the pinned Mn would yield similar relations for  $\delta$  and  $\beta$  (sign and relative magnitude). The fact that the pinned asymmetry fits to a spectra with negative XMCD at the  $L_3$  (thus  $\uparrow\uparrow > \uparrow\downarrow$ ) means that the pinned moments point along the positive field direction. According to the hysteresis of Fig. 5.14, this implies parallel coupling with respect to the Fe.

So the coupling of the pinned Mn moments is found to be parallel to the Fe, but antiparallel to the rotatable Mn which is compatible with the expected spin configuration of a-axis MnPd [91]. In contrast, antiparallel coupling has been reported in CoO and IrMn [100]. This might result from the different spin structure of these antiferromagnets compared to the one in MnPd or to the fact that the system investigated there has a perpendicular magnetisation.

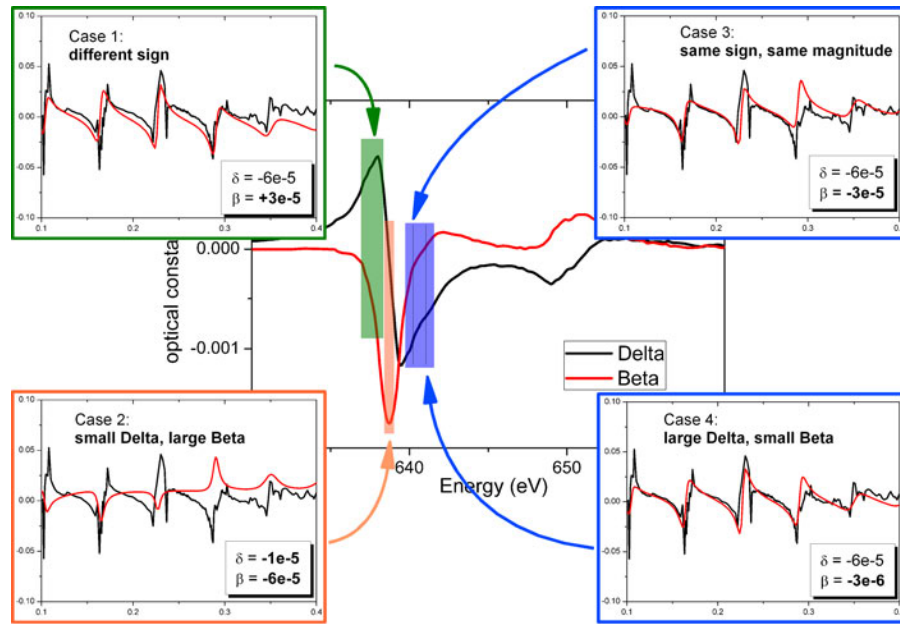
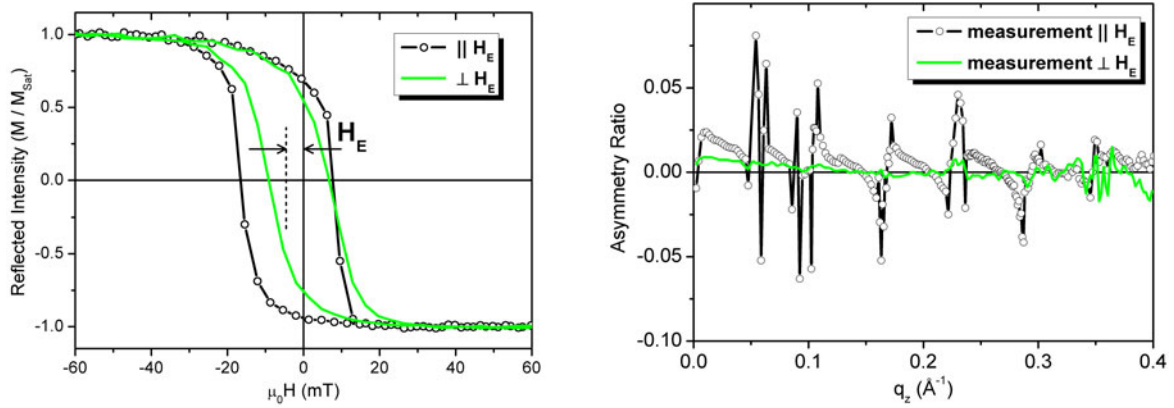


Figure 5.16: The graph in the middle shows the optical constants  $\delta$  and  $\beta$  of ferromagnetic Mn as obtained from literature [92]. Marked in the graph are the three regions corresponding to unique relations of  $\delta$  and  $\beta$ . The four graphs arranged around the centre represent simulations of the pinned asymmetry based on these different  $\delta$ - $\beta$  constellations. The black curve in each figure is the measured data.

The last topic of the investigation on the pinned and rotatable Mn moments in a-axis MnPd are the results of the angle dependent analysis. Exchange bias is a unidirectional effect which goes through a minimum when measuring perpendicular to the bias direction. Accordingly, the projections of the associated pinned moments along the beam direction should show a similar angular dependency. To verify the direct relationship of the pinned Mn moments identified here to the exchange bias, the sample has been rotated azimuthally by  $90^\circ$ . Then, an element selective hysteresis in reflection, similar to the one described above, has been measured at the Fe  $L_3$  edge ( $E = 707.2\text{ eV}$ ,  $\Theta = 11^\circ$ ) and the result is shown in Fig. 5.17(a) (green) along with the parallel reference hysteresis (red). A small remaining bias of  $H_E = -1.2\text{ mT}$  and a coercive field of  $H_C = 8\text{ mT}$  is found perpendicular to the direction of exchange bias.

Next, the magnetic reflectivity was measured for the same energy of  $639.5\text{ eV}$  at the Mn  $L_3$  edge maximum similar to the parallel measurement. The corresponding

pinned asymmetry is plotted in Fig. 5.17(b) as green solid line. As expected, the pinned asymmetry, i.e., the signal from the pinned uncompensated moments is strongly reduced. This result provides strong evidence for a direct relation between pinned asymmetry and exchange bias.



(a) Fe L<sub>3</sub> edge hysteresis parallel and perpendicular to  $H_{eb}$

(b) Corresponding pinned asymmetries parallel and perpendicular to  $H_{eb}$

Figure 5.17: The graph on the left shows two Fe hysteresis curves measured by XRMR at an energy of 707.2 eV and at an angle of incidence of  $\Theta = 11^\circ$ . The first hysteresis ( $\circ$ ) is measured along the field cooling, i.e., the exchange bias direction while the second one (green solid) is measured perpendicular to  $H_{eb}$ . As expected from the unidirectional character of exchange bias, the perpendicular curve exhibits nearly no loop shift compared to the first one. The right graph shows the two corresponding pinned asymmetries as calculated from the respective XRMR curves using equation (5.2). The pinned asymmetry measured perpendicular shows a strongly reduced signal providing evidence for the direct link between the pinned asymmetry and the loop shift  $H_{eb}$ .

### 5.1.9 Significance & Validity of XRMR of Localized Moments

On the last pages, a detailed discussion of the origin and location of localized moments in MnPd took place. An integral part of the discussion are the magneto-

optical profiles and their corresponding simulated asymmetry curves shown in Figs. 5.12 and 5.15. However, the significance of such results is often questioned with the point that a similar result might be obtained from e.g. a Gaussian with same area but less height. In the following we will investigate the effect of shape or position variations of the Gaussian on the simulated asymmetry curve in a systematic way. The investigation will be based on the above presented results for rotatable Mn moments in sample FD041 (Fig. 5.12).

For the first test, the position of the Gaussian distribution of the localized magnetic moments is varied. The distribution is shifted by  $-2 \text{ \AA}$ ,  $-4 \text{ \AA}$  and  $-6 \text{ \AA}$  while the shape of the curve is not changed at all. In Fig. 5.18(a) the corresponding shifted magneto-optical profiles are shown along with the original profile as reference and the optical profile which determines the position of the interface. The resulting simulated asymmetry curves for all four profiles, are shown in Fig. 5.18(b) along with the measured asymmetry. While the periodicity of the peaks is

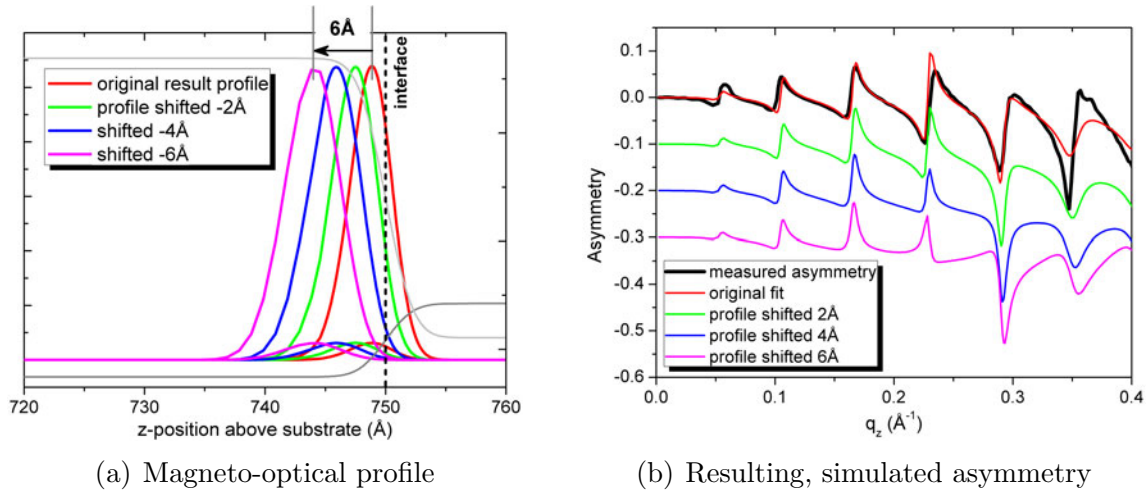


Figure 5.18: Simulated  $L_3$  edge asymmetries of the rotatable Mn moments in MnPd for variations of the magneto-optical profile (compare 5.12). The position of the profile is shifted in  $2 \text{ \AA}$  steps away from the interface and the asymmetry is calculated to illustrate the effect of such a change onto the asymmetry. The pronounced change of the shape between the peaks in the asymmetry for slightly shifted magneto-optical profiles clearly indicates the sensitivity of the method used here.

mostly unaffected, the slope in between changes drastically when shifting the distribution deeper into the MnPd. For the  $-6 \text{ \AA}$  the slope already starts to change its sign for higher  $q_z$  values.

For the second test, the Gaussian distribution is broadened and its height reduced. Again the magneto-optical profiles tested here along with the reference profile and the optical profile are shown in Fig. 5.19(a). Variation 1 has only half the height but a broader distribution compared to the reference profile. Variation 2 is only a quarter of the original height but four times its width and finally, variation 3 is half height but with a much broader distribution than variation 1. It has to be mentioned that the profiles are not shifted. The maximum changes position due to the cut-off effect at the interface which gets more severe for broader profiles. The corresponding simulated asymmetries are shown in Fig. 5.19(b). As

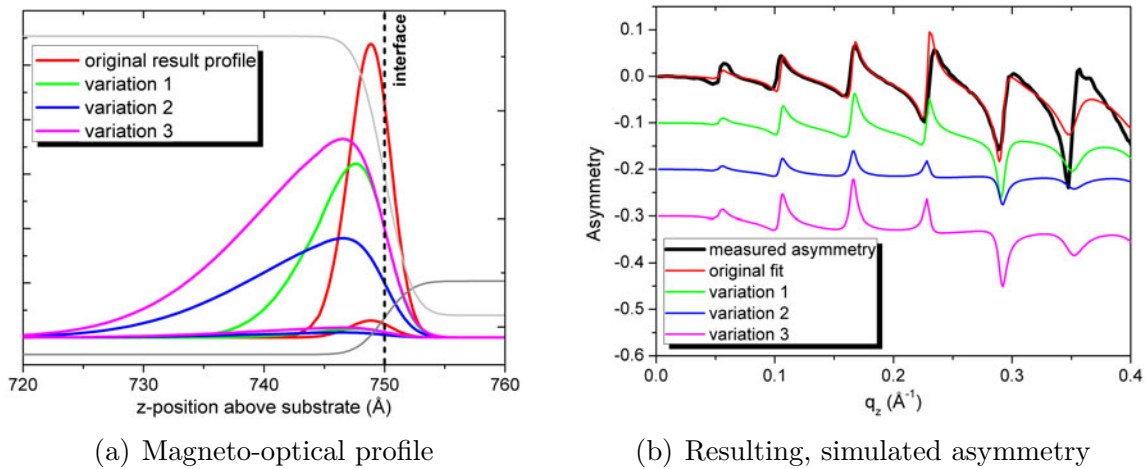


Figure 5.19: Simulated asymmetries for variations of the magneto-optical profile of the rotatable Mn to characterize the effect of a broadening of the distribution onto the resulting curve. The parameters were the same as described for Fig. 5.18. The asymmetry curve is extremely sensitive to small changes in the shape of the profile. Especially a broader but less high profile does not resemble the shape of the measured curve (black solid line).

can be seen, the slope between the peaks is again affected by the variations. But

in contrast to the shifted asymmetries from the previous test, the slope does not change sign. Moreover two effects can be observed here: As one would expect, a direct correlation exists between height of the profile and the amplitude of the peaks. At the same time the broadening only seems to flatten the curve between the peaks.

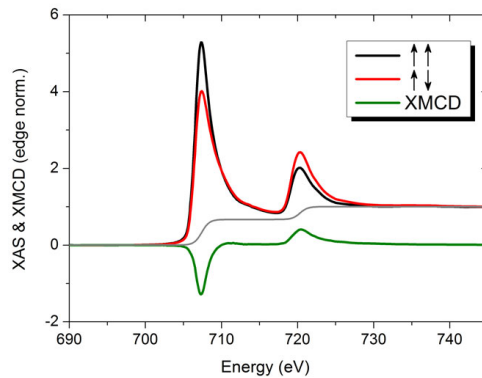
In conclusion already very small changes of the magneto-optical profile either in position and/or shape lead to significant characteristic changes of the resulting simulated asymmetry. Accordingly, the reliability and robustness of the fit solutions presented in the preceding section is very high.

#### 5.1.10 Fe NEXAFS for Samples FD041, 042 and 043

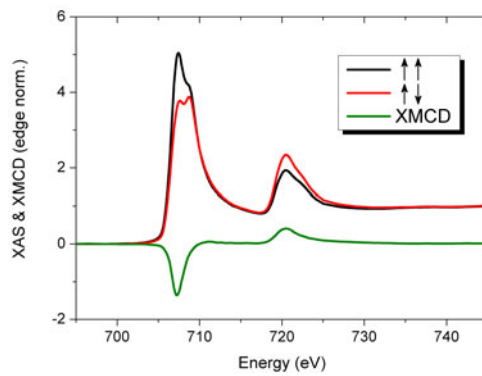
In the next sections the results from the c-axis samples FD042 and FD043 will be discussed and compared directly with the results from sample FD041 from the previous sections. The discussion will start by analyzing the different Fe XAS/XMCD results and then continue with the structural investigation. Eventually the different XRMR curves and corresponding asymmetries will be compared and discussed.

The XAS and XMCD of the Fe layers of the c-axis grown samples FD042 and FD043 were measured analogous to the spectra measured for sample FD041 (see [5.1.3](#)). Again, all measurements used positive circular polarized light and were repeated with negative helicity as control measurement. The spectra were measured in remanence in the same way like sample FD041 and as can be seen from the corresponding VSM hystereses in [Fig. 5.3](#), all three samples are sufficiently saturated for the remanence mode.

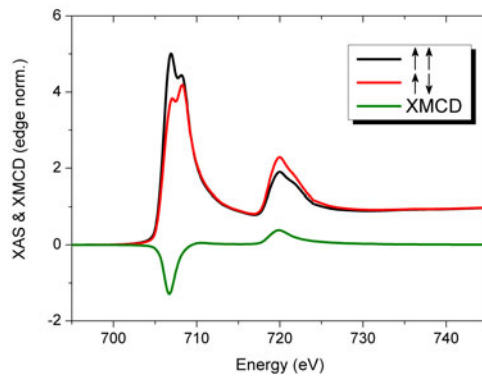
For better comparison of the three samples, the resulting XAS for both field directions (indicated by  $\uparrow\uparrow$  and  $\uparrow\downarrow$ ) as well as the XMCD difference signal are shown in [Figs. 5.20\(a\)](#), [5.20\(b\)](#), and [5.20\(c\)](#) for samples FD041, FD042, and FD043, respectively. Surprisingly the three spectra are not similar in shape but instead show clear differences in the XAS. The spectrum of sample FD041 corresponds in shape and magnitude well with reference data for metallic Fe as has already been discussed in [Section 5.1.3](#). In contrast, the spectra of FD042 and FD043 show



(a) FD041 - Fe XAS & XMCD measured with positive circular light



(b) FD042 - Fe XAS & XMCD measured with positive circular light



(c) FD043 - Fe XAS & XMCD measured with positive circular light

Figure 5.20: XAS and XMCD at the Fe  $L_{2,3}$  edge of samples FD041 (a-axis MnPd), FD042 (c-axis MnPd) and FD043 (c-axis MnPd) as measured by TEY at an angle of incidence of  $\Theta = +45^\circ$  with positive circular polarized X-rays.



a double peak structure at the  $L_3$  and also a shoulder and broadening of the  $L_2$ . The appearance of this second peak at 708.3 eV, which is roughly 1.4 eV above the metallic  $L_3$ , leads to a shift of the maximum of the  $L_3$  with respect to the maximal XMCD effect.

The second peak at the  $L_3$  edge is a clear fingerprint of oxidized iron [101, 102] which means that either  $\alpha - \text{Fe}_2\text{O}_3$  or  $\text{Fe}_3\text{O}_4$  is formed in the sample. However, the latter of the two possible oxide phases can be ruled out by analyzing the corresponding Fe XMCD curves for samples FD042 and FD043 which are shown in Figs. 5.20(b) and 5.20(c). The XMCD signal of the samples exhibiting a iron oxide contribution to the XAS shows no difference to the purely metallic XMCD of sample FD041. Since  $\text{Fe}_3\text{O}_4$ , or magnetite is a ferrimagnet it has a characteristic XMCD signal [103] which is not found in the XMCD spectra measured here. In conclusion, the iron oxide found in samples FD042 and FD043 has to be unmagnetic  $\alpha - \text{Fe}_2\text{O}_3$ . It is likely that the oxidation takes place at the upper interface of the Fe.

A possible reason for the oxidation is the higher growth temperature of samples FD042 and FD043 (325 °C and 290 °C) compared to FD041 (85 °C) in combination with the varying capping layer thickness. However, the fact that sample FD041 was also annealed after preparation for one hour at 250 °C without showing any significant oxidation, implies that the oxidation takes place during the growth process.

To quantify the magnetic spin and orbital moments of samples FD042 and FD043, XMCD sum rules (see equation (3.53) in Section 3.3.4) have been applied in the same way like for sample FD041. Again, the number of  $3d$  holes  $n_h$  is assumed to be  $n_h = 3.39$  [89] and the degree of circular polarization and the angle of incidence have been corrected. Spin and orbital moments of all three samples are given in table 5.3 along with reference data for (fcc) Fe [104, 105] and (bcc) Fe [89]. From the corresponding VSM hystereses, it is possible to correct the incomplete saturation caused by the remanent measurement mode (compare also 5.1.3). Sample FD042 is missing roughly 15% magnetisation to full saturation while sample FD043 only lacks 5% (remember, FD041 lacks  $\approx 15\%$ ). Taking this into account, the magnetic moment can be corrected and the values shown in

| Sample  | $m_{\text{orb}}/m_{\text{sp}}$ | $m_{\text{orb}}$ | $m_{\text{sp}}$ |
|---------|--------------------------------|------------------|-----------------|
| FD041   | 0.021                          | 0.041            | 1.98            |
| FD042   | 0.033                          | 0.060            | 1.84            |
| FD043   | 0.031                          | 0.049            | 1.61            |
| Fe(bcc) | 0.043                          | 0.085            | 1.98            |
| Fe(fcc) | -                              | -                | $\approx 1$     |

Table 5.3: Spin and orbital moments of FD041, FD042 and FD043 determined from XMCD sum rules.

Table 5.3 are obtained.

The reduction of the moment in sample FD042 and FD043 compared to FD041 can be ascribed to the occurrence of the iron oxide. Since the XMCD signal in both samples has the same magnitude and peak shape as in sample FD041, the increase in peak area at the  $L_3$  leads to a reduced moment when applying the sum rules. Assuming that the bulk magnetic moment of Fe is the same for all three samples and setting the escape length of the TEY electrons to 2 nm [81] it is possible to estimate the thickness of the oxidized region in the sample (compare Section 5.3.2) from the correction factor.

The TEY contribution for various thicknesses of a  $\text{Fe}_2\text{O}_3$  layer at the upper interface to the capping layer for the Fe film thickness discussed in the following section (93 Å for FD042 and 83 Å for FD043) has been determined. Then FD042 has a 4.8 Å thick layer of oxidized Fe while FD043 has 8.4 Å. Anticipating the roughness results from the XRR which are discussed in the next section a clear correlation of the oxidation layer and the interface roughness to the Pt capping layer is found from Fig. 5.21.

### 5.1.11 Chemical Profile of FD042 and FD043 Compared to FD041

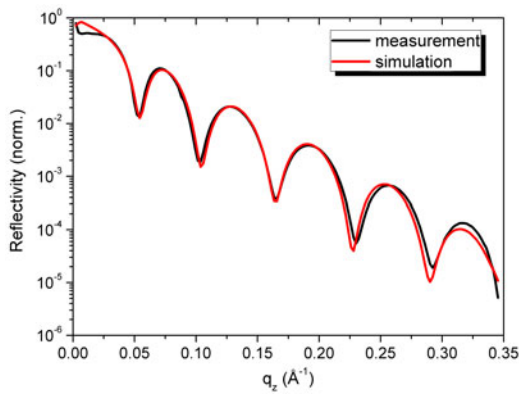
The chemical profile, i.e., the layer thicknesses and roughness is determined from non-magnetic X-ray reflectivity measurements using linear polarized light. All X-

ray reflectivity curves discussed in the following paragraph were measured during the May 2007 and November 2007 beamtimes at the UE56/2-PGM1 beamline at BESSY II. The as-measured raw curves were normalized to the  $I_0$  intensity reference signal (compare Section 6.1.3). Finally the curves were normalized to an initial intensity of  $I_{ref}(\Theta = 0^\circ) = 1$ .

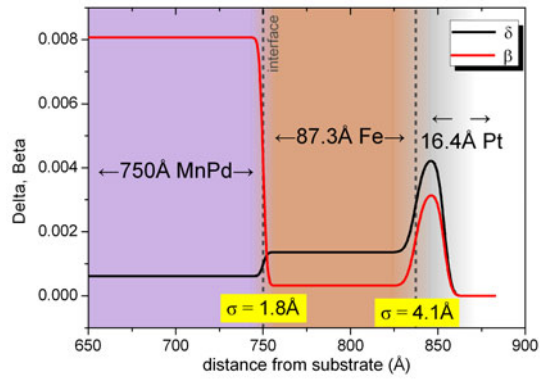
Using the simulation tool ReMagX and the optical constants derived in Section 5.1.3 and from the data in Section 5.1.10, the reflectivity curves are then simulated and the result is compared to the measurement.

In Fig. 5.21 the normalized reflectivity curves measured at the Mn  $L_3$  edge (639.5 eV) with linear polarized X-rays are shown as black solid line in 5.8(a) for FD041, 5.21(c) for FD042, and 5.21(e) for FD043. The associated best fit solution for each measurement is included in the same graph as red solid line. Corresponding optical, i.e., chemical profiles of the best fit solution are shown on the right in Figs. 5.8(b), 5.21(d), and 5.21(f) for FD041, FD042, and FD043, respectively. Although the samples nominally should have the same thickness the found reflectivity curves vary considerably. While FD041 and FD043 show pronounced oscillations they are damped in sample FD042. These oscillations originate from the interference of X-rays reflected from the surface and from the interface between Fe and MnPd, because the interfaces vacuum/sample and Fe/MnPd exhibit the largest changes of the optical constants. When measuring on the resonance of the Mn L edge,  $\beta$  is very large. Accordingly the wavelength of the oscillations correlates with the thickness of the Fe and Pt layers together. The damping of the oscillations is related to the quality of the involved interfaces. Sharp interfaces at the Fe/MnPd interface and the Pt capping layer as is the case in sample FD041 lead to very pronounced oscillations and a large reflectance of the sample. Sample FD042 has a very rough interface between Fe and MnPd which causes a strong damping of the oscillations because the interference with the beam reflected from the surface is distorted. On the other hand FD043 has a slightly sharper interface at the MnPd which immediately restores the oscillations. Nevertheless due to the rough interface compared with sample FD041, the reflected intensity decreases faster in FD043.

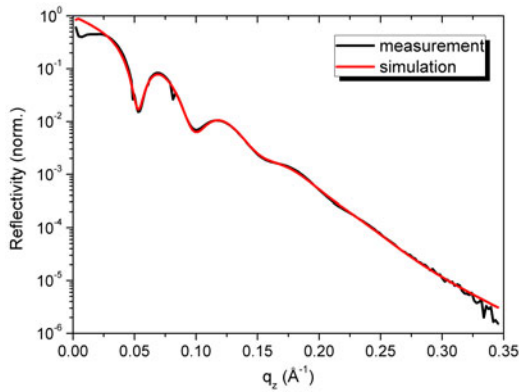
The fit results (red solid lines) are in very good agreement with the measured



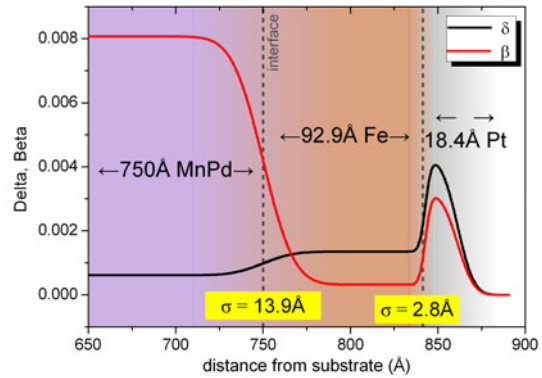
(a) FD041 Reflectivity



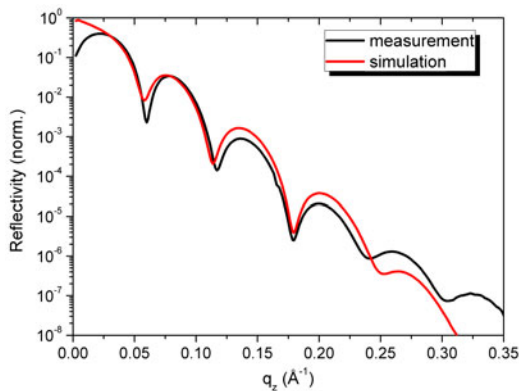
(b) FD041 Optical Profile



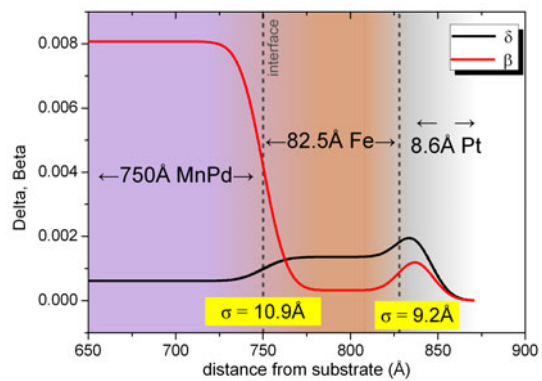
(c) FD042 Reflectivity



(d) FD042 Optical Profile



(e) FD043 Reflectivity



(f) FD043 Optical Profile

Figure 5.21: Resonant reflectivity curves measured at the Mn  $L_3$  edge at an energy of 639.5 eV and the corresponding fit results (red curve) The right column shows the associated optical, i.e., chemical profile.

data. Only for very small and very large angles, a larger discrepancy is visible for all samples which is related to systematic errors. For angles close to  $0^\circ$ , incomplete illumination of the sample leads to a reduction of reflected intensity. For large angles, the signal to noise ratio decreases and the diffuse background increases leading to a poor quality of data. Therefore for the fitting procedure only values in the range from  $q_z = 0.03 \text{ \AA}^{-1}$  to  $q_z = 0.3 \text{ \AA}^{-1}$  have been used.

### 5.1.12 Effect of the Interfacial Roughness on the Reflectance

Before continuing with the general course of the discussion, it is worth investigating the correlation of interfacial roughness and reflectance in more detail. Therefore a series of simulated reflectivity curves based on the optical profile of sample FD043 (see Fig. 5.21(f)) have been calculated for varying roughness of the interface Fe/MnPD. In the original fit result,  $\sigma_{RMS}$  is found to be  $10.9 \text{ \AA}$ . Now the reflectivity curve for an interface roughness of  $\sigma_{RMS} = 14 \text{ \AA}$ ,  $12 \text{ \AA}$ ,  $8 \text{ \AA}$  and  $6 \text{ \AA}$  has been calculated as well. Fig. 5.22 shows the reflectivity curves of all five roughness values. The roughest interface with  $\sigma_{RMS} = 14 \text{ \AA}$  leads to a reflectivity

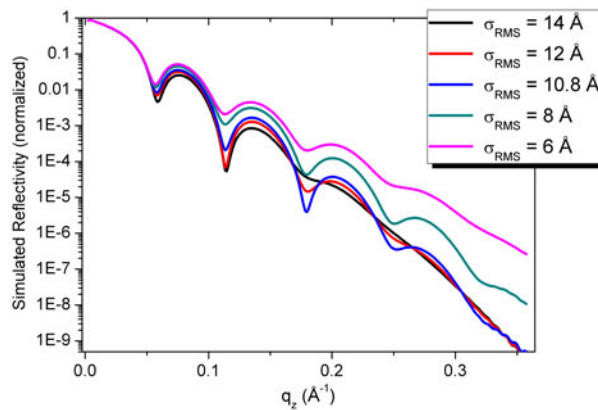


Figure 5.22: Effect of the Fe/MnPD interface roughness on the simulated reflectivity of sample FD043.

curve (black) with nearly no oscillations for larger  $q_z$  values. However, the damping is very sensitive to the roughness and already the  $\sigma_{RMS} = 12 \text{ \AA}$  curve (red)

has significant oscillations. For smaller values of  $\sigma_{RMS}$ , the curve starts to move up because the overall reflection increases due to the mirror like sharp interface. Note that the suppression of the oscillations for very smooth interfaces (especially for the  $\sigma_{RMS} = 6 \text{ \AA}$ ) is related to the roughness of the Pt layer which affects the interference condition.

Now, the reflectivity curves of samples FD041, FD042 and FD043 together with their respective interface profiles will be compared to each other checking whether the above systematics are reflected in the curves. Fig. 5.23(a) shows

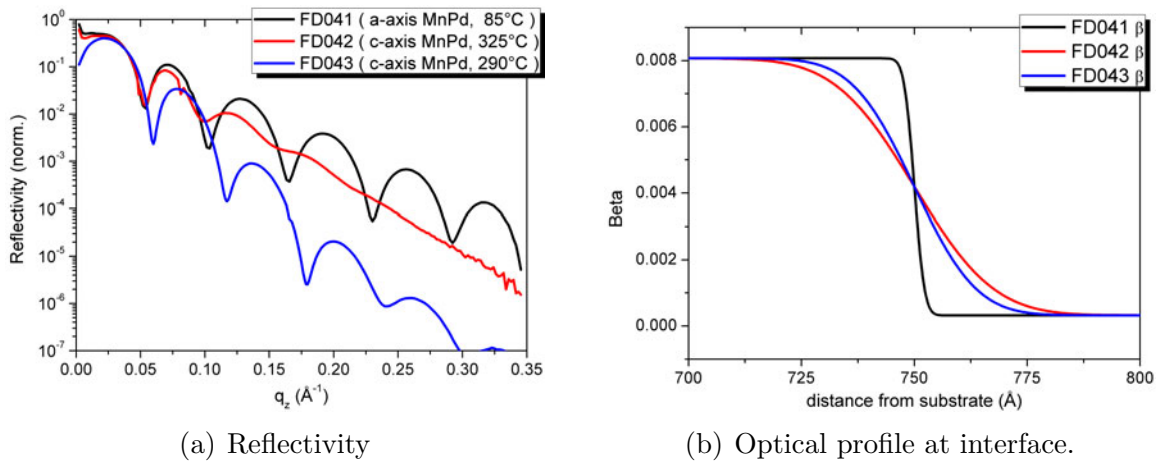


Figure 5.23: Direct comparison of the Mn  $L_3$  edge ( $E = 639.5 \text{ eV}$ ) reflectivity of all three samples and the corresponding optical profile at the Fe/MnPd interface.

the three different reflectivity curves and Fig. 5.23(b) the corresponding optical density profiles at the Fe/MnPd interface plotted together for a better comparison. Obviously the curves perfectly correspond in overall decrease, i.e., absorption as well as the damping of the oscillation with the above derived systematics for such a sample and energy. However, it has to be pointed out that the high overall reflectance of sample FD042 is related to the very smooth surface and not to the properties of the Fe/MnPd interface.

### 5.1.13 FD042 & FD043 – Magnetic Reflectivity of Manganese

As next step, the investigation of the magnetic reflectivity signal, the asymmetry, shall be conducted for samples FD042 and FD043. The considerations about the influence of interfacial roughness on the spectrum already imply that a difference can be expected for the spectra of FD042 and FD043 compared to FD041.

The magnetic reflectivity has been measured in the same way as described for sample FD041 (see Section 5.1.5) during the May 2007 beamtime (for FD042) and the November 2007 beamtime for FD043. The asymmetry ratio has been calculated using equation (5.1) for the measurements using positive circular X-rays. In Fig. 5.24, the asymmetry originating from the rotatable Mn moments in sample FD042 and FD043 are plotted along with the already shown result of sample FD041. As can be seen, both asymmetries of the c-axis samples are strongly

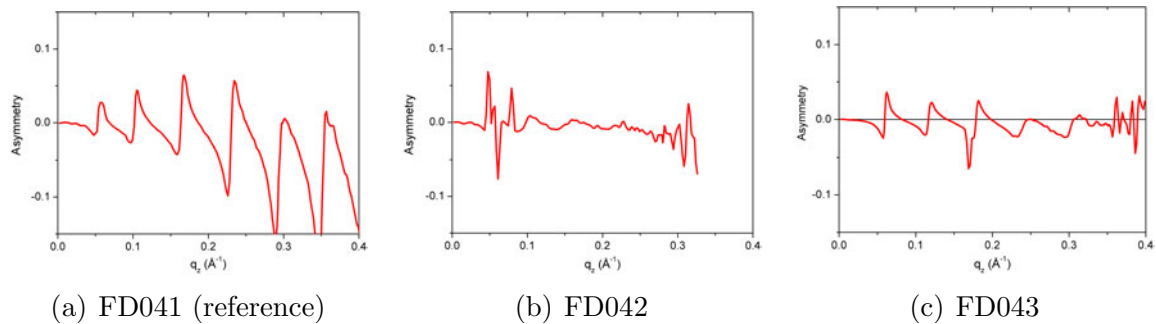


Figure 5.24: Asymmetry ratio from the rotatable Mn moments in samples FD041, FS42 and FD043 measured at the Mn  $L_3$  edge ( $E = 639.5$  eV) using positive circular light.

damped compared to FD041. In fact, the asymmetry shows the same general behaviour as the normal reflectance, the roughness damps away the interference oscillations. Since the oscillations in the asymmetry originate from the interference at the interface and its change due to the magnetic effect, that was expectable. But besides the pure interference, the interface roughness also leads to an overall damping of the effect as can be seen from the systematic investigation of the

asymmetry of sample FD041 shown in Fig. 5.19. The broadening of the localized moment in Fig. 5.19 corresponds precisely to the effect of a rougher interface. This also explains why sample FD043 shows a smaller effect although the interference pattern of the reflectivity is quite dominant.

When trying to fit the measured asymmetry it turns out to be nearly impossible for sample FD042 and very difficult for sample FD043. The pinned asymmetry is far worse in both samples very likely due to the broadened distribution of moments.

#### 5.1.14 Conclusions for MnPd

Several important results for exchange bias can be derived from the precise mapping of the magnetic configuration at the interface between ferromagnetic Fe and antiferromagnetic MnPd.

Mn atoms at the interface with the Fe are affected by the presence of a ferromagnetic coupling in their next neighborhood while the influence from their own antiferromagnetic spin lattice is weakened. As a result the Mn atoms at the interface rather couple to the ferromagnet than the antiferromagnetic spin lattice depending on the local coupling environment. This is a very important result especially in the light of the spin glass model presented in Section 3.2.3. The interfacial Mn is a frustrated spin system which determines its behaviour from its local coupling environment which is not necessarily mostly antiferromagnetic and thus can be interpreted as a spin glass state. This result is stressed by the fact that for a smooth sample like FD041, the area which exhibits induced ferromagnetism or rotatable Mn moments is confined directly to the interface and correlates with the interface roughness.

Anticipating the results from the upcoming sections where the existence of rotatable moments is also reported for the metallic antiferromagnet FeMn (see 5.2) and oxidic NiCoO (see 5.3), a general character of the frustration of antiferromagnetic moments close to the interface with a ferromagnet seems likely. This is further stressed by the fact that the same has been observed in all exchange bias systems investigated by similar techniques so far [31, 34].



Moreover the existence of pinned uncompensated manganese moments has been confirmed for the a-axis grown sample FD041. The precise location of this pinned moments is a broad region of  $(13 \pm 1)$  Å close to the interface with the ferromagnet. It is noteworthy that the pinned moments seem to be located slightly below the rotatable ones although the difference is too small to give a definite answer. Anyway it is an important finding that the pinned uncompensated moments which are responsible for the exchange bias in the system are only present close to the interface. The direct correlation of the pinned moments in the MnPd and the exchange bias loop shift has been proven by investigating the azimuthal dependence in the system.

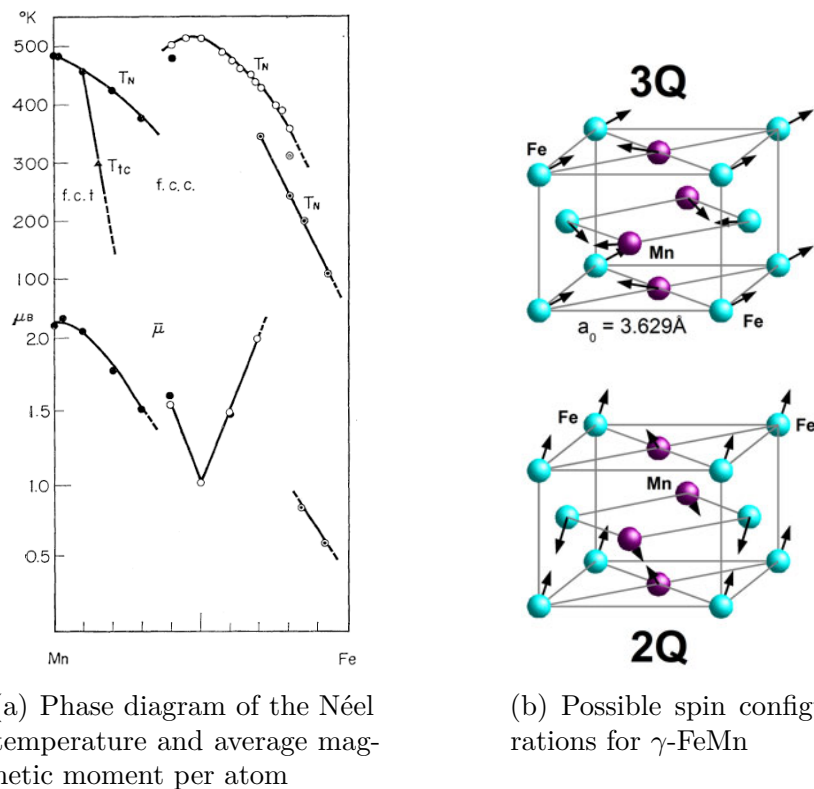
## 5.2 Orbital Moments in FeMn and Their Role for Exchange Bias

Although the precise magnetic map of the interface derived from the MnPd investigation is a big leap forward in the understanding of exchange bias, a quantitative information about the coupling on a microscopic scale is still missing. Therefore, a second exchange bias system was investigated in the framework of this thesis, FeMn/Co. The big advantage of the combination FeMn as antiferromagnet and Co as ferromagnet is, that unlike in the NiCoO/Co system discussed in Section 5.3 the element selectivity of XMCD can be fully deployed and in contrast to MnPd both elements of the antiferromagnet have their magnetic active L edges in the very sensitive soft X-ray regime.

Iron manganese (FeMn) in the  $\gamma$ -phase is an antiferromagnetic alloy with face-centered-cubic (fcc) crystal structure [106]. From neutron diffraction studies on polycrystalline powder samples, the bulk Néel temperature  $T_N$  and also the average magnetic moment per atom has been derived [107] and the corresponding phase diagram is shown in Fig. 5.25(a).

Especially the 50:50 composition of FeMn has been used extensively in exchange bias systems. One of the advantages of FeMn is its relatively high Néel temperature (compare Fig. 5.25(a)) which allows room temperature exchange bias and maybe even more important, exchange bias systems with FeMn exhibit the largest interfacial coupling strength  $J_{eb}$  of all metallic antiferromagnets [22]. Another point is that FeMn can be grown by standard techniques such as sputtering and MBE and that growth of the  $\gamma$ -phase can be accomplished rather easily on a variety of substrates by using adequate buffer layers.

For the following investigation of the magnetic configuration of the antiferromagnets interface, it is important to know the spin structure of the antiferromagnet. Early neutron diffraction studies of the ternary alloy Fe-Ni-Mn [109] already showed that the spin structure of a system with  $\gamma$ -Mn, thus fcc Mn, has a broad variety of possible spin structures.  $\gamma$ -FeMn has three stable antiferromagnetic spin configurations at room temperature [106, 107] of which the ones termed 3Q and 2Q seem to be the ground state configurations [110]. Although the former of the



(a) Phase diagram of the Néel temperature and average magnetic moment per atom

(b) Possible spin configurations for  $\gamma$ -FeMn

Figure 5.25: The left figure shows the Néel temperature  $T_N$  (K) and average magnetic moment per atom ( $\mu_B/\text{atom}$ ) depending on the composition of FeMn. It shows that the 50:50 composition exhibits the highest anti-ferromagnetic ordering temperature and at the same time the smallest magnetic moment per atom (The image is reproduced from [107]). On the right, Fig. 5.25(b) shows the cubic fcc crystal structure [107] of  $\gamma$ -Fe<sub>50</sub>Mn<sub>50</sub>, the chemical order [108] and its antiferromagnetic 2Q and 3Q configurations [106].

two has a slightly lower energy, the difference is so small that both may coexist at room temperature. It has to be mentioned that an influence of the exchange coupling to the ferromagnet might also react upon the stability of the different spin configurations and lead to a new energetic ground state [111]. For the time being it is assumed that the spin configuration of  $\gamma$ -FeMn corresponds to one of the two structures depicted in Fig. 5.25(b).

The investigation of the NiCoO/Co sample and the problems encountered for the XRMR experiments clearly shows the necessity of a properly designed sample system. A good XRMR sample has to comply with several requirements and since

these requirements are of general character it is useful to review them briefly:

- it should be possible to prepare samples of adequate size, i.e., for ERNSt  $5 \text{ mm} < \text{sample} < 10 \text{ mm}$ ;
- the layer stack should be simple;
- absorption spectroscopy (TEY) of all layers should be possible. The best way to realize this is by using several samples of identical material such as Co/FeMn/NiFe/Pt-capping & Co/FeMn/Pt-capping & Co/Pt-capping;
- the substrate should be flat (especially metals are often convex);
- the optical properties of the layers should differ sufficiently;
- layers should not be too thick, i.e., absorption too high especially of the topmost layer.

Based on these aspects, sputtering was chosen for the preparation since it allows preparing several samples simultaneously in a short time. A set of sputtering targets, especially a good Fe<sub>50</sub>Mn<sub>50</sub> alloy target, were already available from a previous investigation of FeMn by M. Harlander [67]. Si from a standard, commercially bought wafer was chosen as substrate material. By cutting the wafer, substrates of arbitrary size and form are available. Needless to say that Si wafers of course fulfill the requirements for flatness and surface roughness.

To promote growth of  $\gamma$ -FeMn, the lattice misfit between the underlying material and fcc FeMn must not be too large. Fe<sub>50</sub>Mn<sub>50</sub> has in its fcc phase a lattice constant of  $a = 3.629 \text{ \AA}$  [107] while Si (100) has a lattice parameter of  $5.43 \text{ \AA}$  which corresponds to a lattice misfit of more than 66 %. On the other hand, untreated Si substrates always have a  $20 - 30 \text{ \AA}$  thick layer of amorphous SiO<sub>2</sub>. Hence in both cases, cleaned and oxidized Si, a buffer layer is necessary. Here, a Cu buffer layer is used to provide a fcc lattice [112–114] with matching lattice parameter allowing a pseudo-epitaxial growth of  $\gamma$ -FeMn. Pseudo-epitaxial means that FeMn grows only on the individual Cu grain epitaxially, and not correlated on larger scales. It should be noted that all films were covered with an aluminium layer of  $15 - 20 \text{ \AA}$  which is enough to prevent oxidation [115, 116] More details about the growth of metallic films and possible buffer layer systems can be found in Westmacott et al. [113].

A systematic investigation of the sample parameters is necessary prior to the XRMR investigation to be able comparing the results here to the work of other groups and to gain experience in preparing FeMn/Co exchange bias systems with tailored properties. In collaboration with A. Köhl, a series of FeMn/Co samples with varying FeMn thicknesses was prepared and then characterized by SQUID magnetometry. Goal was to derive a precise knowledge of the stability, i.e., temperature dependence of the antiferromagnetic spin lattice in FeMn. A detailed description can be found in the bachelor thesis by A. Köhl [117].

Summarizing the result of the investigation it can be concluded that the samples prepared here are polycrystalline films where FeMn and presumably also Co have a fcc structure and grow pseudo-epitaxially on each other. The temperature behaviour of  $H_{eb}$  and  $H_C$  as well as the observed crystallite sizes are comparable to bilayer systems [118, 119] and trilayers [120] of polycrystalline FeMn/Co investigated by other groups.

### 5.2.1 Preparation

All samples were prepared by ion-assisted RF sputtering. Therefore, argon is ionized by irradiation with an electromagnetic wave in the radio frequency (RF) regime and the resulting  $\text{Ar}^+$  ions are accelerated onto the respective target by a voltage of 1 kV. The targets are mounted on a rotatable cube which allows rapid in-situ changes of up to four targets. The growth is monitored by an oscillating quartz which is mounted beside the sample. Fig. 5.26 shows a schematics of the sputtering device used for preparing the samples investigated here.

The average deposition rate under working conditions is roughly  $1 \text{ \AA/s}$  and the Ar partial pressure is  $1 \cdot 10^{-4}$  mbar during growth. Note that the base pressure of the chamber is typically better than  $5 \cdot 10^{-8}$  mbar. Prior to the preparation, the Si substrates were cleaned in Acetone and Isopropanol using ultra-sonics to remove dust and other particles from the surface.

To induce a well defined exchange bias in the as-grown films, a magnetic field is applied during growth. Two high-performance SmCo permanent magnets <sup>1</sup> are

---

<sup>1</sup>SmCo<sub>5</sub>/Sm<sub>2</sub>Co<sub>17</sub> magnet from ChenYang Technologies GmbH & Co. KG

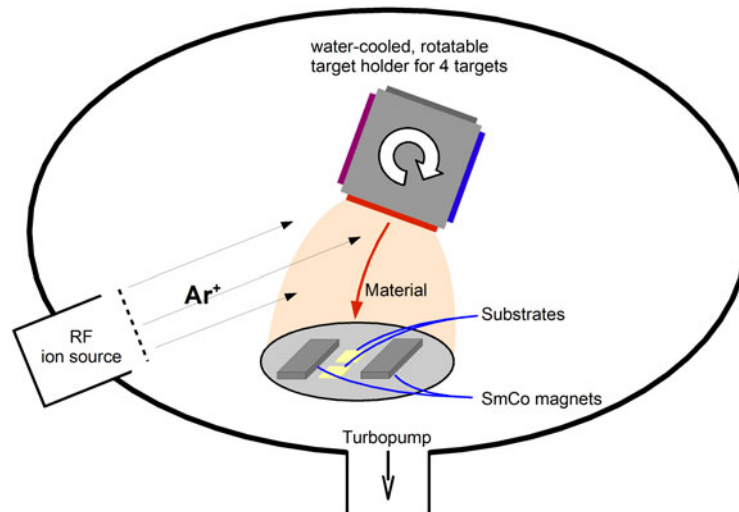


Figure 5.26: Schematic drawing of the sputtering setup used to prepare the FeMn/Co samples.

positioned on the sputtering stage to provide an in-plane field of  $\sim 170$  mT in the gap between them. The substrates are then placed in the gap as is shown by the photograph 5.27 and the chamber is evacuated for the sputtering process.

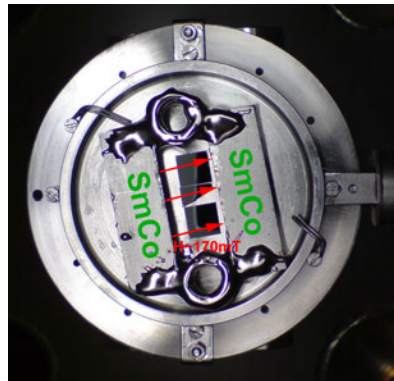


Figure 5.27: Photograph of a set of three substrates located on the sample holder in the sputter chamber directly after depositing the film. The two SmCo permanent magnets provide a field of  $\sim 170$  mT, which induces a well defined unidirectional anisotropy in the as-grown film.

As already mentioned, a series of samples has been prepared to characterize the

systematics of the FeMn/Co films produced in this way.

The nominal thicknesses, which is the thickness according to the sputter time and rate during preparation of the samples relevant for the present thesis are given in table 5.4.

|                                   | SP021 | SP032 | SP036  |
|-----------------------------------|-------|-------|--------|
| Al                                | 15 Å  | 15 Å  | 20 Å   |
| Co                                | 60 Å  | 60 Å  | 100 Å  |
| Fe <sub>50</sub> Mn <sub>50</sub> | 100 Å | 50 Å  | 100 Å  |
| Cu                                | 100 Å | 100 Å | 1000 Å |
| substrate                         |       |       |        |

Table 5.4: Nominal, i.e., from the sputter growth process expected thicknesses of samples SP021, SP032 & SP036.

### 5.2.2 TEM Investigation

To characterize the structural properties of the prepared samples, a high resolution transmission electron microscopy study has been carried out. The sample investigated has a Co layer of 60 Å and a FeMn layer of 100 Å. Although the thickness differs slightly from the samples investigated later by XRMR, some basic conclusions can be derived from such an investigation. Fig. 5.28 shows the hi-res TEM image of the FeMn/Co sample along with a sketch of its nominal composition and the results from three exemplary EDX scans of the sample. The TEM image, 5.28(a), reveals a polycrystalline structure with crystallites (marked red) with an average size of  $\sim 100$  Å. No difference occurs for the individual layers. Only the native SiO<sub>2</sub> oxide layer of the Si substrate can easily be identified. The reason is the small difference in atomic mass of the other atoms. Cu, Co, Fe, and Mn are all neighbors in the periodic system of elements and their atomic mass only varies slightly which means they have more or less the same contrast in TEM. Moreover from the crystalline character of the individual crystallites it can be assumed that

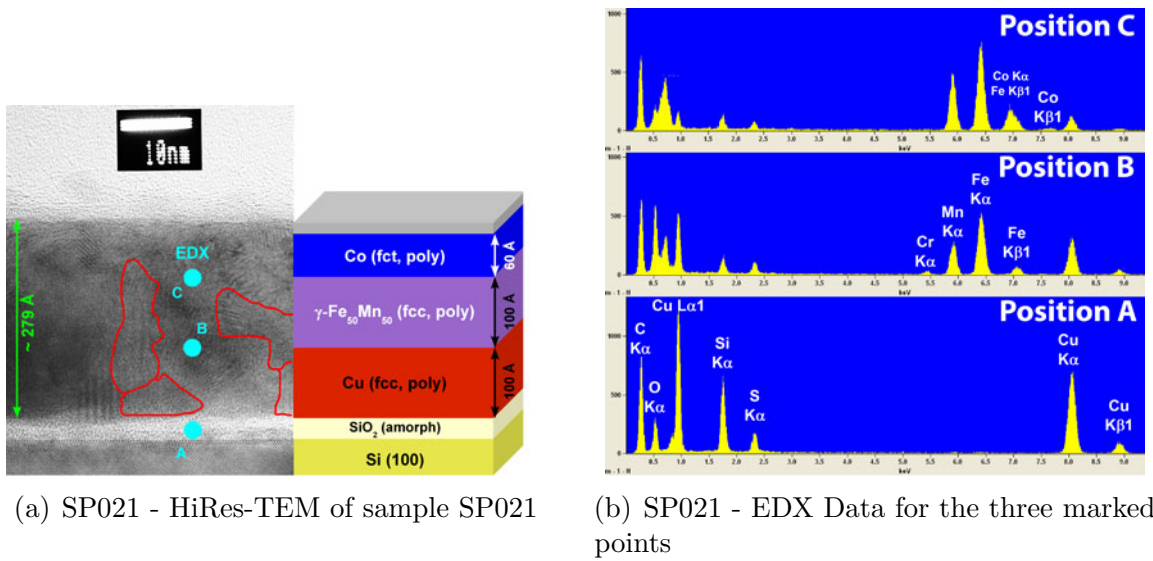


Figure 5.28: Results from a TEM investigation of the precursor sample SP021 which is grown under the same conditions like the other samples investigated here but with slightly varying layer thickness.

a pseudo-epitaxial growth takes place which means that for each crystallite the individual layers grow epitaxial. As will be shown later, all samples investigated here show an exchange bias which means that the FeMn has to be in the antiferromagnetic  $\gamma$  phase. This phase has a face-centred cubic structure and the Co which is then deposited on top adopts this structure and forms a face-centred tetragonal structure [112]. To overcome the problem of a missing contrast for the individual layers, energy dispersive X-ray spectroscopy (EDX) has been carried out during the TEM investigation. EDX measures the characteristic fluorescence light emitted from the atoms in the sample. By focusing the electrons to a spot it is then possible to characterize the composition in that area. In Fig. 5.28(a), three blue dots mark the positions and also sizes of the electron beam during the EDX scans. The resulting spectra are shown in Fig. 5.28(b). The EDX spectra correspond to the expected layer structure of the sample.

From the TEM image it can be concluded that the FeMn and the Co are both polycrystalline with a crystallite size on the order of  $\sim 100 \text{ \AA}$  which is in good agreement with literature values for FeMn [119]. Moreover the crystallites reach through several layers suggesting a pseudo-epitaxial growth of FeMn on the Cu



and also of the Co on the FeMn.

### 5.2.3 Magnetometry

To characterize the exchange bias which will later be discussed with respect to pinned uncompensated moments, temperature and orientation dependent SQUID hysteresis loops have been measured of the samples. To prevent damage to the surfaces during the SQUID measurements, a duplicate sample was used for this investigation. As already mentioned, up to three substrates were used during a preparation run in the sputtering device (compare Fig. 5.27) thus providing several substrates with the same thin film sample on top. First the temperature dependence of the exchange bias in sample SP032 will be investigated. The second part presents an investigation of the room temperature exchange bias in sample SP036 in dependence on the azimuthal orientation. Both investigations are chosen according to their relevance for the XRMR study discussed in Sections 5.2.7 and 5.2.8.

The antiferromagnet of sample SP032 is only 50 Å thick. As a consequence its blocking temperature (compare Section 3.2.4) is significantly decreased [112] and the sample shows no hysteresis loop shift at room temperature [117]. To characterize the temperature dependence of the exchange bias in sample SP032, the sample was field cooled in an external field of +100 mT to a temperature of 50 K. Then three hysteresis loops were measured in a row. It is necessary to measure several loops to get rid of any training in the sample (compare 3.2.4). Subsequently the sample was heated up to 300 K and again three loops were measured. Fig. 5.29 shows the third hysteresis loop measured for 50 and 300 K, respectively. The room temperature hysteresis loop of sample SP032 has a coercive field of  $H_C = 3.8$  mT and does not show any loop shift. In contrast the 50 K loop is shifted by  $H_{eb} = -29.3$  mT while having a slightly increased coercive field of  $H_C = 5.8$  mT. In order to normalize the measured magnetic saturation moment to the number of ferromagnetic atoms, which in the first approximation is only the cobalt in the sample, the volume of the film has to be determined from its mass. Therefore the sample is first weighted using a Metler TOLEDO AX105 Delta Range precision balance which yields a mass of 58.3 mg for sample SP032. Next,

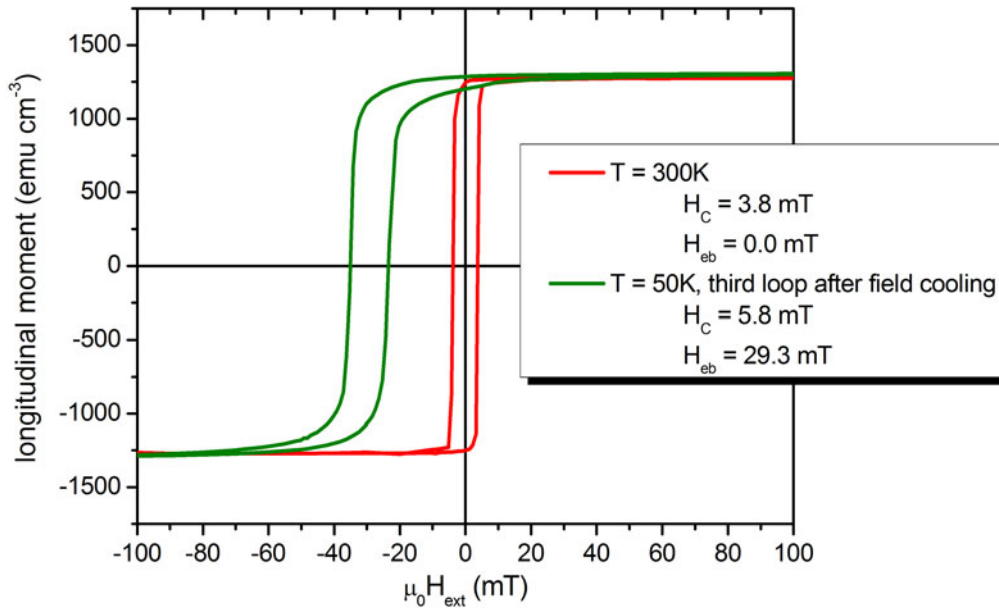


Figure 5.29: Magnetic hysteresis loops measured at 50 K and at 300 K after field cooling the sample from room temperature to 50 K in an external magnetic field of 500 mT. Several subsequent hysteresis have been measured and the last one is shown here to avoid training. The room temperature hysteresis is measured after subsequently heating the sample up to RT.

the thickness is measured using a Mahr Millitron 1501 IC which gives  $531.0 \mu\text{m}$ . Since the deposited film is negligible thin compared to the thickness of the Si substrate, the area of the substrate and thus the film can be calculated from this information using the density of Si. That is made possible by the used Si substrate which is prepared from a standard wafer exhibiting a very homogeneous thickness and an extremely flat surface. The formula to calculate the surface area of the substrate and thus the film is then given by:

$$A = \frac{m}{d_{Si} \rho_{Si}} = \frac{58.3 \cdot 10^{-6} \text{ kg}}{531 \cdot 10^{-6} \text{ m} \cdot 2330 \text{ kg/m}^3} = 0.4712139 \text{ cm}^2 \quad (5.3)$$

Using the nominal thickness of the cobalt layer of  $60 \text{ \AA}$ , the hysteresis can be easily normalized to  $[\text{emu cm}^{-3}]$  as is done for Fig. 5.29.

The formula to calculate the magnetic moment per atom in Bohr magneton is then readily derived making use of the conversion for  $\mu_B$  to the SI system:

$1 \mu_B = 9.274009 \cdot 10^{-24} \text{J/T} = 9.274009 \cdot 10^{-24} \text{Am}^2$  and the one for emu to the SI system:  $1 \text{ emu} = 10^{-3} \text{Am}^2$ . Further using the relation for the atomic number density  $\rho_a$  introduced in Section 4.2 (see equation (4.7)) the formula to calculate the moment per atom starting from  $[\text{emu cm}^{-3}]$  reads:

$$\frac{M_{Sat} [\text{emu/cm}^3]}{\rho_a [\text{atoms/cm}^3]} \cdot \frac{1}{9.274009 \cdot 10^{-21} [\text{emu}/\mu_B]} = \frac{\mu_B}{\text{atom}} \quad (5.4)$$

The atomic number density of cobalt is given by  $\rho_a = N_A/A\rho$  with the atomic weight  $A = 58.93 \text{ g mol}^{-1}$ , the Avogadro constant  $N_A$  and the standard mass density of Co of  $\rho = 8.90 \text{ g cm}^{-3}$ . A magnetic moment of  $1.51 \mu_B$  per cobalt atom at 300 K and  $1.55 \mu_B/\text{Co}$  at 50 K is found by applying equation (5.4) to the data in Fig. 5.29. These values are reduced compared to the bulk value of Co of  $1.7 \mu_B/\text{Co}$  (see [11, 89] and references therein). The discussion of possible reasons for this will be carried out in the following section taking into account the results from the XMCD data.

The second part of the section deals with the magnetometry of sample SP036, the sample with 100 Å FeMn. At this thickness the blocking temperature of the FeMn film is considerably above room temperature (compare [117]). This sample was investigated with respect to its in-plane angular dependence of the exchange bias (compare Section 3.2.1). Accordingly the hysteresis was measured in-plane along the exchange bias direction and perpendicular to it. Fig. 5.30 shows the room temperature hystereses for both orientations. For the measurement parallel to the exchange bias direction, i.e., the direction of the external field during the growth process (see 5.2.1), the sample shows a moderate exchange bias of  $H_{eb} = +4.5 \text{ mT}$  and a coercive field of  $H_C = 2 \text{ mT}$ . Compared to literature data [117, 119], the exchange bias is small. This might be related to the fact that the bias was not induced by a field cooling process as in case of sample SP032 (compare above) but instead originates from the alignment of the magnetic moment during the growth process. Either this method is in general, or with the given field of  $\sim 170 \text{ mT}$  not sufficient to fully align all moments.

The hysteresis measured perpendicular to the exchange bias direction, i.e.,  $90^\circ$  with respect to the magnetic field during the growth process has a very rounded

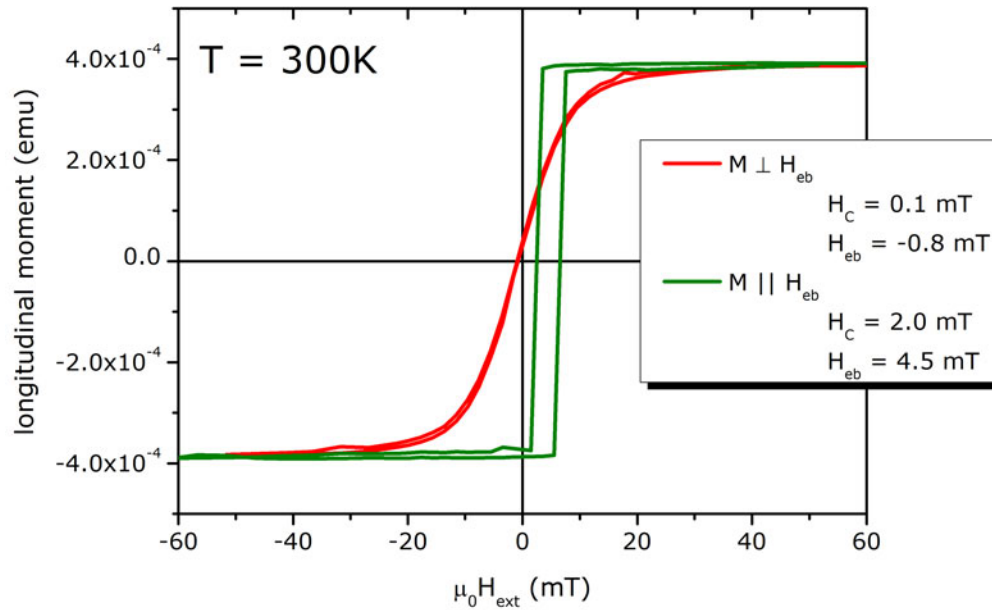


Figure 5.30: Magnetic hysteresis loops of sample SP036 (100 Å FeMn) measured in-plane parallel (green) and perpendicular (red) to the exchange bias direction. Both hystereses were measured at 300 K.

shape. It exhibits nearly no coercivity with  $H_C = 0.1$  mT and the loop is only slightly shifted by  $H_{\text{eb}} = -0.8$  mT. It should be noted that 0.8 mT is below the resolution limit of the x-axis of the SQUID.

#### 5.2.4 Co XAS and XMCD of Sample SP032

X-ray absorption spectra in TEY and TFY mode were measured to investigate the chemical state and XMCD effect of all three elements, Co, Fe, and Mn. These measurements also provide the necessary absorption reference for the optical and magneto-optical constants.

The measurements of the Co absorption and XMCD were carried out in May 2008 at the WERA beamline at the ANKA synchrotron in Karlsruhe using the groups own dedicated XMCD experiment which is described in detail in reference [80]. X-ray absorption spectra were measured using circular polarized X-rays with a degree of circular polarization of 81% (slit +1.8 mm and -1.8 mm). The angle of incidence was set to  $\Theta \sim 45^\circ$  and a magnetic field of 141 mT (projected in-plane component). Dichroic spectra were measured by flipping the applied

magnetic field at every energy value for positive circular polarized light and the measurement was subsequently repeated for negative helicity. The resulting XAS and the corresponding XMCD curves are shown in Fig. 5.31. Fig. 5.31 is a typical

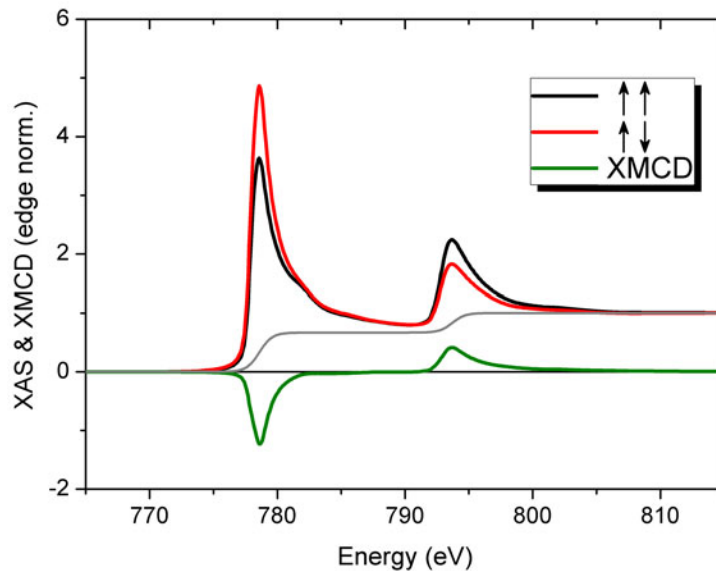


Figure 5.31: XAS and XMCD at the Co  $L_{2,3}$  edge of sample SP032 measured by TEY at an angle of incidence of  $\Theta = +45^\circ$  and with positive circular polarized X-rays.

metallic Co spectrum as it is found in thin film samples [89]. A XMCD effect of 29% with respect to the white line intensity is found. The average magnetic moment per cobalt atom in the sample can be calculated from the XMCD sum rules which were introduced in Section 3.3.4, equation (3.53). Before the actual integration of the peak areas, a standard two step background (compare also Sections 5.3.2, 5.3.3 and, 5.1.3), as it is shown in the figure, was subtracted from the spectra. The result of the integration is multiplied by the number of  $3d$  holes for metallic Co given by  $n_h = (10 - n_{3d})$ . Theoretical calculations give an average number of  $3d$  electrons for Co of 7.51 which leads to a hole number of  $n_h = 2.49$  [89]. Finally the result has to be corrected to account for the angle of incidence, i.e., the projection of the magnetic moments onto the beam direction and also the degree of circular polarization of the X-rays. The former leads to a factor of  $\sqrt{2}$  for the

incidence angle of  $\Theta = 45^\circ$  while the latter gives a factor of  $1/0.81$  (according to the WERA beamline properties). This results in a corrected spin moment of  $m_{\text{sp}} = 1.590 \mu_{\text{B}}$  and orbital moment of  $m_{\text{orb}} = 0.139 \mu_{\text{B}}$ . The corresponding L/S ratio is  $m_{\text{orb}}/m_{\text{sp}} = 0.087$ . These values agree very good with reference data for thin Co films [89]. The small discrepancy for the orbital moment is related to the larger absolute error for that value. Comparing the overall magnetic moment of  $m = 1.729 \mu_{\text{B}}$  from XMCD with the magnetometry data presented in the last section (compare Fig. 5.29), the magnetic moment obtained from the SQUID hysteresis is  $\sim 13\%$  too small.

The XMCD data is obtained from measuring the total electron yield, a technique that probes mostly properties very close to the sample surface. Since the result is in good agreement with the reference data for metallic, not oxidized cobalt it is a direct proof that the cobalt in the sample is also not oxidized. On the other hand, the SQUID data presented in the last section showed a reduced magnetic moment in the sample. The XMCD data now clearly proves that this reduction is not related to oxidation of the ferromagnet. Instead the best explanation for the SQUID data is that the Co film, which is nominally  $60 \text{ \AA}$  thick is very likely to be  $13\%$  thinner.

### 5.2.5 Absorption Spectroscopy & XMCD for FeMn

The manganese was measured on sample SP032 during the May 2008 beamtime at the WERA beamline at ANKA, Karlsruhe. The same parameters as for the Co XMCD discussed in the last section were used and can be found there. The resulting XAS and XMCD signal at the manganese  $L_{2,3}$  edge is shown in Fig. 5.32. A small XMCD signal from the Mn is found in sample SP032.

The Fe data were measured on sample SP036 during a beamtime in December 2008 at the UE56/2-PGM1 at BESSY II in Berlin using the reflectometer setup described in this thesis (compare 6.1). In this case the degree of circular polarization was  $90\%$ , the sample was at an angle of incidence of  $\Theta = 30^\circ$  and the magnetic field had a strength of  $\sim 105 \text{ mT}$  (in-plane projection). The dichroic spectra were obtained using the same method as described above for Co and Mn. The result-

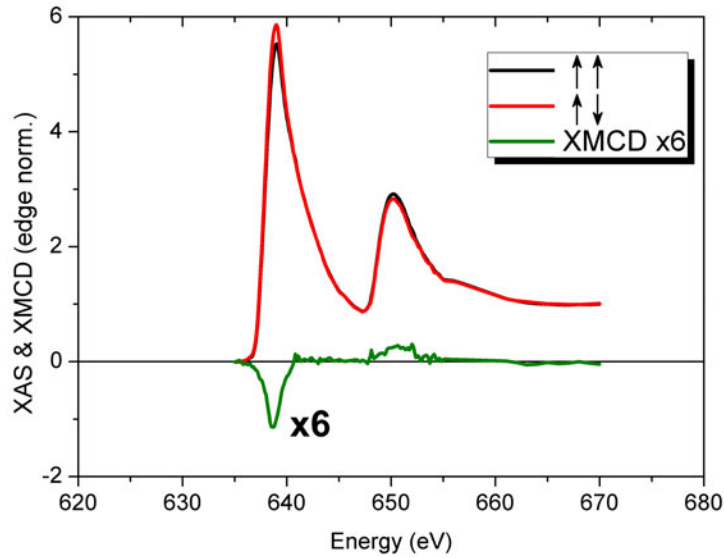


Figure 5.32: XAS and XMCD at the Mn  $L_{2,3}$  edge of sample SP032 measured by TEY at an angle of incidence of  $\Theta = +45^\circ$  and with positive circular polarized X-rays.

ing Fe XAS and XMCD of sample SP036 is shown in Fig. 5.33(a). The TEY spectrum shows a pronounced XMCD effect of 41 % with respect to the white line intensity. Using the already described XMCD sum rules, the magnetic spin and orbital moments for the Fe XMCD were calculated. The correction parameters are then  $1/\cos(30^\circ)$  for the alignment of beam and moment and  $1/0.9$  for the degree of polarization of the beamline. The number of  $3d$  holes for Fe is  $n_h = 3.39$  [89]. Using these values, a spin moment of  $m_{\text{sp}} = 1.11 \mu_B$  and an orbital moment of  $m_{\text{orb}} = 0.10 \mu_B$  is found from Fig. 5.33(a). The corresponding L-S ratio is then  $L/S = 0.09$ . Compared to literature reference data for bcc Fe [89], the value for the spin moment is reduced by a factor of 2. On the other hand the orbital moment found agrees quite well with the reference so obviously the rotatable Fe moments have more orbital moment than usual which might be related to the fact that they are located only at the interface (compare below and Section 5.1.7).

For comparison, Fig. 5.33(b) shows the fluorescence yield data taken during the same measurement like the TEY data shown in Fig. 5.33(a). As can be seen, the TFY only shows a very small XMCD effect. Since TEY is a mostly surface sensitive technique the signal originates only from Fe close to the surface, i.e., close

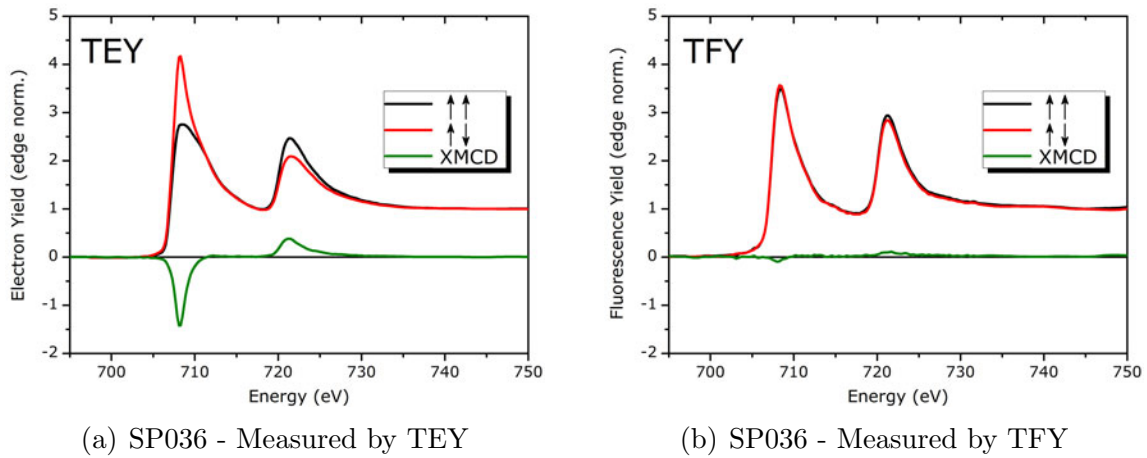


Figure 5.33: XAS and XMCD at the Fe  $L_{2,3}$  edge of sample SP036 measured by TEY on the left (5.33(a)) and TFY on the right (5.33(b)) at an angle of incidence of  $\Theta = +30^\circ$  and with positive circular polarized X-rays. The XMCD effect in the TFY spectrum is very small compared to the TEY. Due to the different depth probing ranges of the two techniques, surface dominated for the TEY while bulk dominated for the TFY, this clearly indicates that the rotatable Fe moments are very likely to be only present close to the upper interface with the Co.

to the interface with the Co. In contrast TFY probes far deeper in the sample thus the spectrum is dominated by the bulk Fe signal. The fact that the spectra obtained from TFY show nearly no XMCD while the TEY ones have a pronounced ferromagnetic signal clearly proves that the rotatable Fe moments have to be close to the upper interface of the FeMn layer which is the one to the ferromagnet here. The majority of the Fe in the bulk of the FeMn is not rotatable.

The Fe and Mn spectra exhibit very broad  $L_2$  and  $L_3$  peaks which indicates that also in FeMn the  $3d$  electrons form a broad  $3d$  band as it is typical for the metallic state. For both antiferromagnetic constituents, Fe and Mn, a XMCD signal is found from the dichroic spectra which gives clear evidence for the existence of ferromagnetism in the nominally antiferromagnetic FeMn. Moreover the relative orientations of the rotatable Fe and Mn with respect to the Co can be directly derived by comparing the sign of the XMCD effect. All three measurements used positive circular light and the XMCD signals all have the same sign, negative at the  $L_3$  and positive at the  $L_2$  edge indicating that the three are oriented parallel



here!

### 5.2.6 Optical Constants for FeMn and Co

The optical constants for the FeMn/Co samples investigated here can be derived from the XAS data presented in the preceding section. The same applies for the magneto-optical constants of the three relevant elements.

Using the scheme described in Section 4.2, the optical and magneto-optical constants for Co were derived from the spectra shown in Fig. 5.31 and the result is shown in Figs. 5.34(a) and 5.34(b) for the optical and magneto-optical constants, respectively.

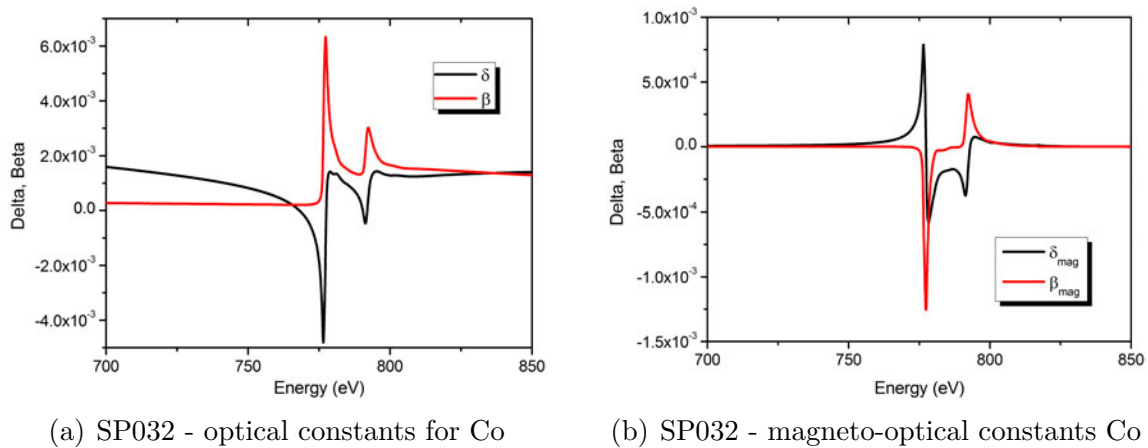


Figure 5.34: Optical and magneto-optical constants  $\delta$  and  $\beta$  for Co in the Co/FeMn samples as obtained by applying the scheme described in Section 4.2 to the data of Fig. 5.31.

The same method was used to obtain the optical constants of FeMn from the respective XAS data presented in the last section. The data shown in Figs. 5.32 and 5.33(a) was fitted onto the respective scattering factors  $f_2$  (compare 4.2) and the Kramers-Kronig transform was used to obtain the corresponding  $f_1$ . Finally the two sets of scattering factors  $f_1$ ,  $f_2$  were put together and the optical constants

were calculated from the curves using the density calculated from the unit cell volume  $V_a = 0.47793 \text{ nm}^3$  [107] and the amount of 2 Fe and 2 Mn atoms in this volume. The resulting optical constants of  $\text{Fe}_{50}\text{Mn}_{50}$  are shown in Fig. 5.35. The

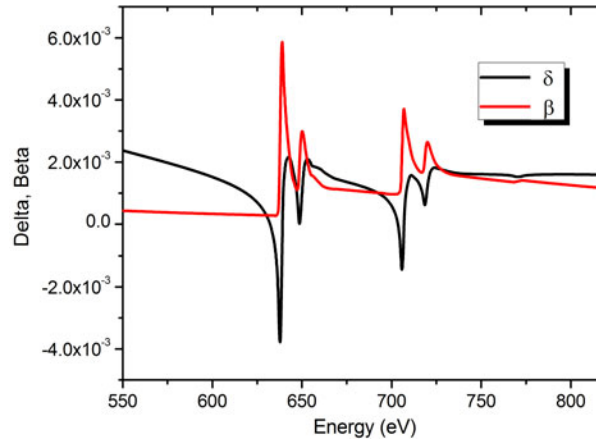


Figure 5.35: Optical constants,  $\delta$  and  $\beta$  obtained by applying the scheme described in Section 4.2 to the datasets of Figs. 5.32 and 5.33.

optical constants are a necessary prerequisite for the qualitative interpretation of the energy dependent scattering which will be discussed in the next section.

### 5.2.7 Temperature Dependence of Pinned Fe Moments in FeMn

A precise picture of the location of rotatable and pinned uncompensated moments in the antiferromagnet was obtained from the investigation of the MnPd/Fe exchange bias samples discussed in Section 5.1. However, the question of the nature of the observed pinned uncompensated manganese moments could not be addressed from the measured dataset. Nevertheless that is an important point for the understanding of exchange bias in general. It can be expected that uncompensated pinned moments in the antiferromagnet exhibit different physics than normal rotatable moments. So instead of dealing with the location of the pinned and rotatable Fe and Mn moments in the FeMn layer of samples SP032 and SP036, the following investigation will try to reveal information on the spectroscopic properties of the pinned uncompensated Fe moments in the two samples.

A new measurement method will be introduced for that purpose: All X-ray measurements so far were either pure absorption spectra or reflectivity spectra. The former gives the average absorption spectrum for all depths accessible by the respective technique, either TEY or TFY. The latter provides structural and magnetic depth information but without any spectroscopic information. Hence a possible approach would be to measure reflectivity spectra for the whole relevant energy range of the absorption edge. Alternatively one could also measure absorption spectra at various angles. However, both methods require dozens of measurements and suffer from the mixture of interference from the layered structure and the variation of the optical constants with energy.

To avoid such mixtures and minimize the complexity, a third way has been chosen; energy scans at a constant  $q_z$ . The advantage of this method is that the interference condition from the structure is simplified since it is now only affected by the change of the absorption with energy and not by changes of the momentum transfer. In order to keep  $q_z$  constant when changing the energy, the  $\Theta$  angle has to be varied accordingly. For convenience, these measurements are further referred to as *constant- $Q_z$*  scans.

The first sample which was investigated by this new technique is sample SP032, the film with only 50 Å FeMn. From the magnetometric SQUID measurements discussed in Section 5.2.3, it is found that an exchange bias induced loop shift can only be observed after field cooling the sample to e.g. 50 K. At room temperature no bias is observed, as can be seen from the corresponding hysteresis loops shown in Fig. 5.29. Accordingly, no signal from pinned uncompensated moments should be present at room temperature while when measuring at 50 K, a pronounced signal can be expected. Therefore temperature dependent constant- $Q_z$  scans were measured during the November 2007 beamtime at the UE56/2-PGM1 beamline at BESSY II.

Energy spectra at a fixed  $q_z = 0.155 \text{ \AA}^{-1}$  were measured at the Fe  $L_{2,3}$  edge for both helicities of the incident X-rays. Note that in contrast to a normal absorption spectrum these spectra were collected by measuring the specularly reflected beam with the detector. To align the rotatable magnetic Fe moments in the sample, an external magnetic field of  $\mu_0 H_{ext} \sim 70 \text{ mT}$  was applied for each data point first

parallel and then antiparallel. The resulting magnetic energy dependent scattering at room temperature for both external magnetic field orientations and both helicities is shown in Fig. 5.36. To remove the contribution from the rotatable

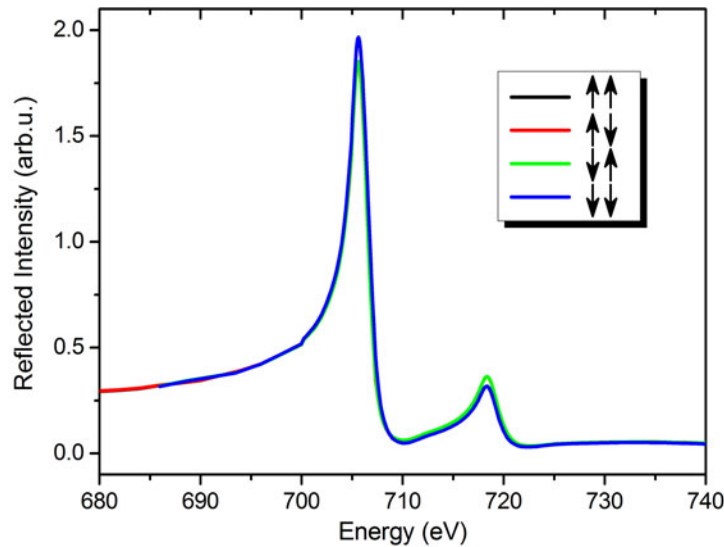


Figure 5.36: Energy scans at a constant  $q_z$  of  $q_z = 0.155 \text{ \AA}^{-1}$  for Fe for both helicities and both magnetic field directions. The arrows indicate the alignment, the first represents the polarization, the second the relative alignment of the magnetic field.

Fe moments and extract the signal from the pinned ones, the same method as described in Section 5.1.6 was applied. However, instead of calculating the asymmetry signal, the simple difference according to the numerator of equation (5.2) was used. The resulting difference from the pinned uncompensated Fe moments in the antiferromagnetic FeMn is shown in Fig. 5.37 for room temperature and for a similar measurement at 50 K after field cooling the sample in an external field of 100 mT. As expected from the hysteresis shown in Fig. 5.29, nearly no signal from pinned, uncompensated Fe moments is found at room temperature (red curve in Fig. 5.37). The situation changes dramatically when repeating the same measurement after field cooling the sample to 50 K: A large difference signal from the pinned moments is found at the  $L_3$  and the  $L_2$  edge as can be seen from the blue curve in Fig. 5.37. The shape of this pronounced difference signal however

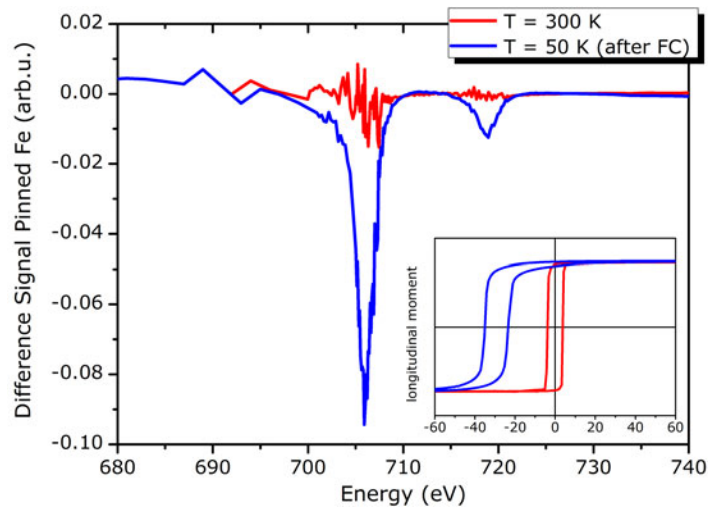


Figure 5.37: Difference signal from pinned moments in the sample calculated from the spectra shown in Fig. 5.36 using the scheme described in the text. No signal is found at all when measuring at room temperature where the exchange bias in the system is zero (compare corresponding hysteresis in Fig. 5.29). After field cooling the sample to 50 K a pronounced signal is found indicating the existence of pinned moments. The shape of this spectrum is special in that it shows the same sign for the  $L_2$  and the  $L_3$  edge. The inset shows the corresponding hystereses measured by SQUID magnetometry from Section 5.2.3.

is unusual: It has the same sign for both, the  $L_3$  and the  $L_2$  edge while usually a XMCD spectrum which is dominated by the spin moment shows a change of the sign between the  $L_3$  and the  $L_2$  edge due to the involved ground state moments [99, 121, 122]. An example for a spin moment dominated XMCD spectrum is the rotatable Fe in Fig. 5.33 or the ferromagnetic Co in Fig. 5.31.

On the other hand, the data in Fig. 5.37 is not calculated from an absorption spectrum but from energy dependent scattering data which exhibits no linear link to the absorption. To verify that the strange shape of the 50 K curve in Fig. 5.37 is not only due to interference, it is important to compare it to the corresponding difference signal from the rotatable Fe moments in the sample. Fig. 5.38 shows the normal difference signal from the rotatable Fe moments. The origin of this difference signal is the Fe XMCD effect from Fig. 5.33. The XMCD equivalent difference signal calculated from energy dependent scattering at a fixed momentum transfer  $q_z$  is shown for room temperature and for 50 K for both helicities of the

X-rays in Fig. 5.38. All four curves have the expected shape where the  $L_2$  edge

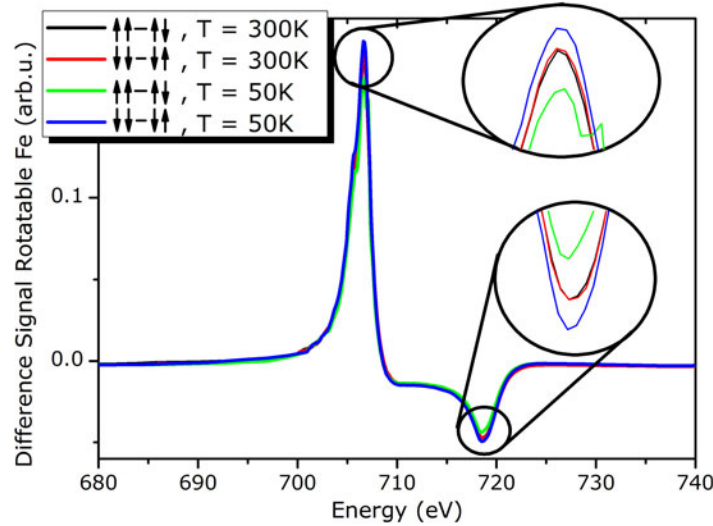


Figure 5.38: Difference signal resulting from rotatable Fe moments in sample SP032 obtained from the spectra shown in Fig. 5.36. The spectra show the normal spin moment associated behaviour for the  $L_3$  and  $L_2$  peaks. The inset shows zooms of the two edges. While the room temperature data does not show any difference between the helicities, at low temperatures a difference occurs further indicating that pinned moments are present.

has the opposite sign than the  $L_3$  edge. This clearly indicates that the overall behaviour especially with respect to the signs of the edges of Fig. 5.37 can not only be explained by interference.

Another very important finding from the signal of the rotatable uncompensated Fe can be seen from the two insets in Fig. 5.38. While the room temperature signal is the same for both helicities, a difference occurs as soon as the pinned uncompensated moments are present. It is noteworthy, that the difference signal from the pinned moments is calculated from two consecutive measurements with different helicity while the spectra leading to the data discussed here are measured such that the two magnetic field directions are measured immediately after one another for each energy value. This means the data shown in Fig. 5.38 is complementary

to the one of Fig. 5.37. The presence of pinned uncompensated moments is also reflected in the normal XMCD difference signal adding further proof to the fact that these moments are really only present at low temperatures.

In summary, spectroscopic information from the pinned uncompensated Fe moments in the antiferromagnet of the FeMn/Co exchange bias system has been obtained. From the data, the pinned moments seem to be dominated by a moment with orbital character. The significance of this finding is proven by the fact that the signal nearly vanishes at room temperature when the antiferromagnet is not ordered any more. This implies a direct correlation of the moments responsible for the curve in Fig. 5.37 with the exchange bias effect. Moreover, the fact that the occurrence of the pinned uncompensated Fe moments is also visible in the corresponding XMCD spectrum measured in reflection further stresses this conclusion.

Before discussing the implications and consequences from these findings in more detail which will take place in Section 5.2.9, the results from a second investigation of the spectral character of pinned uncompensated moments will be presented. This investigation was carried out to add further proof to this surprising and enthralling discovery.

### 5.2.8 Azimuthal Dependence of Pinned Fe Moments in FeMn

In the last section, a detailed investigation of the temperature dependence of energy dependent scattering of sample SP032 revealed that the spectral shape of the signal related to the pinned Fe moments in the antiferromagnet is dominated by an orbital ground state moment for the involved atoms. Here a second approach on a different sample and by different systematics shall be presented to further stress the significance of this finding.

While sample SP032 showed no exchange bias at room temperature due to the thin antiferromagnet, the second sample characterized by SQUID magnetometry, SP036, shows a small loop shift at 300 K as can be seen from the corresponding hysteresis in Fig. 5.30. This azimuthal dependence of the exchange bias, which has been introduced in Section 3.2.1 and was also discussed for the Fe/MnPd

sample in Section 5.1.8, should reflect itself in the difference signal from the pinned moments. Such a measurement is possible because the XMCD effect and with it the corresponding magnetic scattering amplitude is directional. As can be seen from the relation for the magnetic scattering amplitude given in equation (3.48) in Section 3.3.3, the scalar product between magnetisation, i.e., the magnetic moment and the polarization vector of the incident X-rays determines the strength of the magnetic effect.

The energy dependent scattering at the Fe  $L_{2,3}$  edge of sample SP036 (nominal FeMn layer thickness 100 Å) was measured during the December 2008 beamtime at the UE56/2-PGM1 beamline at BESSY II in Berlin. Spectra were measured at a fixed momentum transfer of  $q_z = 0.110 \text{ \AA}^{-1}$  along the direction of the exchange bias effect for both helicities and both directions of an external magnetic field of  $\mu_0 H_{ext} \sim 120 \text{ mT}$ . From the measured reflected intensity curves, the signal of the pinned asymmetry was calculated according to the same scheme used for the temperature dependence in Section 5.2.7 which reads:  $(\uparrow\uparrow - \downarrow\downarrow)$  (or alternatively  $(\uparrow\downarrow - \downarrow\uparrow)$ ). This method blanks out contributions from the rotatable Fe moments (compare Fig. 5.11 in Section 5.1.6) and the remaining difference signal only contains information from pinned uncompensated moments in the antiferromagnetic Fe layer. The result is shown in Fig. 5.39 as blue curve. A pronounced difference signal is found when measuring along the direction of  $H_{eb}$ . The shape of the signal is clearly associated to an orbital ground state moment similar to the result presented in the last section. After that, the sample was rotated azimuthally by  $90^\circ$ , i.e., to the direction perpendicular to the exchange bias in the film and the measurement was repeated with exactly the same parameters. The resulting difference signal from the pinned Fe moments in the sample is plotted as red curve in Fig. 5.39. According to the SQUID hysteresis shown in Fig. 5.30 no exchange bias is found at the perpendicular direction. From Fig. 5.39 it is found that the signal from the pinned moments also vanishes further proving the direct correlation of this moments with the exchange bias loop shift.



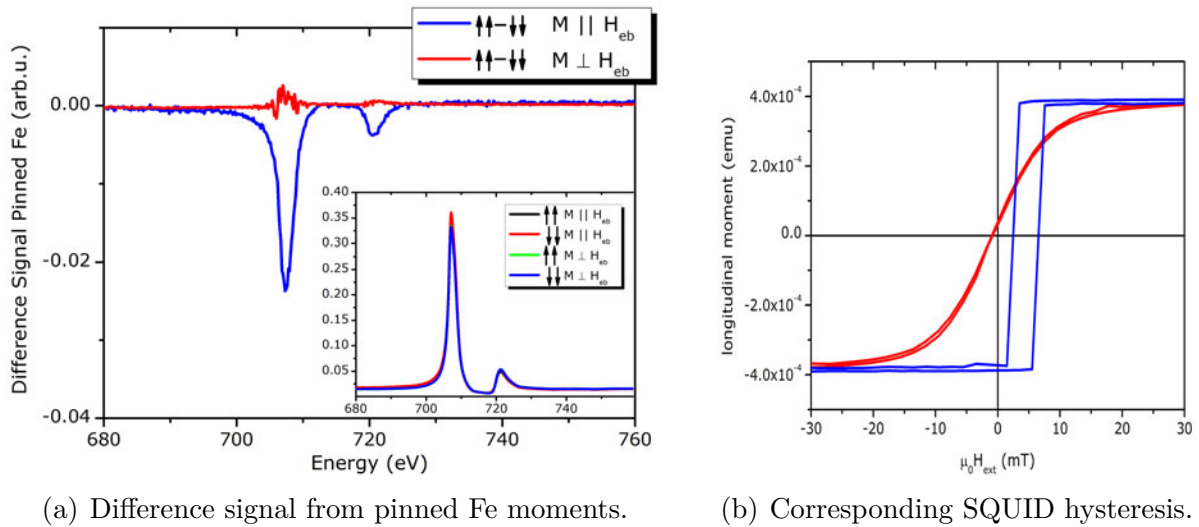


Figure 5.39: Difference signal from the pinned moments in sample SP036 measured at the Fe  $L_{2,3}$  edge. The energy dependence of the reflectivity at a constant  $q_z$  of  $0.11 \text{ \AA}^{-1}$  has been measured for both helicities of the incident X-rays and for both relative field orientations parallel and perpendicular to the exchange bias direction. While a pronounced signal is found from the measurement parallel to  $H_{eb}$ , the perpendicular one does not show a signal. Again the shape of the spectrum, although measured on a different sample and at a different  $q_z$  shows the same characteristics for the relative signs of the two edges. The inset shows the corresponding energy dependent reflectivity scans at a constant  $q_z$  of  $0.11 \text{ \AA}^{-1}$  from which the data was extracted. Sub-figure 5.39(b) shows the corresponding hysteresis loops which have already been discussed in Section 5.2.3.

### 5.2.9 The Role of Orbital Moments for Exchange Bias

In the last two sections, detailed results from energy dependent scattering of the pinned uncompensated Fe moments in antiferromagnetic FeMn were discussed. For both investigations it is found that the spectroscopic character of the pinned moments corresponds to a XMCD spectrum which is dominated by an orbital momentum ground state [99, 121, 122].

In Fig. 5.40, the most important  $2p$ -absorption spectra for each  $3d$  ground-state moment contributing to a difference signal are shown. The spin moment related ground state  $-\bar{w}^{011}$  shows a sign change between the  $2p_{3/2} \rightarrow 3d$  transition and the

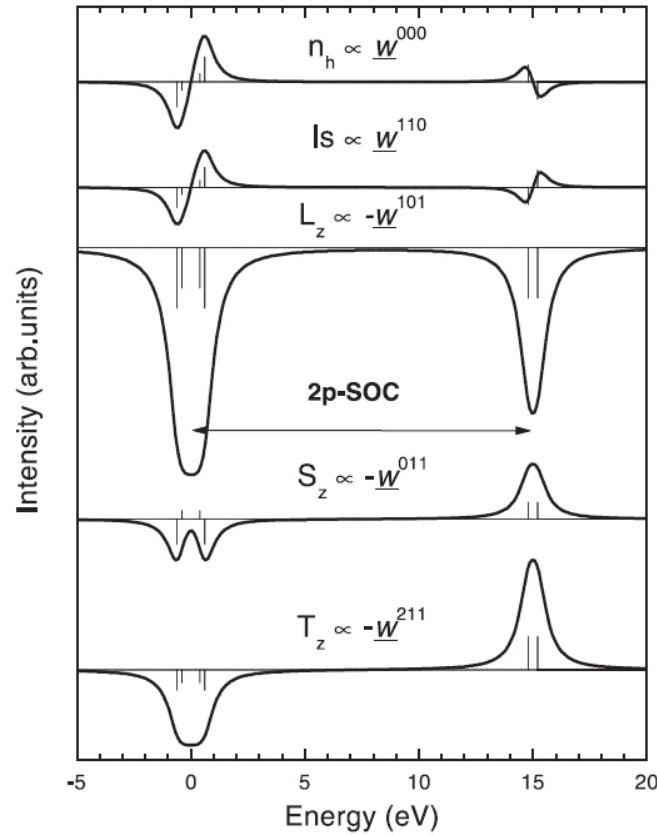


Figure 5.40: Important ground state moment contributions to the XMCD effect for the  $2p$  to  $3d$  transition (image reproduced from [99]).

$2p_{\frac{1}{2}} \rightarrow 3d$  transition. In contrast the ground state moment  $-\underline{w}^{101}$  related to the orbital momentum  $L_z$  has the same sign for both edges. Note that the notation of the ground state moments, namely the  $\underline{w}^{xyz}$  follows the one in reference [121] and [99]. The  $w$ -operators are used to express the multipole moment in the ground state by the  $x$ ,  $y$ , and  $z$ , respectively. Refer to [121] for a detailed description.

All the spectral information which is directly related to the pinned moments in both samples investigated here clearly has the same sign for the  $L_2$  and the  $L_3$  edge. The temperature dependent data shown in Fig. 5.38 of sample SP032 as well as the azimuthal dependent scattering data (Fig. 5.39) of sample SP036.

To further test this results, it is useful to compare the effect of a spin dominated XMCD on the energy dependent scattering with one from a XMCD which is dominated by an orbital momentum. Therefore the XMCD data of sample SP032

from Fig. 5.33 is used as basis of a simulation. Further using the optical constants data presented in Section 5.2.6 and the nominal sample parameters, the energy dependent scattering at a fixed  $q_z$  of  $0.155 \text{ \AA}^{-1}$  was simulated using the software ReMagX which is discussed in Section 6.4 or the diploma thesis of M. Harlander [67].

The magneto-optical constants used for this test are shown in Fig. 5.41(a). The XMCD spectrum without sign change between  $L_2$  and  $L_3$  edge, i.e., the orbital moment spectrum is obtained by multiplying the standard spin moment based XMCD spectrum around the  $L_2$  edge by  $-1/2$ . Using these two sets set of magneto-optical constants for simulating the energy dependent scattering, the difference signals shown in Fig. 5.41(b) are found. The magneto-optical constants

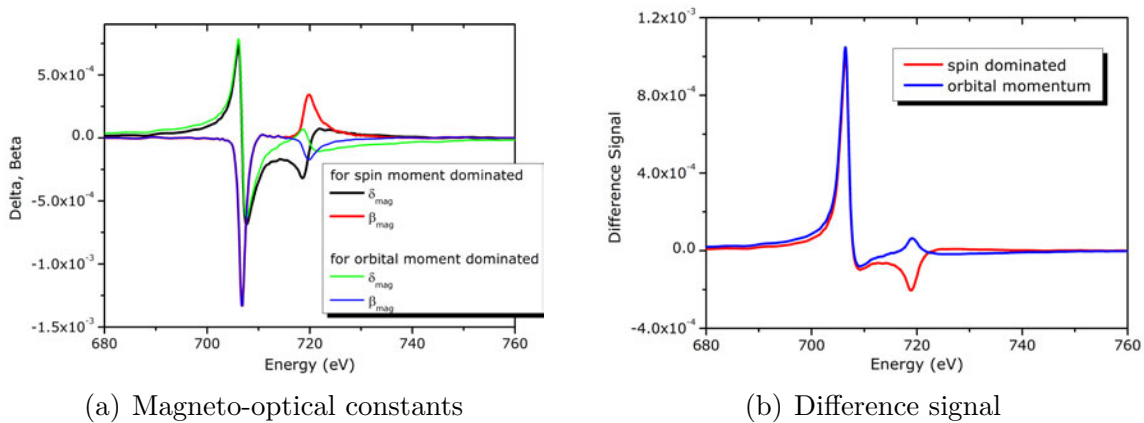


Figure 5.41: Simulated difference signal obtained from simulating energy dependent scattering based on the magneto-optical constants shown in Fig. 5.41(a). The red curve in 5.41(b) is obtained by using normal spin moment dominated XMCD as it is indicated by the red curve in Fig. 5.41(a). The blue curve results when using a  $\beta$  which has the same sign for the  $L_2$  and the  $L_3$  edge (the blue curve in 5.41(a)).

shown in 5.41(a) were calculated based on the XMCD of the Fe of sample SP036 from Fig. 5.33. To simulate the sign change of the  $L_2$  edge, the signal was multiplied by a factor of  $-1/2$ . The resulting difference signal from the energy dependent scattering at constant  $q_z$  clearly shows that the sign of the resonant

peaks and the corresponding magneto-optical constants is reproduced one to one in the spectrum although the data considers interference effects. This test is a further proof that the spectral shape observed for the pinned uncompensated Fe moments can not only be explained by the mode of measurement, i.e., interference.

So it can be concluded that the pinned uncompensated Fe moments which have been found in the antiferromagnet of the FeMn/Co samples investigated here are mostly orbital moments. Since the correlation of the exchange bias related loop shift and those moments can not be denied from the results presented throughout this thesis it can further be summarized that the moments which are responsible for exchange bias and the associated loop shift are orbital moments.

In fact this reasoning is logical. Exchange bias has to be related to a pinned orbital momentum since it is an anisotropy effect. Magnetocrystalline anisotropy is a result of the alignment of the orbital momentum of the magnetic ion in the surrounding electronic environment (compare 3.1.2). Although it needs the spin-orbit coupling to mediate it and it is the spin which ultimately couples to the neighbor moments, the origin of magnetocrystalline anisotropy is the orbital momentum. So to create an anisotropy effect like exchange bias, orbital moments in the antiferromagnet have to play a role.

### 5.2.10 Conclusion

From a detailed spectroscopic investigation of the pinned uncompensated Fe moments in the antiferromagnetic FeMn layer of the FeMn/Co exchange bias system, it is found that the pinned moments responsible for the exchange bias loop shift have a spectrum which corresponds to a mostly orbital momentum final state.

By investigating temperature and azimuthal dependency in this system clear evidence is found that the spectroscopic signal really originates from moments which are responsible for the loop shift. Furthermore the basic shape of the found spectra all show the same sign for the dichroic effect at the  $L_3$  and the  $L_2$  edge. Such a fundamental characteristics can not only be explained by the interference in the sample as has been shown by comparing simulation results for a similar system (compare Fig. 5.41).

The fact that the pinned uncompensated moments show a mostly orbital momentum character is actually not so surprising since exchange bias is an anisotropy phenomenon which are usually associated with orbital moments.

It is not possible that pinned uncompensated Fe does not have a spin moment at all and even if it is reduced it still should lead to a significant contribution in the spectrum. Moreover without spin moment, the pinned Fe atoms could never mediate their anisotropy to the neighboring ferromagnet. Accordingly the only possible explanation is that the spin moment of the Fe atoms discussed here rotates together with the neighboring ferromagnet while the orbital momentum remains fixed in the exchange bias direction.

That means that the exchange bias mechanism in FeMn/Co which induces the unidirectional anisotropy is a pinning of the orbital moment of some atoms in the antiferromagnetic layer by their electronic surrounding, i.e., the antiferromagnet. At the same time, their spin moment which is coupled to the orbital momentum by the spin-orbit coupling couples to the neighboring atoms via exchange interaction. Upon reversal of the ferromagnet, the spin moments follow the neighbors while the orbital momentum remains fixed, the spin-orbit coupling is overcome. From a rough estimate of the magnitude of the spin-orbit coupling in the transition metals [123] it is found that it is indeed sufficient to mediate the observed loop shift in the system.

This conclusion is the only possible explanation for the fact that the spectroscopic character of the Fe moments related to the exchange bias loop shift shows a clear orbital character. Nevertheless it is so far only a working hypothesis and has to be further investigated and tested quantitatively.

### 5.3 Temperature Dependence of the Co Moment In Co/NiCoO

Exchange bias was discovered in Co/CoO nanoparticles [19]. Ever since, oxidic antiferromagnets, namely CoO and NiO, have been used in exchange bias systems. Especially the preparation by oxidizing a Co or Ni sample in a controlled way makes them interesting. Moreover, the highest values for the interface energy, which is a measure for the strength of the effect (compare (3.18) in Section 3.2.1), can be observed in systems using CoO as antiferromagnet [18, 22]. Besides all these pros of CoO, a severe drawback is its Néel temperature of  $T_N = 293$  K for single-crystalline CoO which is below room temperature. Since the blocking temperature (see Section 3.2.4) is always smaller and ranges here typically from 200 – 290 K depending on the sample structure and the preparation conditions, CoO is not suited for applications since it would require an active cooling of the element. On the other hand, NiO has a rather high antiferromagnetic ordering temperature of  $T_N = 520$  K but the interfacial energy density induced is smaller by roughly one order of magnitude for poly-crystalline samples (see e.g. [22] and references therein).

A.E. Berkowitz and co-workers showed already in 1992 that CoO and NiO can be alloyed and that the resulting NiCoO antiferromagnet exhibits characteristic antiferromagnetic properties well in between those of the two compounds [124]. Polycrystalline  $\text{Ni}_{0.52}\text{Co}_{0.48}\text{O}$  is antiferromagnetic at room temperature with a Néel temperature of  $T_N = 417$  K [125, 126]. Furthermore the strength of the exchange bias is stronger than in pure NiO although it doesn't reach the values of CoO.

Fig. 5.42(a) shows the temperature dependence of  $H_{eb}$  in a  $\text{Ni}_{0.52}\text{Co}_{0.48}\text{O}(50 \text{ nm})/\text{Co}(25 \text{ nm})/\text{SiO}_2(5 \text{ nm})$  sample [126]. The sample has been cooled from above its blocking temperature to 4 K in an external field and subsequently the exchange bias has been measured while heating the sample up again. The diagram to the right (Fig. 5.42(b)) shows the so called Thermo-Remanent-Magnetization (TRM) of the same sample which corresponds to the amount of uncompensated spins in the NiCoO [126]. The TRM is obtained by field cooling the sample from above  $T_N$

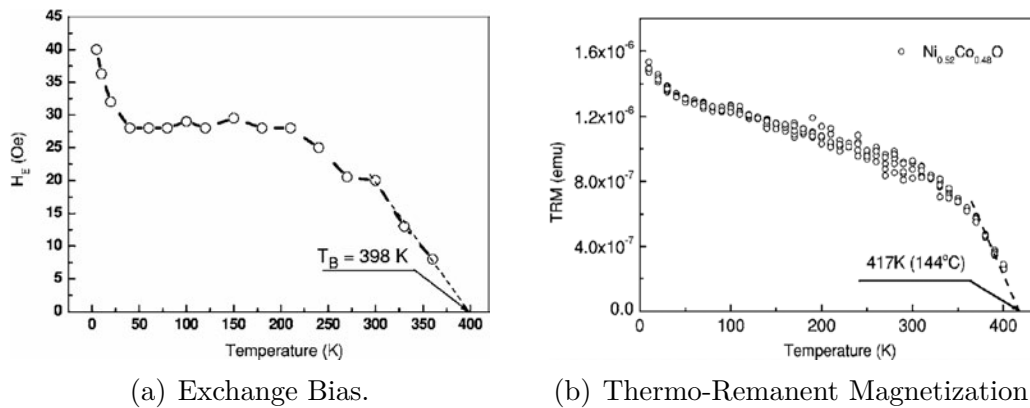


Figure 5.42: Temperature dependence of  $H_{eb}$  and the TRM (see text) in a  $\text{Ni}_{0.52}\text{Co}_{0.48}\text{O}(50 \text{ nm})/\text{Co}(25 \text{ nm})/\text{SiO}_2(5 \text{ nm})$  sample after field-cooling it in an external field from  $T_N$  to 4 K (both graphs are reproduced from reference [126]).

using a large field so that the uncompensated spins in the sample do align with it. Then the saturation magnetisation is measured and the contribution from the ferromagnetic Co on top is removed by using a reference sample without antiferromagnet. The remaining moment can be solely attributed to the NiCoO and thus represents any kind of uncompensated moment including the pinned one in the NiCoO. A clear correlation of the exchange bias of Fig. 5.42(a) and the TRM in Fig. 5.42(b) is found. It is noteworthy that both, the TRM and especially the exchange bias show a steep increase for temperatures below 50 K. It is suspected that this increase is related to frustrated spins at the interface which are pinned along the field cooling direction for very low temperatures [127].

From this observation several questions arise. First and most important, where exactly are these uncompensated moments located. Are they located close to the interface with the ferromagnet or are they distributed throughout the first grains of the NiCoO. The average grain diameter for a NiCoO film as it is investigated here is on the order of 10 nm [126]. The next question at hand is whether both, Ni and Co moments contribute to the signal or whether only one sort of atom is responsible for the effect.

To shed further light on these questions and maybe even give hints to a possible answer, a thorough XMCD investigation has been carried out on a NiCoO/Co

sample which has been prepared in a similar way as the referenced ones.

### 5.3.1 Sample Preparation & Characterization

For the following experiments, very thin samples have been used to enable TEY measurements of all layers (compare the reasoning in Section 5.1.3 and 5.2). A normal Si wafer with (100) surface orientation and with a native oxide layer of roughly 27 Å (compare for example 5.28 in Section 5.2.2) was used as substrate material. The sample has been prepared by DC-magnetron sputtering in a high vacuum system with a base pressure of  $3 \times 10^{-7}$  mbar. First, 500 Å of  $\text{Ni}_{0.52}\text{Co}_{0.48}\text{O}$  have been deposited by reactively sputtering a NiCo (50:50) target under oxygen partial pressure (argon pressure:  $3 \times 10^{-3}$  mbar). Next, a 10 Å Co layer as ferromagnet has been grown followed by a 10 Å ruthenium cap to prevent oxidation. The sample has then been field cooled from above its estimated blocking temperature  $T_B = 398$  K (see Fig. 5.42(a)) to establish a well defined exchange bias.

To characterize the magnetic properties and especially the exchange coupling in the sample, temperature dependent hysteresis loops have been measured using SQUID magnetometry. The sample has been field cooled from room temperature (RT) to 50 K in an external field of 1000 mT. Then the hystereses have been measured for each temperature while heating the sample step-by-step back to RT. The resulting hysteresis loops are shown in Fig. 5.43. A strong increase of the coercive field is observed upon field cooling while the loop shift only shows a moderate increase.  $H_C$  increases from 9 mT at room temperature to over 440 mT at 50 K which corresponds to an increase by a factor  $\sim 50$ . At the same time,  $H_{eb}$  increases from  $-3.9$  mT to  $-61.8$  mT which corresponds to a factor of only  $\sim 16$ . This indicates that the antiferromagnet has a small MCA which means the anisotropy constant  $K_{AF}$  is small (see also Section 3.2.1).

To better visualize the temperature dependence of the two significant parameters, the coercive field  $H_C$  and the loop shift  $H_{eb}$ , both values have been extracted from the hysteresis loops shown in 5.43 and are plotted in diagram 5.44 depending on the measurement temperature. The coercive field decreases continuously when heating the sample up to room temperature. A monotonic decrease of  $H_C$  is typ-



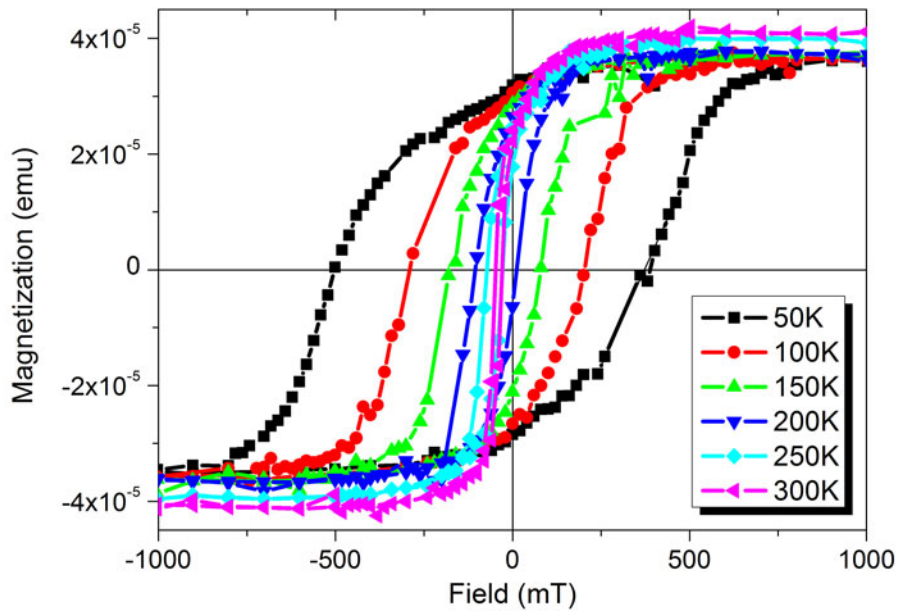


Figure 5.43: Magnetic hystereses of the  $\text{Ni}_{0.52}\text{Co}_{0.48}\text{O}(50\text{ nm})/\text{Co}(1\text{ nm})/\text{Ru}(1\text{ nm})$  sample investigated here. The loops have been measured after field cooling the sample to 50 K and heating step-by-step back to room temperature.

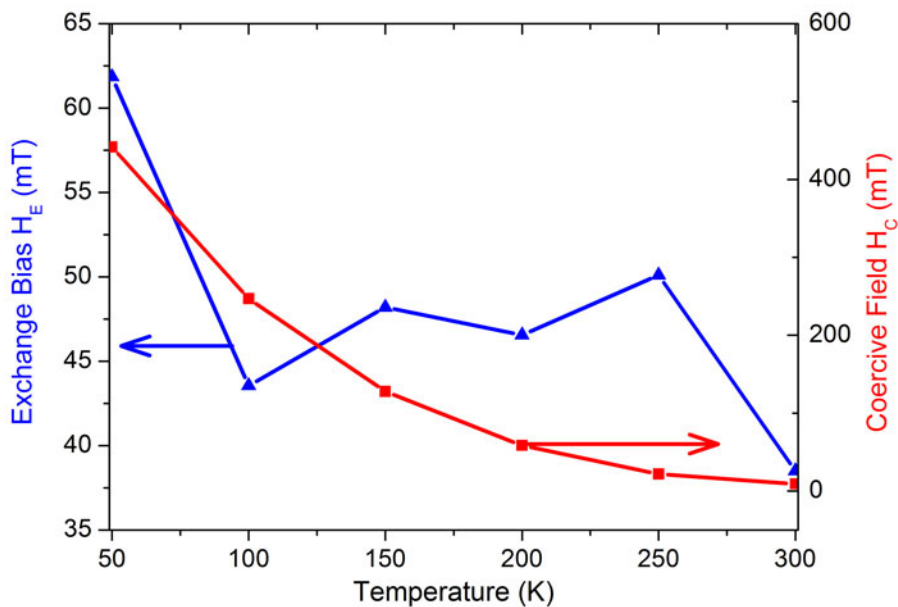


Figure 5.44: Temperature dependence of the two relevant parameters of exchange bias, the loop shift  $H_{eb}$  (blue) and the coercive field  $H_C$  (red) extracted from the hysteresis loops in Fig. 5.43.

ical for an exchange bias system although the curvature of the decrease can vary (see for example reference [117] p.23). The exchange bias also decreases when heating the sample back to RT however a pronounced plateau region of nearly constant  $H_{eb}$  is found for a large temperature range from  $\approx 100$  K to 250 K. This observation is in accordance with results from other NiO and CoO samples and also with alloys of the two [126,127].

### 5.3.2 X-ray Absorption Spectroscopy & XMCD of Co

Soft X-ray absorption spectroscopy (XAS) and XMCD for Co and Ni has been performed to proof the existence of uncompensated moments and identify temperature dependencies. All measurements have been performed at the PGM3 beamline at BESSY II using the groups own dedicated XMCD chamber [80].

The XMCD setup is optimized for absorption spectroscopy providing a fast switching (0.7 T/s) magnetic field of up to 2 T and an outstanding signal to noise ratio better than 0.1% for the TEY [80]. A cryo cooler similar to the one used in the XRMR setup described in Section 6.1, allows cooling either with liquid Nitrogen to 77 K or with liquid Helium to a minimum of  $\sim 7$  K. Bessy's PGM3 beamline uses synchrotron light from a bending magnet of the storage ring and a plane grating mirror for monochromatization. It provides horizontal or circular polarized X-rays with an energy ranging from 20 eV up to 1900 eV, a resolution of 32000 at 64 eV and a photon flux of  $10^9 - 10^{10}$  photons per second.

X-ray absorption spectra (XAS) have been measured in an external field of  $\pm 1$  T parallel to the incident beam and the exchange bias direction. The angle of incidence of the X-rays was set to  $30^\circ$  from the sample surface which leads to an in-plane field component of  $\approx 870$  mT and is sufficient to fully saturate the sample at all temperatures as can be seen from Fig. 5.43. By measuring the total electron yield of the sample and subsequent subtraction of parallel and antiparallel field alignment, XMCD spectra have been obtained for both, the Co and the Ni  $L_{2,3}$  edges. All measurements have been repeated several times and for both helicities of the incident light. The spectra have been corrected for  $30^\circ$  angle between sample and the X-ray propagation direction and for the beamlines'

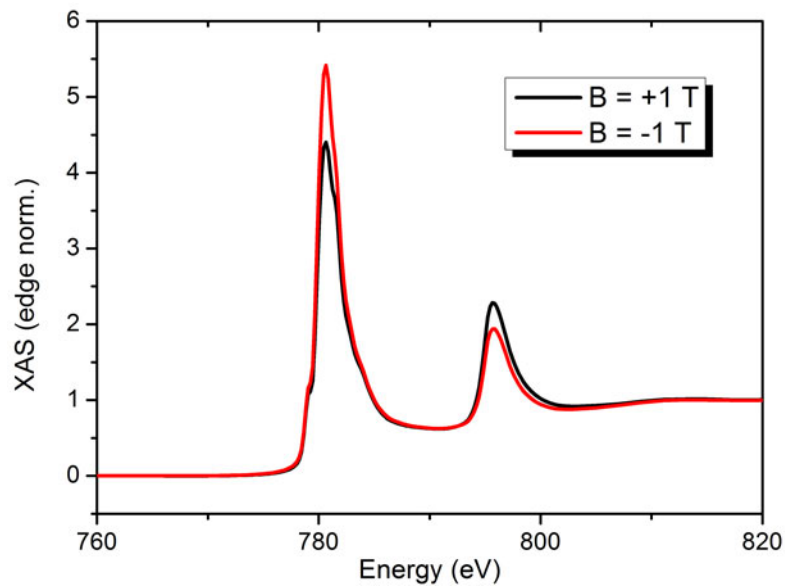
polarization degree of  $(92 \pm 5) \%$ .

The TEY method used to measure the absorption is only sensitive to the first few nanometers of the sample (typically  $\approx 2$  nm) due to the limited mean free path of the electrons [81, 128]. The absorption of the sample at the Co  $L_{2,3}$  edge has been measured at room temperature and at 80 K, the resulting XAS & XMCD spectra are shown in Figs. 5.45(a), and 5.45(b), respectively. The absorption spectra clearly contain contributions from the CoO from the antiferromagnet as can be seen from the pre-edge feature and the kink just above the maximum of the  $L_3$ . Since TEY probes more than the nominal ferromagnetic Co thickness, such a result was expected. It should be noted that all spectra are not corrected for the beamlines' energy shift. Absolute positions for the absorption peaks can therefore not be obtained from the measurements.

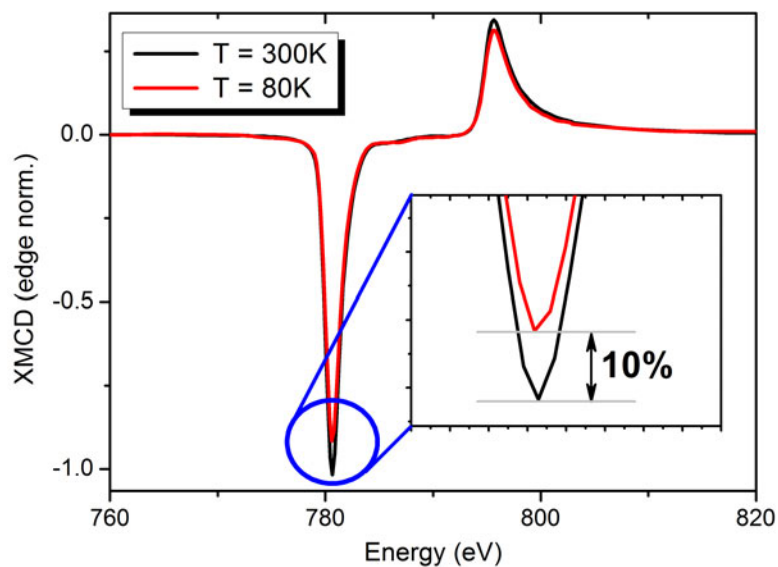
From Fig. 5.45(b) it is found that the XMCD signal decreases significantly when cooling the sample down to 80 K.

To quantify this decrease, the average magnetic moment per atom has been calculated using XMCD sum rules as described in Section 3.3.4. An average Co spin moment per atom at room temperature of  $m_{sp} = (1.03 \pm 0.02) \mu_B$  and a corresponding orbital moment of  $m_{orb} = (0.082 \pm 0.005) \mu_B$  is found. The corresponding  $L/S$ -ratio is then  $L/S = 0.08$ . At 80 K the spin moment is reduced by 10% to  $m_{sp} = (0.92 \pm 0.01) \mu_B$  while the orbital moment remains constant within the error being  $m_{orb} = (0.076 \pm 0.008) \mu_B$ . Before we will discuss the decrease of the magnetic moment in more detail, some considerations about the absolute value are necessary.

Compared to literature values for Co [89], the calculated magnetic moment per atom seems to be too small in the sample. However, this puzzle is solved easily: The small magnetic moment is a result of the TEY measurement method along with the structure of the sample namely the thin ferromagnetic Co layer on top of non-ferromagnetic Co in the NiCoO. The electron yield method is based on measuring electrons which leave the sample as a result of X-ray absorption. These electrons are mostly secondary electrons from photo- and Auger-electrons. The absorption length of X-rays is on the range of several dozens to hundreds of nanometers so electrons are generated throughout the whole sample. However,



(a) Circular dichroic X-ray absorption spectra



(b) XMCD difference signal of the 300 and 80 K measurement

Figure 5.45: XAS and XMCD spectra of the Co L edges  $L_3 = 780.6$  eV and  $L_2 = 795.8$  eV for both magnetic field orientations measured using positive polarized X-rays. The spectra have been obtained by switching the field at any energy value and the measurement was repeated for negative circular helicity (not shown).

since TEY measures the electrons who leave the sample via the surface, its sensitivity is limited by the mean free path of the electrons. If they are generated deep within the film the electrons will not reach the surface due to re-absorption, i.e., self-absorption. The escape depth for electrons in metals is typically on the order of  $2 \sim 3$  nm [81], but the values fluctuate depending on the material, defect density and the crystal structure.

In the present case, a very thin ferromagnetic Co layer ( $10 \text{ \AA}$ ) is grown on top of a thick antiferromagnetic NiCoO film which nominally does not contain rotatable, i.e., ferromagnetic Co moments. As a consequence, a fraction of TEY electrons at the Co L edge originates from the mostly nonmagnetic resonant contribution from the antiferromagnetic cobalt in the AFM-layer since the thin Co and capping layer on top let them pass through. Therefore the calculated spin and orbital moment of the ferromagnetic Co is too small. In particular when dividing the XMCD by the XAS during the sum rule calculation, a too large XAS is used thus resulting in a reduced moment. Also refer to Fig. 3.19 and the corresponding equations for the spin and orbital momentum (3.52) and (3.53), respectively.

Since the real escape length for the photoelectrons is unknown at the Co resonance energy for this special system, the necessary correction can not be calculated exactly. However, a rough estimate can be given: Assuming an exponential law for the absorption of photoelectrons generated at a depth  $d$  of the form

$$I_{electrons} \propto \int_{d_1}^{d_2} e^{-\frac{d}{\xi}} \quad (5.5)$$

It is now straightforward to calculate the relative intensities for all depths  $d$  for a given escape length  $\xi$ . Fig. 5.46 shows exemplarily this exponential decay for the investigated sample using the nominal thicknesses and an escape length of 2 nm [81]. Integrating the areas under the curve and taking into account the Co dilution in  $(\text{Ni}_{0.5}\text{Co}_{0.5})\text{O}$  of 25 %, one can calculate the contributing fractions of both layers to the XAS signal. The integration of equation (5.5) for a range  $d_1$  to  $d_2$  in the sample gives:

$$I(d_1 - d_2) = \left[ -\xi e^{-\frac{d_2}{\xi}} + \xi e^{-\frac{d_1}{\xi}} \right] \quad (5.6)$$

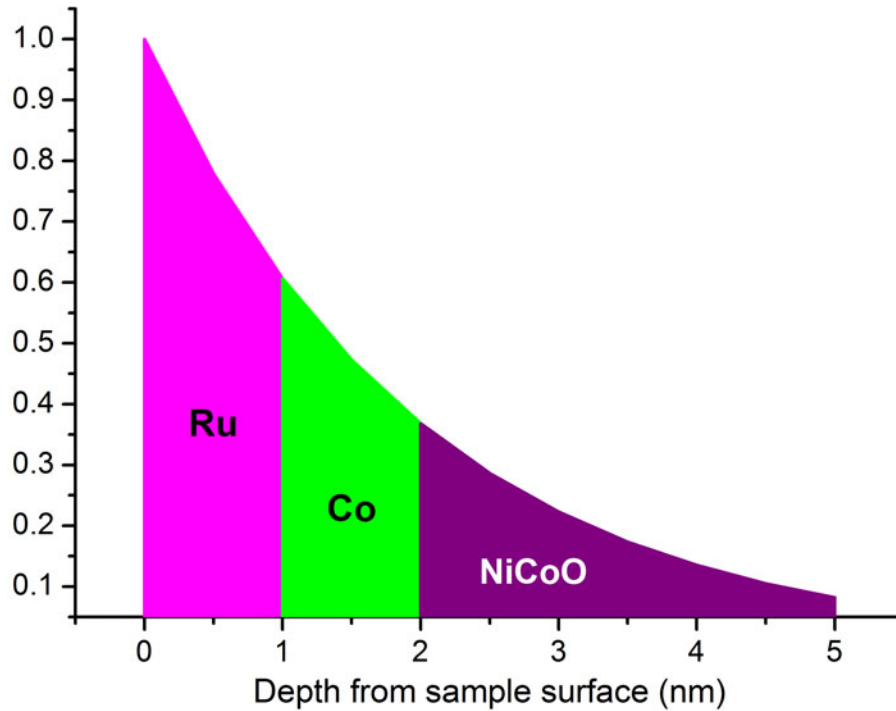


Figure 5.46: Depth dependence of the TEY. The exponential decay describes the probability for photoelectrons to leave the sample. The contribution from the different layers (indicated by the coloring) is then given by integrating the area under the curve.

Using the nominal layer parameters of  $d_1 = 1$  nm and  $d_2 = 2$  nm for the ferromagnetic Co and  $d_1 = 2$  nm and  $d_2 = \infty$  for the antiferromagnetic CoO, it is found that for the nominal values for the layer thicknesses, 72.2% of the XAS arise from the ferromagnetic Co film while the CoO contributes with 27.8% to the absorption edge. Applying these values to correct the sum rule calculation, a resulting spin moment of  $m_{sp} = 1.43 \mu_B$  and orbital moment of  $m_{orb} = 0.114 \mu_B$  is found which is much closer to the reference data for thin, metallic Co of  $m_{sp} = 1.55 \mu_B$  and  $m_{orb} = 0.15 \mu_B$  [89].

The above correction is based on an electron escape length of 2 nm which is the lowest estimate for metallic Co however this is certainly not the real value of  $\xi$  in the sample since, as mentioned, it depends on the intrinsic properties of the system. On the other hand it is reasonable to assume that the Co in the sample investigated here has a magnetic moment similar to the one reported for thin Co films which has been introduced in the last paragraph. Therefore it is justified

to go the opposite way and determine the  $\xi$  of the system from the XAS/XMCD data assuming a magnetic spin moment of  $m_{sp} = 1.62 \mu_B$  [89]. Then a correction factor of 1.57 is required to correct the measured  $m_{sp}$  which corresponds to a contribution of 63.5% from the ferromagnetic Co. Using the integral of equation (5.5) one can calculate the corresponding  $\xi$  by numerical means. It is found that  $\xi$  for this sample here should be on the order of  $\xi_{NiCoO/Co/Ru} = 2.77$  nm which is a reasonable value.

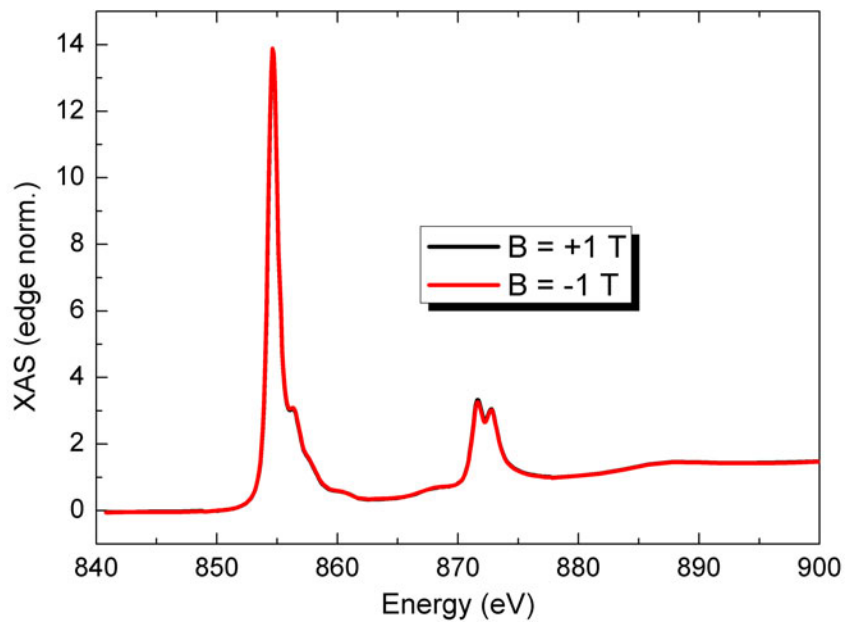
Summarizing, it is likely that the Co in the ferromagnet has a magnetic moment corresponding to reference values for thin Co layers and the electron escape length is  $\xi = 2.77$  nm as long as one assumes that the ferromagnetic Co layer is 10 Å thick.

As already said, the average magnetic moment of the Co in the sample decreases by 10% when cooling the sample to the temperature of liquid nitrogen. This can either be explained by a decrease of the magnetic moment per atom or a decrease of the amount of freely rotatable Co atoms, i.e., more atoms get pinned. The former interpretation is in contrast to the typical behaviour of a FM who exhibits an increase of saturation magnetisation for lower temperatures due to reduced magnon excitations.

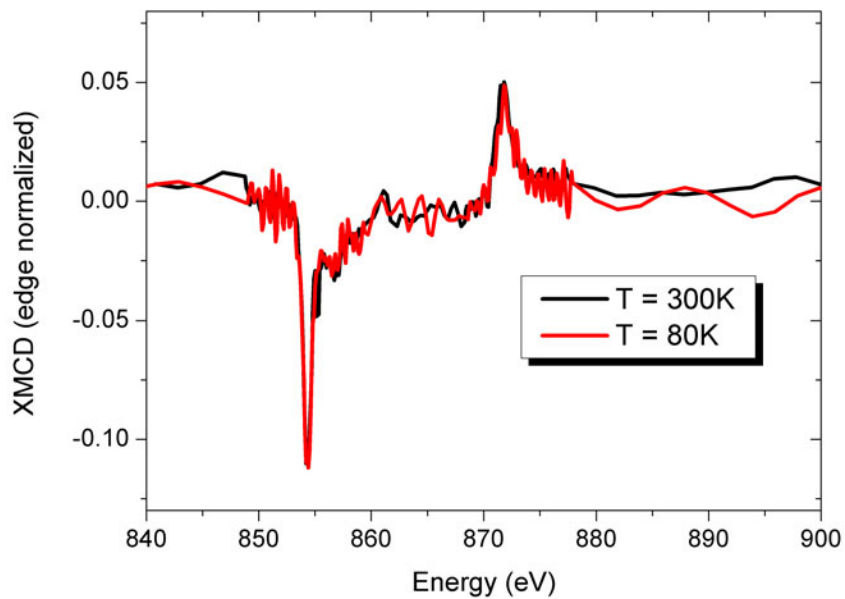
### 5.3.3 XAS & XMCD of Nickel

Before discussing possible reasons for the observed decrease it is imperative to check the situation at the Ni, the second constituent of the antiferromagnet. Therefore a similar investigation has been performed at the  $L_{2,3}$  edge of Ni. Room temperature XAS curves for parallel (black) and antiparallel (red) alignment of magnetic field and X-ray polarization were measured using positive circular polarized light and the result is shown in Fig. 5.47(a). The corresponding XMCD signal for both measured temperatures is shown in Fig. 5.47(b). A small XMCD signal of roughly 0.8% with respect to the white line intensity is found. Using sum rules to calculate the corresponding magnetic moment one obtains a spin moment of  $m_{sp} = (0.037 \pm 0.002) \mu_B$  and a corresponding orbital moment of  $m_{orb} = (0.006 \pm 0.002) \mu_B$  hence a  $L/S$ -ratio of  $L/S = 0.16$ .

The question is whether this Ni XMCD signal originates from rotatable or



(a) Circular dichroic X-ray absorption spectra



(b) XMCD difference signal of the 300 and 80 K measurement

Figure 5.47: XAS and XMCD spectra of the Ni  $L_{2,3}$  edges (854.6 eV and 872.2 eV) for both magnetic field orientations measured using positive polarized X-rays. The spectra have been obtained by switching the field at any energy value and the measurement was repeated for negative circular helicity (not shown).



paramagnetic Ni close to the interface like for the Co or whether the signal is just the tilting of the antiferromagnetic sub-lattices due to the external field. Here the full external magnetic field of 1 T has to be considered since the polycrystalline character of the sample implies an isotropic distribution of easy-axes in the NiCoO.

From literature reference data [129, 130], the magnetic susceptibility of NiO at 300 K is found to be  $7.5 \cdot 10^{-6} \text{ cm}^3/\text{g}$  perpendicular to the NiO easy-axis while it is  $2 \cdot 10^{-6} \text{ cm}^3/\text{g}$  parallel to it. Using the definition of the magnetic susceptibility [6, 14],

$$\chi = \frac{1}{V} \frac{m}{\mu_0 H}, \quad (5.7)$$

where  $V$  is the volume, one can calculate the magnetic moment of NiO per volume for the two directions. The result with respect to the direction of an external field of 1 T, which is also the propagation direction of the X-rays, is a magnetic moment of  $m_{\perp} = 7.5 \cdot 10^{-6} \text{ Am}^2$  and  $m_{\parallel} = 2 \cdot 10^{-6} \text{ Am}^2$  per volume  $V$ . Assuming an isotropic distribution of the easy-axes, i.e., the crystallite orientations in the film, the magnetic moment from the Ni in the sample should be  $m_{\perp} = 5.7 \cdot 10^{-6} \text{ Am}^2$ .

On the other hand, the unit cell of  $\text{Ni}_{0.5}\text{Co}_{0.5}\text{O}$  has a lattice parameter of  $a_0 = 4.229 \text{ \AA}$  [124] which gives a volume of  $V = 75.633 \text{ \AA}^3$ . Assuming the chemical ordering and structure described in reference [23] the number of Ni atoms in NiCoO (thus accounting for the dilution) per volume is given by  $\rho_a = 2.0659 \cdot 10^{20} \text{ atoms/cm}^3$ .

The calculus to transform a magnetic moment from the associated field strength [ $A/m$ ] into [ $\mu_B$ ] is  $1 \text{ Am}^2 = 1.0783 \cdot 10^{23} \mu_B$  (compare also Section 5.2.3). So the magnetic moment per Ni atom from NiO is

$$m_{\text{NiO,average}} = 0.00297 \mu_B/\text{atom} \quad (5.8)$$

which is one order of magnitude smaller than the value found here. Hence, the observed XMCD signal or Ni magnetic moment can not only be explained by antiferromagnetic Ni moments. The only possible explanation is that either some of the Ni is paramagnetic or rotatable. The corresponding low temperature measurement at 80 K reveals that the Ni XMCD, in contrast to the cobalt, does not change at all. The observed Ni moment is the same for room temperature and

80 K. This result rules out the paramagnetic option since paramagnetic Ni should show a Curie-Weiss behaviour for the temperature dependence and should not remain constant.

### 5.3.4 Magnetometry & Interpretation of the Results

To prove the general character of the decrease of the cobalt moment, an investigation of the temperature dependence of the magnetisation and its reversal has been carried out using SQUID magnetometry. The saturation moment  $M_{Sat}$  of the sample has been measured for a temperature range from 300 to 80 K at external fields of  $-3$ ;  $-2$  and  $-1.5$  T. Another feature which is investigated at the same time is the vertical shift or asymmetry introduced in the hysteresis due to magnetic moments in the antiferromagnet which are pinned, either uncompensated or compensated upon cooling down. This effect manifests itself by an asymmetry between  $-M_{Sat}$  and  $+M_{Sat}$ .

The resulting temperature dependencies for  $M_{Sat}$  averaged over several measurements and field values in saturation is shown in Fig. 5.49. A decrease of the samples saturation moment of approximately 13% is found which corresponds in magnitude with the observed decrease of Co XMCD signal when cooling the sample.

From the estimation of the correction factor for the Co as well as the unknown location and quantity of rotatable Ni moments it is obvious that a depth profile of the magnetism for both elements would be nice to have. However it turns out that the sample investigated here exhibits a reflectivity spectrum which has too few features to be fitted for all relevant energies. This is related to the vanishing Co film thickness compared to the NiCoO.

Before discussing possible scenarios which explain the observed temperature dependence it is helpful to briefly recapitulate all findings:

- From XMCD, the Co moment reduces by 10% when cooling the sample from RT to 80 K.
- The electron escape length in the sample is found to be  $\xi = 2.77$  nm.

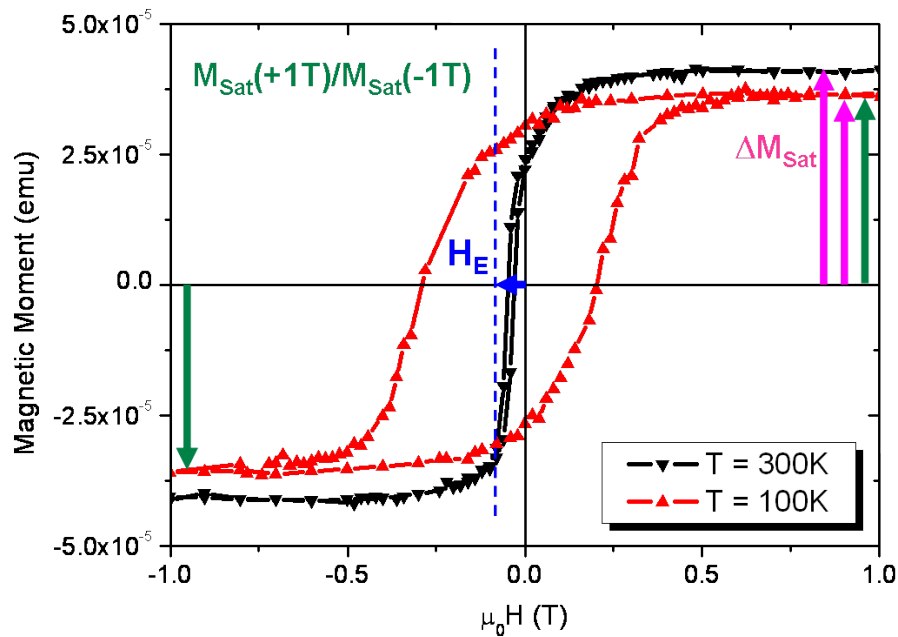


Figure 5.48: Exemplary hysteresis loops of the sample at 300 K and 100 K. The change of the saturation magnetisation  $M_{Sat}$  is clearly visible. The vertical asymmetry for the two magnetisation directions should correspond to the amount of frozen, i.e., pinned moments. Note that both curves are corrected for the diamagnetism from the substrate.

- A small XMCD signal is found at the Ni  $L_3$  edge proving the existence of rotatable Ni in the antiferromagnet.
- The Ni moment does not change with temperature which rules out the possibility of paramagnetic Ni.
- From SQUID magnetometry a decrease of 13% for the overall saturation moment is found which is slightly more than found from the XMCD results.

Two possible scenarios can explain the observed decrease of the Co moment: either Co atoms in the FM-layer located directly at the interface get pinned by the AFM. Or cobalt atoms in the first monolayers of the AFM are ferromagnetic at RT but couple to the antiferromagnet for lower temperatures. The first scenario implies the existence of uncompensated pinned moments in the sample at 80 K which are not present at room temperature. Uncompensated pinned moments would lead to a difference between the saturation magnetisation at +1 and -1 T, i.e., an asymmetric hysteresis. The second explanation is motivated by the

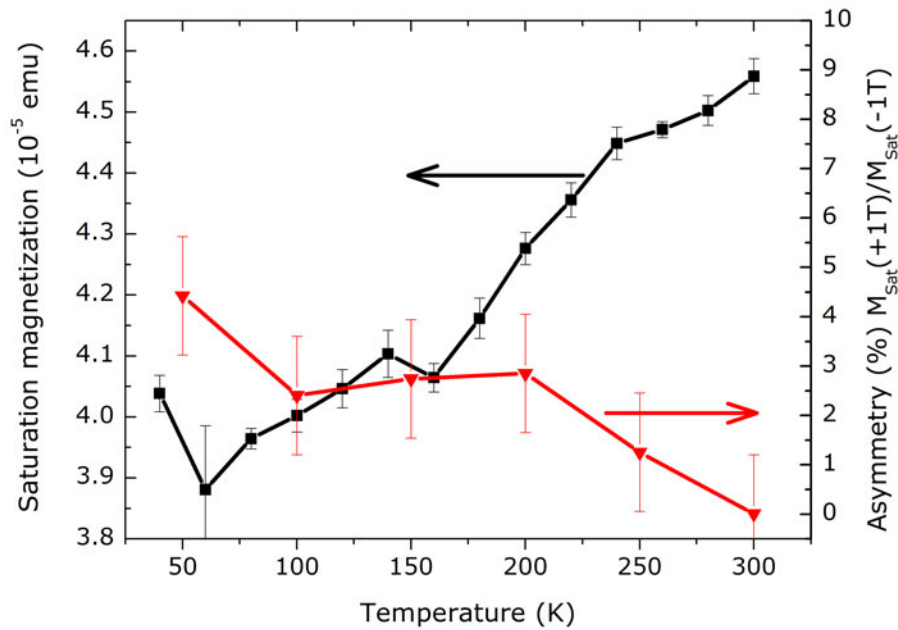


Figure 5.49: Temperature dependency of the saturation magnetisation  $M_{Sat}$  and the asymmetry between the saturation magnetisations for the two field directions according to  $M_{Sat}(+1\text{ T})/M_{Sat}(-1\text{ T})$  in %. The former indicates that moments are frozen in either compensated or uncompensated, the latter shows that most of the frozen in moment is compensated however a small fraction of 4% is pinned. Refer to Fig. 5.48 for a graphical illustration of the two quantities.

fact that the Néel-temperature of CoO is typically around 293 K, related to the AFM coupling strength, whereas NiO is already antiferromagnetic at RT. In this case, the hysteresis loops should remain symmetric for parallel and antiparallel field alignment. To shed further light on this issue, the field asymmetry of the saturation magnetisation at 1 T is shown in Fig. 5.49. While nearly 0 at RT, the asymmetry increases to +4.4% at 80 K (see Fig. 5.49).

The fact that the asymmetry between the two saturation magnetisations does not correspond in magnitude to the overall decrease of  $M_{Sat}$  which is roughly 13% indicates that a large fraction of the vanishing Co moment is compensated when cooling down. This means that Co which is rotatable at room temperature is ordering antiferromagnetic, i.e., it is pinned in a compensated way when cooling down to 80 K.

On the other hand, the increase of the asymmetry and the fact that it is positive

is a direct proof for rotatable Co moments which get pinned uncompensated when cooling the sample. From the sign of the asymmetry it is found that the saturation moment in positive direction of the external field is larger than the one in negative field direction. Hence the corresponding pinned uncompensated moments are oriented in the positive field direction and should result in an increase of the exchange bias in negative direction (compare also 3.9 in Section 3.2.1). This agrees perfectly with the observed increase of the negative bias shown in Fig. 5.44.

In conclusion, the XMCD data presented here, clearly shows the existence of freely rotatable, i.e., not antiferromagnetic coupled Ni and Co atoms in the AFM. As for Co, a reduction of the average magnetic moment per atom is found when cooling the sample from RT to 80 K. From a thorough analysis of the temperature dependence of the hysteresis in the system measured by SQUID magnetometry it is proven that this reduction of the Co moment is related to Co moments which are getting pinned, either compensated or uncompensated in the sample. The different behaviour of Ni and Co in the system is explained by the different coupling strength of the two constituents.



## 6 Experimental Aspects

Chapter [6.1](#) reprinted with permission from Sebastian Brück, Steffen Bauknecht, Bernd Ludescher, Eberhard Goering and Gisela Schütz , *Review of Scientific Instruments*, **79**, 083109, 2008. Copyright 2008, American Institute of Physics.

## 6.1 ERNSt – An Advanced Magnetic Reflectometer

This section describes the newly build magnetic reflectometer setup. A completely new development was necessary because fundamental design restrictions in the old setup made a further upgrade impractical. The major drawbacks of the old design were the too small overall size of the UHV chamber which did not allow for a larger magnet or more detectors and the missing in-situ sample transfer and load-lock system which made sample changes a nuisance. Changing a sample during beamtime took at least 24h since the whole chamber had to be backed again to reach a  $10^{-9}$  mbar vacuum. Finally the used sample holder was too small and was only capable of cooling down to roughly 120 K. These problems in sum led to a demand for a complete new design and construction. They also define the most important design requirements which the new reflectometer should fulfill. These are summarized by the following points:

- Higher magnetic fields.
- Low temperature measurements (L-He cooling).
- Simultaneous detection of  $I_{\text{Reflectivity}}$ , TEY, TFY, and  $I_0$ .
- Sample transfer system with UHV magazine for storage.
- Ultra-high vacuum; The reduced carbon contamination allows TEY measurements.
- Space for an optional 2D detector.

The result of two years of development and construction is the new *Stuttgart Novel Reflectometer Experiment* ( ERNSt). It is a highly versatile and upgradeable experiment for highest quality XRMR, XMCD, diffuse scattering and off-specular measurements [79]. Fig. 6.1 shows an overall CAD drawing of the reflectometer experiment.

### 6.1.1 General Setup

The specular reflection of X-rays from a multilayered thin film sample is measured in a so called  $\Theta$ - $2\Theta$ -geometry, where the sample is rotated by an angle  $\Theta$  and the



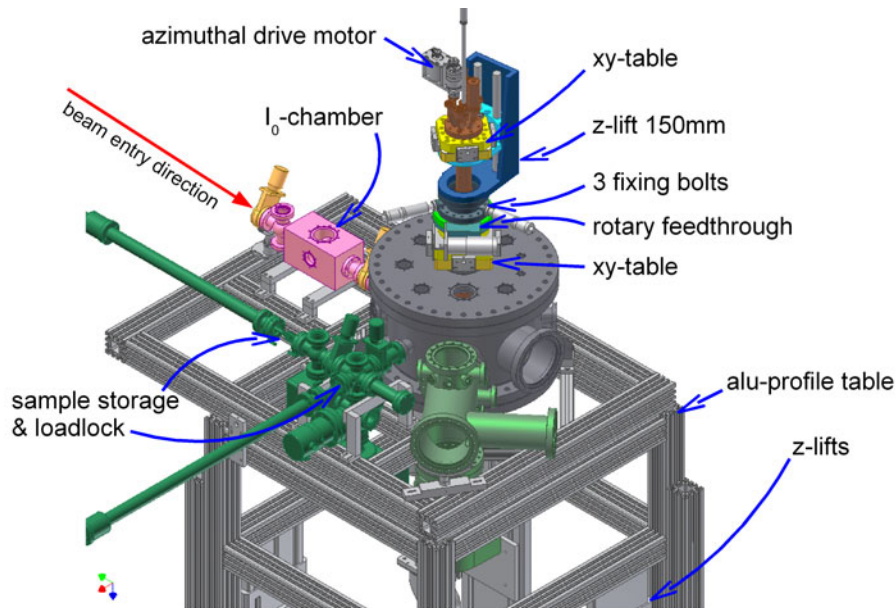


Figure 6.1: CAD drawing showing the whole experimental setup for soft X-ray resonant magnetic reflectivity.

detector by the double angle  $2\Theta$ . Such a measurement requires the detector and the sample to be freely rotatable and their axes to be aligned properly. Beside this general setup, two other major issues originate from the fact that the experiment is intended for XMCD measurements. The magnetic relevant L edges of the  $3d$  transition metals and M edges of the rare earth metals are all in the soft X-ray regime ( $E_{\text{photon}} < 2\text{keV}$ ) which requires ultra-high vacuum conditions for the experiment. Furthermore a magnetic field should be applicable to be able to change the magnetisation of the sample. This is achieved by a magnet which is also rotatable and can be moved freely or synchronous with the sample on the  $\Theta$  axis. Fig. 6.2 shows a schematic of our experimental setup realized in a UHV chamber. The experiment is connected to the beamline on the left side. The X-rays pass through a horizontal entrance slit which, in combination with the beamlines' vertical exit slit allows controlling the beam size and energy resolution. Another feature of the entrance slit is the beam positioning which is realized by measuring the photocurrent from the two faces forming the gap. If the gap is closed so that it cuts off a small fraction of the beam ( $< 5\%$ ), it is possible to check the beam position by comparing the asymmetry of the two photocurrents. This method provides a horizontal positioning of the beam with a resolution  $< 10\ \mu\text{m}$ . Directly after, the

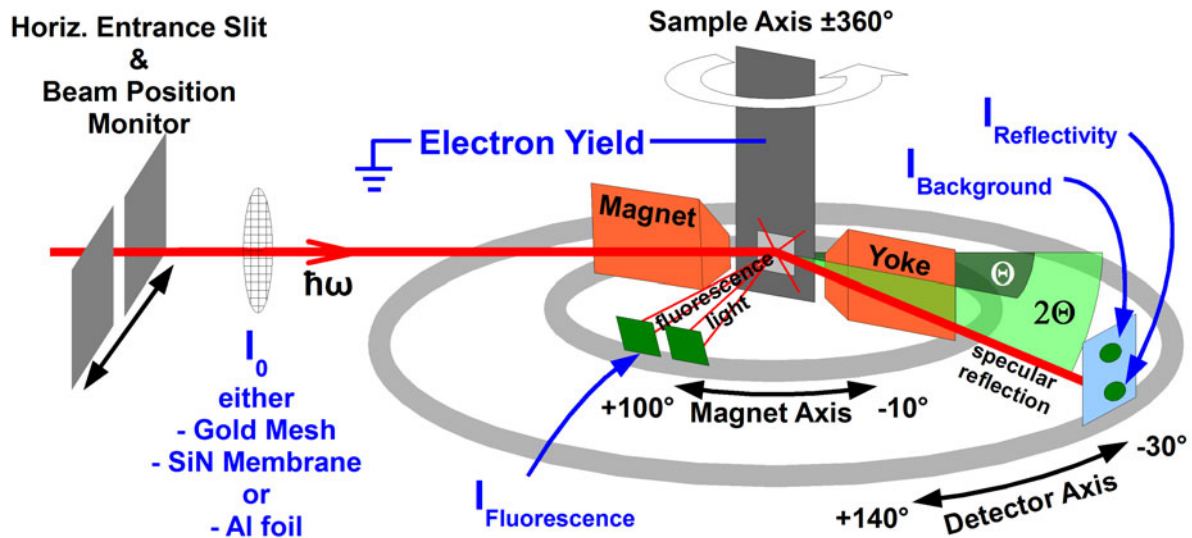


Figure 6.2: Schematic drawing of the experimental setup. The experiment is connected to the beamline on the left side.

X-ray beam passes through a changeable frame with windows for three different  $I_0$ . The standard is a gold mesh with 44% transmission, the two other options are a SiN membrane (standard TEM support membrane) with a 100 nm SiN window of  $5 \times 5 \text{ mm}^2$  opening and a 400 nm thick aluminium foil. Each of those can be used as intensity reference  $I_0$ . Slit and  $I_0$  are located in a separate vacuum chamber in front of the main reflectometer. The actual reflectivity experiment takes place in a cylindrical UHV chamber of 450 mm diameter and a height of 296 mm thus providing enough space for all components. Most of the chamber is made of 316 and 304 type low magnetic steel, except all parts of the lower flange which are made of forged 316LN type non-magnetic steel. Fig. 6.3 shows a CAD drawing of the main chambers interior with all relevant items. The sample is mounted on a cryo sample holder (1) and (4) which will be described later. The whole cryo-sample-holder is mounted on a CF100 differentially pumped rotary feedthrough (see Fig. 6.1) allowing for  $360^\circ$  free rotation. The absolute position is measured by a commercially bought angle encoder <sup>1</sup> providing a resolution of 400 nm which corresponds to an angular resolution of  $0.0003^\circ$ . Accordingly the relative position resolution and reproducibility of the sample axis ( $\Theta$ ) is roughly  $0.0003^\circ$ . The ab-

<sup>1</sup>RSF Elektronik GmbH encoder head MSR 20.54 - 1 M with  $\times 25$  integration. Encoder grating is a metal band with  $40 \mu\text{m}$  grating.

solute orientation of the sample with respect to the incident beam is only limited by the finite size and flatness of the sample. Typically the absolute position is better than  $0.01^\circ$ .

The detector (2) for the specular reflected beam is mounted in a distance of 146 mm from the centre of the chamber and the sample. It can be rotated freely from  $-30^\circ$  to  $+140^\circ$  with respect to the beam direction. The reproducibility and resolution is found from experiment to be better than  $0.003^\circ$  while the numerical resolution is  $0.00004^\circ$ . It should be noted that the detector resolution is not critical since the detector size corresponds to  $2\Theta \approx 0.8^\circ$  which is much larger than the typical beam size on the detector. The magnet yoke (3) is mounted on a separate axis with free rotation from  $-10^\circ$  up to  $+100^\circ$ . All three axes can be moved independently from each other.

For the magnet and detector axes rotation, large play-free UHV ball-bearings (5 and 6 in the figure) have been used. This allows us to carry heavy weights (magnet yoke) and use large diameters without the need of large differentially pumped rotary feedthroughs which do consume a lot of space and introduce vibration. These custom made ball bearings have an aluminium body and ceramic balls in order to be non-magnetic. To drive the ball bearings, a play-free, high torque, ferrofluidic rotary feedthrough on a CF40 flange has been used for the detector circle, while the magnet is externally driven via magnetic coupling through the chamber wall. This magnetic coupling of the yoke is achieved by bakeable SmCo high-performance permanent magnets attached to the magnets ball bearing. They have a closed field and are under  $90^\circ$  with respect to the magnet yoke to minimize stray field losses in the yoke. Besides  $I_0$ -chamber and main chamber, the experiment has a fast loadlock system with attached sample magazine for up to 12 samples. Omicron type sample holders are used to carry and transfer the samples. They are picked up from the magazine via a pincer which is mounted on a magnetic linear and rotary motion drive and moved into the main chamber where they are clamped to the cryo-sample-holder. The vacuum generation is realized with a combination of turbo pumps and titanium sublimation pumps (TSP). The  $I_0$ -chamber next to the beamline is pumped by a Varian V70 turbo pump and a TSP. Typically the vacuum in this section of the experiment is better

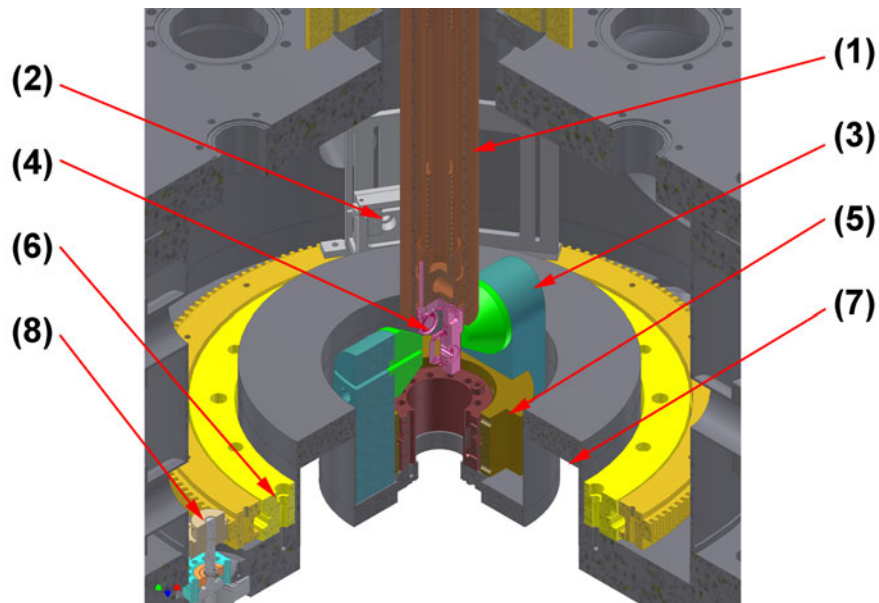


Figure 6.3: Close-up CAD drawing of the main chamber interior. Marked by (1) is the copper cryo-VTI described in 6.1.2, the detector (2), the in UHV magnet yoke (3). The sample holder (4) with the azimuthal drive (compare 6.1) and the two ball bearings for the inner magnet yoke (5) and the detector (6) are marked. Finally the drive for the detector ball bearing (7) and the trench for the outer magnet yoke (8) which are described in the text.

than  $2 \cdot 10^{-10}$  mbar. For the main chamber, a combination of a large 550 litres/sec Varian TV551 Navigator pump and a TSP is used which leads to a typical vacuum better than  $5 \cdot 10^{-10}$  mbar during the experiment. The loadlock system is pumped by a Pfeiffer TMU 071 turbo pump and operates typically in the  $5 \cdot 10^{-8}$  mbar range since it is not baked.

### 6.1.2 Cryo-Sample-VTI

The cryo-sample-VTI (variable temperature inset) is intended to provide a large temperature range for measurements while allowing azimuthal sample rotation and measurement of the samples electron yield via the total drain current. It consist of two parts, the cryo-cooler build of copper (item (1) in Fig. 6.3) and the sample-holder itself which is made of BeCu (item (4)). The sample-holder also carries the mechanics for the azimuthal rotation. The whole sample-holder

is electrically isolated from the cryo-cooler by a sapphire plate thus enabling the measurement of the total photocurrent, i.e., the total electron yield (TEY) of the sample. The isolation of the sample-holder is better than  $200\text{ G}\Omega$  ensuring a very good signal to noise ratio. Furthermore the sample can be set to a negative bias voltage to optimize drain current measurements.

The azimuthal rotation is realized by a molybdenum disk carrying the sample which can rotate on the BeCu holder. To ensure a good thermal connection, a spring presses the disk to the BeCu surface. Several gearwheels and a worm gear are used to transmit the rotation of an axle shaft running down the cryo-cooler to the molybdenum disk. Finally, a UHV magnetic rotary drive from VG Scienta couples the axle shaft to a computer controlled external stepper motor. The reproducibility of the azimuthal rotation is better than  $0.1^\circ$ .

For cooling, either liquid Helium (L-He) or Nitrogen (L-N<sub>2</sub>) can be used. Heating is realized by pumping hot air through the heat exchanger. The temperature of the cryo-cooler is measured by a Si-diode mounted close to the BeCu sample holder. The necessity of electrical isolation and especially the rotatable and clamped mounting reduces the thermal conductivity between sample and cryo-cooler. This leads to an increasing difference between sample and cryo-cooler temperature for very low temperatures. To characterize the thermal coupling between sample and cryo-cooler, i.e., obtain the difference between the two, a test with a second Si-diode directly mounted on a molybdenum "Omicron" type sample holder has been done. Liquid Helium has been used for cooling and the temperature has been changed by varying the L-He flow rate. Fig. 6.4 shows the measured temperatures at the sample position and of the permanently mounted temperature sensor during the test run. The offset scales with the temperature and is roughly 13 K for 29.6 K which is the lowest cryo-cooler temperature measured.

### 6.1.3 Detector Systems

A broad variety of sensors and detectors is included in the experiment in order to be able to measure not only the specular reflection but also absorption and fluorescence from the sample. The diffuse scattered light from the sample can be

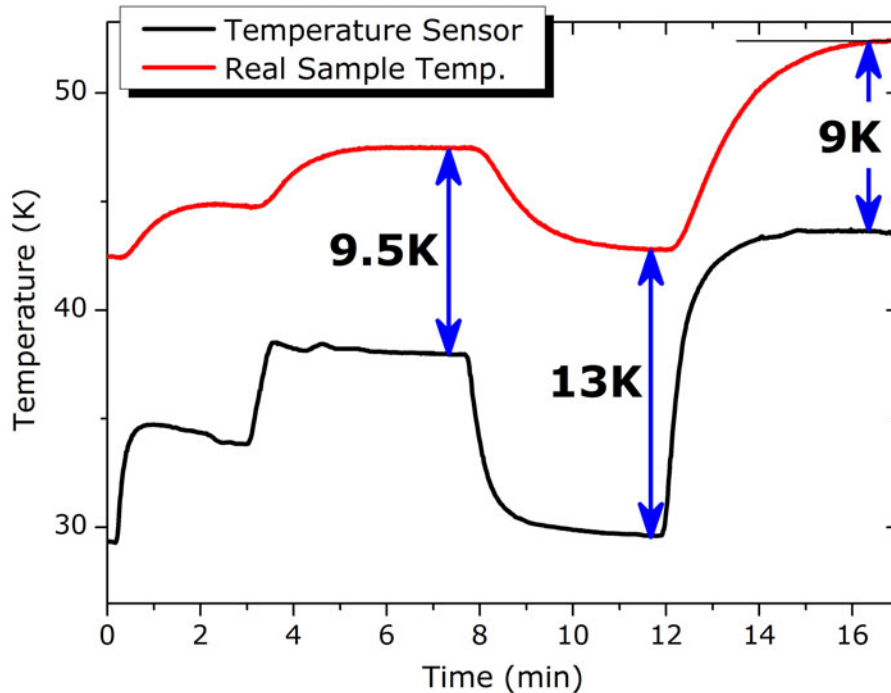


Figure 6.4: Offset between temperature sensor and real sample temperature for various L-He flow rates. As can be seen from the graph, the offset depends on the absolute temperature and reaches up to 13 K for the lowest measured temperature of 29.6 K. Both values have been obtained using the same type of Si diode. One mounted permanently on the cryo (labeled: temperature sensor in the graph), the other mounted on a standard Mo sample holder in exactly the same way like the samples are mounted.

obtained by measuring line profiles. The absorption of the sample is measured indirectly by the so called total electron yield (TEY) [128,131,132]. Therefore the sample is electrically isolated as was described already in Section 6.1.2 and the photocurrent is measured by a Keithley 6517A electrometer. Besides electrons, the sample also emits fluorescence light. Two Hamamatsu GaAsP diodes (G1740 type) each with an active area of  $5.6 \times 5.6 \text{ mm}^2$  are mounted in front below the sample and measure the fluorescence light emitted. Due to the close relation between absorption and emitted fluorescence light, this so called fluorescence yield (FY) is another way to measure the soft X-ray absorption of the sample [133]. The main detector for the reflected beam is a Hamamatsu GaAsP diode (G1116 type) with  $2.7 \times 2.7 \text{ mm}^2$  active area which is mounted on the  $2\Theta$ -Goniometer described

above. Note that the reduced active area leads to smaller dark currents. Fig. 6.5 shows a photograph of the detector mounted in the experiment.

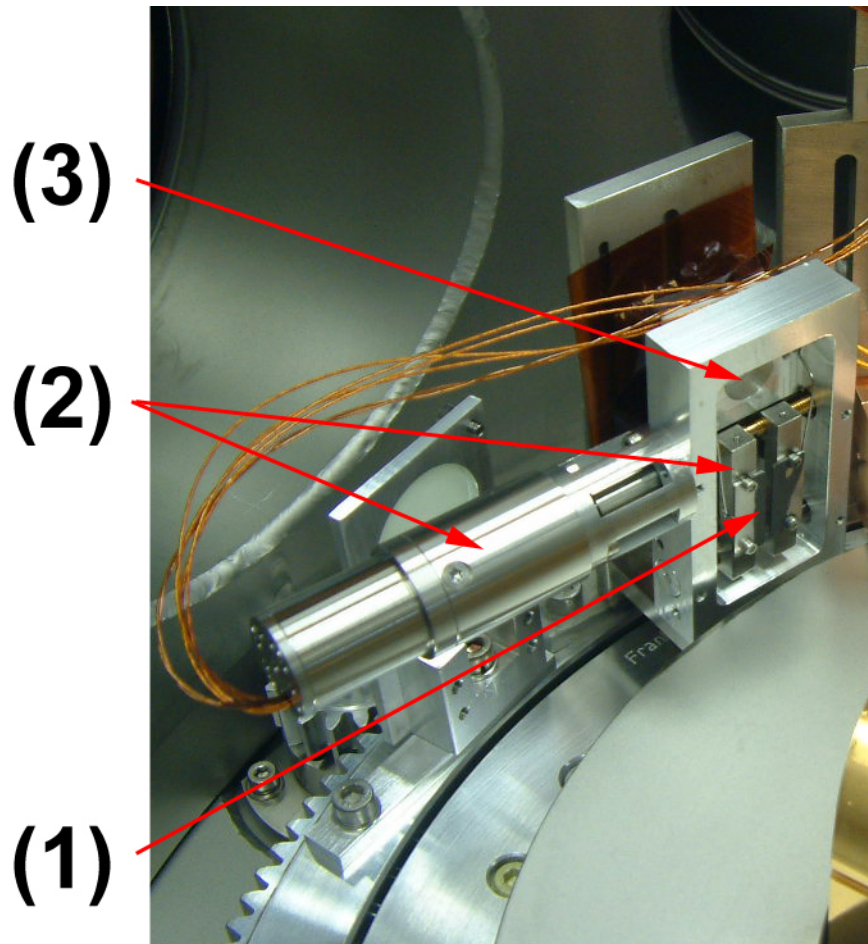


Figure 6.5: Photography of the detector mounted in the chamber. (1) is the opening of the detector which is mounted behind; (2) is the motor driven aperture slit and (3) is an additional diode of the same type which acts as background reference.

The aperture of the main detector can be controlled via an in-situ motorized slit. Two metal plates are moved by a UHV compatible stepper motor (Phytron VSS motor with UHV planetary drive) which allows precise adjustment of the aperture in a range from 0 to 2000  $\mu\text{m}$ . A reproducibility of better than 6  $\mu\text{m}$  is found for the slit opening. Besides the main reflectivity detector, a second GaAsP

diode of same type is mounted 28 mm above the scattering plane to measure the diffuse background emitted from the sample.

Finally it has to be mentioned that all detectors,  $I_0$ , TEY, FY,  $I_{\text{Refl}}$  and the diffuse background are always measured simultaneously.

#### 6.1.4 Magnet-System

To be able to measure magnetic reflectivity curves, element selective hystereses and dichroic X-ray absorption spectra, it is necessary to apply an external magnetic field to the sample. This field should be fast switching and freely scalable. Two field coils with yoke setup are used to achieve this. The copper coils, 1300 turns each, produce a magnetic flux of up to 860mT in air (centre bore). They are located outside the UHV chamber and are water cooled during operation. The magnetic flux is guided by an iron yoke (ARMCO pure iron) to the sample. To guide the magnetic flux into the chamber, the yoke consists of an inner (part number (3) in Fig. 6.3) and an outer part which link at a specially thinned out region of the UHV chamber. The outer yoke runs in the trench of the UHV flange and the thinned out region is realized at the wall of the trench as can be seen from Fig. 6.3. Since the link is realized by a gap which adds up to a total of  $\approx 10$  mm for both sides a significant loss of flux takes place. This is outweighed by the fact that the coils can be operated under normal conditions and the whole magnet system remains freely rotatable with respect to the UHV chamber. The inner yoke, i.e., the yoke inside the UHV chamber, has variable pole shoes which allow gap sizes of 10, 20 and 30 mm, note that Fig. 6.3 shows the 30 mm gap configuration. Fig. 6.6 shows the measured magnetic flux for the 30 mm and 10 mm gap. The two coils are connected in parallel to a Kepco H-BOP four-quadrant power supply which supplies up to 10 A current. The switching time from +10 A to -10 A is roughly 2 seconds which corresponds to the time needed to stabilize the output current. The magnetic field in the sample gap is monitored by a Hall probe which is permanently attached to one of the pole shoes. This allows to monitor the field during measurement and also to compensate for the yokes coercive field. The inset in Fig. 6.6 shows the low field region of the 30 mm gap. As can be seen from the



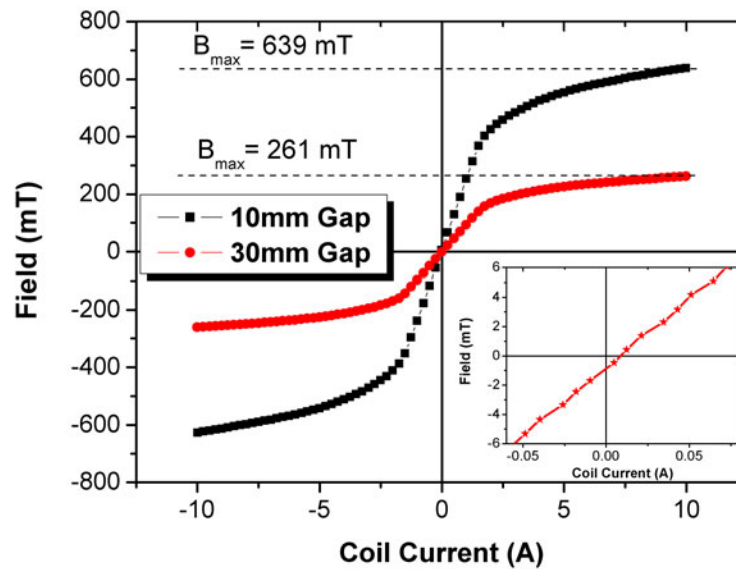


Figure 6.6: Magnetic field as measured with the hall probe attached to the pole shoe. The red curve shows the standard configuration with 30 mm gap while the black curve is the field for a gap of 10 mm. The inset shows the low field region of the 30 mm gap configuration.

graph, the yoke has a remanent magnetic field of less than 1 mT and the accuracy is better 0.5 mT.

Finally note that the inner yoke has been coated with a 500 nm thick gold layer to avoid unwanted fluorescence light from the yokes iron.

### 6.1.5 Control & Instrumentation

For one simple measurement cycle, 6 motors, a power supply, the monochromator control and 7 instruments have to be handled. This is achieved by using a dedicated software in combination with simple and reliable controllers and interfaces.

To keep things simple, the variety of motors and controllers used is kept as small as possible. Therefore, the axes (sample-, magnet- and detector-rotation) are all three realized using the same stepper motor<sup>2</sup> with 32:1 planetary gear. For

<sup>2</sup>Phytron ZSS 57.200.2,5-GPL with GPL 52.2 32:1

the azimuthal rotation a stepper motor without gear<sup>3</sup> has been used since the axis does not require much momentum. The detector slit is moved by a special UHV capable motor<sup>4</sup> also supplied by Phytron GmbH. Only one type of controller, the IMS MicroLynx<sup>5</sup> is used to control all these motors. It is a so called micro-step controller which means that it can do also fractions of steps thus increasing the steps per revolution far above the 200 steps the motors do. Besides it uses a very simple but versatile command language and serial communication for interfacing. The MicroLynx allows up to 256 micro steps which means each motor step is divided into 256 sub-steps. This leads to a resolution of 51200 steps/revolution or  $0.007^\circ$  without, and 1,638,400 steps/revolution with 32:1 gear.

The monochromator is controlled by BESSY and not directly accessible. Commands are instead send via serial communication (RS232) to the BESSY computer which then moves the monochromator accordingly.

Keithley 6517A type electrometers are used to measure  $I_{\text{Ref}}$ ,  $I_{\text{TEY}}$ ,  $I_{\text{TFY}}$ ,  $I_{\text{FYB}}$  and  $I_0$ . This type of electrometer is capable of measuring currents ranging from several  $\mu\text{A}$  down to less than 1 fA. A Lakeshore 330 temperature controller is used to measure the Si diode which acts as temperature sensor on the cryo-cooler (see 6.1.2). Finally a Keithley 196 type system DMM measures the voltage of the Hall probe mounted on one of the pole shoes of the magnet. All instruments and the magnet power supply<sup>6</sup> communicate via GPIB (General Purpose Interface Bus, also IEEE488). As already mentioned, communication with the control computer is either by GPIB bus or serial communication. For maximum flexibility these interfaces are not realized by extension cards but instead by USB adapters. A Keithley KUSB488 GPIB to USB interface adapter allows communication with all GPIB devices by one USB port. A hub in combination with several USB to RS232 adapters is used to communicate with the motor controllers and the monochromator. By this, the whole experiment can be controlled through three USB connections. Moreover this allows replacing the current PC by any computer with USB 2.0, drivers for the adapters and LabView.

---

<sup>3</sup>Phytron ZSS 52.200.2,5

<sup>4</sup>Phytron VSS 19.200.0,6-UHV-GPL-4LP with 49:1 VGPL 22.2-UHV planetary gear

<sup>5</sup>IMS Microlynx-4 / Typ: MX-CS100-401

<sup>6</sup>KEPCO H-BOP 4-quadrant powers supply

A standard x86 Dual-Core PC running Windows XP is the final control unit of the whole experiment. The software for the experiment is written in LabView Version 8.5, a graphical programming language based on C.

### 6.1.6 The New Continuous Measurement Mode

All measurements described so far are usually carried out in a way which can be described as step-by-step measurement. Each  $x$ -value is set, then all motors and the monochromator for energy scans are stopped and the measurement is done. Subsequently the detector is moved to the next  $2\Theta$  value and again stopped before measuring. This is necessary to reduce vibrations and the associated noise in the detectors. For the monochromators at BESSY, a stepwise measurement was the only available drive mode available so far.

During the commissioning week in early 2008 some BESSY monochromators were upgraded to allow for a continuous change of the energy. Therefore both, grating mirror and undulator gap have to be moved synchronously which is realized by a special beamline control software accessible via DAMC/EMC <sup>7</sup>.

Motivated by this, a new set of programs was developed to allow doing all measurements mentioned in the previous section (except the hysteresis measurement) in a continuous way. A new measurement sequence ('UltraFast\_Measure\_Sequence.vi') which is capable of reading all relevant values, Keithleys, monochromator as well as sample, and detector axis position in less than 50 ms ( $< 70$  ms guaranteed). This is achieved by using optimized drivers for the components which are capable of parallelization and by setting the Keithley integration time to one power line cycle ( $\equiv 20$  ms). It should be mentioned that a further acceleration of the measurement time might be achieved by using more than one GPIB bus. Moreover the measurement period is not constant which means that the time between two measurements varies slightly ( $< 10$  ms). In the following, a brief overview of the capabilities and restrictions of the new FAST mode measurements will be given.

It is obvious that the detection speed of the respective signal compared to the velocity is the crucial measure here. For all angle scans ( $\Theta$ ,  $2\Theta$  and  $\Theta - 2\Theta$ ), the

---

<sup>7</sup>DAMC/EMC is the BESSY monochromator control interface

relevant signal is the main detector diode described in Section 6.1.3. Due to its small size this diode is reasonably fast and measurement speeds of up to  $0.1^\circ/\text{s}$  are possible. Another limiting factor is the bandwidth of the pre-amplifier of the used Keithley 6517A electrometer. Fig. 6.7 shows test measurements of both modes, step-by-step and continuous, performed at BESSY during the February 2008 beamtime. Linear polarized X-rays were used to measure the reflectivity of a FeMn/Co sample (SP032) at an energy of 776.4 eV (before Co  $L_3$  edge). For the step-by-step measurement, the integration time was set to  $\equiv 400$  ms and the delay before each point was  $\equiv 500$  ms. The FAST mode measurement uses 1 power line cycle (here 20 ms) as integration time<sup>8</sup> and the speed was set to  $v_\Theta = 0.1^\circ/\text{s}$ . The

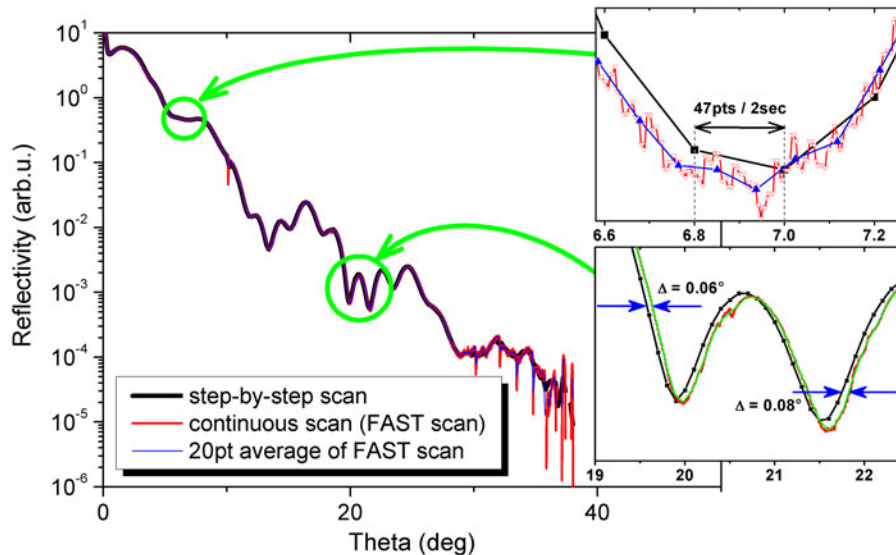


Figure 6.7: The same reflectivity curve of a FeMn/Co sample (SP032) at the an energy of 776.4 eV measured by standard step-by-step mode (black) and the new FAST mode (red). The blue curve is the 20 point average of the FAST mode curve. The overall time for the step-by-step measurement was 772 s while the FAST mode was by a factor of 1.8 faster (420 s).

FAST mode measurement and also a 20pts average of it match very well the step-by-step reference curve. However, the zoom on the lower right of Fig. 6.7 reveals

<sup>8</sup>The Keithley 6517A measurement speed setting “normal” is 1 NPLC (20 ms) integration time.

that the FAST mode curves show a slight offset i.e., are shifted along the x-axis due to the response delay of the detector diode. Moreover this shift is not constant but depends on the slope of the curve which indicates that it is related to the inherent capacitance of the pn-layer of the diode. It is very important to always measure a reference curve and take the offset into account when post-processing the FAST mode data.

The upper inset in Fig. 6.7 shows the effect of the 20 points average. Averaging is necessary because the raw FAST mode curve shown here (red) is composed of more than 8000 data points which significantly slows down the processing. Moreover this is far above the resolution limit of the measurement.

For absorption spectroscopy, the monochromator and undulator gap has to be driven synchronously which is realized by a BESSY program controlled by the measurement software. The speed is set in eV/s and a maximum of 1 eV/s is possible however this is too fast for precise spectra. It should be noted that a standard long energy range overview spectrum of a sample can be measured by a speed of  $\Delta E = 1$  eV/s and thus takes less than 10 min. In Fig. 6.8 an example energy scan over the Oxygen K edge of a LaCaMnO sample is shown. The TEY measurements were carried out using vertically, linear polarized light and the speed of the continuous scan was 0.2 eV/s. The two insets clearly show that not only horizontal but also vertical shifts occur for FAST energy scans. Here, only the TEY signal is shown which has a considerably faster response than the TFY. Hence even larger shifts can be expected for the latter.

The benefit of the FAST mode is the reduction of measurement time. For the first example, the  $\Theta - 2\Theta$  scan shown in Fig. 6.7, the step-by-step reference measurement took 772 s (or 12' 52'') while the FAST measurement only took 420 s (or 7') which is a factor of 1.8 faster. Its real strength is to speed up energy scans: The conventional step-by-step energy scan from Fig. 6.8 took 1466 s (24' 26'') while the FAST energy scan shown in the same figure only took 450 s ((7' 30'') at a speed of 0.2 eV/s. A factor of 3.2 between standard and FAST mode is achieved!

So far, the only drawback of the energy FAST scan mode is that the undulator shift can not be driven continuously yet leading to a variation of the degree of circular polarization with energy. Hopefully that will be fixed in a future upgrade

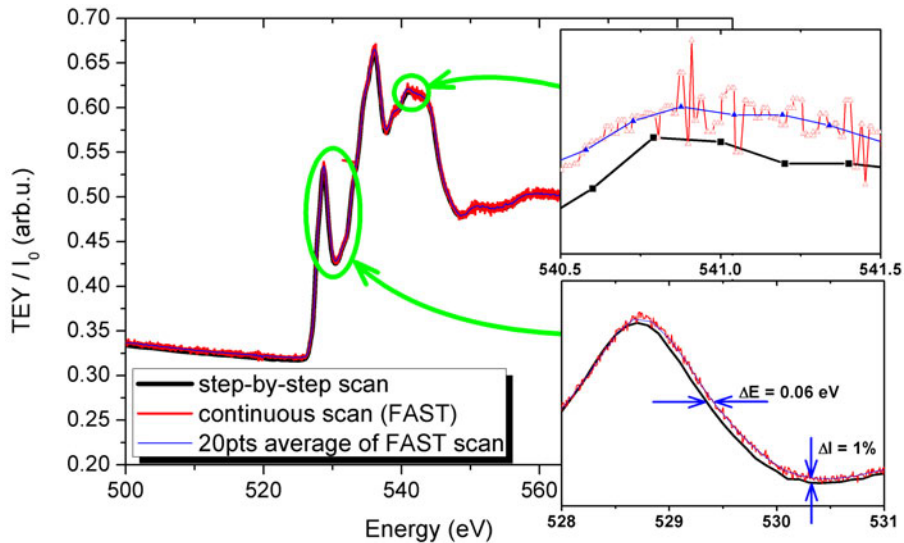


Figure 6.8: X-ray absorption spectra of the O K edge of a LaCaMnO sample measured by standard step-by-step mode (black) and the new FAST mode (red). The blue curve is the 20 points average of the FAST mode curve.

by BESSY.

## 6.2 First Results (With ERNSt)

The first experiments with the new reflectometer setup *ERNSt* have been carried out in May 2007, November 2007 and February 2008 on the UE56/2-PGM1 beamline at BESSY II in Berlin, Germany (see also Sections 5.1 and 5.2). In the following section, a selection of measurements will be presented as examples for the characteristics and capabilities of the new experiment:

For absorption spectroscopy *ERNSt* provides two different detection systems, the TEY via the sample holder leak current and TFY which is measured by two GaAsP diodes (for more details, see Section 6.1.3). The test system here is a bilayer composed of 60 Å Co which is grown on a 500 Å, polycrystalline Ni<sub>0.52</sub>Co<sub>0.48</sub>O layer on a Si substrate. Finally it is capped by a 20 Å SiO<sub>2</sub> layer to prevent oxidation of the Co. This structure is similar to the sample described in Section 5.3 except that the ferromagnet is thicker. More details can be found in the corresponding articles [33, 126].

Dichroic X-ray absorption spectra have been measured by TEY and TFY simultaneously at the Co  $L_{2,3}$  edge. The sample was set to an angle of incidence of  $45^\circ$  and the beamline to positive circular X-rays with 90% polarization. The spectra have been measured in remanence which means applying a field for a few seconds and then measuring with the field turned off. This mode is favourable since the magnetic field disturbs the trajectories of the electrons leaving the sample due to the photo-effect. It is applicable in this case because the hysteresis (not shown here) is squared shape leading to a remanence close to saturation.

The resulting absorption spectra for parallel and antiparallel alignment of X-ray polarization and the sample magnetisation are shown in Fig. 6.9. The left graph (6.9(a)) shows the Co  $L_{2,3}$  spectra obtained by measuring the total electron yield (TEY) while the right one, 6.9(b), shows the fluorescence yield signal (TFY) measured simultaneously. As can be seen from the figures, the spectra resemble

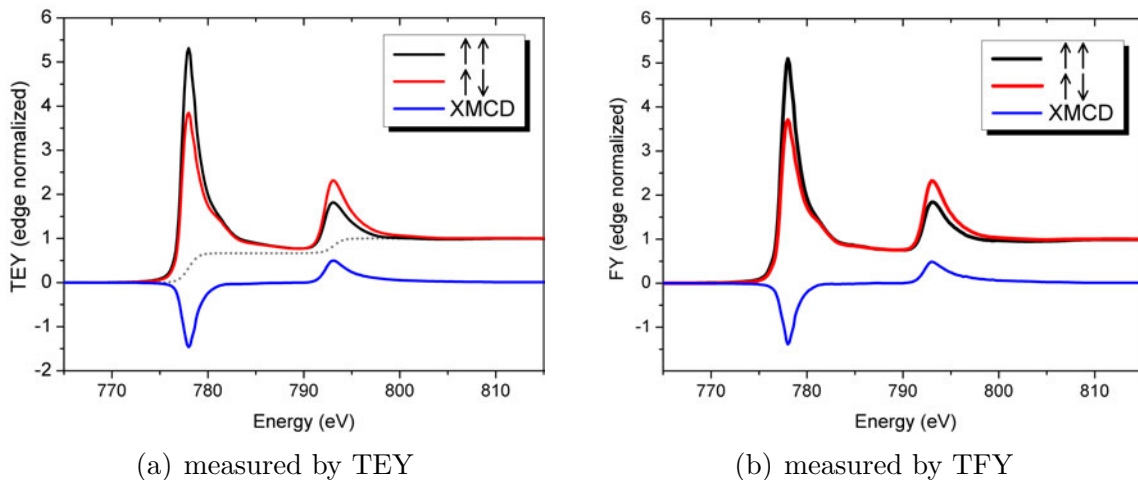


Figure 6.9: XAS and XMCD spectra measured simultaneously by (a) total electron yield (TEY) and (b) total fluorescence yield (TFY) for the Co  $L_{2,3}$  edge. The spectra are edge normalized. The dotted line in Subfigure (a) is the two-step background subtracted prior to integrating for the sum rule calculation.

each others shape perfectly proving that interfacial and bulk Co are in the same state. The form of the spectra corresponds to purely metallic Co and proofs that

no oxidation took place. The small differences in amplitudes are related to the so called self-absorption of the TFY signal, since fluorescence light is absorbed when going through the Co. Nevertheless, it can be seen from the close-up of the XMCD spectra shown in Fig. 6.10 that this effect is small. Moreover it shows

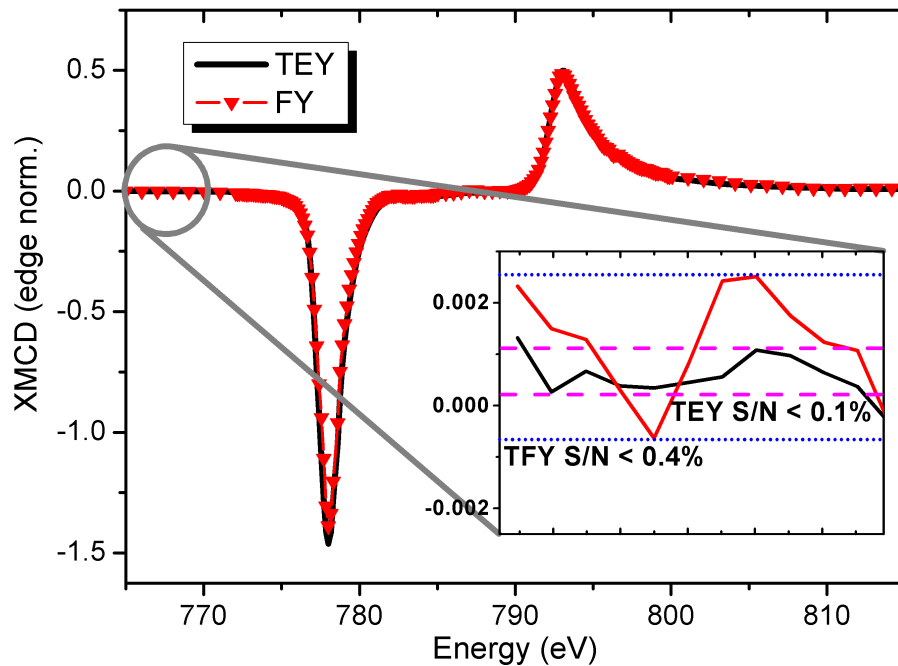


Figure 6.10: Comparison of XMCD spectra obtained by measuring TEY and TFY. The different amplitude at the  $L_3$  edge results from self-absorption of the TFY signal. The field has been flipped at each energy point. The inset shows the noise level of both measurements at an integration time of 400 ms.

that there is no reduction of the magnetisation in the surface region due to e.g. oxidation. The inset in Fig. 6.10 shows the signal to noise ratio for both modes, TEY and TFY as calculated from the curves in the marked area. The integration time of both measurements was 400 ms per point. Note that the absolute noise level of the TEY signal is only 5 fA.

The magnetic spin and orbital moments have been calculated from Fig. 6.9(a) and Fig. 6.10 using the XMCD sum rules. For more details on sum rules and their



calculations refer to Sections 3.3.4, 5.3.2, and 5.1.3. Therefore, a standard two-step background is subtracted from the XAS spectra and the XAS and XMCD curves are integrated. Assuming a number of  $3d$  holes of  $n_H = 2.49$  [89] and taking the  $45^\circ$  alignment between incident beam and applied magnetic field into account, a spin moment per Co atom of  $m_S = 1.74 \mu_B$  and an orbital moment of  $0.16 \mu_B$  is found. These values are slightly increased compared to literature values of thin films [89]. Please note that the calculated values have been corrected for a degree of circular polarization of 90%, the curves in the figures are not corrected.

The second test example is a magnetic, i.e., dichroic, reflectivity curve of the same NiCoO/Co sample at an energy of 776.5 eV, i.e., just before the Co  $L_3$  edge. Fig. 6.11 shows the resulting two reflectivity curves for parallel and antiparallel alignment of the magnetic field and the X-ray polarization. At this energy, the ab-

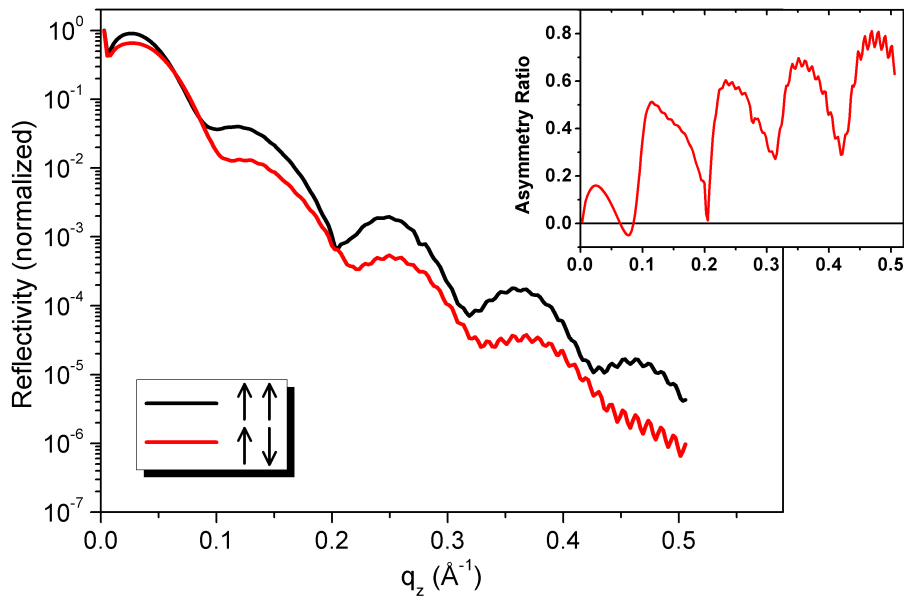


Figure 6.11: Dichroic reflectivity measured before the  $L_3$  edge of Co (776.5 eV) using positive circular polarized light. The inset shows the corresponding asymmetry ratio.

sorption is small and the reflectivity spectrum is dominated by the Co dispersion. The data has been processed according to the scheme described in Section 4.1. A

long periodic oscillation is clearly visible which is related to the thickness of the ferromagnetic cobalt layer. Accordingly this periodicity is also found in the asymmetry between the two field directions which is shown as inset in Fig. 6.11. Besides this, a short period oscillation is found for higher  $q_z$  which can be attributed to interference between the Co/NiCoO interface and the NiCoO/substrate interface thus being the NiCoO layer thickness. This oscillation corresponds to a thickness of roughly  $(570 \pm 10)$  Å. The asymmetry ratio already mentioned represents the magnetic contribution of the reflectivity as it is defined in Section 5.1.5.

Here the reflectivity curve could be measured up to angles of  $40^\circ$  till the signal is too small compared to the noise level. It is noteworthy that the absolute noise level for the reflectivity measurements was roughly  $10 fA$  and is related to dark current fluctuations of the diodes.

Another feature of magnetic X-ray reflectivity is the ability to directly measure element selective hystereses. By measuring the specular reflectivity at maximum XMCD effect at a fixed angle, high quality hysteresis loops for the respective element can be obtained. It has to be mentioned that such hystereses depend on the scattering condition in the sample and their sign and absolute magnitude might therefore depend on the  $k$ -space position. Fig. 6.14 in Section 6.14 shows the hysteresis of the Fe/MnPd sample FD041 described in Section 5.1.1ff measured by VSM, XRMR, and MOKE, respectively. As can be seen, the hysteresis measured by XRMR resembles perfectly the VSM reference curve. The slight field offset is related to the coercivity of the reflectometers' magnet yoke (see 6.1.4) or to the calibration of the Hall probe. Anyway the shape is perfectly reproduced by XRMR clearly proving the capability of the method.

### 6.3 L-MOKE Add-On

An important point prior to any XRMR investigation at the synchrotron is to characterize the magnetic properties of the sample. This is usually done using either SQUID or VSM magnetometry. However, a severe drawback of such an investigation is that the sample has to be remounted or attached to another holder which always brings the risk of damaging the sample surface. It is therefore

preferable to have a non-contact method for measuring magnetisation hysteresis in a broad temperature range – the answer to this demand was an attachable in-situ, Laser-based Magneto-Optical Kerr Effect (MOKE) system for the reflectometer experiment.

The advantages of such an “add-on” MOKE are perfectly obvious: An in-situ MOKE allows using all facilities of the reflectometer experiment like e.g. the same magnetic field as in the XRMR experiment, a broad temperature range (also elevated temperatures), UHV conditions for annealing processes and the sample must not be removed or remounted. Besides it allows measuring the hysteresis also during a beamtime, for example after an annealing process or after changing the samples azimuthal orientation.

In the following sections the longitudinal Laser-MOKE setup as it has been set up throughout the last years will be presented. The first section briefly introduces the the magneto-optical Kerr effect. In the second section, the general setup and the optical path will be introduced in detail. The section closes with a very brief presentation of test measurements which show the potential and capabilities of the experiment.

### 6.3.1 The Magneto Optical Kerr Effect

The magneto-optical Kerr effect is the change of the polarization and also often intensity of an electromagnetic wave upon reflection from the surface of a magnetic material. The decrease of the intensity and the rotation of the polarization are directly proportional to the magnetisation. Three different kinds of MOKE can be distinguished by the orientation of the magnetisation of the sample with respect to the scattering plane: Longitudinal MOKE, transverse MOKE and polar MOKE.

In the longitudinal MOKE geometry, the scattering plane and the magnetisation are parallel and the magnetisation is in-plane with respect to the reflecting surface. The transverse geometry has the magnetisation perpendicular to the scattering plane but still in-plane while the polar geometry is for normal to surface magnetisation. Fig. 6.12 shows the three typical geometries for measurement of the magneto-optical Kerr effect. For more details on the magneto-optical

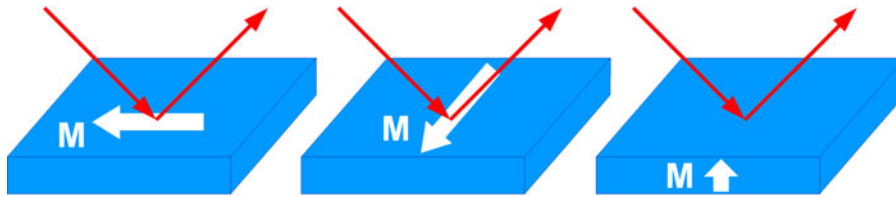


Figure 6.12: The three different standard MOKE geometries. From left to right, longitudinal MOKE, transverse MOKE and polar MOKE.

Kerr effect and the experimental realization of such an experiment refer to references [134–136] and especially to the Ph.D. theses by A. Tillmanns [137] and T. Schmitte [138].

### 6.3.2 Experimental Setup – the Optical Path

As mentioned in the introduction, the MOKE benefits from the existing infrastructure provided by the reflectometer setup. The maximum applicable magnetic field is  $\approx 260$  mT with the 30 mm gap and the temperature range for measurements is 40 to 480 K (compare 6.1).

Besides the advantages, the reflectometer requires the MOKE to be easily removable to allow baking the system. Special shaped adapters which can be imposed on a CF40 UHV flange have been designed to fast and easily fix the optical setup to the UHV chamber. As mounting for the optical components, the *Microbench* system from Linos is used. It consists of four high precision stainless steel rods and mounting plates. The whole MOKE setup attached to the main chamber of the reflectometer is outlined in Fig. 6.13. In the following, the optical path of the experiment will be discussed step-by-step in the same order as the light passes it. The first element is a *Flexpoint* laser module commercially bought from Laser Components GmbH. The Flexpoint FP-64/16ADE-AV-SD5-1MHz provides linear polarized light with  $\lambda = 638$  nm and a maximal power of 16 mW. The power output of the laser module can be tuned from 0 to 16 mW by a screw on the backside. Moreover this module allows modulating the intensity by an external voltage (0...5 V) with an arbitrary waveform. This feature is important since it allows using the Lock-In technique to improve the signal to noise ratio considerably [137]

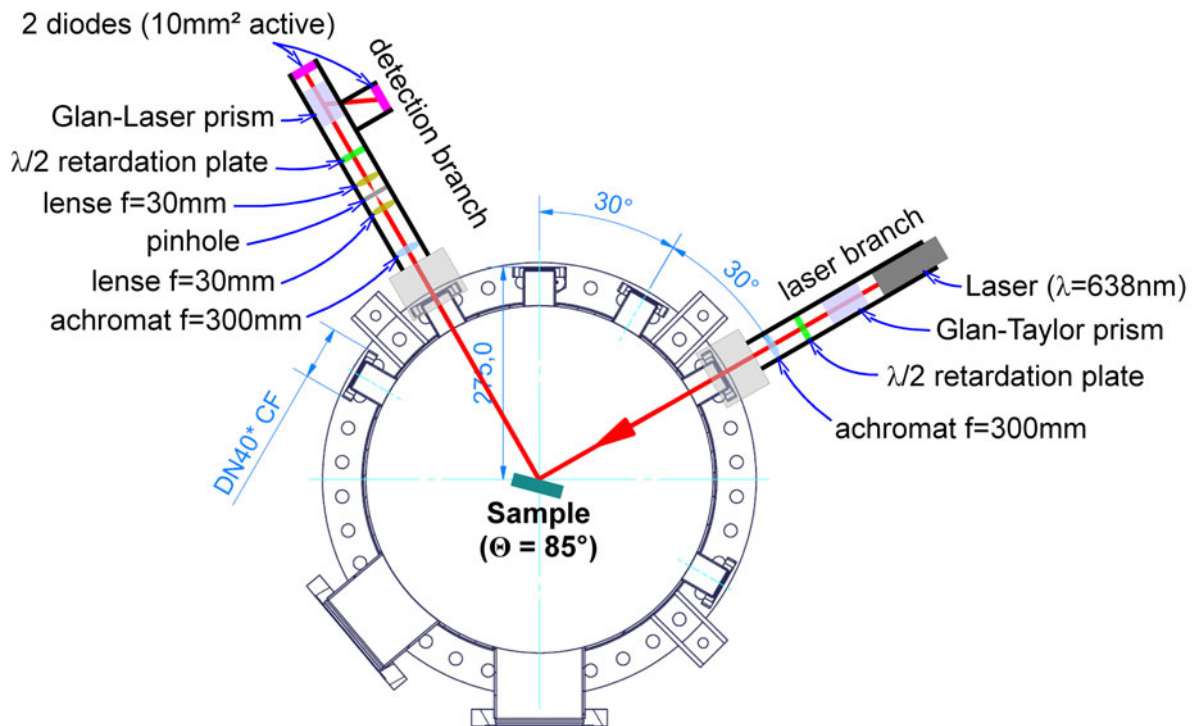


Figure 6.13: Schematical drawing of the MOKE setup attached to two of the CF40 flanges of the reflectometer UHV chamber.

without a chopper. The modulation frequency for the Laser should be well above 50 Hz and far away from its multiples to avoid noise from the power line.

Next, the modulated, linear polarized light passes through a Glan-Taylor prism which is oriented with its optical axis coinciding with the Lasers' polarisation plane. Glan-Taylor prisms have an extinction ratio of  $5 \times 10^{-5}$  or 99.995 % linear polarization whereas typical laser modules only provide polarization degrees of 95 % to 99 %.

The Glan-Taylor prism is followed by a rotatable  $\lambda/2$  retardation plate. These plates rotate the polarization plane by doubling the angle  $\Theta$  between the incident plane and the crystals optical axis. The plate allows rotating the plane of the light without having to align the prism and Laser module every time. The last element on this branch is an achromat with 300 mm focal length for focusing the beam onto the sample.

The sample is mounted in the centre of the reflectometer and set to an angle

of incidence of roughly  $85^\circ$  with respect to the usual X-ray direction. The light is then incident at an angle of  $45^\circ$  which is the optimum angle for longitudinal MOKE [135, 137].

On the detection branch, the light passes again through an achromat which parallelizes the beam. Subsequently two standard convex lenses with a focal length of  $f = 30$  mm in combination with a pin hole follow. The lenses are placed exactly 60 mm from each other and the pin hole sits in the focus point. This setup effectively eliminates double reflections and diffractions from the optical path.

The last two components are a  $\lambda/2$  retardation plate to rotate the polarization plane of the light followed by a Glan-Laser prism to split the beam in its ordinary and extraordinary parts. The former is important to align the polarization plane with respect to the subsequent prism. Finally, two standard photo diodes are used to detect the two components from the Glan-Laser prism.

The current signals from the diodes are converted to voltages using a home-made current-to-voltage converter based on a simple operation amplifiers. The same electronics also inverts the resulting voltages thus providing the signals  $A$ ,  $-A$ ,  $B$  and  $-B$ . Those are then detected by two Stanford Research SR830 100 kHz DSP lock-in amplifiers in a way that one measures  $A - B$  and the other  $A + B$ . The formula which relates the asymmetry signal measured here with the longitudinal Kerr effect, i.e., the Kerr rotation is given in reference [137] page 16ff.

### 6.3.3 Tests & Results

The example demonstrates the high quality of the MOKE results by comparing them to reference data obtained by standard vibrating sample magnetometry and also by the complementary method of XRMR. As mentioned in Section 5.1 the hysteresis of sample FD041 (a-axis MnPd/Fe) was measured by VSM (Fig. 5.3) and XRMR (Fig. 5.1.7). For comparison the same measurement has been repeated using the MOKE during the same beamtime as the XRMR Fe and Mn hystereses were measured. Fig. 6.14 shows all three measurements, VSM, XRMR, and MOKE in one plot. Note that the XRMR hysteresis as well as the MOKE have been normalized to their saturation values.

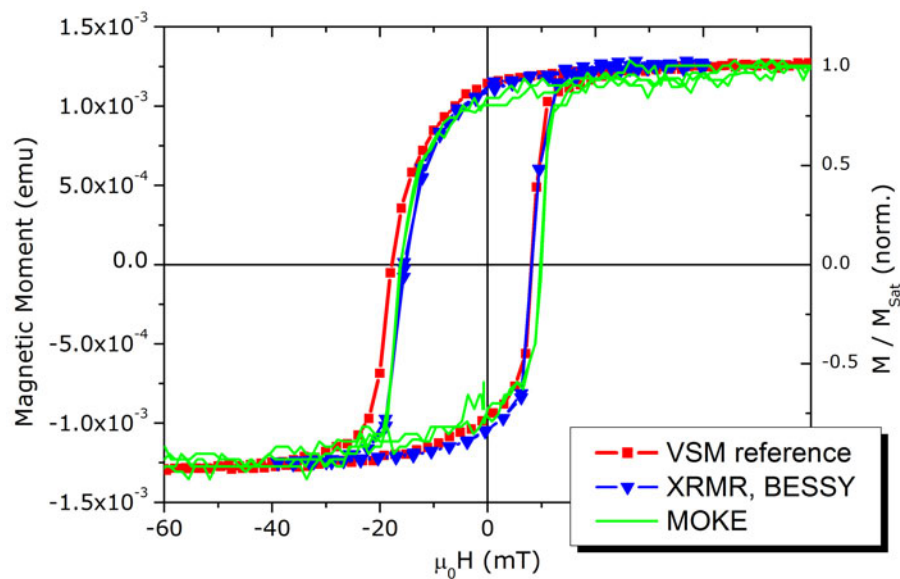


Figure 6.14: Comparison of the XRMR hysteresis (blue) measured at the Fe  $L_3$  edge with a reference curve measured by vibrating sample magnetometry (red). The VSM hysteresis was measured by X. Ji at the University of Washington.

As second example refer to the bachelor thesis of A. Köhl [117] Section 4.6 where a detailed investigation of the azimuthal dependence of the exchange bias loop shift in a FeMn/Co thin film sample is presented. The whole investigation has been measured in the reflectometer setup using the MOKE described here.

## 6.4 ReMagX - A Tool To Fit Magnetic Reflectivity

The development of ReMagX started in 2003 as part of the diploma thesis of Max Harlander [67]. Accordingly, many basic concepts of the program namely the multi-slicing, the calculation of the optical profile, and the implementation of the Parratt algorithm are described there. ReMagX has been improved ever since and some important concepts were added during the course of the work presented here.

The most important feature is a new simulation algorithm. As described in Section 3.4.1, the Parratt algorithm makes a small systematic error when it comes to simulating the magnetic contribution to the scattering amplitude. This error originates from the fact that Parratt neglects any intrinsic changes to the polarization, i.e., it does not account for a change of the ratio between the parallel and perpendicular components of the incident light within the layer stack. Therefore it became necessary to introduce a new method to simulate the reflectivity curve, at least for cases where the polarization changes drastically within the sample. The *Magneto Optical Approach* described in Section 3.4.2 has been successfully implemented in ReMagX to solve this problem.

### 6.4.1 The Matrix Formalism in ReMagX

The magneto-optical approach to describe the specular reflection from a multilayer which was introduced in Section 3.4.2 has been implemented in ReMagX. It is now possible to switch unambiguously between Parratt (compare 3.4.1) and matrix formalism (compare 3.4.2) at any time in the program. An important distinction between the two exists however: the Parratt formalism can use the Nevot & Croce approach to describe the interface roughness analytically (compare [68] and references therein and for the implementation [3, 67]). In contrast the matrix formalism as it has been implemented here requires a slicing of the interface in order to cope with roughness at the interface.



### 6.4.2 Fit Algorithms

A simulated reflectivity curve has to be fitted to the measured data by refining the simulation parameters. Manual refinement of the parameters is very tedious. It is more efficient to use mathematical optimization to achieve this task. ReMagX uses three principal methods for fitting the simulated reflectivity curve as obtained by one of the methods described in 3.4 to the measured data.

- The downhill simplex algorithm (a.k.a. Nelder-Mead method) [139].
- The Levenberg-Marquardt algorithm (abbrev. LMA) [140,141].
- A so called evolution strategy a.k.a. genetic algorithm (abbrev. GA). More information can be found in [142,143] and especially [144].

all three methods have their pros and cons and in the following the most important of these shall be reviewed. The downhill simplex algorithm is an optimization algorithm for non-linear functions of many parameters which can be used for curve fitting. The algorithm does not have to evaluate the derivative of the function to determine the gradient but instead obtains it by an approximation process [139]. This makes the algorithm very robust and versatile. As representative of the classical downhill algorithms it is very vulnerable to local minima. The algorithm approximates the gradient and follows it to the next minimum, independent of whether its a local one or the global minimum (which is the one searched for).

The Levenberg-Marquardt algorithm (LMA) is, like the Simplex, a downhill algorithm but is based on the so called least squares method [140,141]. In contrast to the Simplex algorithm, it obtains the gradient by evaluating the derivative. The Levenberg-Marquardt converges faster than the simplex but descends even faster into the next minimum which makes it difficult for the LMA to find the global minimum if the parameter landscape is very hilly (as is the case for reflectivity).

The newest fit algorithm available is the Genetic Algorithm (GA) which is a metaheuristic optimization technique from the class of the so called evolution algorithms [144]. GA is not based on a purely downhill movement in the parameter landscape but follows an approach which is best described as: arbitrary scanning of the landscape followed by a condensation in the region of the global minimum

(for the given parameter set). In contrast to downhill algorithms it is very robust against trapping in local minima.

The principle idea is to create a population of  $N$  individuals, which means here simulated reflectivity curves. Then these curves are compared to the measured data using an evaluation function (e.g.  $\chi^2$  or weighted least squares.) to obtain the so called fitness of each individual. Individual in this context means a simulated reflectivity curve. Only individuals with good fitness are taken and used to create a new generation by mixing two individuals (parents) and then mutating the child to a certain extent. The new generation is formed from the children of the first plus several fittest individuals from the old generation. This process is repeated till a certain convergence is reached. Fig. 6.15 illustrates the individual steps of the GA in more detail.

The big advantage of the GA is, that due to the large number of arbitrarily generated individuals, it is able to scan the parameter landscape very fast. Moreover it is far more effective in finding the global minimum compared to the downhill algorithms. Consequently it is extremely well suited for fitting reflectivity data as has been shown already [142,143].

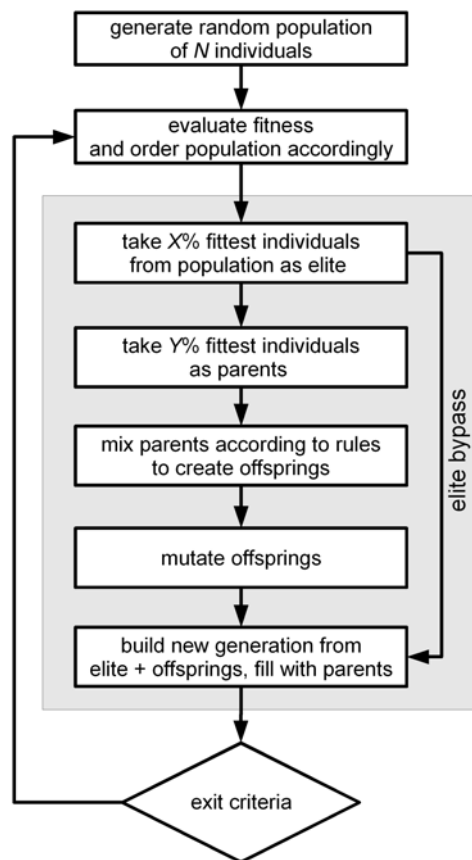


Figure 6.15: Principle workflow for the genetic algorithm as it has been implemented in ReMagX.



## 7 Summary

### Results

The aim of this work was to answer several fundamental questions about the microscopic origin of the exchange bias effect by using X-ray magnetic reflectivity and X-ray magnetic circular dichroism. Three different exchange bias systems, each of with special properties tailored to the individual problem, were investigated for that purpose.

The magnetic configuration at the interface between ferro- and antiferromagnet was investigated in the Fe/MnPd exchange bias system. Energy dependent scattering was performed on the Co/FeMn system to reveal the spectroscopic character of the pinned uncompensated moments in this system. Finally, the exchange bias system Co/NiCoO, a system with an oxide antiferromagnet, was investigated to reconfirm the former findings for this class of systems as well. This summary of the key findings follows the same chronology as does the detailed presentation of the results in Section 5.

A precise map of the magnetic configuration at the interface with the ferromagnetic Fe is obtained from the XRMR investigation of Mn in the antiferromagnetic alloy MnPd.

- A roughly 1 to 2 monolayer, or  $(4 \pm 1)$  Å thick region of rotatable Mn is found directly at the interface with the Fe.

This result clearly proves the existence of rotatable Mn in the antiferromagnet. The reason for this effect is very likely to be the strong ferromagnetic coupling in the ferromagnet which affects neighboring manganese atoms on the other side of the interface. This interpretation is stressed by the fact that the region of induced ferromagnetism shows a one-to-one correspondence with the interface roughness

and that the rotatable Mn shows exactly the same magnetisation reversal such as the Fe.

Anticipating the results from the two other systems investigated here and also taking into account findings from other groups, the existence of rotatable moments in the antiferromagnet of an exchange bias system seems to be a general intrinsic attribute of the phenomenon.

The magnetic depth profile of pinned moments in the Mn was also obtained from the same XRMR investigation of the Fe/MnPD exchange bias system.

- It is found that pinned uncompensated Mn moments exist deeper in the antiferromagnet in a  $(13 \pm 1)$  Å broad region close to the interface.

A direct correlation of these moments with the exchange bias loop shift  $H_{eb}$  is found from the azimuthal dependence.

The second investigated system is a bilayer structure consisting of ferromagnetic cobalt grown on antiferromagnetic  $\gamma$ -FeMn. By measuring the energy dependent scattering at the Fe  $L_{2,3}$  edge, the spectral character of the pinned uncompensated Fe moments in this system is investigated. To prove the direct correlation of the observed spectrum with the exchange bias effect in the system, two different samples with a unique on-off character of the exchange bias effect are compared. The first sample shows a pronounced temperature behaviour which leads to no loop shift, thus  $H_{eb} = 0$  at room temperature while for lower temperatures a large exchange bias of  $H_{eb} \approx 30$  mT at 50 K occurs. The second sample investigated here was measured parallel and perpendicular to the exchange bias effect. Due to the unidirectional character of  $H_{eb}$  no loop shift is observed when measuring in the perpendicular direction. The same on and off behaviour should be found in the signal from the pinned uncompensated Fe moments.

The energy dependent scattering at a fixed  $q_z$  value was investigated in both samples at the Fe L edge to identify the signal from the pinned uncompensated Fe moments in the antiferromagnet. A direct correlation of the signal with the loop shift is found from comparing the signal for the situation with exchange bias to the one without.

- A relation between the observed difference signal attributed to pinned mo-

---

ments in the antiferromagnet and the exchange bias loop shift observed by magnetometric means is proven.

- The shape of the difference signal from the pinned uncompensated Fe moments in the Co/FeMn exchange bias system clearly resembles a spectrum which is only dominated by an orbital momentum.
- This behaviour is found in both samples and comes/goes in both cases with the loop shift.

This implies that the magnetic moments responsible for the exchange bias loop shift are mostly orbital moments. The shape of the signal and also the relation of this signal with the exchange bias loop shift is ascertained beyond doubt by the comparative character of the investigation and the tests performed.

Another implication of this finding is the fact that the spin moment of the Fe atoms seems to be rotatable, otherwise it should contribute significantly to the difference spectrum. If the orbital momentum is pinned but the associated spin moment rotates then the spin-orbit coupling in this system seems to be overcome. This result just follows from the observed spectral shape and has to be proven by a more thorough investigation of this feature in the future.

As third and last exchange bias system, oxide NiCoO as antiferromagnet in combination with Co as ferromagnet was investigated by XMCD and magnetometric means.

- A  $\sim 10\%$  decrease of the Co moment is found from the XMCD investigation when cooling the sample from room temperature to 80 K.

A detailed analysis of the temperature behaviour of the corresponding hysteresis loops reveals that this reduction is related to ferromagnetic, i.e., rotatable Co presumably in the antiferromagnetic NiCoO. The majority of the vanishing Co moments couple antiferromagnetic at lower temperatures and thus are compensated and not rotatable anymore. A small fraction is pinned in an uncompensated way.

## Experimental Achievements

In the course of this thesis several improvements and advances in the measurement technique of XRMR were achieved. The most important one is certainly the new UHV magnetic reflectometer for soft X-ray energies which was built and tested during the first  $1\frac{1}{2}$  years of this work. This new setup, which is described in detail in Section 6.1 and in the corresponding publication [79], brings a considerable improvement in all relevant parameters of such an instrument. The most notable features of the new reflectometer experiment are:

- UHV conditions (typically better than  $5 \cdot 10^{-10}$  mbar) for all experiments.
- Full measurement range from  $\Theta = 0^\circ$  to  $70^\circ$  with encoder positioning with a resolution of  $\Delta\Theta = 0.0003^\circ$ .
- A magnetic field up to 260 mT with 30 mm gap (630 mT with 10 mm gap).
- Simultaneous measurement of total electron yield, fluorescence yield, reflectivity, diffuse-scattering and  $I_0$ .
- A temperature range from 38 K up to 480 K for all measurements.
- A precise, motor driven  $360^\circ$  azimuthal sample rotation.
- An in-situ Laser-MOKE for magnetic characterization of the samples.
- A fast loadlock and sample transfer with magazine for storage of up to 6 samples under UHV conditions.
- Highly accurate position monitoring of the incident X-ray beam (better than  $10 \mu\text{m}$ ).

With these parameters the instrument is extremely versatile and can be used to investigate a broad variety of magnetic and non-magnetic systems in a fast and reliable way and under varying conditions. A good measure of the success and outstanding performance of this instrument is the fact that in the two years since its completion, several very successful weeks of beamtime were carried out by the authors own group and collaborating groups.

Besides the achievements of the instrument, several very important improvements in reflectivity data processing have been realized throughout this work:



- 
- The implementation of the magneto-optical method (see Section 3.4.2) as a new, more precise calculation method for magnetic reflectivity.
  - The adaption and realization of a novel fitting routine based on evolution strategies which allows fitting more complex sets of parameters with less iterations (see Section 6.4).
  - Finally, a new speed optimized way of calculating the Kramers-Kronig transform necessary for determining the optical constants of the samples was developed and is described in Section 4.2.

Together, the instrumental and the processing improvements mean a big leap forward for XRMR and were a necessary prerequisite for the experimental results presented here.

## Outlook

This summary will close with an outlook for both aspects of the thesis, for the X-ray magnetic reflectivity and for exchange bias.

Two major improvements will increase the capabilities and physical information obtainable from XRMR: The first is replacing the currently used detector diode with a 2D detector in the form of a movable, UHV-capable CCD. This would enable measuring and quantifying the diffuse magnetic scattering. Such a measurement provides information from the in-plane variations of the magnetism in an element selective. This would enable investigations of e.g. the magnetic domain formation in the sample.

Another feature, which has already been used for this thesis although only in a qualitative way, is the energy dependent scattering. This technique likely has the biggest potential since it not only provides spectral information but also contains information on the depth distribution of this spectral information. A quantitative analysis in the form of a fitting procedure for energy scans at a constant momentum transfer  $q_z$  will eventually allow determination of spectral data such as XAS and XMCD in a depth resolved way. It should be noted that the above mentioned CCD is necessary for this quantitative analysis.

As for the exchange bias, the next steps which have to be taken are related to the spectral shape, i.e., the character of the pinned uncompensated moments in the antiferromagnet. Certainly the most important one is to identify the spectral character of those moments in other exchange bias antiferromagnets and thus verify the findings presented here. Another very important point is to quantitatively analyse the orbital moments to obtain a new model for the exchange bias effect. Finally, a direct proof in the form of magnetic mapping such as the one obtained for the Fe/MnPd interface, has to be obtained for the pinned moments to verify that the corresponding spin moment is really rotatable.

## Bibliography

- [1] J. P. Hannon, G. T. Trammell, M. Blume, and D. Gibbs, *Physical Review Letters*, vol. 61, no. 10, p. 1245, 1988.
- [2] D. Lott, *Magnetic X-ray Reflectivity*. PhD thesis, Ludwig-Maximilians-Universität München, 2001.
- [3] J. Geißler, *Magnetische Streuung an Grenz- und Viellagenschichten*. PhD thesis, Julius-Maximilians-Universität Würzburg, 2003.
- [4] U. Grüner, *Resonante magnetische Röntgenuntersuchungen an einem Co/Cu/Co-Schichtsystem und an Platinlegierungen*. PhD thesis, Universität Stuttgart, 2006.
- [5] R. C. O’Handley, *Modern Magnetic Materials: Principles and Applications*. Wiley-Interscience, 1999.
- [6] J. Stöhr and H. Siegmann, *Magnetism*. Springer, 1 ed., 2006.
- [7] H. Kronmüller and S. S. P. Parkin, eds., *Handbook of Magnetism and Advanced Magnetic Materials*. Chichester ; Weinheim [u.a.]: Wiley, 2007.
- [8] T. Mayer-Kuckuk, *Atomphysik. Eine Einführung*. Teubner Verlag, 5., durchges. u. erw. a. ed., 2007.
- [9] B. T. Jonker, A. T. Hanbicki, D. T. Pierce, and M. D. Stiles, *Journal of Magnetism and Magnetic Materials*, vol. 277, pp. 24–28, 2004.
- [10] E. Goering, *Untersuchungen zur mikroskopischen Ursache der magnetokristallinen Anisotropie mit Hilfe des magnetischen Röntgenzirkulardichroismus und der resonanten magnetischen Röntgenreflektometrie*. Habilitation, Julius-Maximilians-Universität Würzburg, 2003.
- [11] C. Kittel, *Introduction to Solid State Physics*. Wiley, 7 ed., 1995.

- 
- [12] P. Bruno, *Physical origins and theoretical models of magnetic anisotropy*. Jülich: Forschungszentrum Jülich, 1993.
- [13] G. van der Laan, *Journal of Physics: Condensed Matter*, vol. 10, no. 14, pp. 3239–3253, 1998.
- [14] H. Kronmüller, *Manuskript zu Vorlesung Magnetismus Teil 1*. Universität Stuttgart, 1995.
- [15] A. Hubert and R. Schäfer, *Magnetic Domains: The Analysis of Magnetic Microstructures*. Springer, corrected ed., 2008.
- [16] E. Stoner and E. Wohlfarth, *Nature*, vol. 160, no. 4071, pp. 650–651, 1947.
- [17] E. C. Stoner and E. P. Wohlfarth, *Philosophical Transactions of the Royal Society of London. Series A, Mathematical and Physical Sciences*, vol. 240, pp. 599–642, 1948.
- [18] F. Radu and H. Zabel, *Exchange Bias Effect of Ferro-/Antiferromagnetic Heterostructures*, vol. 227 of *Springer Tracts in Modern Physics*, pp. 97–184. Springer Berlin / Heidelberg, 2008.
- [19] W. H. Meiklejohn and C. P. Bean, *Physical Review*, vol. 105, p. 904, 1957.
- [20] W. H. Meiklejohn, *Journal of Applied Physics*, vol. 33, pp. 1328–1335, 1962.
- [21] S. Brück, J. Sort, V. Baltz, S. Suriñach, J. Muñoz, B. Dieny, M. Baró, and J. Nogués, *Advanced Materials*, vol. 17, no. 24, pp. 2978–2983, 2005.
- [22] J. Nogués and I. K. Schuller, *Journal of Magnetism and Magnetic Materials*, vol. 192, pp. 203–232, 1999.
- [23] A. E. Berkowitz and K. Takano, *Journal of Magnetism and Magnetic Materials*, vol. 200, pp. 552–570, 1999.
- [24] M. Kiwi, *Journal of Magnetism and Magnetic Materials*, vol. 234, pp. 584–595, 2001.
- [25] R. Jungblut, R. Coehoorn, M. T. Johnson, J. aan de Stegge, and A. Reinders, in *38th Annual Conference on Magnetism and Magnetic Materials*, vol. 75, (Minneapolis, Minnesota (USA)), pp. 6659–6664, AIP, 1994.

- [26] P. Blomqvist, K. M. Krishnan, and H. Ohldag, *Physical Review Letters*, vol. 94, no. 10, p. 107203, 2005.
- [27] N. Kurti, ed., *Selected Works of Louis Néel*. New York: Gordon Breach, 1988.
- [28] A. P. Malozemoff, *Physical Review B*, vol. 35, no. 7, p. 3679, 1987.
- [29] Y. Imry and S. Ma, *Physical Review Letters*, vol. 35, p. 1399, 1975.
- [30] U. Nowak, K. D. Usadel, J. Keller, P. Miltényi, B. Beschoten, and G. Güntherodt, *Physical Review B*, vol. 66, p. 014430, 2002.
- [31] F. Offi, W. Kuch, L. I. Chelaru, K. Fukumoto, M. Kotsugi, and J. Kirschner, *Physical Review B*, vol. 67, no. 9, p. 094419, 2003.
- [32] F. Radu, A. Nefedov, J. Grabis, G. Nowak, A. Bergmann, and H. Zabel, *Journal of Magnetism and Magnetic Materials*, vol. 300, no. 1, pp. 206–210, 2006.
- [33] S. Brück, E. Goering, Y. J. Tang, G. Schütz, and A. E. Berkowitz, *Journal of Magnetism and Magnetic Materials*, vol. 310, no. 2, Part 3, pp. 2316–2318, 2007.
- [34] M. R. Fitzsimmons, B. J. Kirby, S. Roy, Z. Li, I. V. Roshchin, S. K. Sinha, and I. K. Schuller, *Physical Review B*, vol. 75, p. 214412, 2007.
- [35] J. M. Tonnerre, M. D. Santis, S. Grenier, H. C. N. Tolentino, V. Langlais, E. Bontempi, M. Garcia-Fernandez, and U. Staub, *Physical Review Letters*, vol. 100, p. 157202, 2008.
- [36] S. Brück, G. Schütz, E. Goering, X. Ji, and K. M. Krishnan, *Physical Review Letters*, vol. 101, no. 12, pp. 126402–4, 2008.
- [37] D. Mauri, E. Kay, D. Scholl, and J. K. Howard, *Journal of Applied Physics*, vol. 62, no. 7, pp. 2929–2932, 1987.
- [38] R. L. Stamps, *Journal of Physics D: Applied Physics*, vol. 33, no. 23, pp. R247–R268, 2000.
- [39] J. Kouvel and C. G. Jr., *Journal of Physics and Chemistry of Solids*, vol. 11, pp. 220–225, 1959.

- [40] J. Kouvel, *Journal of Physics and Chemistry of Solids*, vol. 24, pp. 795–822, 1963.
- [41] R. K. Zheng, H. Liu, X. X. Zhang, V. A. L. Roy, and A. B. Djurisić, *Applied Physics Letters*, vol. 85, no. 13, pp. 2589–2591, 2004.
- [42] H. Wang, T. Zhu, K. Zhao, W. N. Wang, C. S. Wang, Y. J. Wang, and W. S. Zhan, *Physical Review B*, vol. 70, no. 9, p. 092409, 2004.
- [43] N. H. March, P. Lambin, and F. Herman, *Journal of Magnetism and Magnetic Materials*, vol. 44, pp. 1–19, 1984.
- [44] M. Ali, P. Adie, C. H. Marrows, D. Greig, B. J. Hickey, and R. L. Stamps, *Nature Materials*, vol. 6, no. 1, pp. 70–75, 2007.
- [45] C. Schlenker, S. S. P. Parkin, J. C. Scott, and K. Howard, *Journal of Magnetism and Magnetic Materials*, vol. 54-57, pp. 801–802, 1986.
- [46] P. Nordblad, L. Lundgren, and L. Sandlund, *Journal of Magnetism and Magnetic Materials*, vol. 54-57, pp. 185–186, 1986.
- [47] D. Paccard, C. Schlenker, O. Massenet, R. Montmory, and A. Yelon, *Physica Status Solidi B*, vol. 16, no. 1, pp. 301–311, 1966.
- [48] K. Zhang, T. Zhao, and H. Fujiwara, in *J. Appl. Phys.*, vol. 91, pp. 6902–6904, AIP, 2002.
- [49] B. L. Henke, E. M. Gullikson, and J. C. Davis, *Atomic Data and Nuclear Data Tables*, vol. 54, pp. 181–342, 1993.
- [50] C. Cohen-Tannoudji, B. Diu, and F. Laloe, *Quantenmechanik, Teil 1 & 2*. Gruyter, 2. auflage ed., 1999.
- [51] M. Blume, *Journal of Applied Physics*, vol. 57, pp. 3615–3618, 1985.
- [52] J. C. Maxwell, *Lehrbuch der Electricität und des Magnetismus : in 2 Bdn.* Berlin: Springer, 1883.
- [53] J. P. Hannon, G. T. Trammell, M. Blume, and D. Gibbs, *Hyperfine Interactions*, vol. 50, pp. 477–479, 1989.
- [54] J. P. Hill and D. F. McMorrow, *Acta Crystallographica Section A*, vol. A52, pp. 236–244, 1996.

- [55] G. Schütz, W. Wagner, W. Wilhelm, P. Kienle, R. Zeller, R. Frahm, and G. Materlik, *Physical Review Letters*, vol. 58, p. 737, 1987.
- [56] B. T. Thole, P. Carra, F. Sette, and G. van der Laan, *Physical Review Letters*, vol. 68, no. 12, p. 1943, 1992.
- [57] P. Carra, B. T. Thole, M. Altarelli, and X. Wang, *Physical Review Letters*, vol. 70, p. 694, 1993.
- [58] R. Wu, D. Wang, and A. J. Freeman, *Journal of Magnetism and Magnetic Materials*, vol. 132, pp. 103–123, 1994.
- [59] L. G. Parratt, *Physical Review*, vol. 95, p. 359, 1954.
- [60] L. G. Parratt and C. F. Hempstead, *Physical Review*, vol. 94, p. 1593, 1954.
- [61] D. R. Lee, S. K. Sinha, D. Haskel, Y. Choi, J. C. Lang, S. A. Stepanov, and G. Srajer, *Physical Review B*, vol. 68, no. 22, p. 224409, 2003.
- [62] J. Zak, E. R. Moog, C. Liu, and S. D. Bader, *Journal of Applied Physics*, vol. 68, pp. 4203–4207, 1990.
- [63] J. Zak, E. R. Moog, C. Liu, and S. D. Bader, *Journal of Magnetism and Magnetic Materials*, vol. 89, pp. 107–123, 1990.
- [64] J. Zak, E. R. Moog, C. Liu, and S. D. Bader, *Physical Review B*, vol. 43, no. 8, p. 6423, 1991.
- [65] M. Born and E. Wolf, *Principles of Optics: electromagnetic theory of propagation, interference and diffraction of light*. Oxford [u.a.]: Pergamon Pr, 1975.
- [66] P. Colombi, D. K. Agnihotri, V. E. Asadchikov, E. Bontempi, D. K. Bowen, C. H. Chang, L. E. Depero, M. Farnworth, T. Fujimoto, A. Gibaud, M. Jergel, M. Krumrey, T. A. Lafford, A. Lamperti, T. Ma, R. J. Matyi, M. Meduna, S. Milita, K. Sakurai, L. Shabel'nikov, A. Ulyanenkov, A. V. der Lee, and C. Wiemer, *Journal of Applied Crystallography*, vol. 41, pp. 143–152, 2008.
- [67] M. Harlander, *Untersuchung über die Grenzflächenmagnetisierung an (FM) Kobalt- und (AFM) Eisen-Mangan-Schichten*. Diploma thesis, Universität Stuttgart, 2005.

- [68] L. Nevot and P. Croce, *Revue de Physique Appliquee*, vol. 15, no. 3, pp. 761–779, 1980.
- [69] S. A. Stepanov and S. K. Sinha, *Physical Review B*, vol. 61, p. 15302, 2000.
- [70] M. Mansuripur, *Journal of Applied Physics*, vol. 67, no. 10, pp. 6466–6475, 1990.
- [71] J. Zak, E. R. Moog, C. Liu, and S. D. Bader, *Physical Review B*, vol. 46, p. 5883, 1992.
- [72] R. M. Azzam and N. M. Bashara, *Ellipsometry and Polarized Light*. Elsevier Science Publishing Co Inc, reprint ed., 1987.
- [73] B. L. Henke, E. M. Gullikson, and J. C. Davis, “Henke-Gullikson atomic scattering factors.” [http://henke.lbl.gov/optical\\_constants/](http://henke.lbl.gov/optical_constants/), 2008.
- [74] C. T. Chantler, K. Olsen, R. A. Dragoset, J. Chang, A. R. Kishore, S. A. Kotochigova, and D. S. Zucker, “Chantler atomic scattering factors.” <http://physics.nist.gov/ffast>, 2005.
- [75] C. T. Chantler, *Journal of Physical and Chemical Reference Data*, vol. 24, no. 1, pp. 71–643, 1995.
- [76] C. T. Chantler, *Journal of Physical and Chemical Reference Data*, vol. 29, pp. 597–1056, 2000.
- [77] R. de L. Kronig, *Journal of the Optical Society of America*, vol. 12, pp. 547–557, 1926.
- [78] K. Ohta and H. Ishida, *Applied Spectroscopy*, vol. 42, no. 6, pp. 952–957, 1988.
- [79] S. Brück, S. Bauknecht, B. Ludescher, E. Goering, and G. Schütz, *Review of Scientific Instruments*, vol. 79, no. 8, pp. 083109–6, 2008.
- [80] S. Gold, *Angle- and temperature dependence of the magnetocrystalline anisotropy energy and the microscopic magnetic moments of the ferromagnetic half metal CrO<sub>2</sub>*. PhD thesis, Julius-Maximilians-Universität Würzburg, 2006.
- [81] R. Nakajima, J. Stöhr, and Y. U. Idzerda, *Physical Review B*, vol. 59, no. 9, p. 6421, 1999.



- [82] N. C. Koon, *Physical Review Letters*, vol. 78, p. 4865, 1997.
- [83] T. C. Schulthess and W. H. Butler, *Physical Review Letters*, vol. 81, p. 4516, 1998.
- [84] W. Kuch, L. I. Chelaru, F. Offi, J. Wang, M. Kotsugi, and J. Kirschner, *Nature Materials*, vol. 5, pp. 128–133, 2006.
- [85] G. Schütz, E. Goering, and H. Stoll, *Synchrotron radiation techniques based on X-ray magnetic circular dichroism*, vol. 3, p. 3064. Chichester ; Weinheim [u.a.]: Wiley, 2007.
- [86] H. Ohldag, H. Shi, E. Arenholz, J. Stöhr, and D. Lederman, *Physical Review Letters*, vol. 96, no. 2, p. 027203, 2006.
- [87] J. Geissler, E. Goering, M. Justen, F. Weigand, G. Schütz, J. Langer, D. Schmitz, H. Maletta, and R. Mattheis, *Physical Review B*, vol. 65, no. 2, p. 020405, 2001.
- [88] L. Pál, E. Krén, G. Kádár, P. Szabó, and T. Tarnóczy, *Journal of Applied Physics*, vol. 39, pp. 538–544, 1968.
- [89] C. T. Chen, Y. U. Idzerda, H. Lin, N. V. Smith, G. Meigs, E. Chaban, G. H. Ho, E. Pellegrin, and F. Sette, *Physical Review Letters*, vol. 75, p. 152, 1995.
- [90] P. Blomqvist, K. M. Krishnan, and D. E. McCready, *Journal of Applied Physics*, vol. 95, pp. 8019–8022, 2004.
- [91] N. Cheng, J. Ahn, and K. M. Krishnan, in *J. Appl. Phys.*, vol. 89, pp. 6597–6599, AIP, 2001.
- [92] W. L. O’Brien and B. P. Tonner, *Physical Review B*, vol. 50, no. 5, p. 2963, 1994.
- [93] J. Fujii, F. Borgatti, G. Panaccione, M. Hochstrasser, F. Maccherozzi, G. Rossi, and G. van der Laan, *Physical Review B*, vol. 73, pp. 214444–5, 2006.
- [94] S. Voss, M. Fonin, U. Rudiger, M. Burgert, U. Groth, and Y. S. Dedkov, *Physical Review B*, vol. 75, no. 4, pp. 045102–7, 2007.
- [95] B. T. Thole, R. D. Cowan, G. A. Sawatzky, J. Fink, and J. C. Fuggle, *Physical Review B*, vol. 31, p. 6856, 1985.

- [96] S. Andrieu, E. Foy, H. Fischer, M. Alnot, F. Chevrier, G. Krill, and M. Piecuch, *Physical Review B*, vol. 58, p. 8210, 1998.
- [97] J. Mullay, *Estimation of atomic and group electronegativities*, pp. 1–25. 1987.
- [98] R. Carboni, S. Giovannini, G. Antonioli, and F. Boscherini, *Physica Scripta*, vol. T115, pp. 986–988, 2005.
- [99] E. Goering, S. Gold, and A. Bayer, *Applied Physics A: Materials Science & Processing*, vol. 78, pp. 855–865, 2004.
- [100] I. Schmid, P. Kappenberger, O. Hellwig, M. J. Carey, E. E. Fullerton, and H. J. Hug, *Europhysics Letters*, vol. 81, p. 17001, 2008.
- [101] T. J. Regan, H. Ohldag, C. Stamm, F. Nolting, J. Lüning, J. Stöhr, and R. L. White, *Physical Review B*, vol. 64, p. 214422, 2001.
- [102] O. Dmitrieva, M. Spasova, C. Antoniak, M. Acet, G. Dumpich, J. Kastner, M. Farle, K. Fauth, U. Wiedwald, H. Boyen, and P. Ziemann, *Physical Review B*, vol. 76, no. 6, pp. 064414–7, 2007.
- [103] E. Goering, M. Lafkioti, and S. Gold, *Physical Review Letters*, vol. 96, no. 3, pp. 039701–1, 2006.
- [104] D. Schmitz, C. Charton, A. Scholl, C. Carbone, and W. Eberhardt, *Physical Review B*, vol. 59, p. 4327, 1999.
- [105] W. Kuch, J. Gilles, S. S. Kang, F. Offi, J. Kirschner, S. Imada, and S. Suga, in *J. Appl. Phys.*, vol. 87, pp. 5747–5749, AIP, 2000.
- [106] H. Umebayashi and Y. Ishikawa, *Journal of the Physical Society of Japan*, vol. 21, pp. 1281–1294, 1966.
- [107] Y. Endoh and Y. Ishikawa, *Journal of the Physical Society of Japan*, vol. 30, pp. 1614–1627, 1971.
- [108] F. Süß and U. Krey, *Journal of Magnetism and Magnetic Materials*, vol. 125, pp. 351–362, 1993.
- [109] J. Kouvel and J. Kasper, *Journal of Physics and Chemistry of Solids*, vol. 24, pp. 529–536, 1963.

- [110] T. C. Schulthess, W. H. Butler, G. M. Stocks, S. Maat, and G. J. Mankey, in *J. Appl. Phys.*, vol. 85, pp. 4842–4844, AIP, 1999.
- [111] J. Wang, W. Kuch, L. I. Chelaru, F. Offi, and M. Kotsugi, *Applied Physics Letters*, vol. 86, no. 12, pp. 122504–3, 2005.
- [112] F. Offi, W. Kuch, and J. Kirschner, *Physical Review B*, vol. 66, no. 6, p. 064419, 2002.
- [113] K. H. Westmacott, S. Hinderberger, and U. Dahmen, *Philosophical Magazine A*, vol. 81, 2001.
- [114] L. Brück, *Annalen der Physik*, vol. 418, no. 3, pp. 233–257, 1936.
- [115] L. Gan, R. D. Gomez, C. J. Powell, R. D. McMichael, P. J. Chen, and J. Egelhoff, *Journal of Applied Physics*, vol. 93, pp. 8731–8733, 2003.
- [116] M. Brück, *Aufbau einer UHV-Oberflächenanalysenapparatur und Untersuchungen an Aluminiumoberflächen*. PhD thesis, Eberhard-Karls-Universität Tübingen, 1984.
- [117] A. Köhl, *Untersuchungen zum Exchange Bias in polykristallinen Co/FeMn-Schichten*. Bachelor thesis, Julius-Maximilians-Universität Würzburg, 2007.
- [118] K. A. Seu, H. Huang, J. F. Lesoine, H. D. Showman, J. Egelhoff, L. Gan, and A. C. Reilly, *Journal of Applied Physics*, vol. 93, pp. 6611–6613, 2003.
- [119] B. T. Bolon, M. Haugen, A. Abin-Fuentes, J. Deneen, C. Carter, and C. Leighton, *Journal of Magnetism and Magnetic Materials*, vol. 309, pp. 54–63, 2007.
- [120] C. W. Leung and M. G. Blamire, *Physical Review B*, vol. 72, no. 5, pp. 054429–7, 2005.
- [121] G. van der Laan, *Physical Review B*, vol. 55, p. 8086, 1997.
- [122] G. van der Laan, *Journal of Physics: Condensed Matter*, vol. 9, no. 18, pp. L259–L265, 1997.
- [123] G. van der Laan and I. W. Kirkman, *Journal of Physics: Condensed Matter*, vol. 4, no. 16, pp. 4189–4204, 1992.

- [124] M. J. Carey and A. E. Berkowitz, *Applied Physics Letters*, vol. 60, pp. 3060–3062, 1992.
- [125] D. Martien, K. Takano, A. E. Berkowitz, and D. J. Smith, *Applied Physics Letters*, vol. 74, no. 9, pp. 1314–1316, 1999.
- [126] A. E. Berkowitz, M. F. Hansen, R. H. Kodama, Y. J. Tang, J. I. Hong, and D. J. Smith, *Physical Review B*, vol. 72, no. 13, p. 134428, 2005.
- [127] K. Takano, R. H. Kodama, A. E. Berkowitz, W. Cao, and G. Thomas, *Physical Review Letters*, vol. 79, no. 6, p. 1130, 1997.
- [128] J. C. Fuggle, *Unoccupied Electronic States: Fundamentals for XANES, EELS, IPS and BIS*, vol. 69 of *Topics in Applied Physics*, p. 359. Springer, 1992.
- [129] M. Seehra and H. Wijn, *CoO - CuO*, vol. 27 of *Landolt-Börnstein - Group III Condensed Matter*, pp. 16–25. 1992.
- [130] G. Srinivasan and M. S. Seehra, *Physical Review B*, vol. 29, p. 6295, 1984.
- [131] M. Abbate, J. B. Goedkoop, F. M. F. de Groot, M. Grioni, J. C. Fuggle, S. Hofmann, H. Petersen, and M. Sacchi, *Surface and Interface Analysis*, vol. 18, no. 1, pp. 65–69, 1992.
- [132] E. Goering, A. Fuss, W. Weber, J. Will, and G. Schütz, *Journal of Applied Physics*, vol. 88, pp. 5920–5923, 2000.
- [133] L. Tröger, D. Arvanitis, K. Baberschke, H. Michaelis, U. Grimm, and E. Zschech, *Physical Review B*, vol. 46, no. 6, p. 3283, 1992.
- [134] P. N. Argyres, *Physical Review*, vol. 97, no. 2, p. 334, 1955.
- [135] D. A. Allwood, G. Xiong, M. D. Cooke, and R. P. Cowburn, *Journal of Physics D: Applied Physics*, vol. 36, no. 18, pp. 2175–2182, 2003.
- [136] M. Grimsditch and P. Vavassori, *Journal of Physics: Condensed Matter*, vol. 16, no. 9, pp. R275–R294, 2004.
- [137] A. Tillmanns, *Magnetisierungsumkehr und -dynamik in Exchange-Bias-Systemen*. PhD thesis, RWTH Aachen, 2006.

- 
- [138] T. Schmitte, *Bragg-MOKE and Vector-MOKE Investigations: Magnetic Reversal of Patterned Microstripes*. PhD thesis, Ruhr-Universität Bochum, 2002.
- [139] J. A. Nelder and R. Mead, *The Computer Journal*, vol. 7, no. 4, pp. 308–313, 1965.
- [140] K. Levenberg, *The Quarterly of Applied Mathematics*, vol. 2, pp. 164–168, 1944.
- [141] D. W. Marquardt, *SIAM Journal on Applied Mathematics*, vol. 11, pp. 431–441, 1963.
- [142] J. Tiilikainen, V. Bosund, M. Mattila, T. Hakkarainen, J. Sormunen, and H. Lipsanen, *Journal of Physics D: Applied Physics*, vol. 40, no. 14, pp. 4259–4263, 2007.
- [143] A. Ulyanenko and S. Sobolewski, *Journal of Physics D: Applied Physics*, vol. 38, no. 10A, pp. A235–A238, 2005.
- [144] L. Davis, *Handbook Of Genetic Algorithms*. Van Nostrand Reinhold Company, 1 ed., 1991.

## Danksagung

Zum Schluss das eigentlich Wichtigste: Nämlich die Erkenntnis, dass diese Arbeit ohne die Hilfe und Unterstützung durch meine Kollegen, Freunde und Familie so nie möglich gewesen wäre. Daher möchte ich die Gelegenheit nutzen und an dieser Stelle allen danken die zum erfolgreichen Gelingen beigetragen haben, ganz besonders,

Frau Prof. Dr. Gisela Schütz für die freundliche „Wiederaufnahme“ in ihrer Abteilung und die Möglichkeit diese Arbeit durchzuführen.

Herrn Prof. Dr. Jörg Wrachtrup für die freundliche Übernahme des Mitberichts.

Meinem Betreuer PD Dr. Eberhard Goering für das spannende Thema und vier tolle, sehr lehrreiche Jahre. Besonders auch für die Bereitschaft immer 5 Minuten zu opfern um meine „dummen“ Fragen zu beantworten. Und nicht zu vergessen seinen Einsatz und Engagement am Ende.

Meinen Kollegen in der Arbeitsgruppe, Daniela Nolle, Thomas Tietze, Patrick Audehm, Khalid Zafar und Valeriano Ferreras Paz für die super Atmosphäre und gute Zusammenarbeit und das gemeinsame Durchstehen so mancher Strahlzeit.

Mein besonderer Dank gilt Bernd Ludescher für die viele Hilfe und den Einsatz bei der Realisierung des Reflektometer-Experiments. Ohne seine mehr als tausend Zeichnungen und Ideen wäre das Reflektometer sicher nicht so ein Erfolg geworden.

Sebastian Macke der seit Jahren in seiner Freizeit unsere Software ReMagX immer weiter programmiert hat. Nur dank seiner Begeisterung für ein Programm das nur ein Hobby ist war es möglich ReMagX überhaupt weiter zu entwickeln und all die Verbesserungen die im Rahmen dieser Arbeit vorgenommen wurden umzusetzen.

Meinen Kooperationspartnern in den USA, Prof. Kannan M. Krishnan und sein ehemaliger Doktorand X. Ji von der University of Washington in Seattle die mir die hervorragenden Fe/MnPd Proben zur Verfügung gestellt haben. Und Prof. Ami

E. Berkowitz und seiner Gruppe von der University of California in San Diego die mir maßgeschneiderten NiCoO Proben für die Untersuchungen bei BESSY hergestellt haben.

Birgitt Zada und Dr. Willy Mahler von der UE56/2-PGM1 Beamline sowie dem ganzen BESSY II Team für die gute Unterstützung und so wenig Pannen.

Theresa Dragon und Ingrid Sorger für die Präparation der Substrate und der TEM Proben und Ulrike Eigenthaler für die Präparation der TEM Lamellen am FIB.

Fritz Phillipp, Peter Kopold und besonders Vesna Srot vom Stuttgarter Zentrum für Elektronenmikroskopie für die TEM, HR-TEM und EDX/EELS Untersuchungen an meinen Proben.

Den verschiedenen Servicegruppen und Werkstätten am MPI für ihre Unterstützung.

Natürlich auch allen anderen Mitarbeitern in der Abteilung Schütz für vier schöne Jahre. Besonders, Achim Breitling, Lars Bommer, Thomas Bublat, Barbara Panella, Christos Kostoglou, Reinhard Singer, Daniel Steiauf, für „Joe Penas“, die „10 km“, immer Zeit für ein Schwätzchen und eine angenehme Arbeitsatmosphäre.

Last but not least meinen Freunden Sebastian, Matthias, Christoph, Georg, Frank, Peter und Felix für die sehr wichtige, nicht-physikalische „Unterstützung“ in all den Jahren.

Meiner Freundin Ina für einfach alles, vor allem viel Verständnis.

Schließlich meinen Eltern die mir ein sorgenfreies Physikstudium ermöglichten, mich bei all meinen Plänen immer unterstützten und bis zum Schluss nie die Hoffnung aufgegeben haben das ich eines Tages doch noch fertig werde.